Multiple Satellite Communication System for Low Earth Orbit and High Altitude Platforms

Jones, Emma

Award date:
2018

Awarding institution:
University of Bath

Multiple Satellite Communication System for Low Earth Orbit and High Altitude Platforms

Emma Leigh Jones

A thesis submitted for the degree of Doctor of Philosophy

University of Bath
Department of Electronic & Electrical Engineering

September 2018

This page intentionally blank to aid printing.

Abstract

With increasing growth in the number of satellites and aircraft in the high altitude and low Earth orbit region, and the data rates required for the services they provide needing to also increase, there is a need for research to develop new techniques for improved and efficient allocation and management of RF spectrum in the region in support of higher data rates with lower latency.

This thesis contributes a new combined antenna topology and communications architecture supporting satellite and high altitude platform communications, based on a novel cell sector topology and handover methodology, and which allows for spectrum re-use between space, air and ground. By utilising, modifying and combining existing standards, the actions of communications attach, connect, handover, and link tear down are developed to work with the proposed communications architecture in which the cell sectors are in motion relative to platforms and to the ground.

To understand the implications of this problem a mathematical model was constructed, and to improve the fidelity of the model the ITU-R P.2041 standard was implemented in software code and used to provide simulation results using constraint data derived from a detailed literature survey.

Using this model, three experiments were considered to explore approaches to providing improved communication data rate and spectrum usage. Of these it was concluded, using mathematical modelling in software, and using satellite simulation tools, that a solution with a system architecture using RF gradient optic antennas, Space Division Multiple Access (SDMA), Direct Sequence Spread Spectrum Code Division Multiple Access (DSSS-CDMA), protocols from the Third Generation Partnership Project - Universal Mobile Telephony System (3GPP-UMTS), with a Cooperative Multi-Point Multiple Input Multiple Output (CoMP-MIMO)–like architecture was the most successful of the approaches studied in fulfilling the need for a novel improved communications capability for the high altitude, low Earth orbit region.

From this research it was found that there is a way to provide managed spectrum vertical three-dimensional spatial re-use through the creation of communication "moving-cells-in-the-sky", and that these 'cells', analogous in a sense to ground mobile phone cells, can be individually addressed, and data transferred to and from users within each of these three dimensional spatial cells. The methods to achieve this novel capability are described herein.

In addition to concluding how to create such three dimensional communication cells in vertical space, it was found that the cells could support vertical RF spectrum re-use, with the useful and novel feature of allowing ground user equipment to operate using the same RF frequencies as air and space craft with insignificant levels of interference, and with considerable increases in data rates and capacity. Finally the research shows that handover between cells can be achieved based on careful re-use of existing standards for ground mobile phone systems.

The research concluded with the identification of further work, which includes extending the results to other application areas, both on the ground and in space.

.

Table of Contents

List of Publications

Jones, E., “Exploring the mesosphere as a key to understanding exoplanet atmospheres: How to detect a mesosphere on an alien world”, Peer reviewed paper presented at the Royal Astronomical Society (RAS), National Astronomy Meeting (NAM) 2014

This page intentionally blank to aid printing.

List of Figures

This page intentionally blank to aid printing.

List of Tables

This page intentionally blank to aid printing.

List of Abbreviations

2G	Second Generation
3G	Third Generation
3GPP	Third Generation Partnership Project
3GPP2	Third Generation Partnership Project 2
A	Amp
ADS	Airbus Defence and Space
Ah	Amp-hour
AIT	Assembly Integration and Test
AL	Aluminium
ALOHA	Additive Links On-line Hawaii Area
AOCS	Attitude and Orbital Control System
ATDMA	Asynchronous TDMA
BER	Bit Error Rate
BLER	Block Error Rate
BSC	Base Station Controller
CCSDS	Consultative Committee for Space Data Systems
CDMA	Code Division Multiple Access
CFDP	CCSDS File Delivery Protocol
CNES	Centre National D'études Spatiales
CoMP	Cooperative Multi-Point
DAMA	Demand Assigned Multiple Access
dB	Decibel
DE-QPSK	Differentially Encoded QPSK
DLL	Data Link Layer
DOCSIS	Data Over Cable Service Interface Specification
DSN	Deep Space Network
DSSS	Direct Sequence Spread Spectrum
DVB	Digital Video Broadcast
ECSS	European Cooperation for Space Standards
EDRS	European Data Relay Satellite
EIRP	Equivalent Isotropically Radiated Power
ETSI	European Telecommunications Standards Institute
FCC	Federal Communications Commission
FDMA	Frequency Division Multiple Access
FEC	Forward Error Correction
FLOP	Floating Point Operation
FSOC	Free Space Optical Communication
FSPL	Free Space Path Loss
Gbps	Giga-bit per second
GEO	Geosynchronous Earth Orbit
GHz	Giga-Hertz
GMR	GEO Mobile Radio
GNC	Guidance Navigation and Control

GNSS	Global Navigation Satellite System
GPRS	GSM Packet Radio Service
GPS	Global Positioning System
GSM	Global System Mobile
GTO	Geosynchronous Transfer Orbit
HALE	High Altitude Long Endurance
HEO	High Earth Orbit, Highly Eccentric Orbit
HF	High Frequency
HLR	Home Location Register
HPBW	Half Power Band-Width
HTPB	Hydroxyl-Terminated Polybutadiene
IMEI	International Mobile Equipment Identity
Inc	Incorporated
IP	Internet Protocol
IPSec	Internet Protocol Security
ISO	International Standards Organisation
ITU	International Telecommunications Union
KBPS	Kilo-Bit Per Second
kbps	Kilo-Bits Per Second
Kg	Kilogram
Km	Kilometre
LCP	Left hand Circular Polarisation
LEO	Low Earth Orbit
LLC	Limited Liability Company
LNA	Low Noise Amplifier
M2M	Machine to Machine
MALE	Medium Altitude Long Endurance
Mbps	Mega-Bits Per Second
MCC	Mission Control Centre
MEO	Medium Earth Orbit
MF-TDMA	Multi-Frequency TDMA
MHz	Mega-Hertz
MIMO	Multiple Input Multiple Output
MIPS	Millions of Instructions Per Second
MMH	Mono-Methyl Hydrazine
MODIS	Moderate Resolution Imaging Spectrometer
MSC	Master Switching Centre
MTP	Message Transfer Protocol
NASA	National Air and Space Administration
Ni-H2	Nickel Hydride
O3b	The Other 3 Billion
OBC	On-Board Computer
OG2	Orbcomm Generation 2
OOK	On-Off Keying
OQPSK	Offset QPSK
OSI	Open Systems Interconnection

PN	Pseudo Noise
POP	Point Of Presence
PROM	Programmable Read Only Memory
PSK	Phase Shift Keying
QPSK	Quadrature Phase Shift Keying
RAM	Random Access Memory
RCP	Right hand Circular Polarisation
RCS	Return Channel via Satellite
RF	Radio Frequency
RFNA	Red Fuming Nitric Acid
RPAS	Remotely Piloted Air System
RR	Radio Resource
SCC	Satellite Control Centre
SCPS-TP	Space Communications Protocol Specifications TCP
SDMA	Space Division Multiple Access
SDS	Space Data Satellite
SIM	Subscriber Identity Module
SKA	Square Kilometre Array
SSL	Space Systems Loral
SSPA	Solid State Power Amplifier
Tbps	Tera-bit per second
TC	Telecommand
TCP	Transport Control Protocol
TDM	Time Division Multiplexing
TDMA	Time Division Multiple Access
TDRS	Tracking and Data Relay Satellite
TDRSS	TDRS System
TFLOP	Tera-FLOP
TM	Telemetry
TSAT	Transformation Satellite programme
TT&C	Telemetry, Tracking and Control
TV	Television
UAV	Unmanned Aerial Vehicle
UDMH	Unsymmetrical
UDP	Unidirectional Data Protocol
UHF	Ultra High Frequency
UMTS	Universal Mobile Telephony System
UN	United Nations
US	United States (of America)
USA	United Station of America
V	Volts
VHF	Very High Frequency
VHT	Very High Throughput
VLR	Visitor Location Register
VSAT	Very Small Aperture Terminal
W	Watts

This page intentionally blank to aid printing.

Chapter 1

Introduction to the thesis

1.1 Topic and motivation

The issue of the availability of radio spectrum continues to be a driver in the design and development of communications systems. Technological developments have attempted to improve the efficient use of existing spectrum through the use of diversity - frequency, spatial, polarisation, for example - and have optimised the number of users within the spectrum by reducing the overhead in protocols to the point of being close to the channel Shannon limit (as demonstrated by the Digital Video Broadcast - DVB-SX2 waveform [1] for example).

Recent advances in communications protocols have focused on improving signal recovery through coding – turbo and Low Density Parity Code (LDPC) [2], for example – and through increased channel performance with spatial coding – Multiple Input, Multiple Output (MIMO) [3] for example.

Other technological approaches intended to improve the efficient use of spectrum include applying organising principles to the use of existing spectrum using coordination algorithms – white space communication [4], and cognitive radio [5] for example. Other approaches have taken to increasing the amount of spectrum required for the channel and developed waveforms that optimise to this larger resource [6]. A consequence of this latter approach is that there has been an inexorable move to develop communications technologies at higher frequencies – Q, V and W band are currently being developed for new communications systems [7], for example.

Little specific work seems to have been carried out in the area of improved signal cancellation to provide increased spatial use of existing spectrum – Distributed Input, Distributed Output (DIDO) [8] is the only novel approach to have appeared in the last few years. Industry standards, such as the 3GPP mobile telephony protocols

[9] apply interference cancellation – Successive Interference Cancellation (SIC) in 3G UMTS protocols, for example.

Along with ground spectrum availability issues, a similar problem occurs at high altitude in the atmosphere, and in space [10]; satellite and aircraft communication spectrum is limited by transmitted signals from the ground, and ground is limited by transmitted signals from high altitude or space. As such there is no vertical spatial separation of spectrum, which would alleviate the spectrum availability problem, particularly in the high altitude, low orbit environment. The purpose of this thesis is to study the spectrum issue and the electronic systems and infrastructures that could be used to provide alternative solutions to the problem of how to improve spectrum availability for ground and space systems.

The approach taken for this study is a thorough literature review to determine existing and upcoming approaches to communication in the high altitude and low orbit environment; to consider communications systems being developed in other orbits, and for other applications; and to develop a standardised propagation model of the atmosphere to allow realistic comparison of potential alternative solutions to the spectrum availability problem. The study will then move to the development of alternative solutions and will use the propagation model to identify solutions that may provide vertical optimisation of spectrum availability. The study concludes with an analysis of the results; concludes with a recommendation for a way forward; and identifies further work.

1.2 Research objectives and original contributions

The initial premise for this study was to investigate the possibility of providing a vertically ‘layered’ communication capability in the high altitude low Earth orbit region to alleviate spectrum availability issues as increasing numbers spectrum users, requiring higher data rates, are predicted (Section 1). It was determined that there was very little in the literature on such an approach (Section 2), and as such investigation began at first principles by considering RF transmission through the atmosphere and how this might be manipulated to produce distinct and vertically

separable RF regions that could provide spectrum re-use (captured in Section 4.3, Experiment 1 – An Initial Approach).

Though amplitude and phase/frequency modulation approaches were investigated, the outcome was not satisfactory in resolving the fundamental spectrum availability issue. As a result the work was progressed by the addition of coded modulation that would result in spatial correlation regions, and which in essence appears as a translation of GPS from time based to spatial based, termed here 'reverse GPS', (described in Section 4.4 Experiment 2 - The Concept of 'reverse GPS'). Although the results showed promising vertical layering with RF spectrum re-use, ultimately the exquisite positioning and number of transmission nodes required proved inadequate for the wide-scale and practical spectrum re-use required. A new approach was needed.

In the third and last investigation (Section 5 Experiment 3 – Layered Communication with Directional Antennas) the introduction of a number of techniques were considered, which resulted in the selection of directional antennas as the key technology needed to provide vertical spectrum layering. In and of itself the directional antenna approach did not fulfil a generic vertical layering of spectrum re-use, however, but with a combination of lessons learned from the correlated modulation researched in Experiment 2 the directional antenna techniques from Experiment 3 study resulted in a viable solution to the spectrum availability issue by demonstrating vertical spectrum re-use through the provision of RF 'cells in the sky' from a combination of signal processing techniques from satellites in orbit (described and compared against existing techniques in Sections 5 and 6 respectively).

To ensure that all simulations were comparable with each other, and with comparable with other published results, an implementation of the ITU-R P.2041 standard [11] for Earth-Space communication channel was carried out as part of the investigation (described in Section 4. The software code for which is provided in Appendix A). Similarly, to constrain the number of frequencies, and orbital and aircraft altitudes that were used in the simulations, sets of typical values were derived from data refined from the literature review (described in Section 3).

The resulting vertical spectrum re-use technique proposed in this study (summaries in Section 7) is generic and has applicability in other contexts, of particular interest for further work is to consider its application to horizontal spectrum re-use at ground level, as this could potentially provide a new avenue for cellular mobile phone research in the provision of higher data rates to increased numbers of users.

1.3 Structure of the thesis

The study is presented in the order in which it was investigated. Section 2 describes the extensive literature review carried out as background for the study, including a description of the atmosphere and its constituents from an RF perspective; consideration of satellite types, orbits, waveforms, access protocols, and performance; through to review of the various technologies that are discussed in later Sections, such as ALOHA and MIMO.

Sections 3 and 4 describe the implementation of ITU-R P.2041 Earth-space channel model in the context of the problem being addressed in this study and datasets are derived for frequency and altitudes of aircraft and satellites that are used in later Sections.

Section 5 builds on the previous Sections to consider potential solutions to RF spectrum availability, and describes investigation of a number of techniques that attempt to introduce vertical spectrum re-use.

Section 6 provides a synthesis and analysis of the results identified in the investigations of Section 5 to consider the viability of the identified approach.

Section 7 summarises and discusses the results and provides a conclusion of the study with consideration of further work.

References

[1] "Digital Video Broadcasting (DVB); Second generation framing structure, channel coding and modulation systems for Broadcasting, Interactive Services, News Gathering and other broadband satellite applications; Part 2: DVB-S2 Extensions (DVB-S2X)", ETSI EN 302 307-2 V1.1.1

[2] Condo, C., Masera, G., "Unified turbo/LDPC code decoder architecture for deep-space communications", Condo, Carlo, IEEE transactions on aerospace and electronic systems , 2014, Vol.50(4), p.3115

[3] King, P. R., "Land mobile-satellite MIMO capacity predictions", Electronics letters, 2005, Vol.41(13), p.749

[4] Mishra, A. K., Johnson, D. L., "White Space Communication: advances, developments and engineering challenges", Springer, 2015

[5] Fette, B. A., "Cognitive Radio Technology", Elsevier Science 2nd ed. 2009

[6] Sacchi, C., Rossi, T., et.al., "Efficient Waveform Design for High-Bit-Rate W-band Satellite Transmissions", IEEE Transactions on Aerospace & Electronic Systems. 04/01/2011, Vol. 47 Issue 2, p974-995

[7] De Fina, S., Ruggieri, M., Bosisio, A. V., "Exploitation of the W-band for High Capacity Satellite Communications.", IEEE Transactions on Aerospace & Electronic Systems. Jan2003, Vol. 39 Issue 1, p82

[8] Forenza, A., et.al., "System and Method for DIDO precoding interpolation in multicarrier systems", US Patent 2010/0316163A1, Dec. 2010

[9] "Technical Specification Group Services and System Aspects; General Universal Mobile Telecommunications System (UMTS) architecture (Release 13)", 3GPP TS 23.101 V13.0.0, 2015

[10] Dekker, H., Bram, V. D. E., et.al., "Spectrum availability for next generation satellite services: Coexistence with terrestrial mobile services", Lecture Notes of the Institute for Computer Sciences, Social-Informatics and Telecommunications Engineering, 2013, Vol.52, pp.44-52

[11] “Prediction of path attenuation on links between an airborne platform and Space and between an airborne platform and the surface of the Earth”, Recommendation ITU-R P.2041

Chapter 2

Background on Multi-Satellite Communication and Broadcast Systems

2.1 Historical review of the spectrum issue

Spectrum is a finite resource; the need for new and novel techniques to manage and share it efficiently is, as always, a major problem to be solved in any RF system development. In the largely unregulated flight area of high altitude and low Earth orbit operation, the need for solutions to this problem are pressing as more users operate in the region and their spectrum requirements increase. High altitude UAVs (Unmanned Aerial Vehicle) and RPAS (Remotely Piloted Air System) platforms operating with high data rate payloads [1], increased networking of aircraft for services that include ADS-B (Automatic Dependent Surveillance – Broadcast) [2], maintenance information [3], and passenger internet [4], along with potential increase in low Earth orbit use by commercial rocket launch companies [5, 6], using lower cost smallsat and cubesat platforms [7], all need coordinating and require communication resources, which ultimately results in a need for increased spectrum. This problem is not new however, and the need for rapid increases in data capacity that drive increased spectrum usage can be traced back to the origins of communication satellite development.

The development of communications electronic systems and infrastructures in the high altitude and low orbit region of the Earth can historically be traced to the military need for Cold War surveillance [8]. Surveillance initially required image capture with information returned as exposed film via re-entry capsule: however, this made the satellite life-limited and disposable, and the data several weeks old. A communication capability was an obvious extension and as a result, and in parallel, communications payloads, and communication satellites were developed [9].

Until the development of satellite communications in the 1960's all long distance, particularly cross-ocean communications, were carried by cable 'bundles' [10]: a

legacy that stretches back to the long-distance subsea telegraphy cables of the Victorian era.

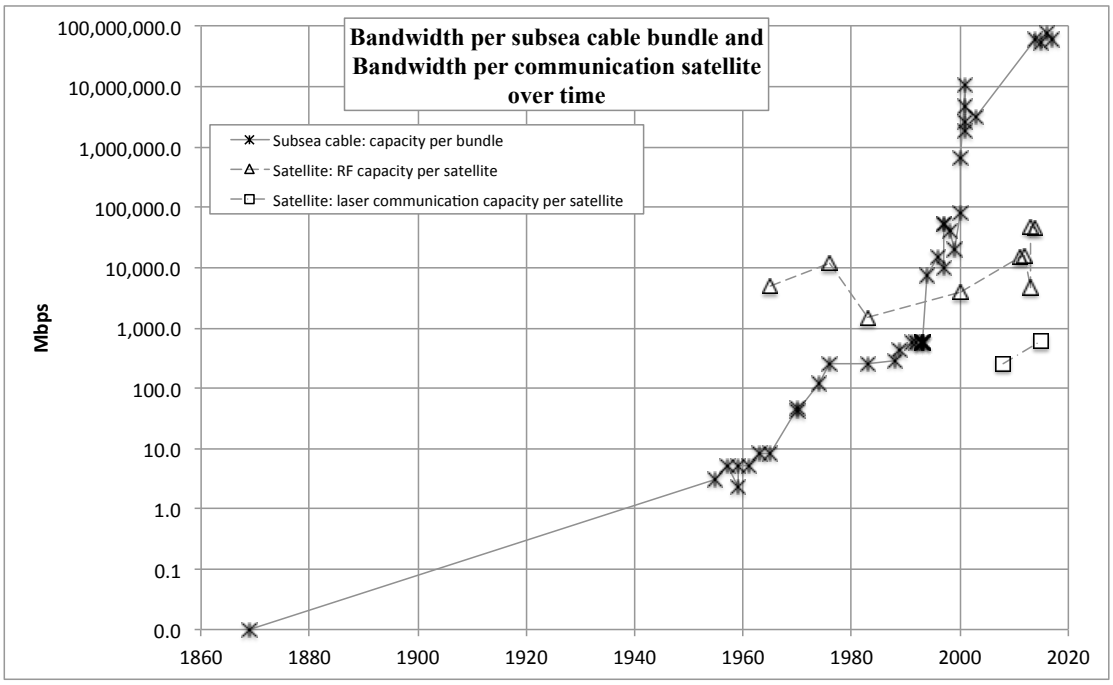

Figure 2.1 - Temporal improvement in the capacity of subsea cable bundles, communication satellites, and laser satellite communication systems (derived from *Glover* [11], *UN satellite dataset* [12], and *EDRS factsheet* [13])

Illustrating the accelerating need for overall communication capacity, Figure 2.1 shows the data carrying capability of subsea cables, per bundle, alongside RF data carrying capacity, per satellite, over time. Also plotted for comparison is the data carrying capacity of free space laser communication, per satellite; a technology that promises to perhaps further increase satellite communication capacity.

Figure 2.1 highlights several points in the development of high data rate satellite and ground systems.

1. There is an inflection point in the data for subsea cable bundles in the mid-1960s that corresponds to the dramatic improvement in capacity with the introduction of fibre-optic cables and repeaters in place of copper cables.

2. There is a further inflection point in the data for subsea cable bundles in the late 1990s that relates to a rapid increase in the data rate carried by each fibre optic cable, through faster signalling and multiple wavelengths per fibre, and the number of fibres per bundle [14]. Interestingly this inflection point occurs just at the point when global Internet achieves considerable growth [15], suggesting that technology fed the growth of the Internet and that growth fed the development and deployment of fibre technology in a virtuous circle; the outcome of which, unfortunately, was over-supply and a slow-down of the communications industry for several years as noted by the data.

3. Only 30 years elapsed from the introduction of RF communication satellites in the 1960's to the point at which fibre-optic subsea bundles exceeded their capacity. Since the introduction of RF communication satellites, data capacity on orbit shows only modest performance increases in comparison with subsea fibre optic bundles.

4. Recent developments in satellite free space laser communication show growth potential for increasing satellite capacity beyond that available using RF technology, but this is a new technology in a developing market and has several issues to address [16].

It would appear then that subsea fibre-optic bundles are the best long distance communication medium, and this is confirmed when considering the latency of a signal transmitted from London to New York, for example, using subsea and space routes. To achieve a similar end-to-end data 'time-of-flight' latency to subsea fibre-optic bundles requires 78 satellites in low Earth orbit (LEO) and though the number of satellites required decreases with increasing orbital altitude, the latency increases dramatically (Figure 2.2).

Since the latency is 'speed of light' limited it cannot be decreased. As a result, two-way-voice communication becomes progressively more difficult with increased orbital altitude. For example, at GEO with a two-way latency of nearly 300 msec it becomes difficult to hold a conversation because of conversation overlap [17].

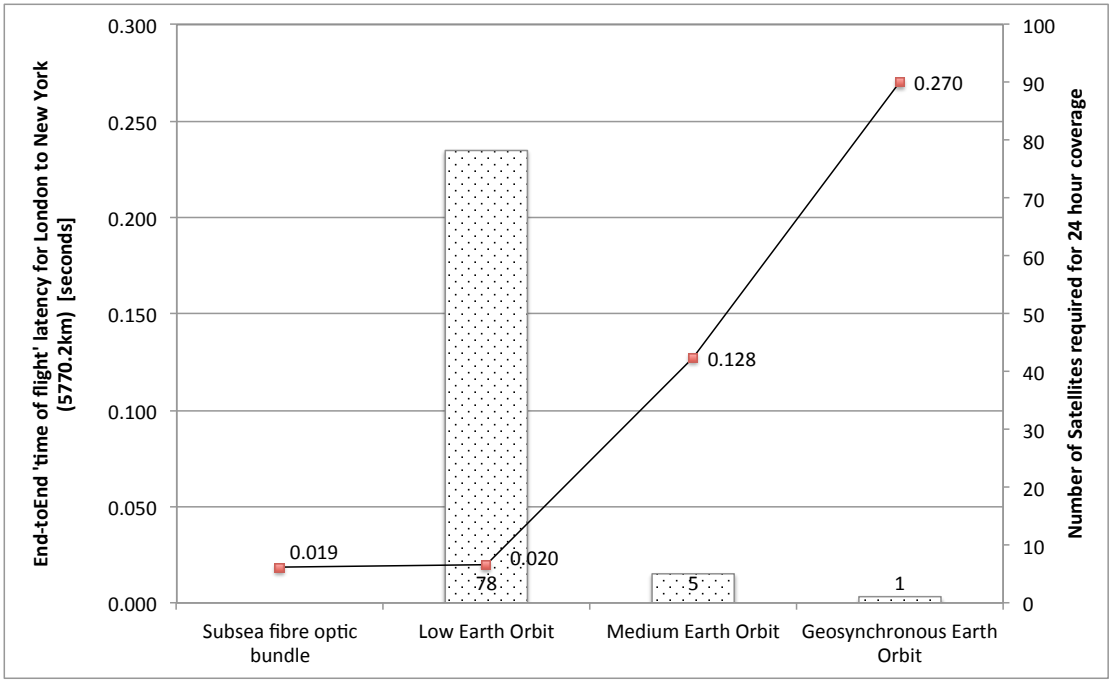

Figure 2.2 – Comparison of the 'time-of-flight' latency of communication from London to New York across subsea and satellite routes, alongside the number of satellite platforms required to provide 24-hour coverage for such a link

In addition to the latency problem, satellite design for higher orbital altitude is more complex since coverage is now a substantial proportion of the Earth's surface, requiring provision of support for more voice or data channels, and requiring higher power transmission to match the communication channel performance of satellites in lower orbits. This power and channel increase results in the need for larger solar panels, which in turn adds mass; with the mass to orbit being limited by launcher capacity: current maximum GEO satellite launch mass is around 6-7 tonnes [18].

In a very general sense, a GEO satellite can be thought of as providing the capability of one third of a LEO constellation (around 26 satellites), in one satellite. And for typical MEO orbital altitudes, a GEO satellite can be thought of as providing the capability of around 8 MEO satellites. This drives a wide range of trade offs, both technical and commercial.

To illustrate some of these technical trade-offs, although miniaturisation of communication transponders and switching elements reduce mass, with optical switching and processing for Very High Throughput (VHT) GEO satellites being

developed [19] for example, it is difficult to further improve amplifier efficiency without increasing the power required, which adds solar panel power increase requirements, and amplifier cooling requirements, which increase the launch mass. Typically, however, some of the amplifier increase can be offset with larger antennas providing additional gain. Such antennas are a triumph of origami in their ability to fit alongside the satellite within the launcher shroud [20], but their complex mechanisms add additional risk to the satellite deployment and operation, and become exceptionally hard to design at high frequencies due to the RF 'flatness' requirement of the antenna surface to make them usefully efficient.

Ultimately, the GEO, MEO, LEO selection for a satellite or constellation is dependent on the frequency allocation agreed with the ITU via National Authorities [21], such as OFCOM in the UK, and for GEO the availability of the 2º 'slot' in the GEO-ring above the region that the satellite service is to be used. GEO slots are allocated in agreement with the ITU, which operates a 'first-come first-served' approach [22]. GEO slots and frequency allocations are so highly sought after that once acquired they are rarely released, which leads to a need for novelty in satellite developments and orbits for new players in the market.

Recent approaches to GEO capacity increase have been to move to higher frequencies to provide higher data rates in wider transponder bandwidths, and to add more flexible management of beam ground pattern and coverage, but even these advances increase power and are therefore ultimately limited. For this, latency, capacity, and many other commercial reasons, GEO satellite capability has recently been challenged by low cost LEO constellations [23].

Returning to Figure 2.1, satellite communication capacity had continued to exceed that of subsea cable bundles until the late 1990's when multiple wavelength fibre optic bundles finally exceeded satellite performance [24]. The continued increase in capacity of subsea fibre optic cable bundles, along with the lower latency of communications across the Earth in comparison to satellite repeater links is set to continue: it is, comparatively speaking, easier, lower cost, and provides far more capacity, to add more fibres to new subsea cable bundles than to develop a new satellite constellation, as the bundles are, to some extent, repairable and upgradable

post deployment. A recent challenge to this position is the introduction of programmes to look at satellite maintenance and refuel on orbit [25], but it is early in the development of these technologies.

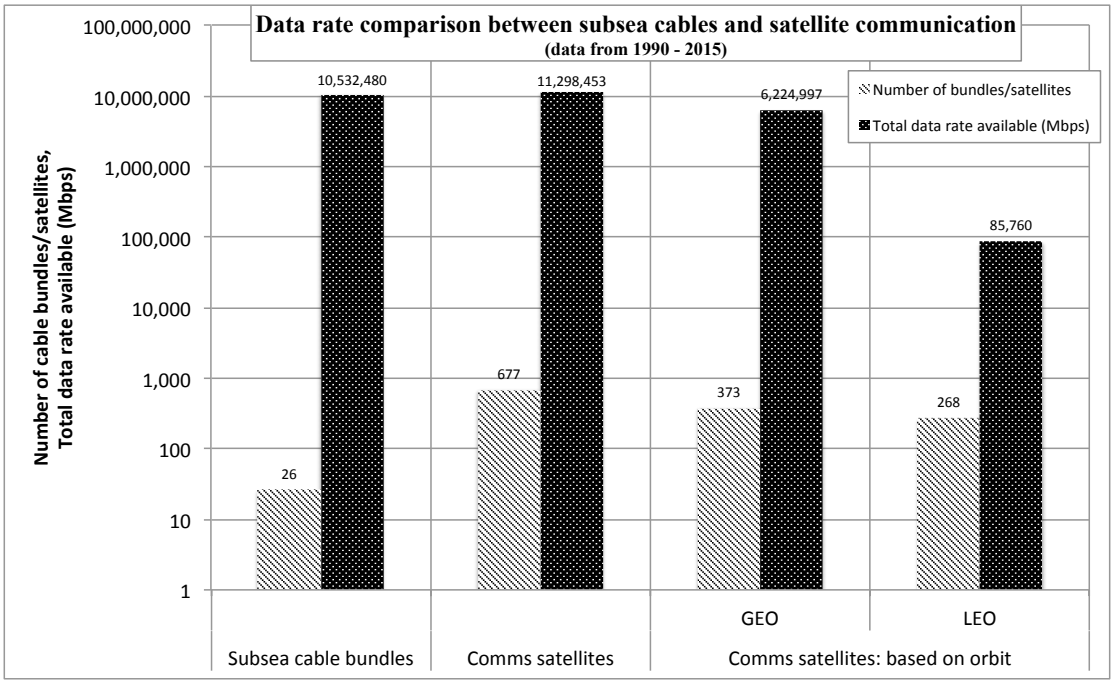

Figure 2.3 – Comparison of an estimate of the aggregate data rate available in ground fibre-optic communications compared to the aggregate data rate available via satellite, with a further breakdown (to the right) of the aggregate satellite data rate by GEO and LEO orbit altitude

Interestingly, based on the data of *Glover* [11], *United Nations* [12] and others (with the satellite data collated from estimates of transponder numbers and published satellite performance), Figure 2.3 shows that the aggregate data capacity in the ground communications networks are, to first order, similar to the aggregate data capacity that is currently available in on-orbit satellite networks. As can be seen, however, for roughly the same number of satellites, there is far higher capacity in GEO satellites than is provided by LEO satellites.

The conclusions that can be drawn from Figure 1.3 are that (i) there is a need to provide a communications capacity between ground networks and space networks to make good use of the data capacity of both, and (ii) that the data rate performance per LEO satellite is in need of improvement if the assumed need for increased low-

latency high-capacity is required. And since data rate performance has a dependency on bandwidth (and satellite transponder capacity, etc. as discussed previously in this Section) there is the need for more spectrum to be made available.

The development of free space optical communication, which can potentially provide very high data rates between satellites, and between satellites and high altitude aircraft, is limited by the inability to transmit optically (including infrared and ultraviolet) through dense water vapour, and this impacts the availability of such links, particularly if required to reach the ground. Above the atmosphere the argument for the use of optical communications for increased data rate is apparent, but there are limitations and trade-offs that support the choice of RF communications in preference: such as the fact that RF supports broadcast signals but laser communication systems are point-to-point, for example.

The key benefit of optical communication is that, for the moment at least, it by-passes the spectrum availability problem by moving to very high frequencies, and provides potentially higher data rates than RF transponders can achieve, as a result of the higher energy density. However, the use of wide beams for optical signal search and beaconing will become more of an interference issue as optical communication system use increases and joint operation occurs within smaller spatial regions; there are issues to solve in the long term.

In the move to higher frequencies atmospheric effects dominate and as with RF signals free space optical communication systems suffer from atmospheric performance issues. Atmospheric effects have provided the main constraint on the growth of this technology to date. For example, NASA MODIS data [26] suggests that on average, globally, cloud cover at a given location is present for about 67% of the time. Given that carrier grade fibre-optic links and bundles meet availability requirements of 6-nines (that is, to be available 99.9999% of the time, or to be only out of service for a maximum of around 30 seconds a year); a figure of 33% cloud cover per year suggests the chance of free space optical satellite communication reaching 6-nines is a very distant prospect without extremely large diversity schemes. Typical, existing, RF satellite communications systems exceed 3-nines - a

figure comparable with most ground level RF communications systems; a figure not possible to achieve with currently proposed optical communication solutions.

Some attempts to improve the optical satellite communication situation have been explored: including diversity receive, as is regularly implemented for high frequency satellite RF systems; to consider correlation techniques given that the bulk of the disturbance of space to Earth laser communications occurs close to the ground in the troposphere, where a small spread of optical receivers may be able to compensate for some of the atmospheric distortion; and to consider laser guide star adaptive optics for the ground to space communication link.

Other approaches to diversity include using multiple ground optical receive stations, with satellite scheduling and weather modelling to predict the best communication path for the satellite to Earth communication.

For non-telecommunication applications, such as Earth observation and science satellites, the level of availability is less of an issue allowing use of the potential improvement in data rate.

The effect of the atmosphere on RF signals has led to a great deal of research effort into the development of better atmospheric models, across wider frequency ranges, and under more complex atmospheric conditions, alongside the development of the signal processing algorithms and techniques necessary to get as much performance out of the RF channel as possible. As RF frequencies are increased, to provide the bandwidth needed to continue the increased data rates, as plotted previously (Figure 2.1), the atmospheric effects become more constraining. Attenuation of signals due to absorption by atmospheric oxygen and water vapour increases significantly at higher frequencies (Figure 2.4).

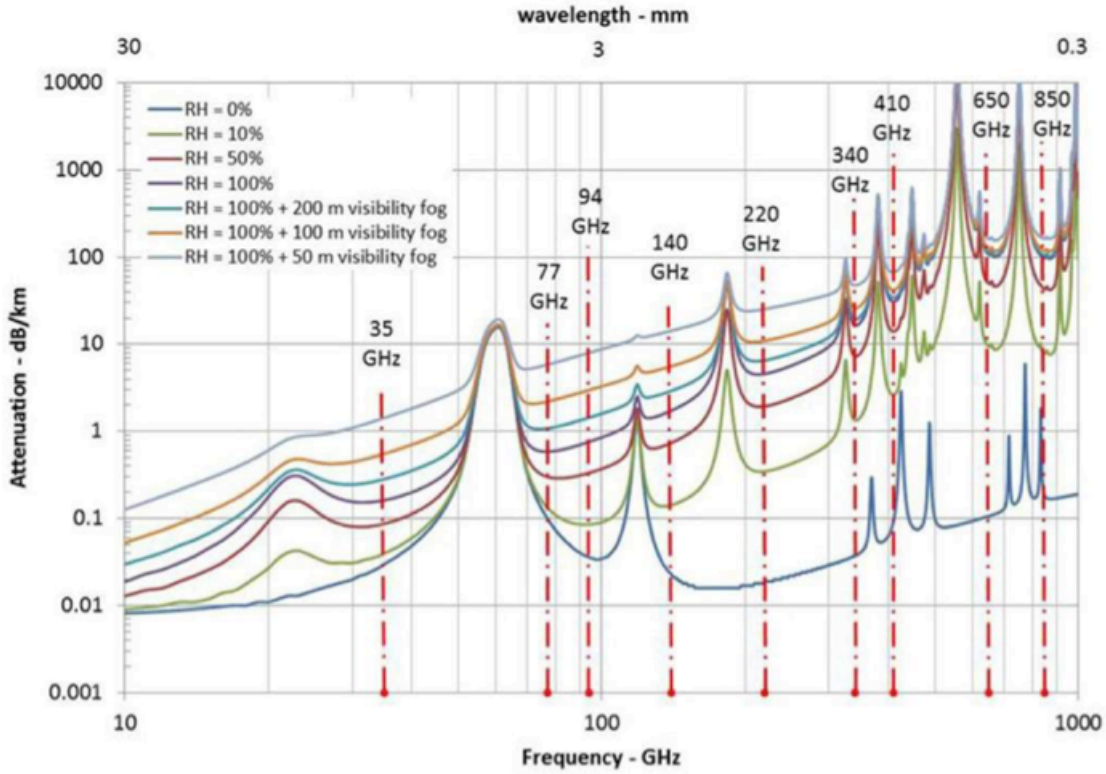

Figure 2.4 – Attenuation of the electromagnetic spectrum due to absorption by atmospheric Oxygen and water vapour in Earth's atmosphere at different levels of Relative Humidity (after *Richard et.al* [27])

At lower frequencies additional constraints introduced, not only by atmospheric effects, but by the increasing number of atmospheric noise sources whose amplitude increases at lower frequencies (Figure 2.5), and by Ionospheric effects (Figure 2.6), which can be dominant to VHF/UHF frequencies when solar activity is high, and where measurement shows increases to 10 dB or more [28].

These effects are dynamic, geographical location dependent, frequency, power, and slant angle from the Earth dependent. As a result waveform developments have focused on providing and optimizing for more complex dynamic transmission and reception property updates using real-time measurement of the channel [39], on the basis of increases in compact faster processors for signal processing.

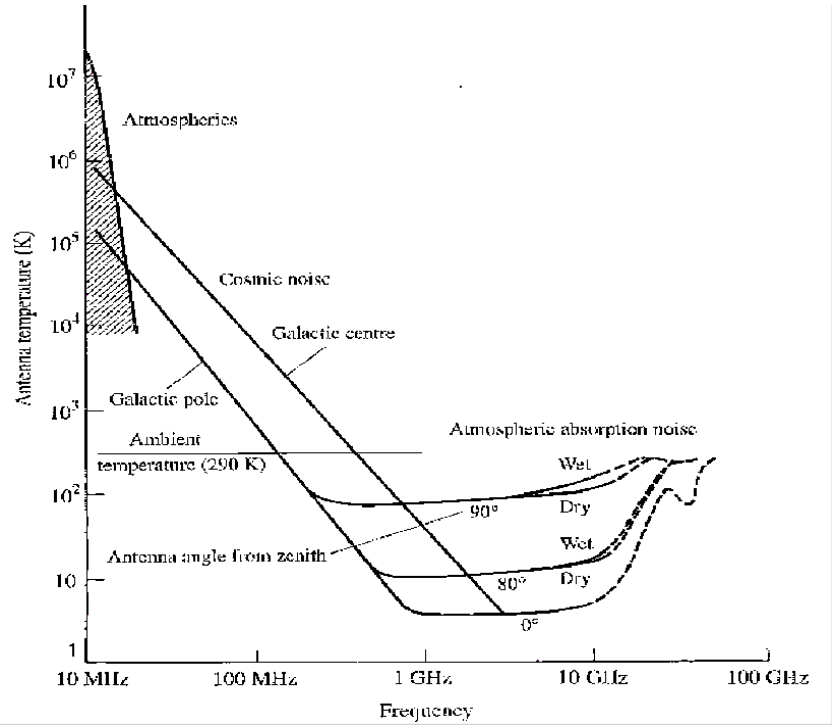

Figure 2.5 – Chart illustrating typical RF noise sources (after *Kraus* [29]).

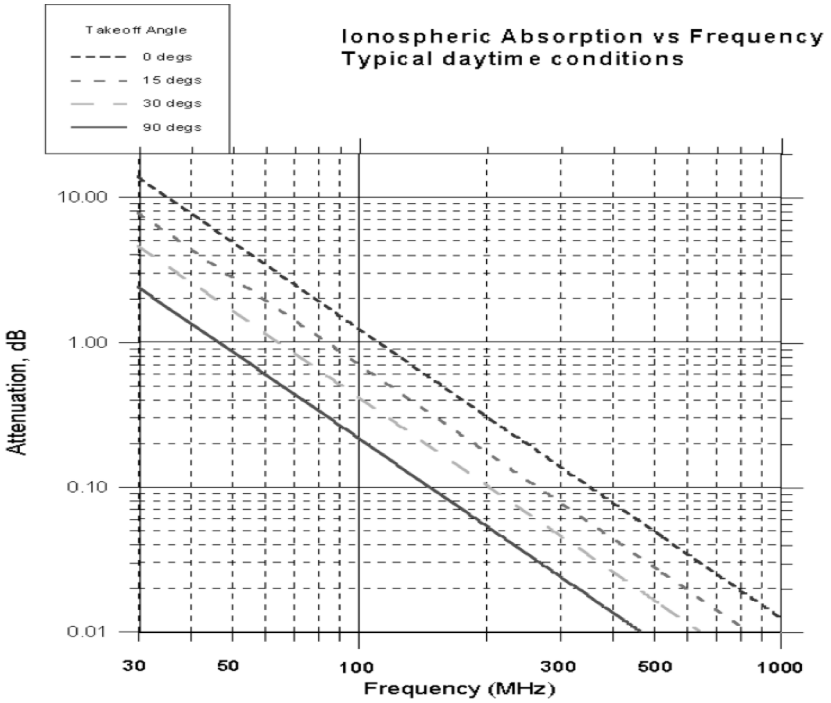

Figure 2.6 – Chart illustrating typical Ionospheric attenuation (after *Emerson* [30]).

This historic review of the spectrum availability problem has laid out the primary issues that have arisen, and the technological attempts to resolve the availability over time. As described in this Section, the need for higher data rates and better spectrum management indicates that new approaches are required, and this study is aimed at exploring alternative solutions to the problem.

2.2 The atmospheric context

2.2.1 Overview

The high-altitude low-orbit region around the Earth can be defined as covering that part of the atmosphere from the top of controlled airspace at 18.2km (60,000ft) to the upper edge of Low Earth Orbit (LEO) at 2,000km. This region covers high altitude airspace military and research aircraft, and Low Earth Orbit (LEO) communications and scientific satellites; it is then of interest for a number of communication applications and for science applications with high communication rate requirements. Based on the *United Nations Register of Space Objects* [12], there are around 4,000 registered Low Earth Orbit satellites, with the lowest having a perigee of 87km.

This combined high-altitude and low-orbit region is considered an important part of the Earth's atmosphere, where *Tinsley* [31] describes how the Earth's plasma flux affects weather, *Gadson* [32] describes the development of ephemeral noctilucent clouds, which also appear to have an affect on weather, and where the Ionospheric belts reside (Figure 2.7).

From an applications perspective, *Harris* [33] highlights why the high-altitude low-orbit region is important for remote sensing, and *Smith and Griffin* [34] extend this to consider high altitude research in general. There is a need to provide observation platform communications to this region.

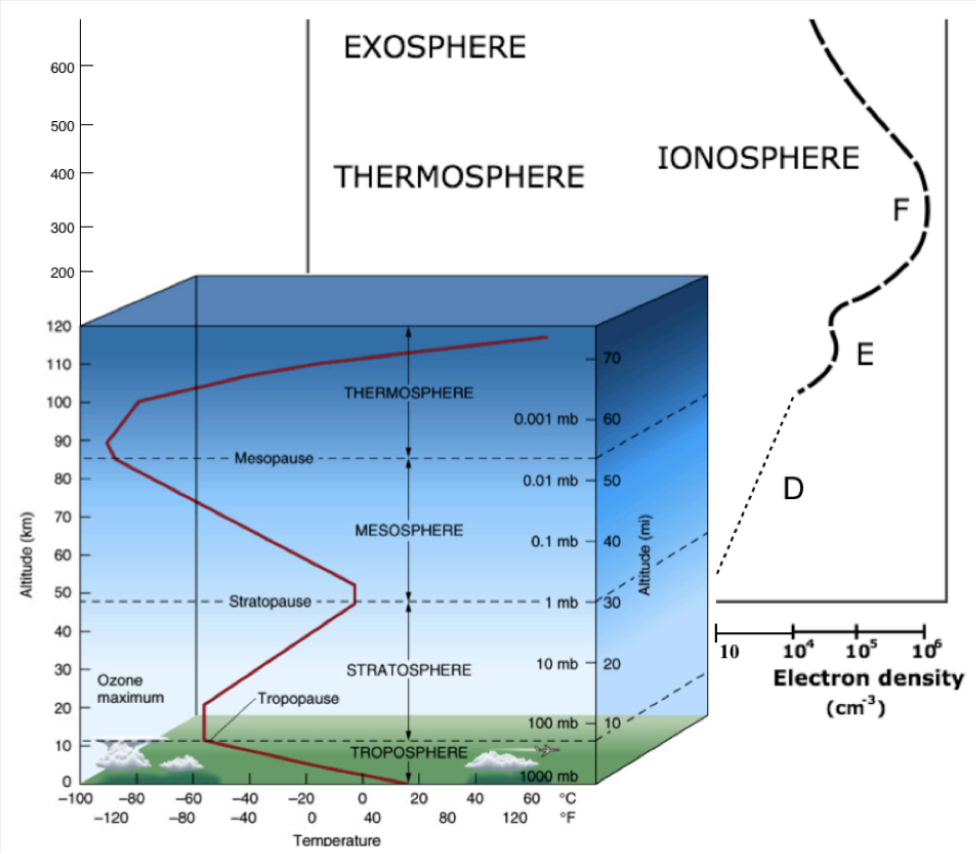

Figure 2.7 - The high-altitude low-orbit region covers the stratosphere, mesosphere, thermosphere (including the ionosphere), and exosphere (after *Aguado* [35])

2.2.2 The mesosphere

Exploration of the mesosphere is of particular scientific interest as it contains the chemically complex ionospheric *D-Layer* (*Wait* [36]), scattering sources such as the debris of meteorites *(Damazio & Takai* [37]), metallic vapour layers known to contribute to *Sporadic-E layers* (*Pavlov* [38]), of which, for example, the 5km thick sodium layer is typically used by astronomers to create laser stimulated artificial guide stars for adaptive optics imaging systems (*Max, et.al.* [39]).

Movement of the upper stratosphere causes atmospheric tides (*Pancheva et.al*. [40]) that are amplified in the mesosphere and sweep around the planet affecting weather and atmospheric dynamics. Red Sprite (*Luque & Ebert* [41]) and Blue Jet (*Wescott & Sentman* [42]) phenomena are created in this region by lightning lower in the atmosphere. The mesosphere is a very active and important region yet it is currently

impossible to maintain an experimental presence there for any period of time: almost everything we know about the mesosphere is from transient sounding rockets or remote sensing, and these require communication links to return scientific data.

2.2.3 The stratosphere

The main constraints on transmission in the stratosphere, and above, are due to ionisation of gases and the molecules that form the various layers of the ionosphere. For example, the *D-layer* typically reflects 10s through to 100s of kHz, the *E-layer* low Megahertz, and the *F-layer* up to tens of Megahertz. There is little Radio Frequency reflection and refraction (or ducting) beyond the High Frequency (HF: 3-30 MHz) and low Very High Frequency (VHF: 30 MHz - 300 MHz) bands. Higher frequencies - in the high VHF and Ultra High Frequency (UHF: 300 MHz - 3000 MHz) range, for example - can suffer reflection and refraction as a result of scintillation from passing through regions of high 'total electron content', such as one might find in the ionospheric layers. This adds propagation and group delay, which has a significant effect on satellite global navigation system (GNSS) calculations (*Rius et.al.* [43]), but has limited effect on the attenuation of the signals themselves.

The lower edge of the high-altitude low-orbit region reaches into the stratosphere, which ranges from 10 km (32,800 ft) altitude to the Tropopause at 50 km (164,000 ft). In this region resides the *Ozone layer*: a region of the atmosphere in which ultraviolet light from the Sun is absorbed by, and decomposes, O_3 molecules to atomic oxygen; in the process preventing harmful ultraviolet radiation from reaching the Earth's surface, and which is affected by many processes (*Larin* [44]).

A consequence of this energy absorption is the creation of a temperature inversion layer which, at higher stratospheric altitudes at least, leads to a reasonably stable region of the atmosphere with little turbulence (*Lefohn & Wernli* [45]).

Altitude records for powered aircraft at 112.01 km (*Binnie* [46]) and buoyant platforms such as helium balloons at 53.0 km (*Yamagami* [47]), all reside within the stratosphere.

The reason for this is that powered aircraft rely on forward thrust to create lift from aerodynamic surfaces, and buoyancy craft rely on lift developed by volume displacement, both of which are limited by atmospheric density. As the atmosphere becomes more tenuous at higher altitudes, wing surfaces need to increase to dimensions that are currently infeasible to build, and need aerodynamic surfaces that operate in very low Reynolds number environments (*Greer et.al.* [48]). Buoyancy craft need to expand to such large volumes that the weight of the balloon envelope negates the available lift.

In all cases there is an asymptote beyond which further energy must be introduced to reach higher altitudes, and since there is very little in the way of available sources for this energy at high altitude - solar power and atmospheric oxygen being the most abundant - the primary method of reaching higher into the stratosphere is typically through the use of chemical combustion in the form of a rocket engine. There have been a number of novel attempts to reach higher stratospheric altitudes, such as micron thick balloon envelopes, and the use of hydrogen as a fuel instead of jet fuel in turbojet engines (*Fleming et.al.* [49]), but the application of chemical rocket driven platforms still dominates. A summary of aircraft, suborbital craft, and atmospheric phenomena is shown in Figure 2.8.

2.2.4 The thermosphere

The region from 80 km to 600 km above the Mesopause consists of tenuous atmospheric gases that are heated by ultraviolet light from the Sun. Densities are so low above 160 km that molecular collisions are too infrequent to communicate sound.

The internationally recognised ‘boundary of space' occurs in the thermosphere at an altitude of 100 km (328,000 ft). As previously noted, the lowest orbiting spacecraft was at an altitude of only 87 km (*United Nations register* [12]), although atmospheric drag becomes an increasing problem in the lower thermosphere leading to a reduction in the amount of time a spacecraft can maintain orbit (Figure 2.9).

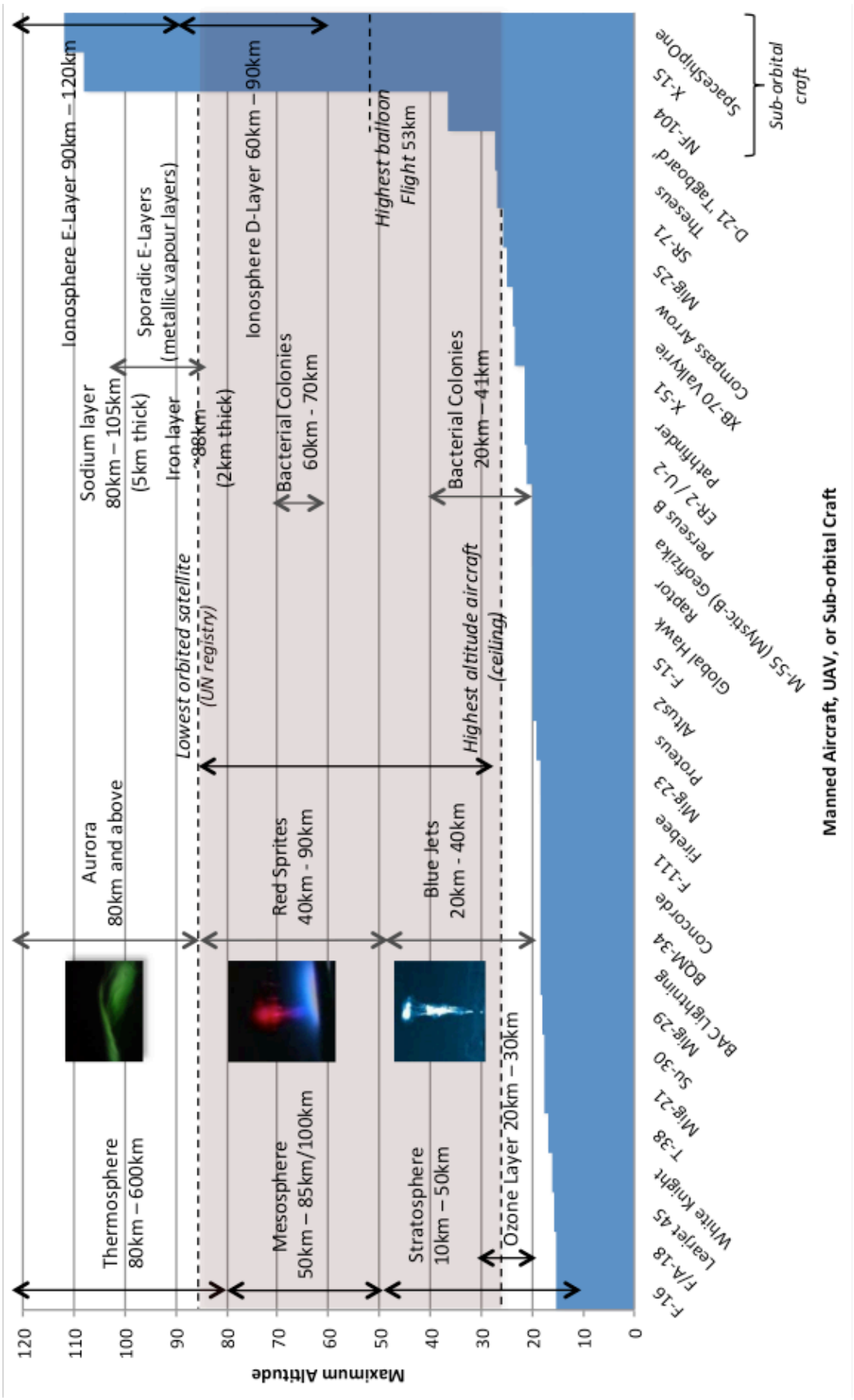

Figure 2.8 – The high-altitude airspace environment

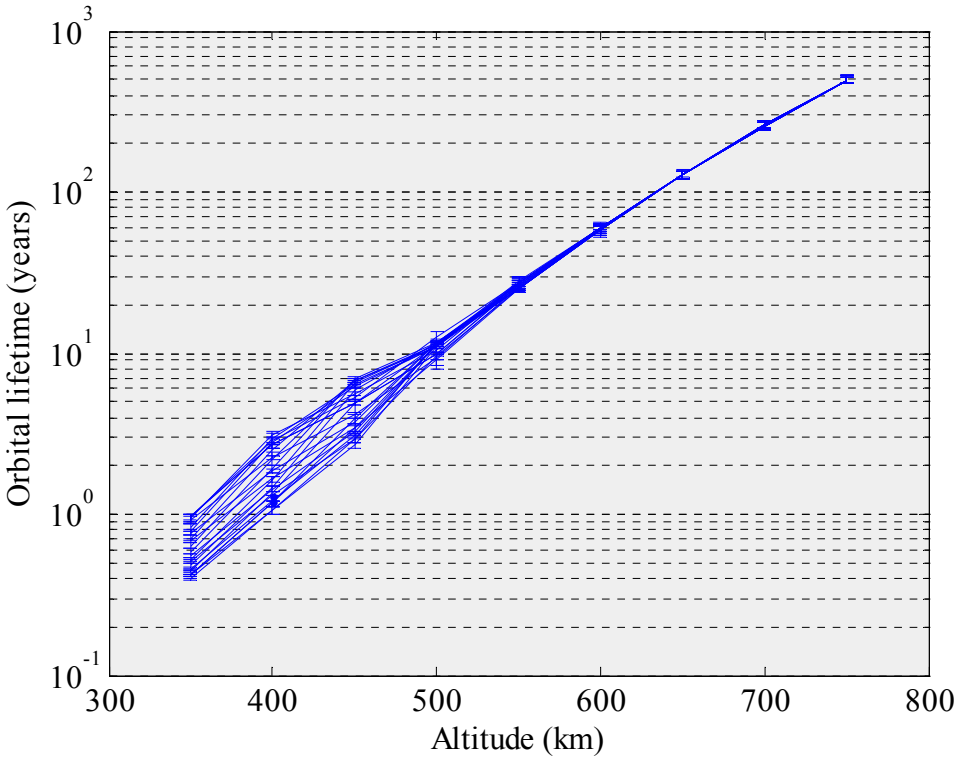

Figure 2.9 – Chart illustrating typical orbital lifetime versus orbit altitude for a small 'cubesat' satellite (after *Cojuangco* [50])

At higher altitudes drag is minimal and stable orbits can be maintained. For example, the International Space Station maintains a stable orbit at around 400 km altitude with regular need to boost its velocity. There are many factors that determine orbital lifetime, velocity change, and drift (*Owens et.al.* [51]).

From an RF perspective, the thermosphere contains the ionospheric *F-layer* and *sporadic-E layers*, which affect signals in the tens of Megahertz range. Transmissions are also affected by auroral events in the thermosphere as a result of charged particles from the solar wind interacting with the magnetosphere and creating regions of ionised atmospheric gas. Of particular concern with regard to the magnetosphere for satellites that pass through the thermosphere in low altitude orbits is the so called 'South Atlantic anomaly" (*Ginet et.al.* [52]), where the inner Van-Allen belt reaches so low that the proton flux is dangerously high and can be damaging to electronic devices that are not properly shielded (*Curtis* [53]).

2.2.5 The exosphere

The edge of the atmosphere, at almost near vacuum, reaches to extreme distances from the Earth. The exosphere region begins at the Thermopause at around 600km and extends upwards. The exosphere contains the bulk of the magnetosphere and the Van Allen belts.

2.3 The space context

2.3.1 Satellite communication standards

In the following sections the available satellite communication standards will be described and compared. These standards provide interoperability between satellite implementations.

2.3.2 CCSDS standards

The CCSDS (Consultative Committee for Space Data Systems) is a group within the International Standards Organisation (ISO) supported by eleven space agencies (Figure 2.9). The purpose of the CCSDS is to coordinate and define communications interoperability standards for spaceflight applications (Figure 2.10).

CCSDS 131.0-B-2	TM Synchronisation and Channel Coding
CCSDS 131.2-B-1	Advanced Coding & Modulation for High Rate Telemetry
CCSDS 132.0-B-2	TM Space Data Link Protocol
CCSDS 232.0-B-3	TC Space Data Link Protocol
CCSDS 352.0-B-1	CCSDS Cryptographic Algorithms
CCSDS 401.0-B-25	RF and Modulation Systems: Earth Stations & Spacecraft
CCSDS 414.1-B-2	Pseudo-Noise (PN) Ranging Systems

Table 2.1 – CCSDS interoperability standards for TT&C

The standards are divided into the different domains of the communication process. Primarily, however, they are aimed at the bus not the payload. That is, towards the

supporting functionality (summarised as propulsion, navigation, station keeping, and control), rather than the communications or science payload itself.

There are multiple standards to cover Telemetry, Tracking and Control (TT&C) links, covering the terms, telemetry (TM) and telecommand (TC) (Table 2.1).

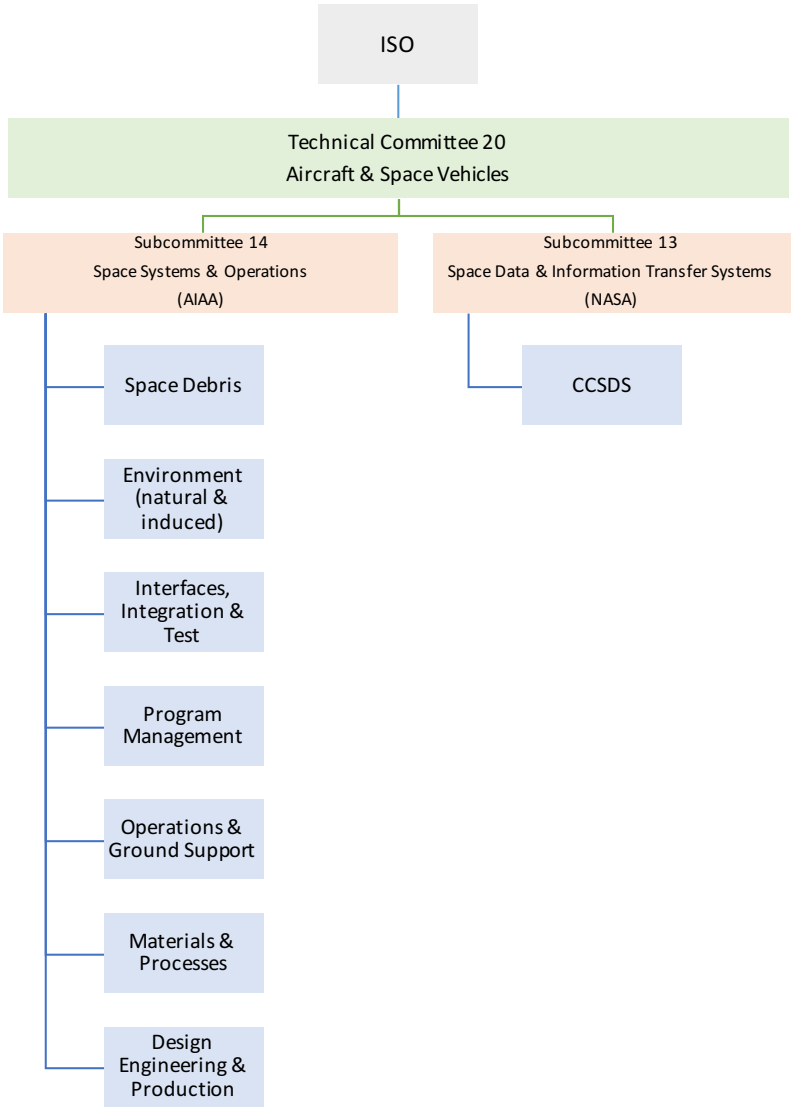

Figure 2.10 – Chart illustrating the ISO committee structure and the position of the Consultative Committee for Space Data Standards (CCSDS)

The TT&C standards can be mapped to the OSI seven layer model [54] (Figure 2.11). For this study the most relevant standard is CCSDS 401.0-B-25 [55] which describes standardized RF and modulation schemes. In the standard the RF

specification for Earth-space for non deep-space (CCSDS Category A) communication links is defined (Tables 2.2 and 2.3).

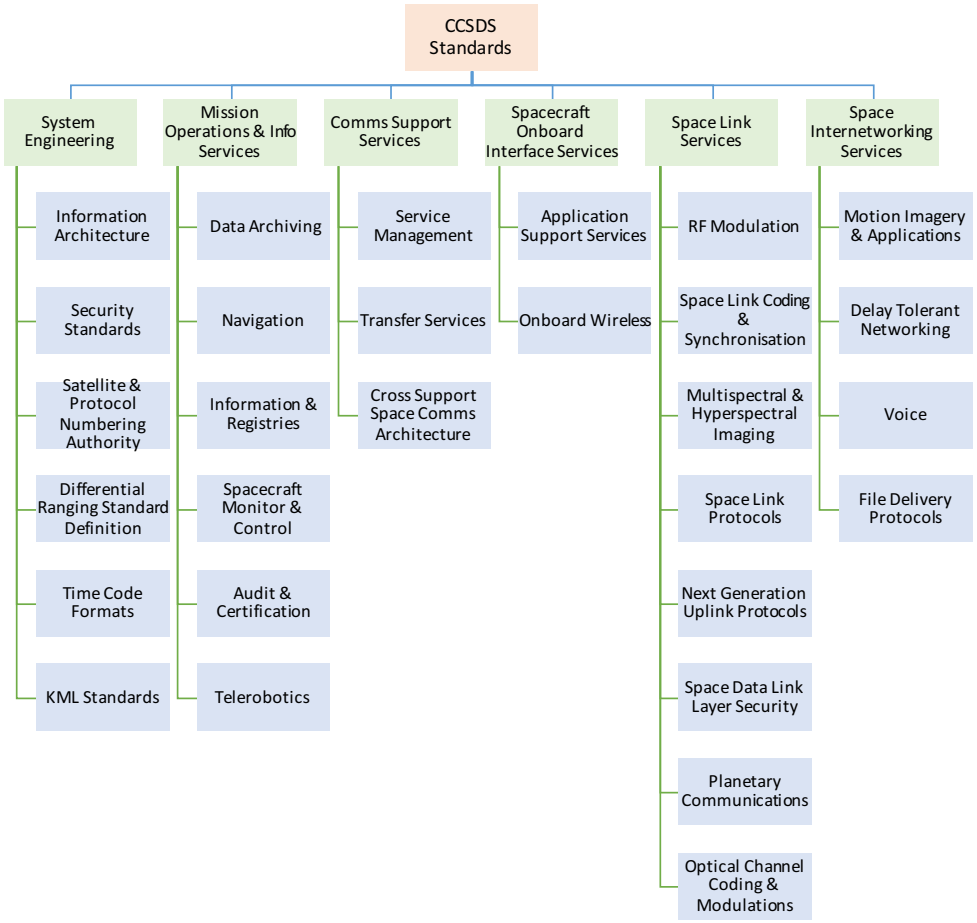

Figure 2.11 – Chart illustrating the coverage of the CCSDS interoperability standards for space communications

As can be seen in Tables 2.2 and 2.3, the RF specification is quite ‘loose’, defining as it does a bounding box, rather than specific values. This is because different space agencies implement slight differences in the standards.

However, provided that the TM and TC messages (in this instance) and encoding are consistent, then a phase shift keyed (PSK) waveform with the required Doppler tolerance and meeting the transmission mask and compression would work for the majority of Earth-space and space-Earth links.

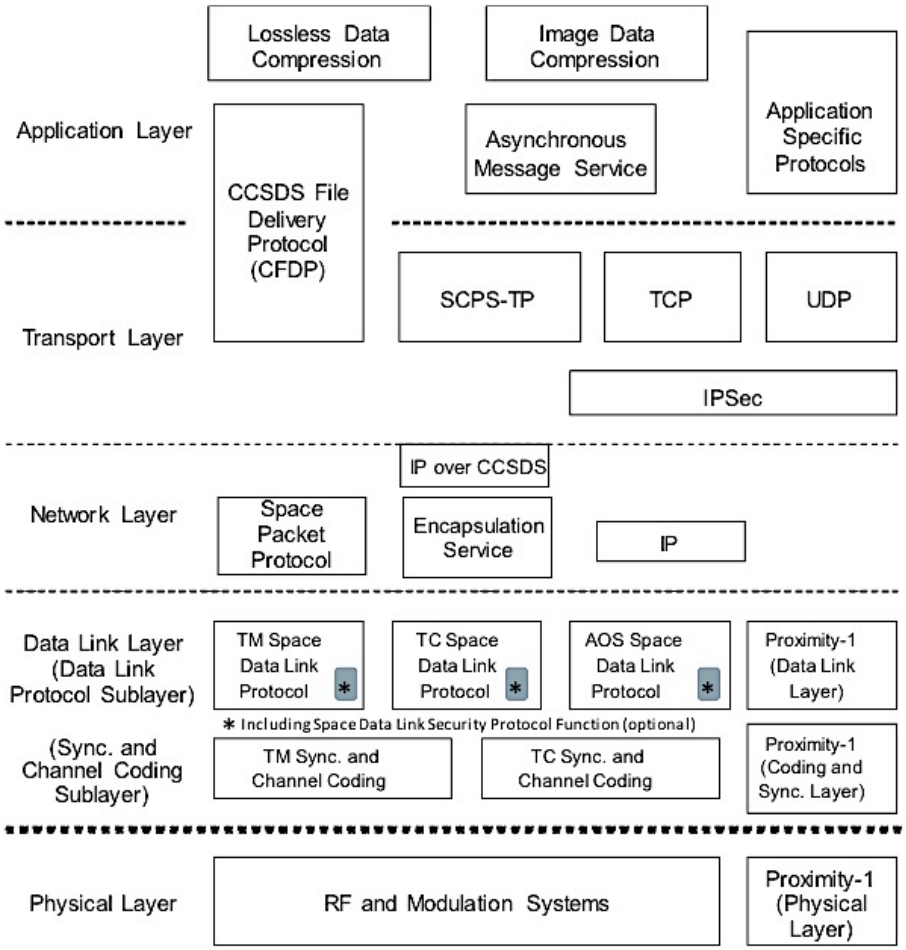

Figure 2.12 – CCSDS standards mapped to the OSI seven layer model (after [54])

In terms of the telecommunications payload, however, they may operate any waveform that the payload transponders can adapt to: there is no specification beyond that of Proximity-1 and the CCSDS packet standards (Figure 2.12). Payload communications standards tend to be application specific.

Ref	Recommendation	Notes
2.1.1	Phase modulation	Use with residual carriers
2.1.2	Circular polarisation	Ability to switch polarisation required
2.1.3	+/- 1-150 kHz, +/- 1-500 kHz	Minimum acquisition sweep range at 2 GHz, and 7 GHz (for Doppler compensation)
2.1.4	500 Hz/s ≤ 50 kHz/s	Minimum acquisition sweep rate range (for Doppler compensation)
2.1.5	Pos voltage -> Pos Phase Shift	Modulator input voltage to carrier phase shift
2.1.6	10 dB carrier suppression	Maximum carrier suppression resulting from

		all signals
2.1.7	Mod indices; Data rates codes	Constraints from simultaneous service operations
2.1.8	Uplink freq steps <101 Hz	Minimum Earth station transmitter frequency resolution

Table 2.2 – CCSDS 401.0-B-25 Earth to Space RF recommendations

Ref	**Recommendation**	**Notes**
2.2.1	Residual carriers	Use with low bit rate telemetry systems
2.3.2	Suppressed carriers	Use where carriers exceed PFD limits
2.3.3	+/- 150 kHz, +/- 600 kHz, +/- 1800 kHz	Minimum acquisition sweep range at 2 GHz, 8 GHz, and 26 GHz (for Doppler compensation)
2.3.4	100 Hz/s ≤ 200 kHz/s	Minimum acquisition sweep rate range at 2 GHz, 8 GHz, and 26 GHz (for Doppler compensation)
2.3.5	Circular polarisation	Ability to switch polarisation required
2.3.6	Pos voltage -> Pos Phase Shift	Modulator input voltage to carrier phase shift
2.3.7	+/- $5x10^{-13}$ ($0.2 \leq s \leq 100$)	Minimum Earth station reference frequency stability
2.3.8	10 dB sine; 15 dB square	Maximum carrier suppression resulting from all signals

Table 2.3 – CCSDS 401.0-B-25 Space to Earth RF recommendations

2.3.3 ETSI GMR standard

The European Telecommunications Standards Institute (ETSI) standards body has defined a variation to the GSM (Global System Mobile) mobile phone standard as defined by the 3GPP standards body (GSM was originally managed by ETSI), which describes a space capable waveform (the *Um* interface in Figure 2.12). The Master Switching Centre (MSC), of which there may only be between 1 and 4 typically, uses a protocol stack (not relevant for this discussion) to communicate with a number of out-lying Satellite Control Centres (SCC), represented in the figure by the image of the ground station satellite dish.

Data in the form of Message Transfer Protocol (MTP) packets is converted into the GMR physical link format, along with additional Radio Resource (RR) and Data Link Layer (DLL) control, before being modulated onto the GMR RF signal (GEO Mobile Radio [56][57][58]). The satellite in the GMR model acts as a 'bent-pipe' transponder and receives, amplifies, typically changes the frequency of the signal (Ku or C-band to L-band in the case of Figure 13), and retransmits it at higher power back to the ground. In this case to a mobile handset (labelled MES).

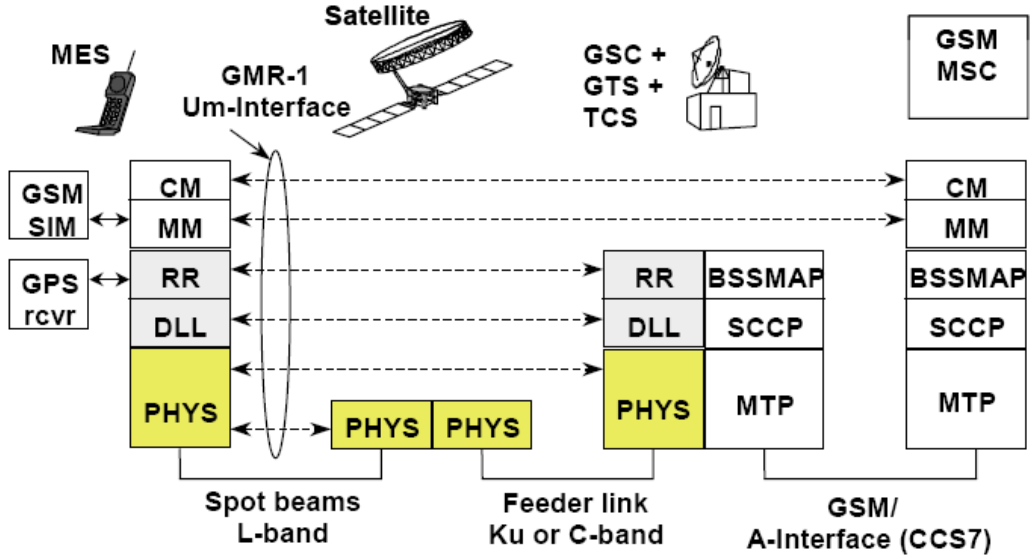

Figure 2.13 – ETSI GMR standard maps to the ETSI/3GPP standards model for GSM (after ETSI TS 101 376-1-3 standard [58])

The ETSI GMR standard is widely used in the geostationary (GEO) communications satellite industry (Inmarsat's iSatPhonePro service uses GMR for example), and has followed the various improved 3GPP standards upgrades and releases (Table 2.4).

The supporting ground MSC functions, and SIM card security protocols have also been changed to keep pace. As the 3GPP standards move through 4G (addition of Orthogonal Frequency Division Modulation - OFDM) to 5G (addition of massive MIMO – multiple input to multiple output antennas and transceivers), it will be interesting to see if there is an effort to map them to further GMR releases. At time of writing there is no development beyond GMR Release 3.

Release	Rough equivalence
GMR Release 1	2G GSM
GMR Release 2	2G GPRS
GMR Release 3	3G UMTS

Table 2.4 – Mapping of GMR standards releases to 3GPP standards releases

For GMR release 1 the modifications to the RF signal (at the *Um* interface in Figure 2.4) are minimal; frequencies are translated from mobile phone frequency bands to satellite L-band (around 1.5 GHz space to Earth, around 1.6 GHz Earth to space), using left hand circular polarisation for Earth to space, modulation is $\frac{\pi}{4}$ Quadrature Phase Shift Keying (QPSK), channels are mapped on a spacing of 31.25kHz [57]. Some of the main changes from GSM relate to dealing with the delay timing, which in GSM is used to align the transmitted Time Division Multiple Access (TDMA) signals with corresponding timing at the receiver, and which is defined for ground application dimensions; the 'TDMA multiplex' of GSM is also modified in GMR to accommodate additional channel types for signalling.

Similarly, there are few changes between GMR-release 3 (GMR-1 3G) and the 3GPP UMTS (3G) standard, with Direct Sequence Spread Spectrum (DSSS) [59] and improvements in security.

2.3.4 ITU standards

The International Telecommunication Union (ITU) is a branch of the United Nations (UN) tasked with harmonising and developing international communications standards. For satellite communication, the key standard is ITU-R P.2041 [60], which provides a standard model for the RF environment of Earth-space communication for ground terminals, aircraft, and satellites. It does not mandate particular communication schemes, but effectively harmonises the channel model so that designs can ensure they will work together when implemented. The standard allows for performance comparison between different implementations and models. The following chart illustrates the various elements that contribute to the ITU-R P.2041 channel model (Table 2.5), and related ITU standards.

The ITU is also responsible for allocating satellite orbits and frequencies. For geosynchronous Earth orbits (GEO), the trade-off between the location above the Earth and the separation needed for RF transmission interference avoidance divides the 'GEO ring' into orbital 'slots'. The ITU also defines the GEO 'graveyard orbit' to where GEO satellites must be boosted at end of life to avoid collision and debris incidents with other satellites in the GEO ring.

ITU Standard		Dependencies	Standard	Further dependencies	Standard	Further dependencies	Standard
P.2041	Prediction of path attenuation on links between an airborne platform and Space and between an airborne platform and the surface of the Earth	P.618	Troposhperic Scintillation and rain aatenuation	P.839	Tropospheric Scintillation, rain height	P.453	Refraction
				P.531	Ionospheric scintillation		
				P.676	Gaseous attenuation	(below)	
				P.1511	Topographic maps for altitude		
				P.837	Rain attenuation		
				P.838	Rain attenuation extension to 1, 000 GHz		
		P.676	Gaseous attenuation	P.836	Rainfall		
				P.835	Reference standard atmosphere		
				P.453	Refractivity information		
		P.531	Ionospheric scintillation	P.1239	Reference ionospheric characteristics and software	P.1144	Guide to application of methods
		P.528	Multipath				
		P.840	Cloud attenuation	P.1144	Guide to the applocation of methods		
		P.453	Refractivity information				
P.525	Calculation of free-space attenuation						
P.619	Propagation data required for the evaluation of interference between stations in space and those on the surface of the						
P.679	Propagation data required for the design of broadcasting satellite systems						
P.680	Propagation data required for the design of Earth-space maritime mobile telecommunication systems						
P.681	Propagation data required for the design of Earth-space land mobile telecommunication systems						
P.682	Propagation data required for the design of Earth-space aeronautical mobile telecommunications systems						
P.1621	Propagation data required for the design of Earth-space systems operating between 20 THz and 375 THz						
P.1622	Prediction methods required for the design of Earth-space systems operating between 20 THz and 375 THz						
P.1623	Prediction method of fade dynamics on Eath-space paths						

Table 2.5 – ITU-R standards defining the Earth-space-aircraft channel propagation model ([61] to [91])

The graveyard orbit is typically 300 km above the GEO orbital altitude. The region from GEO altitude to 200 km above GEO altitude is kept clear to provide a place for repositioning of satellites within the GEO ring. These additional distances must be taken into account when designing satellite communications systems, particularly those providing TT&C capability.

2.3.5 VSAT and Satellite Broadband standards

Very Small Aperture Terminal (VSAT) satellite systems are primarily used for data services. There is no fixed standard and many variants are implemented. Typical variants are DVB-RCS (Return Channel via Satellite), which is a variant of the ETSI Digital Video Broadcast standards, such as DVB-S2 and DVB-S2X [92]. Internet Protocol over Satellite (IPoS) [93] is another standard, which is described by ETSI but has only been implemented by one manufacturer. Satellite-DOCSIS, a further standard, is based on a modification of the cable modem standards.

Typical and well-known examples of enterprise VSAT satellite broadband systems include the satellite communication infrastructure for the UK National Lottery terminals. VSAT systems rely on the satellite providing a 'bent-pipe' communication channel, typically to a central ground station where the data is connected with the ground communications infrastructure, such as fibre-optic links into the Internet.

Satellite broadband services, typically using VSAT antennas with 66cm diameter, use a two-way data path usually in the Ka-band. Data rates per user are fixed by the capacity of the satellite, the number of spot beams per satellite, over which capacity may be dynamically shared, and the time and frequency multiplexing of the signals in the spot beam to support multiple users. Demand for VSAT and home user satellite Internet service drives the need for increasing satellite capacity.

The next chart (Figure 2.14) projects the point at which per-satellite capacity will exceed 1 Tbps, based on existing satellite technology trends.

As previously noted, the main constraints on reaching and exceeding this capacity level are power and thermal dissipation. For reference, satellites in the 100Gbps to 1Tbps range can typically have a mass of around 6 tonnes, and with a volume that fits within existing launcher payload shroud dimensions at about 6m. 6 tonnes is about the limit of most commercial Assembly Integration and Test (AIT) facilities globally.

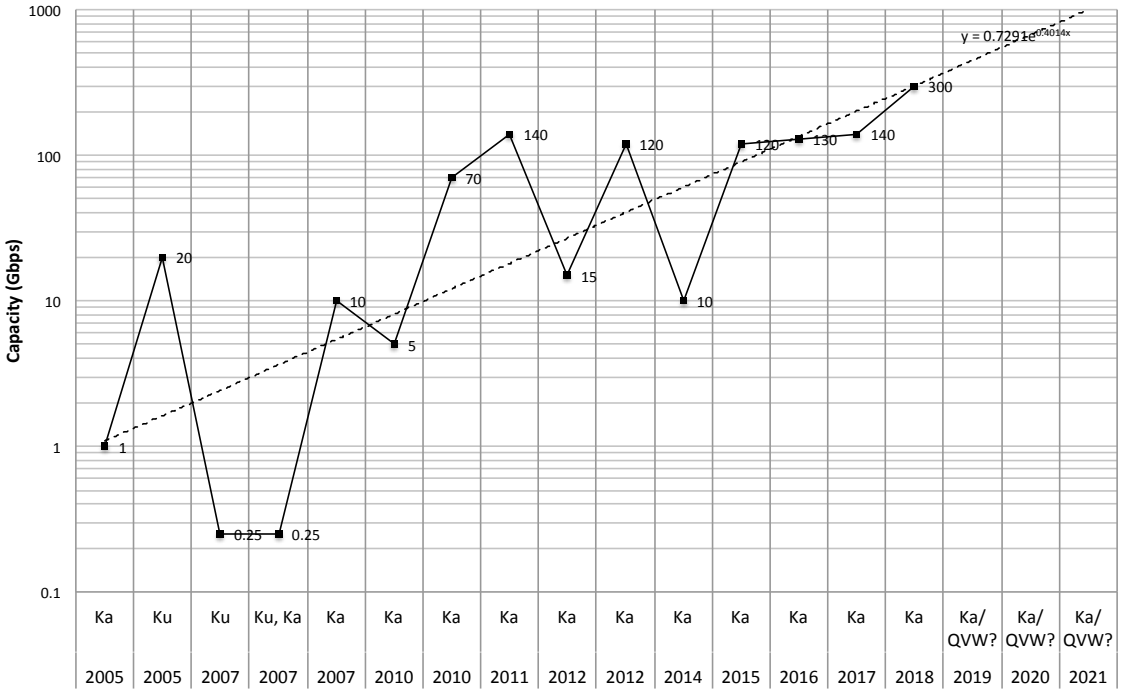

Figure 2.14 – Projection of current per-satellite capacity forward to 2021
(data sourced from *Ofcom* [94] and *Via Satellite* [95] and then projected forward)

To go beyond 1Tbps per-satellite throughput capacity requires new and novel technologies, with considerable research currently focussed on the fields of photonics processing, more efficient power amplifiers, and large lightweight antennas, amongst others.

2.3.6 Satellite Television standards

Satellite television standards are primarily driven under the ETSI DVB (Digital Video Broadcast) banner. Again assuming that the satellite is operating as a 'bent-pipe' transponder, the focus of the standard is on the broadcast waveform. In its latest variant, DVB-S2X [96], the performance for satellite TV traffic is very close to the Shannon limit (Figure 2.15). Satellite television systems typically operate in the Ku-band.

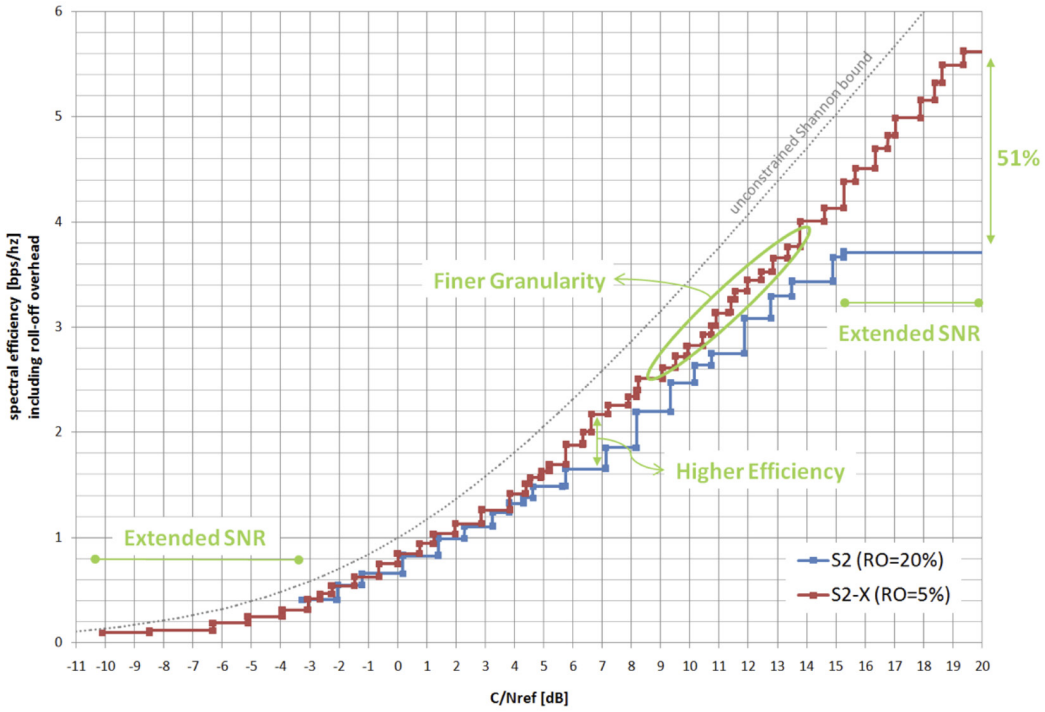

Figure 2.15 – Comparison of DVB-S2 and the DVB-S2X standards illustrating how performance gains were achieved (after *DVB fact sheet* 2014 [96])

2.3.7 ECSS standards

The European Cooperation for Space Standards (ECSS) defines a complete life cycle for satellite and ground station development, from components to system engineering. The standards are divided into engineering (E-series), management (M-series), policy (P series), quality (Q-series) and summary (S-series).

For this study key documents include ECSS-E-ST-50-01 to -50-05 ([97] to [101]) that describe harmonisation of ECSS with the CCSDS space data links for TM and TC; the communications standards are summarised in ECSS-E-ST-50C [102]. The main ECSS change from the CCSDS standards for TT&C is the inclusion of DSSS waveform. As with the CCSDS standards, there is no definitive standard within the ECSS for the payload RF system - these are assumed to be bespoke, or follow one of the common telecommunications standards described above.

2.4 Communication satellites

The following sections cover the different types of orbits, satellites, and satellite features and performance that can be found in existing and planned satellite systems and constellations. The review covers satellites at all orbital altitudes and orbit topologies.

2.4.1 Orbits

Satellite orbits are minimally defined in terms of their orbital altitude above the surface of the Earth (Table 2.6). The highest point of the orbit (apogee) and the lowest point (perigee) correspond to the highest and lowest altitudes of the orbit ellipse.

No orbit around the Earth is perfectly stable. Due to the geodetic shape of the Earth, Earth's atmosphere, and space plasma pressure, these additional 'torques' on the satellite cause it to precess, or drift.

Orbit	**Altitude range**	**Note**
LEO	87 km to 2,000 km	Low Earth Orbit
MEO	2,000 km to 35,768 km	Medium Earth Orbit
GEO	35,768 km	Geosynchronous Earth Orbit
HEO	Perigee as low as 1,000 km, Apogee above 35,768 km	Highly Elliptical/Eccentric Orbit. High Earth Orbit is that above 35,768 km
Polar	All altitudes	Polar orbits pass over, or very close to, the Earth's poles. The orbits have high inclination.
Sun Synchronous	Similar to polar	Orbit period designed to ensure that the Earth surface below the satellite is in sunlight at all times.
Tundra	35,768 km	High inclination GEO orbit
Molniya	HEO with typical inclination of 63.4^{o}	Period of a sidereal day. These orbits have preferential cover over a hemisphere.

Walker	LEO and MEO altitudes	Not a single orbit, but a series of orbits that make up the structure of a constellation of satellites.
Brandon	HEO altitudes	Not a single orbit, but a series of orbits that make up the structure of a constellation of HEO satellites.

Table 2.6 – Summary of typical communication satellite orbits

To achieve a stable orbit these torques must be compensated by the addition of thrust. Since thrust is supplied by fuel (and thrusters), it is typically the amount of fuel that is the limiting factor for most satellite mission lifetimes. Also, fuel equates to additional launch mass, and there is a mass limit imposed by the launcher. Efficiency (and reliability) of thrusters and conservation of fuel are key areas of research with the aim of increasing mission lifetimes, or optimising fuel to reduce overall satellite launch mass. This aim is the primary drive behind the move from chemical to electric propulsion for GEO satellites.

2.4.2 Satellite structure

Satellites typically consist of two structural units, the satellite bus, and the satellite payload. For many science missions the convention is to describe this as bus plus instrument. For deep space missions there may also be an additional service support unit.

The satellite bus contains all the support functions for the satellite, such as propulsion, which includes thrusters and fuel tanks, the attitude and orbit control system (AOCS), guidance navigation and control (GNC), which typically requires an on-board computer (OBC), and the telemetry, tracking and control (TT&C) RF link. The payload provides the bespoke payload for the mission. Payloads for communications satellites are typically in the form of either ‘bent-pipe’, or ‘processing’ transponders. A ‘bent-pipe’ transponder receives the signal (uplink or feeder link) and rebroadcasts it at a different frequency (downlink or user link). A ‘processing’ transponder performs some level of protocol decode and recode before retransmission.

2.4.3 Ground system structure

Ground system architectures vary but usually consist of points-of-presence (POPs) ground stations, which connect the 'space segment' satellite communications payload to the 'ground segment' network. The 'ground user segment' describes the ground elements of modem and antenna, such as those found on dwellings to provide satellite TV, or handheld and portable units that utilise satellite service connectivity.

The 'ground control segment' describes the elements of the Spacecraft Control Centre (SCC), which communicates via the TT&C to the satellite and provides the command and control link, of which are usually several sites to provide resilience, and the Mission Control Centre (MCC), sometimes linked into a Network Operations Centre (NOC), which provides overall mission control of the satellite constellation.

ECSS standards exist that cover all aspects of ground control systems, software and architecture. Ground user equipments are typically bespoke. For science missions there is typically no ground user segment.

2.4.4 Communication satellite constellations

Any full Earth coverage satellite system must be a constellation. For orbits below GEO, constellations are typically configured as variants of polar Walker constellations, although other orbit topologies, such as equatorial, Tundra and Molniya, are occasionally used.

The benefits of lower altitude orbits are the use of potentially lower cost bus platforms, particularly if not within the high radiation Van Allen belts. Lower launch costs, and typically shorter time to develop and launch the satellites compared to larger satellites are a significant commercial benefit. Alongside reduced latency and shorter communication channels – which allow for higher data rates – are key features of most so-called 'New Space' and 'Mega-constellation' satellite constellations.

LEO Comms Constellations	MEO Navigation Constellations	MEO/GEO Comms Relays	Molniya and HEO Constellations
Teledesic	Navstar GPS	TDRS	Molniya
Iridium	Galileo	EDRS	SDS
Globalstar	Glonass	TSAT	
Orbcomm	Beidou		
O3b			
LeoSat			
OneWeb			
MicroSat (SpaceX)			
Telesat*			
Boeing*			
Kepler*			

Table 2.7 – Examples of communications and navigation satellites
(Those not discussed in this thesis are marked with an asterisk)

The following section describes several communication and navigation satellite systems and their performance parameters. The data is collected from open sources and is referenced (Table 2.7).

2.4.5 Teledesic

Teledesic [103][104] was an early consortium effort that included, at various times, Microsoft, Boeing, Motorola, and ICO to create a low earth orbit (LEO) satellite constellation to provide Internet access. The original mid-1990s proposal consisted of a constellation of 840 LEO satellites, which was pared back to 288 LEO satellites by the late 1990s, then reduced to 30 satellites in medium earth orbit (MEO) by the early 2000s. Beyond an initial demonstration launch, the constellation was never built or launched.

The intention was to provide a 64Mbps downlink, 2Mbps uplink asymmetric, or 64Mbps uplink symmetric user capacity, and incorporate on-board decode and switching of traffic using a distributed routing algorithm architecture. Multi user access would be achieved with MF-TDMA (Multi-Frequency Time Division

Multiple Access) on the uplinks, and ATDMA (Asynchronous Time Division Multiple Access) on the downlinks. Downlinks were to operate on a band around 19 GHz, and uplinks on a band around 28.8 GHz (Ka-band). The target availability was, the typical for the satellite communications industry, of three-nines (99.9%).

2.4.6 Iridium

The Iridium network started in the 1990s as a Motorola driven LEO communications satellite constellation, seen at the time as an obvious next-step and adjunct to ground-based mobile phone communications, providing coverage of a much larger customer base with the attendant revenue this might generate [105].

The original Iridium satellite constellation consists of 66, 3-axis stabilised, 670kg satellites (Figure 2.16) in polar LEO following a Walker Delta constellation topology with 6 planes of satellites 31.6^{o} apart each containing 11 satellites; satellites in adjacent planes were offset by half the satellite-to-satellite distance along the plane, and satellites in planes 1 and 6 orbit in a counter-direction to the other planes. The satellites orbited at an altitude near 780 km. Spare satellites were held in a parking orbit at 666 km [106].

The communication payload user links operated in the L-band (at around 1.6 GHz) and used phased array antennas to create a cellular pattern of 48 cells within each Iridium satellite's footprint (that is, three phased array antennas per satellite, each with 16 spot beams); the number of outer ring cells in each footprint varied to avoid interference as the satellites approached each other at the poles. Each satellite used a cellular-like frequency re-use strategy with a cluster size of 12. Satellites needed to appear 8^{o} above the horizon to permit connection from a ground user terminal.

Multiple access is achieved using a similar frame structure to mobile phone technologies such as GSM (2G), with Iridium using a TDMA/FDMA approach but built around a 90msec frame. The frame structure is shown in Figure 2.17. The simplex downlink slot contains a globally allocated 500 kHz band between 1626.0 MHz and 1626.5 MHz containing 12 frequency slots carrying control channels for broadcast and synchronisation.

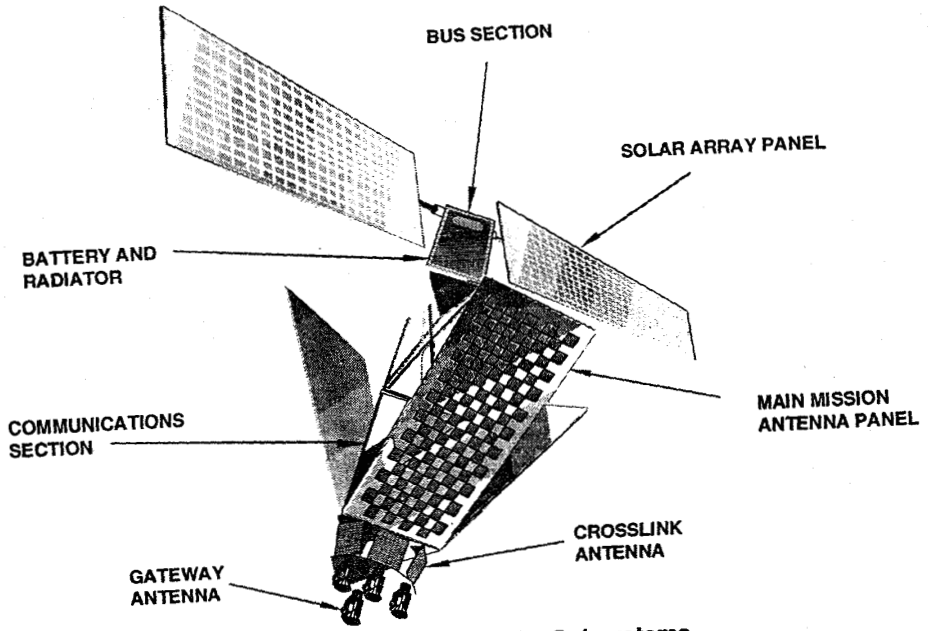

Figure 2.16 – Iridium satellite (after *Maine, Devieux and Swan* [107])

Data rate is carried as synchronous 2400 bps in paired (duplex) up/downlink slots with a modulation rate of 25k samples per second with Differentially Encoded QPSK (DE-QPSK), giving 2250 symbols per frame. Pulses are shaped using a root-raised cosine filter.

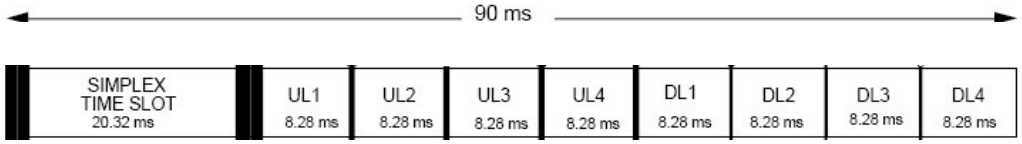

Figure 2.17 - Iridium TDMA Structure [79]

Error coding is added in various forms, including frame check sequences. Control channels use DE-BPSK to add 3dB margin to the signal, and as in GSM (2G), the user slot structure can be used to carry vocoder derived voice data or user data. Slot alignment at each end of the link is carried out using time of flight measurement during acquisition – which uses the ALOHA protocol – and guard intervals to ensure slot integrity once aligned.

Each FDMA slot covers 41.667kHz, within which are carried 8 sub-slots – similar in structure to GSM (2G) - with satellite geographical frequency re-use to make best use of the available spectrum: frequency is also reused within the satellite cellular

beam structure. The total bandwidth used is 10 MHz. Management of beams, time slots, frequency slots, and sub-slots are coordinated to support optimisation of the system in cases of heavy load at particular geographic locations.

Adaptive power control is used – again, in a similar manner to GSM (2G) – which, along with modulation and beam optimisation, is designed to exceed 10^{-2} BER and to operate with a link margin of 15.5dB; this margin being also to cope with urban multipath at the user handset or terminal.

The core network that supports the operation of Iridium is identical in operation to that of GSM (2G). Users are identified by their allocated IMSI number, with their location information and other call data stored in a Home Location Register (HLR). Though users have a SIM card in their devices, it is only the device ID (the IMEI as in GSM) that is used to identify the user. The core network approach is also very similar to that used in the GMR-2G satellite standard [58].

A unique feature of the Iridium satellite network is the inter-satellite communication, which provides data routing paths from any satellite back to a ground station. There are numerous benefits to this, but the most tangible is the removal of the need to site ground stations in other countries; something which is expensive to achieve, can be politically difficult, and has the issue of then requiring ground connectivity back to the home country or international network.

Iridium's inter-satellite links operate at 25Mbps via four vertically polarised antennas on the satellite; the bandwidth used for each link is 200 MHz. Two antennas are static and point forward and backward around the orbit, and two are steerable to track satellites in adjacent orbital planes. The frequencies used are in the band from 22.55 GHz to 23.55 GHz.

The gateway links for the constellation are maintained by satellites that pass overhead the ground anchor stations, and as a result the gateway satellite changes as the constellation moves. The gateway connectivity uses right hand circular polarised antennas with 100 MHz for uplink, and 100 MHz downlink bandwidth in the 27.5 GHz to 30.0 GHz, and 18.8 GHz to 20.02 GHz respectively.

Although “IRIDIUM uses a proprietary algorithm for link assignment and routing.” [77], given its close alignment with the GSM (2G) standards, it seems likely that the method used to route calls and data is similar to that of the GSM standard. Except that in this case the mobile user terminals are in effect static, and it is the base stations (BTS) that are moving. By applying the same logic of location updates, location area codes, tracking of the information in the HLR/VLR (Home Location Register/Visitor Location Register), and given a known, if dynamic, satellite constellation, the GSM standard routing approach could be applied to the Iridium Walker Delta network. There are many published papers that try to second-guess the Iridium routing algorithm, but to my mind at least the simplest approach perhaps would be to consider that it adapts the GSM standard directly with slight modifications.

Mobility management as a control layer in the architecture, as in GSM, provides the necessary Base Station Controller (BSC) functions of handover control, neighbour identification, reporting to the user terminal, and information on when to handover based on BER and BLER in the satellite user data link. As in GSM handover is best performed by the user terminal, under the direction of the core network (BSC mobility management). And since the handover is break-before-make, there is a requirement to perform the usual synchronisation and control channel hand-off, and camp-on procedures that would be found in GSM. The main difference in the Iridium case is in the handover between cells of one satellite, and then to handover of cells created by another satellite (see Figure 2.18). If we assume that all of the satellite cells are in the same ‘location area’, then handover and mobility management architecture and operation can be considered as very similar to typical GSM topologies.

2.4.7 Iridium Next

The original lifetime of the Iridium satellites was around 5-7 years and most of the satellites in the constellation have exceeded this. However, it is now over 15 years since the first launches, and the current owner, Iridium Holdings LLC, determined that an upgrade would be required, not only to replace existing Iridium satellites as they reach end of life, but also to make use of the opportunity to improve the

capability and performance of the constellation with a new satellite bus and new communications payloads. Though the general constellation topology and mode of operation are unchanged from the original Iridium network, the data rates and satellite capabilities have been improved [108].

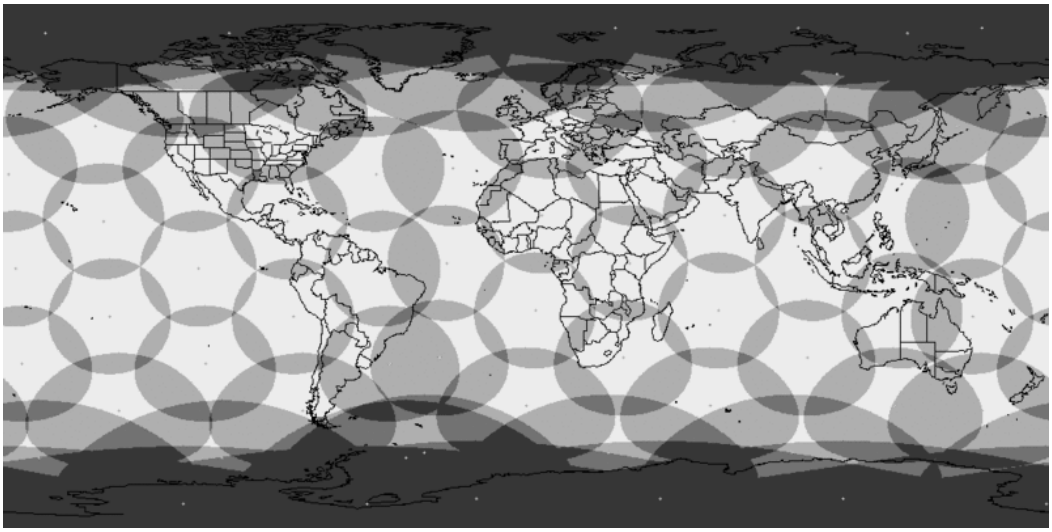

Figure 2.18 – Snapshot illustration of ground footprint of the Iridium constellation (*Credit: SaVi, the satellite constellation visualisation software*).

Iridium Next (Figure 2.19) is based on the Thales Alenia Space ELiTeBUS-1000 platform with the Iridium communications payload installed by OrbitalATK in the USA. There are also hosted payloads on many of the Iridium Next satellites. The satellites fit into the existing Iridium topology at 780km and replace the older satellites. The 860kg satellites have a 15-year on-orbit design lifetime and are provided with 2.2kW of power from rotating solar panels.

The Iridium Next payload provides increased user rates of up to 128kbps for mobile users and 1.5Mbps for static users. The Ka band feeder and cross-links communication system provides increased capacity at more than 8Mbps. The communications payload is manufactured by SEAKR Engineering Inc. and has a dual redundant software defined regenerative signal processing capability with a flexible modem and channeliser, and around 1 TFLOP of processing performance [109].

Figure 2.19 – Iridium Next satellite illustrating the phased array Iridium user antenna, and at the corners, the inter-satellite and feeder link antennas (Image credit *Thales Alenia Space/Iridium*)

The user connectivity is in L-band, as with the original Iridium payloads, with a 48-beam phased array antenna creating the ground cells. The inter-satellite links consist of two fixed and two steerable Ka-band, 23 GHz communications links. And there are two 20/30 GHz steerable feeder links to terrestrial gateways. The Telemetry, Tracking and Control (TT&C) link operates at 20/30 GHz using an omni-directional antenna.

2.4.8 Globalstar

In a similar manner and timescale to Iridium, in the early 1990's, Globalstar proposed a cellular based (Figure 2.20) satellite based global coverage service, utilising CDMA technology (c.f. IS-95) provided by their partner company Qualcomm. The satellites were manufactured by Space Systems Loral (SSL).

The technology solution chosen was to utilise a bent-pipe transponder architecture so that all the complex processing could be carried out on the ground. This with the aim of simplifying, and lowering the cost, of the satellite space segment, and allowing for straightforward technology upgrades over time [110]. The first eight, first generation satellites were launched in 1998.

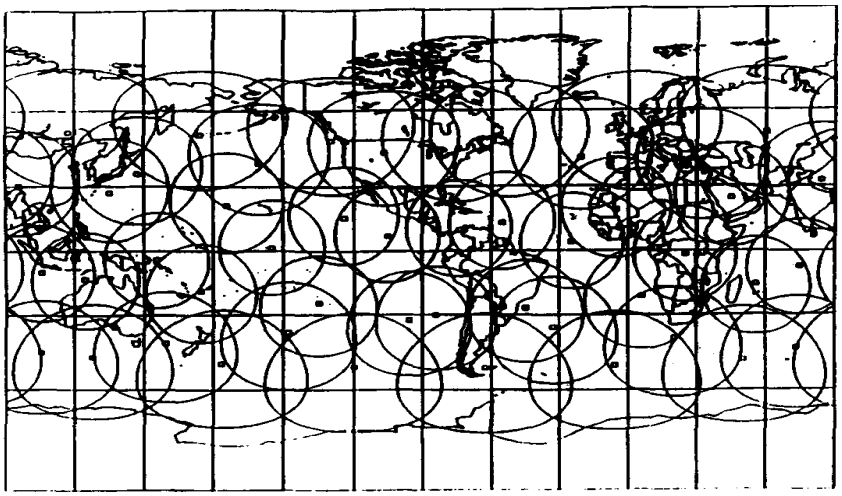

Figure 2.20 – Globalstar first generation satellite global coverage noting equatorial focus (after *Dietrich, Metzen and Monte* [110])

Globalstar added to the constellation providing around 32 satellites at 1440km orbital altitude with bent-pipe repeater communications connectivity in L-band and S-band. The bent-pipe architecture requires that the satellites are in direct line of sight of a ground segment anchor terminal; there are no inter-satellite links as in the Iridium architecture.

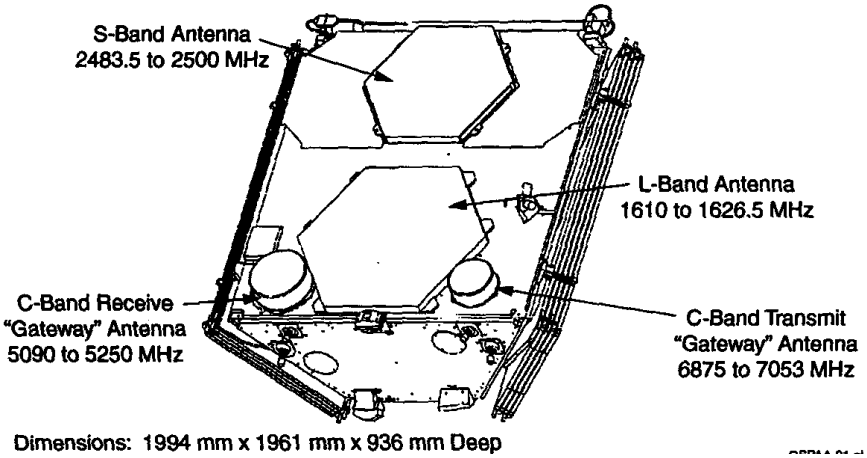

Figure 2.21 – Globalstar first generation satellite external RF design (after [111])

The first generation Globalstar constellation has a Walker 48-8-1 topology, consisting of 8 planes of 6 satellites at 52^{o} inclination [83]. The Globalstar constellation does not provide global coverage and duplex data connectivity is only available over certain areas of the Earth where connectivity can be maintained with one of 40 ground stations. The communications payload (Figure 2.21) consists of L-

band and S-band patch panel antennas, with C-band 'feeder' link connectivity and TM/TC provision. The satellite bus characteristics are described in Figure 2.22.

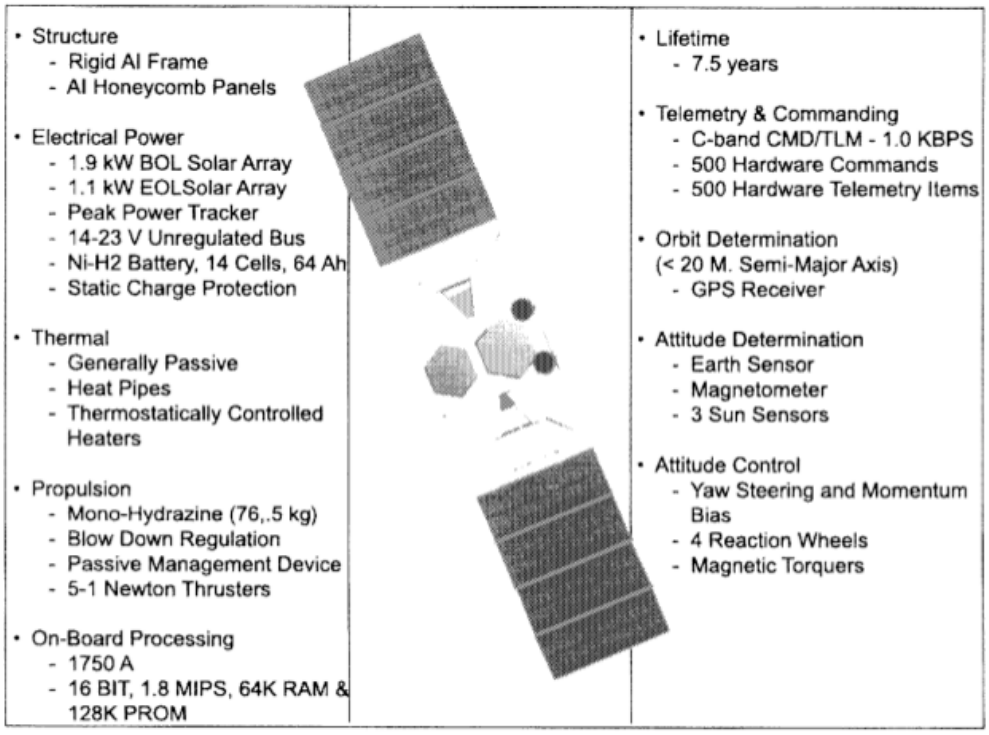

Figure 2.22 – Globalstar first generation satellite bus design summary (after [111])

Globalstar uses a relatively unusual way to describe the RF channel, directly incorporating the satellite loss in the path loss description. For example, the forward link from the gateway to the user terminal is described as 41dBW EIRP with a receive signal (with satellite diversity) of 3.9dB, and 9.2dBW and 5.7dB for the return path. The channel is protected by a forward error correction code (FEC) and rate ½ convolutional code, and uses standard CDMA IS-95/CDMA-2000 (following 3GPP2 – a US variant of the 3GPP standards) DSSS-CDMA signalling in 1.23 MHz bands using Walsh codes with a chip rate of 1.2288 Mchips/sec.

Typical data rates supported are 4.8 kbps; enough for voice and low-rate data services. A pilot channel is used to ensure synchronisation, again similar to the 3GPP2 standard. The signals from each of the user terminals arriving at the gateway terminal may suffer from the DSSS-CDMA 'near-far problem' which can cause dynamic range issues at the receiver. This is overcome with dynamic transmit power control to the user terminals.

On the satellites, diversity receive using soft combining (i.e. before symbol decoding) across two satellites can be performed, to increase the E_b/N_o at the receiver. This soft combining allows for moving user terminal soft (that is continuous make-before-break) hand-off between antenna projected 'cells', and attempts to directly mimic the standard 3GPP2 mobile phone cellular approach.

2.4.9 Globalstar Second Generation

The short lifetime of first generation Globalstar satellites required a replacement constellation to be added. As a result, 24 second-generation satellites were introduced, each with an extended lifetime of 15-years, and with upgraded antenna technology. Figure 2.23 illustrates the three beam formed antennas of the upgraded design.

Figure 2.23 – Production line development of Globalstar second-generation satellites illustrating the three types of beam forming antenna (Image credit: *Thales Alenia Space/Globalstar*)

Communications protocol and overall constellation architecture remained the same as the first generation design. The second generation satellites weigh around 700kg, are 3-axis stabilised, and have an improved phased array antenna system (Figure 2.24).

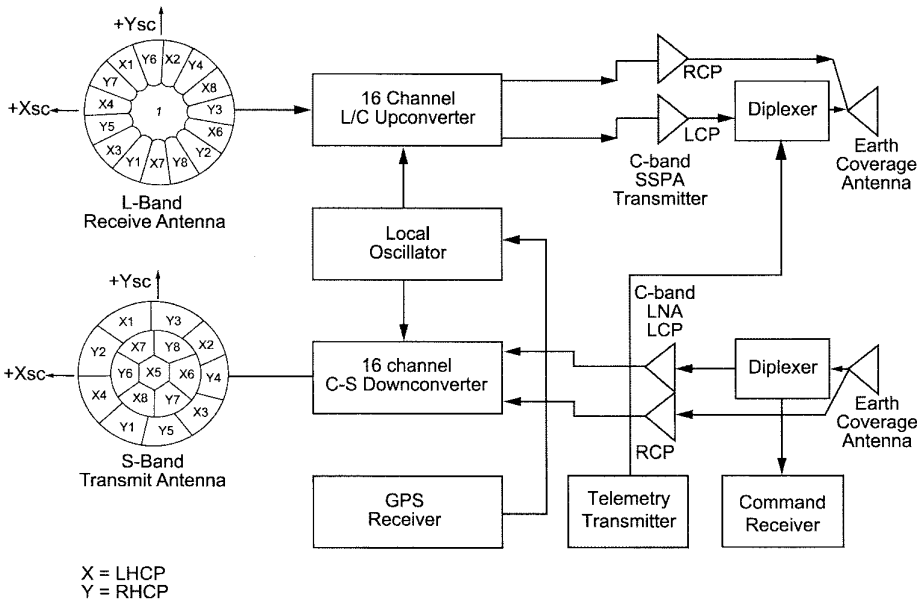

Figure 2.24 – Globalstar second-generation phased array antenna system (after [111])

2.4.10 O3b

O3b Networks (the Other 3 billion) is a satellite services company with the ambition to provide low cost Internet connectivity to a large proportion of the Earth's population. Owned by satellite services company SES Inc. and funded by Google Inc. amongst others, the O3b satellites, unlike Iridium and Globalstar, orbit at around 8,063km in MEO. The O3b constellation consists of 12 satellites orbiting the equator and providing communications links in the Ka-band.

Because of the equatorial orbit, comms service can only be provided to +/-45^{o} from the Equator, however, because of the increased orbital altitude, O3b can provide full Earth coverage (within this geographical band) with only 12 satellites, though only 6 are currently operational. The only problem is that at this orbital altitude, the satellites operate in the very high radiation environment of the Van Allen belts, and thus must be designed to survive this. Also, because they are not in geosynchronous orbit, they pass overhead five times a day.

The Ka-band communications system consists of 12 steerable dish antennas per satellite (Figure 2.25), with two channels per beam, providing around 600 Mbps per

satellite. Two of the beams connect with feeder ground stations, with 10 dishes for user terminals, each beam occupies 216 MHz providing aggregate 1.2 Gbps per beam (uplink plus downlink). Each beam's footprint is around 700 km at the Earth.

Figure 2.25 – O3b constellation satellites, with 12 steerable dish antennas, being attached to a launch adapter (Image credit: *Thales Alenia Space/O3b/CNES*)

The satellite bus is a Thales Alenia Space trapezoidal shaped ELiTeBus-1000 with a design lifetime at this orbit of 10 years. The first satellite was launched in 2007. The satellite has a mass of around 700 kg, is three-axis stabilised, and has eight 1 N hydrazine thrusters for attitude control. There is very little further published information.

2.4.11 O3b Next Generation

O3b next generation is an eight satellite constellation as a follow on to the original O3b satellites. There is no further published information.

2.4.12 Orbcomm

Orbcomm has a LEO constellation of low data rate communications satellites (Figure 2.26) that support machine-to-machine (M2M) communication, voice, and short message services. The satellite 'disc' design makes it very efficient for multiple satellite launches, and is unique in the industry.

The satellites were developed by Orbital ATK Inc. Second generation variants (termed OG2) of the design, designed by Sierra Nevada Corp. follow a similar footprint but with a 'cube'-like design. Orbcomm has 36, 1.4 tonne satellites on orbit with the latest orbiting at 750km in several planes at 0^o, 45^o, 70^o and 108^o inclination. Power is provided using two rotating solar panels providing around 135W [112].

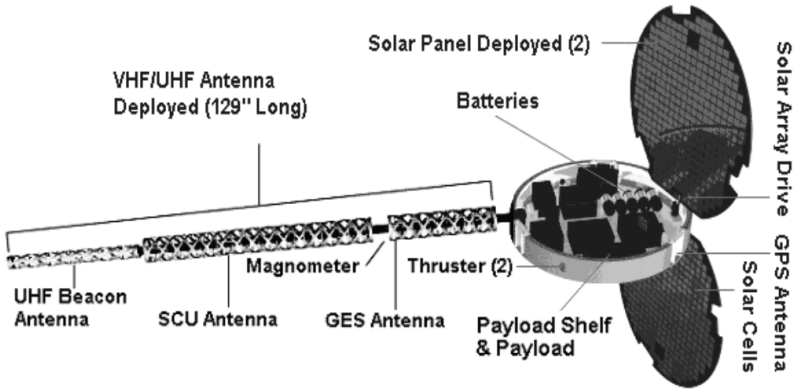

Figure 2.26 – Orbcomm first generation satellite RF external structures (after *Ilcev* [84])

The communication payload consists of six uplink receive transponders and two downlink transmit transponders operating around 150 MHz uplink and 138 MHz downlink at up to 40 W in the VHF band. Supported data rate is 2.4 kbps. There is no inter-satellite link connectivity, and as such all communication is via feeder links which take up one receiver and transmitter pair. Modulation is Orthogonal QPSK (OQPSK) and multiple access is by TDMA. There is a 1 W UHF beacon transmitter to allow ground alignment and Doppler compensation with the relatively fast moving satellites at this low orbit [113].

2.4.13 LeoSat

LeoSat is, at the time of writing, in the development phase. The aim is to provide a 78 satellite LEO Walker constellation with very high throughput communications for backhaul trunking and high data rate enterprise use.

Published data is very sparse on detail, with the LeoSat Inc. web page describing the communications performance as providing data rates between 50Mbps and 1.6Gbps (up to a maximum of 5.2Gbps). Each satellite will be manufactured by Thales Alenia Space and is planned to have ten steerable Ka-band antennas with two steerable gateway/feeder antennas of up to 10Gbps. Each satellite will also contain four high data rate optical inter-satellite links.

2.4.14 OneWeb

The OneWeb constellation is, at time of writing, at the development phase. Previously known as 'WorldVu', and using spectrum previously allocated to the failed 'SkyBridge' constellation project, the intention is to orbit mid- to high-hundreds of small (circa 140kg), and low cost (circa $500k) satellites in around 20 orbital planes following a Walker topology at an altitude of around 1200km.

OneWeb has an interesting development model because hitting $500k per satellite will be quite challenging. Reducing capability to the bear minimum, using components from the automotive rather than aerospace industry, and using previously space-qualified modules, along with a business model that offers suppliers delivery quantities that support multiple hundreds of satellites, and access to the satellite production line facility post OneWeb constellation launch, are all, from published sources, being used as incentives. It will be interesting to follow this development model as its implementation unfolds.

Communication goals, as published on their website, are 6Gbps throughput per satellite with up to 50Mbps/user. The spectrum allocation is in the Ku band, and this has led to a potential interference issue with GEO Ku band satellites when OneWeb satellites cross the equator. To overcome this, OneWeb is planning to implement a technique called 'progressive tilt' which adjusts the antenna angle at the equator to prevent direct transmission towards Ku band satellites in GEO orbit.

It is an interesting and novel approach, and it will be interesting to see if this works well enough to overcome the problem, particularly for any Ku band GEO satellites

operating with small inclinations. An interesting planned feature of the OneWeb satellites is the ability to hand-off to Intelsat satellites in GEO.

It has been published that each OneWeb satellite will be in the 'small satellite' class (100-200kg) with a phased array antenna of approximately 36x16cm. The OneWeb satellites are being designed by Airbus Defence and Space (ADS), with ADS building the first 10-20 satellites at their facility in Toulouse, France, before handing off build to a production line facility in the US.

2.4.15 MicroSat

MicroSat is a constellation programme being developed by SpaceX Inc. and supported by Google Inc. Very little is known at the time of writing beyond information filed with the US Federal Communications Commission (FCC) as part of an application for use of the ground station frequencies [114]. Based on this information, the first two test satellites will be operating in the Ku-band (around 14.25 GHz uplink and 11 GHz downlink) with an S-band uplink at 2 GHz. The satellites will be placed in a nominally circular orbit at 625 km and inclination of 86.6^{o}.

The satellites will likely be launched as secondary payload on a Falcon-9 launch from Vandenberg, California. The completed constellation will contain up to 4,000 satellites.

2.5 Global Navigation Satellite Systems (GNSS) Constellations

Alongside communications satellites, there are other users of RF signals in orbit. Prime amongst these are the global navigation systems satellites. These typically utilise high accuracy in-orbit timekeeping and project multiple signals towards Earth at around 1.4 GHz using spread-spectrum signals. These satellite systems are considered in the following section.

2.5.1 Navstar GPS

The Navstar GPS (Global Positioning System) system (*Maine* [115]), as a typical example of a global navigation satellite system (GNSS), provides location information for ground terminals anywhere on Earth where there exists clear RF 'line of sight' to four or more satellites. The 24 Navstar GPS satellites orbit at 20,180km in six orbital planes with 55^{o} inclination (Figure 2.27).

Figure 2.27 – Illustration of the Navstar GPS satellite constellation (after *Rose* [89])

As *Allain* [116] and *Rose* [117] describe in each of their summaries of the system, in the simplest case, GPS allows location to be calculated by ensuring that (i) all satellites have the same time; achieved by ensuring reference to a common Stratum-1 timing reference [118]. And (ii), that the positions of all the satellites are known. Given this information, a ground receiver, takes the measured time of arrival (t_{TOA}) and subtracts the time of transmission (t_{TOT}), which is encoded in the transmitted signal. From the timing difference, a pseudo-range (P_R) can be calculated to the satellite.

$$\mathrm{P}_R = t_{TOA} - t_{TOT}$$

By geometry, four such measurements allow the location of the receiver on the surface of the Earth or in three-dimensional space, and also allows for the estimation of time error at the receiver relative to the satellite's common GPS timing reference.

If we represent the Earth in a Cartesian coordinate system then the following four equations describe the pseudo-ranges from a point on, or near, the Earth to the four satellites (*Langley* [119]).

$$\begin{aligned} P_{R1} &= \sqrt{(X-x_1)^2-(Y-y_1)^2-(Z-z_1)^2} - c.dT_{Offset} \\ P_{R2} &= \sqrt{(X-x_2)^2-(Y-y_2)^2-(Z-z_2)^2} - c.dT_{Offset} \\ P_{R3} &= \sqrt{(X-x_3)^2-(Y-y_3)^2-(Z-z_3)^2} - c.dT_{Offset} \\ P_{R4} &= \sqrt{(X-x_4)^2-(Y-y_4)^2-(Z-z_4)^2} - c.dT_{Offset} \end{aligned} \quad (1)$$

Where P_{Rx} represents the pseudo-ranges to each satellite, c is the speed of light, and (x_k, y_k, z_k) represents the location of each satellite k. Solving these simultaneous equations to provide the location (X, Y, Z) and time offset dT_{offset} can be achieved using a least squares approach, though other techniques with greater accuracy have also been developed [117]. From an RF and signal processing perspective, what is of interest here is the method by which the timing information and ephemeris are communicated to the receiver.

GNSS rely on signals with high autocorrelation and low cross correlation. Where the autocorrelation of the signals is defined as:

$$R(\phi) = \int_0^T f(t)f(t+\phi)dt \Big|_{\substack{\phi = 0 \text{ = High Autocorrelation} \\ \phi \neq 0 \text{ = Low Autocorrelation}}} \quad (2)$$

And the cross correlation of the signals is defined as:

$$S_{IJ}(\tau) = \int_{-\infty}^{\infty} PRN_I(t)PRN_J(t+\tau)dt = 0\Big|_{I \neq J} \quad (3)$$

Communications from the satellites are in the form of Gold code spread spectrum signals with 1,023 orthogonal values used at a spreading rate of 1.023Mchips/sec: that is, the sequences are transmitted within 1msec. Each satellite is allocated a unique Gold code which allows a set of correlating receivers to determine the local

arrival time (t_{TOA}) of the signal from each satellite; accurate, however, only to the chip rate.

As would be expected, there are a number of error sources, which include propagation errors, relativistic effects, noise, Sagnac bias, clock errors, satellite position errors, ionospheric errors, satellite antenna offset, and so on (see *Langley* [91] for a summary), and these affect the frequency difference between the satellites and the receiver.

The measured phase shift is proportional to the time difference, which allows determination of a 'pseudo-range' distance, that with four such measurements allows determination of position. Typically, however, it is not possible for GPS codes to be completely uncorrelated for all phase shifts, as the Gold codes are not completely orthogonal.

In a 'cold start' scenario the receiver needs to determine and align to the transmit frequency, as well as the timing offset. This is achieved by repeating the correlation calculations across the frequency band – including additional spectrum for Doppler – until the best signal strength is achieved.

The receiver (*Meng* [120] for example) then treats this as the first satellite lock and begins to retrieve its information from the data modulated onto the Gold code de-correlated signal. This data is made up of 1,500 bit messages sent at 50 bits/sec every 30 seconds and contains ephemeris, clock offset and other information. A feature of the latest Navstar GPS satellites is the inclusion of inter-satellite communication links, which are intended to aid monitoring, and control of the GPS satellite constellation.

2.5.2 Glonass

Glonass (Global Navigation Satellite System) is the Russian Federation equivalent to Navstar GPS and uses 24 satellites in 3 planes at 68.4^{o} inclination in a 19,130km orbit.

The payload operates in a very similar manner to Navstar GPS using similar Direct Sequence Spread Spectrum (DSSS) signals and Binary Phase Shift Keying (BPSK) modulation, with correlation of known PN (Pseudo-Noise) codes with the received signal to create the four pseudo-range values for the geometric position calculation (*Dale and Daly* [121]).

2.5.3 Galileo

Galileo is the name of the European Union funded GNSS system. It follows the same model as Navstar GPS and Glonass. The 24 satellites, built by OHB Gmbh, operate in 3 planes with inclination 56^{o}, in an orbit at 29,600km [122].

The payload operates identically to that of Navstar GPS with two changes, first, the frequencies and modulation are designed to not interfere with Navstar GPS, and second, instead of feedback register PN codes, Galileo uses a set of pre-computed feedback codes (called 'memory codes') that are produced from Gold codes through a genetic algorithm that insures their orthogonality and correlation properties [123].

2.5.4 BeiDou

BeiDou ('compass') is China's variant of GNSS. It's initial architecture varies considerably from Navstar GPS, Glonass, and Galileo in that it uses GEO satellites, and requires a two way communication exchange to a central server in order to determine the user terminal location, called the 'common view' calculation: in all other GNSS systems, the user terminal itself calculates the position, which is not reported back into the GNSS system.

The five geosynchronous satellites are located in slots at 58.75^{o}E, 80^{o}E, 110.5^{o}E, 140^{o}E, 160^{o}E; the uplink frequency is around 1.62 GHz and the downlink around 2.5 GHz (*Hongwei* [124]).

In a second phase, a Walker constellation with three planes of MEO satellites at 21,500 km at inclination of 55^{o} is being added as a 'passive GNSS', implemented in

a similar manner to other GNSS systems, along with three additional inclined GEO satellites at 55^{o} inclination [125].

The waveform is spread-spectrum CDMA based on a QPSK modulation with a design receive power level of -163 dBW. Position calculation for passive satellites is identical to that of Navstar GPS using pseudo-range measurements.

2.6 Data Relay Satellite Constellations

Communications satellites have a number of different configurations, depending on the application: from bent-pipe transponder repeater architectures, to high throughput multi-beam multi-downlink television satellites, through to Very High Throughput (VHT) bi-directional communication satellites with on-board channelisation and processing. Another class of satellite that is of particular utility for science and communications applications, where direct sight of a ground station is not available, is the data relay satellite. The following section considers the features and performance of data relay satellites.

2.6.1 NASA TDRS

The Tracking and Data Relay Satellite (TDRS) System (TDRSS) constellation was originally developed by NASA to remove the need for ground stations outside US territory. There have been twelve satellites deployed since the project was established in 1973 [126].

The satellites provide communications between missions and ground stations in the USA, and use inter-satellite communication to provide the links necessary to retrieve data from satellites at any point around the globe. Though not specifically designed for polar communication, the TDRS system supports South Pole stations using inclined GEO orbit TDRS satellites.

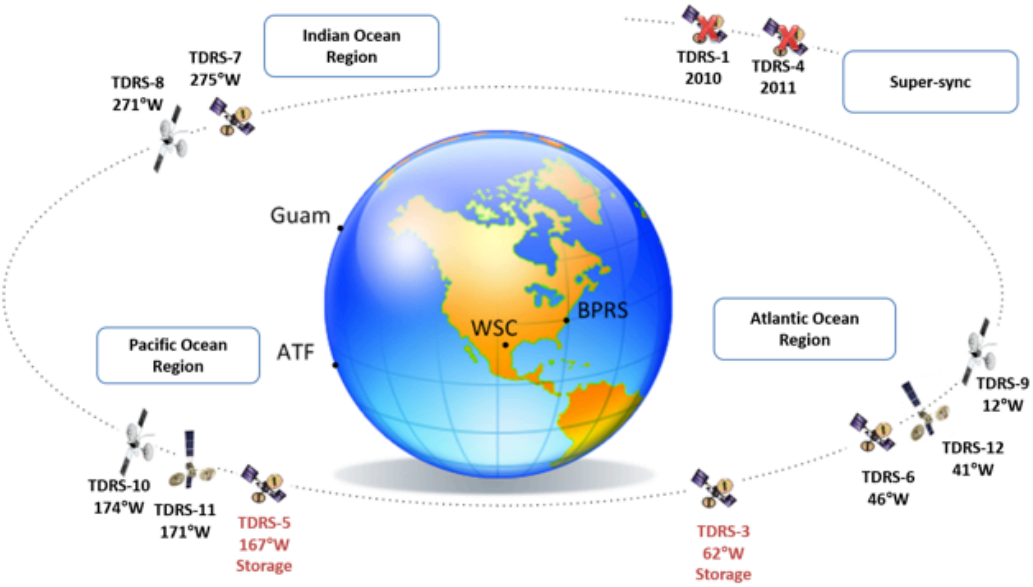

Figure 2.28– TDRSS satellite constellation (Credit: *NASA*)

There have been three generations of TDRS satellites that have progressively improved the TDRSS performance: TDRS A, B, C, D, E, F, G – first generation, TDRS H, I, J – second generation, TDRS K, L, M, N – third generation. Currently TDRS E, F, G, H, I, J, K, L and M (also known as TDRS 3 to TDRS 11) are operational (Figure 2.28).

2.6.2 TDRS first generation

First generation TDRS satellites (Figure 2.29) are based on a Boeing 601 bus generating 3.5kW, with on-board beam-forming for the S-band multi-access service. Along with a single access service, a multiple access service is also provided.

There are several TDRSS waveforms, with the legacy waveform being constructed of a spread spectrum signal carrying QPSK with 3 Mchips/second, with command data on the in-phase carrier, and range data on the quadrature phase; both sets of data are also BPSK (Binary PSK) modulated prior to the QPSK construction. Data rates supported are 10kbps to 25Mbps per user (up to 800Mbps for the latest satellites), depending on the satellite resources used. Transmission is polarised, left or right hand selectable.

On the downlink, three different modulation schemes are available to meet different applications and data rates; these are SQPSK (Staggered QPSK), QPSK with spread signal only on the in-phase carrier, or BPSK. FEC is rate ½ convolutional coding, with optional data interleaving. Signal frequencies, and receiver tolerance, support Doppler compensation.

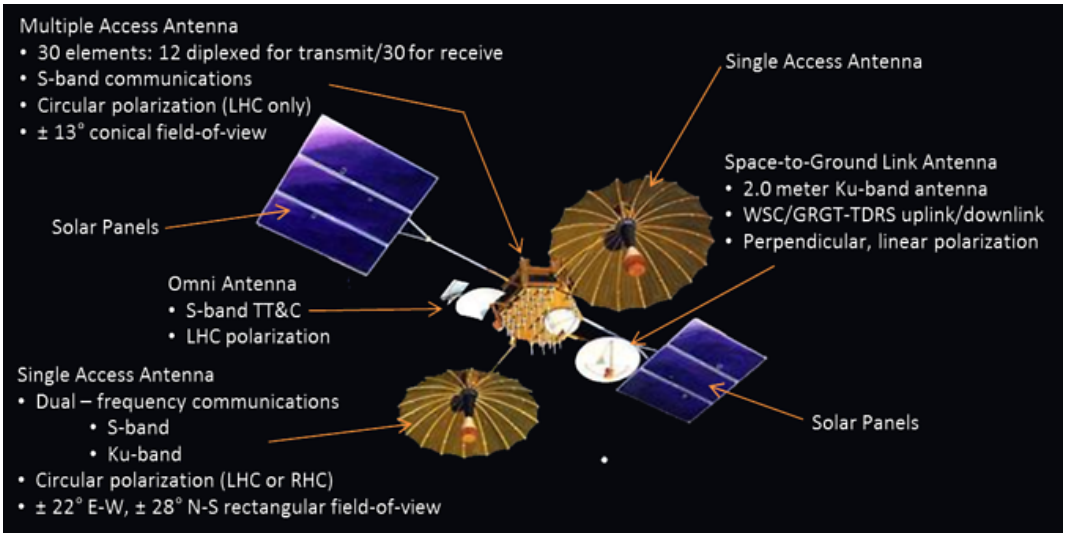

Figure 2.29 – TDRS first generation satellite external RF architecture
(Credit: *NASA*)

Each user system is allocated a PN code to identify the system to the TDRSS. There are two types of service provided, single access, where a user system has full access to a transponder resource, and multiple access which allows for TDM of multiple users. Single access channels are supported by the two large dish antennas, multiple access channels utilise an array antenna. First generation TDRS can support up to 12 diplexed, or 30 receive only (cross strapped to a single access channel) channels. The uplink frequencies are around 2.1 GHz and 13.775 GHz. (*Muhonen* [127]).

2.6.3 TDRS Second Generation

Second generation TDRS replaces the fine mesh ‘umbrella’-style antennas with flexible mesh antennas that fold against the spacecraft at launch. These are more robust and less prone to failure (see NASA Galileo mission antenna failure description [128], for example).

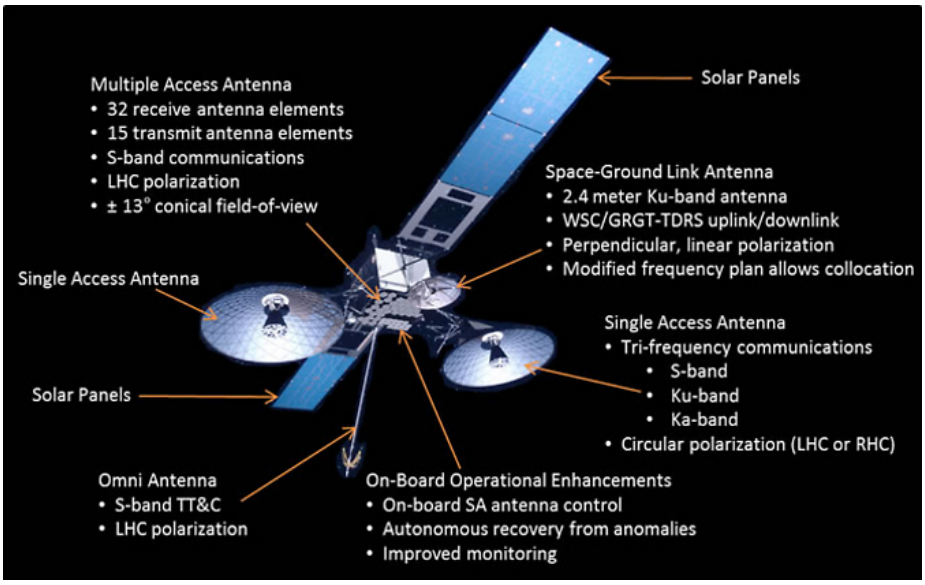

Figure 2.30– TDRS second-generation satellite external RF architecture (Credit: *NASA*)

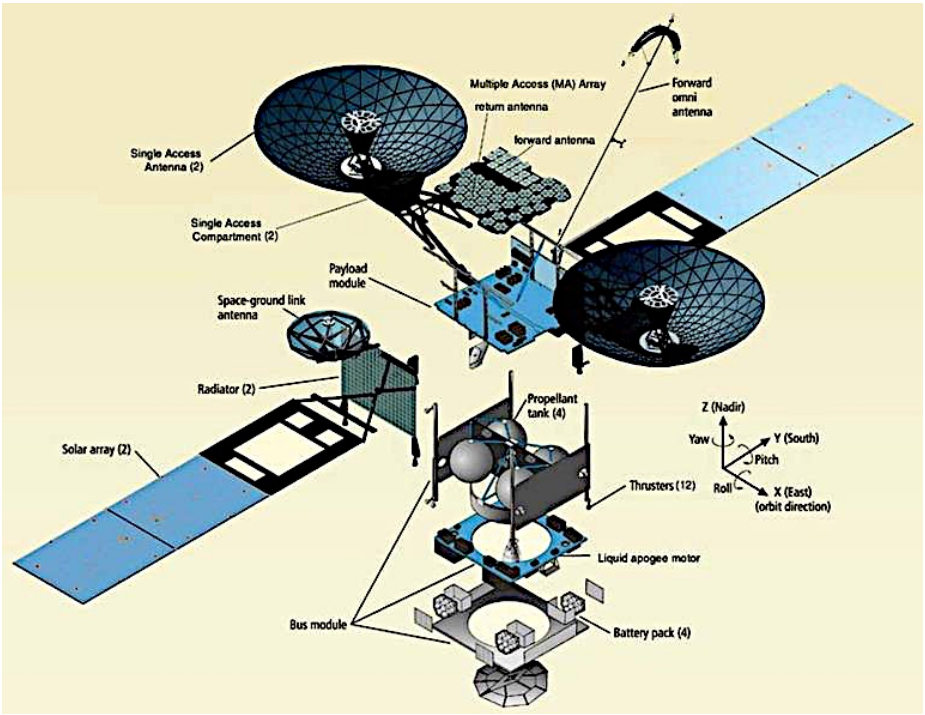

Figure 2.31 – TDRS second-generation satellite internal structure (Credit: *NASA*)

Along with changes to the antenna design, further transponders were added to support Ka-band, and two additional multiple access antennas in the array. Further, antenna control, which was carried out from the ground on the first generation

satellites was implemented on-board the second generation TDRS (Figure 2.30). An illustration of the major subsystems of the TDRS satellite is shown in Figure 2.31.

2.6.4 TDRS Third Generation

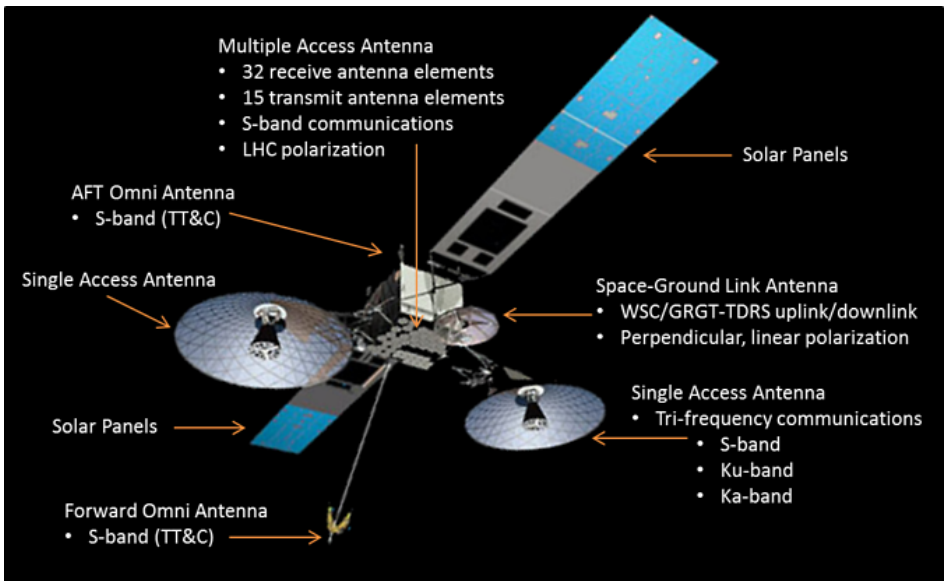

Figure 2.32 – TDRS third generation satellite external RF architecture (Credit: *NASA*)

Third generation of TDRS satellites (Figure 2.32) weigh 3.2 tonnes fully fueled and are three-axis stabilised. The solar panels provide around 3kW of power. The third generation increases the communication performance and provides on-board antenna array processing.

It is stated that the third generation satellites can support five user system satellites operating at different frequencies simultaneously, with user data rates of 800Mbps for Ka-band, 300Mbps for Ku-band and 6Mbps for S-band transponders [129].

2.6.5 ESA EDRS

In direct analogy with NASA's TDRSS, the European Space Agency (ESA) co-funded development of a European equivalent in a public-private partnership with Airbus Defence and Space (ADS). The partnership gives ADS the rights to sell

services of the European Data Relay System (EDRS) to science satellite and other users.

The EDRS system has been deployed in experimental steps: EDRS-A was installed as a hosted payload on the Eutelsat 9B GEO satellite and contained a Ka-band inter-satellite link and experimental laser communications terminal (LCT). EDRS-B is proposed, but not funded. EDRS-C is an ESA funded satellite containing a Ka-band payload funded by Avanti as the Hylas-3 payload, and a LCT [102].

A further satellite Inmarsat-4 (also known as Alphasat), co-funded between ESA and Inmarsat, alongside the primary L-band GEO commercial communications payload, contains several hosted technology demonstration payloads, including a LCT, and a Q/V-band transponder.

The performance of EDRS is stated as 300Mbps to 1.8Gpbs (Ka-band), and from 600Mbps to 1.8Gbps (laser communication) for LEO to GEO, with additional RF to Earth links [130][131][132].

Though much explored over the last twenty years, EDRS will be one of the first commercial services offering laser communications links. However, there are several key problems that need to be resolved to make such links, and relay service, viable for commercial communication services. The waveform used is typically BPSK with a homodyne receiver, using around 2.2W laser power at 1064nm wavelength. There have been attempts to develop solutions at the more eye-safe wavelength of 1550nm, though it is not clear if these are targeted at EDRS operation.

The key problems for EDRS and similar laser communication systems [133] can be listed as:

- payload - current LCTs weigh around 50kg, are about 1m cubed in dimension, and require around 180W power;
- data rate - current LCT data rates are very similar to existing Ka-band RF systems;

- acquisition - laser communications links currently require around 90 seconds to acquire and align before communication can commence;
- jitter - link performance can be variable, dependent on closed-loop alignment jitter between two LCTs on distant satellites;
- broadcast - there is no mechanism yet employed to allow laser communication to adopt a broadcast or multicast capability in support of data distribution to multiple satellites, or to provide resilience and link redundancy;
- torque - as rotational mechanical systems, current LCTs are active torque generators and can contribute to movement of a satellite's primary payload alignment if not counteracted;
- sun - although a similar problem of sun 'blinding' signal 'overload' occurs with RF systems, the issue is exacerbated for current LCTs because of the intensity of the sun at the infrared wavelengths used;
- latency - because there is currently only one LCT on each of the EDRS compatible satellites, and the LCTs are point-to-point, there is a latency issue as each user satellite requiring use of the EDRS service must wait to be allocated a communication slot; there is no concurrent communication capability to date because the LCTs are large, which militates against more than one of them being installed on a satellite;
- clouds - currently there is no solution to the problem of providing high availability laser communication connectivity for satellite-ground links in the presence of cloud;
- interoperability - currently there are no interoperability standards for laser communication systems, and all systems (ESA and NASA included) are closed systems owned and not released by those organisations and their co-funded partners, access is only via incorporation of key technology modules provided by the organisations and partners, there is no open market.

Although there is considerable research effort taking place to resolve these issues, at time of writing, they are largely unresolved.

2.6.6 TSAT

Prior to the development of EDRS' LCTs and laser communication infrastructure, the US TSAT (Transformational Satellite) communications system programme attempted to implement a fully integrated RF and laser communication system. The planned TSAT system consisted of five satellites with combined capability of supporting 8,000 RF links and 20-50 laser communications links (Figure 2.33).

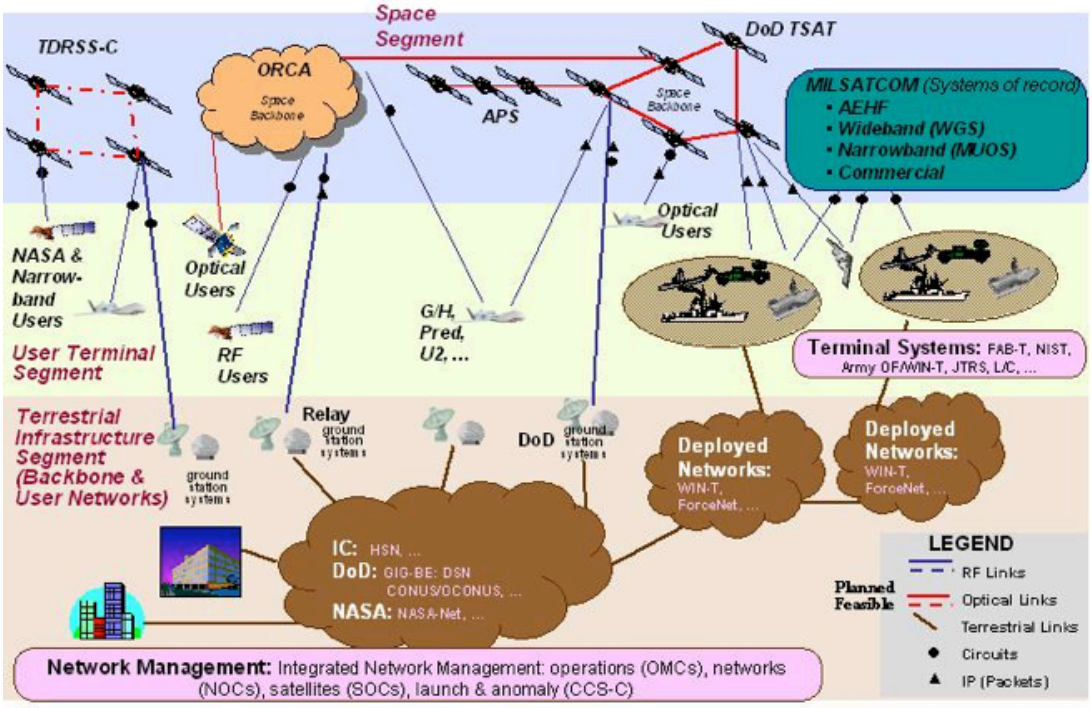

Figure 2.33 – Overview of where the proposed TSAT system would connect with the wider US DoD communications architecture (after *McKinney* [105])

It was cancelled in 2009 with the reasons for the TSAT system failure described by *McKinney* [105]. Primarily the technology was at too low a Technology Readiness Level (TRL), the laser terminals were too large to meet the number of connections required, and hence the system could not provide the bandwidth needed to meet the programme's requirements.

Many of the issues and problems are those described in the context of EDRS above. The breadboard model of the TSAT laser communications terminal, for example, was exceptionally large and only reached TRL-6 (demonstrator technical readiness level) before being cancelled.

2.6.7 Molniya HEO constellation

The Russian Molniya communication satellite system not only refers to the constellation, but has also lent its name to the type of inclined highly eccentric orbit where the satellite spends the majority of its time above the Earth's northern hemisphere.

The Molniya satellite constellation was first initiated in the 1960's and has subsequently been regularly refreshed up to the present day. The constellation is nominally around 16 satellites in HEO with inclinations of around 65^{o}, and with uplinks around 4 GHz and downlinks around 6 GHz. There are no inter-satellite links. Apogee is typically 40,000 km, with a perigee of around 500 km.

2.6.8 SDS constellation

The US equivalent of the Molniya HEO constellation is arguably the Satellite Data System (SDS), which operates satellites with inclination of around 63^{o}. It is published that the satellites are similar to those of the TDRSS. Little is known or published about these satellites.

2.6.9 Summary of communication and navigation satellite metrics

Table 2.8 contains a summary of the satellite constellations covered in this literature survey. In particular, this section highlights the use of industry standards in most cases, the use of Walker constellations for LEO coverage, and the start of adoption of inter-satellite links for constellations.

The majority of the communications systems use low order modulation; PSK, BPSK, GMSK, QPSK, combined with, in some cases, DSSS CDMA with various

chip rates. OFDM is not particularly common, although OFDM techniques in waveforms such as DVB-SX2 are present, but primarily for broadcast satellite systems.

Ref	Satellite payload	Satellite Bus	Orbit (km)	Number of satellites	Orbit Topology	User data rate	Feeder data rate	Inter-satellite data rate
1	Teledesic	Not flown	--	--	--	--	--	--
2	Iridium	LM-700A	780	66	Walker	<64kbps	200kbps	200kbps
3	IridiumNext	ELiTeBUS	780	66	Walker	1.5Mbps	8Mbps	8Mbps
4	Globalstar	LS-400	1,410	32	Walker	4.8kbps	120kbps	--
5	Glo. 2ndGen	ELiTeBUS	1,410	24	Walker	4.8kbps	120kbps	--
6	O3b	ELiTeBUS	7,825	12	Equatorial	800Mbps	1.6Gbps	--
7	O3b 2ndGen	ELiTeBUS	7,825	8	Equatorial	800Mbps	1.6Gbps	--
8	Orbcomm	MicroStar	720	36	Walker	4.8kbps	120kbps	--
9	Orb 2ndGen	Sterkh	670	5	LEO	4.8kbps	120kbps	--
10	Orb 3rd Gen	SN-100A	750	18	Walker	4.8kbps	120kbps	--
11	LeoSat	ELiTeBUS	TBD	78	Walker	1.2Gbps	TBD	TBD
12	OneWeb	Custom	1,200	648	Walker	50Mbps	TBD	TBD
13	MicroSat	In development	--	--	--	--	--	--
14	NavstarGPS1	Custom	20,200	10	Walker	--	--	--
15	Navs. GPS2	Custom	20,200	51 total	Walker	--	--	--
16	Navs. GPS3	A2100A	20,200	2017+ launch	Walker	--	--	Not published
17	Glonass	Custom	19,100	129 total	Walker	--	--	--
18	Galileo	Custom	23,222	30	Walker	--	--	--
19	BeiDou	DFH-3	36,000	16	GEO	--	--	--
20	BeiDou	DFH-3	21,519	9	Walker	--	--	--
21	TDRS	B-601	36,000	13 total	GEO	800Mbps	Unknown	--
22	EDRS	EuroStar	36,000	1	GEO	1.8Gbps	1.8Gbps	600Mbps
23	TSAT	Not flown	--	--	--	--	--	--
24	Molniya	KAUR2	40,000	166 total	Molniya	Unknown	Unknown	Unknown
25	SDS	SSL-1300	--	20 total	HEO	Unknown	Unknown	Unknown

Table 2.8 – Comparison of LEO, MEO, GEO, Molniya and HEO communication and navigation satellite constellations

User data rates rarely exceed 1 Gbps, and then only at the higher frequencies and with the wider bandwidths of Ka-band and above. Transponders of either bent-pipe or processing type are used, with typical transmit power of less than 100 W. Typical satellite power, particularly for constellations, is less than 5 kW, though there are much higher power levels available on larger GEO and HEO satellites, where this can exceed 10kW in some cases.

What is apparent is that each satellite constellation has specific data rate, antenna type, and particular standards for each specific market targeted; from machine-to-machine, to 'optical-fibre rate' backhaul connectivity, to mobile phone voice and data, to high data rate systems, through to extremely high data rate support for a small number of scientific satellite users.

2.7 High altitude aircraft communications

All aircraft whether manned or unmanned (Unmanned Aerial Vehicles – UAVs, or Remotely Piloted Autonomous Systems – RPAS), must follow the regional 'rules of the air' regulations [134], and the international standards agreed by the UN International Civil Aviation Organisation (ICAO) to allow freedom of use and over-flight of countries airspace for commercial operation as defined in the Chicago protocol [135].

As part of the protocol there are minimum equipment standards, which identify the types of RF communication and navigation equipment that must be carried by all air vehicles.

One further key requirement is that within controlled airspace, all aircraft must respond to Air Traffic Control (ATC) verbal requests; it is this latter requirement, amongst others, that drives requirements for UAV and RPAS communications. Further, UAV and RPAS systems typically are operating to provide imagery or other information and pass that back to a remote ground station, typically via satellite.

General Aviation Aircraft		
ATC Comms	VHF communications	108 - 137 MHz
ADF	Automatic Direction Finder	190 - 1750 kHz
DME	Distance Measurement Equipment	1025 - 1150 MHz
VOR	VHF Omni-Range	108 - 117.95 MHz
Transponder	Secondary surveillance transponder	1030 MHz, 1090 MHz
NDB	Non Directional Beacon	190 – 530 kHz, 1.6 - 1.8 MHz

ILS	Instrument Landing system	75 MHz, 329.3 – 335 MHz
ADS-B	Mode-S modified transponder	1090 MHz
GPS	Global Positioning System (option)	1575.42 MHz
Commercial Aviation Aircraft *(above plus)*		
HF Comms	High Frequency Comms	2.860 – 17.952 MHz
TCAS	Traffic Collision & Avoid. System	1030 MHz, 1090 MHz
EGNOS	European Nav. Overlay Service	1575.42 MHz
WAAS	Wide Area Augmentation System	1575.42 MHz
ACARS	Automated Reporting System	129.125 - 136.975 MHz
Military Aviation Aircraft *(above plus)*		
ATC Comms	UHF communications	225 – 400 MHz
TACAN	Tactical Air Navigation	962 - 1024, 1151 – 1213 MHz
Military GPS	Global Positioning System	1227.6 MHz

Table 2.9 – Aircraft RF equipment frequencies (excluding radars)

The above list (Table 2.9) describes the required communication and navigation systems capability for all aircraft and their corresponding frequency ranges; based on CAA, FAA and EASA requirements.

Airspace is typically divided into classes. With Class-A being controlled airspace, and Class-G being uncontrolled airspace. By convention, above 60,000ft (18.3 km) is considered uncontrolled airspace, however, recent moves to give CAA and FAA responsibility for this airspace and LEO, in response to the advent of commercial spaceflight, means that there will likely be changes to the classification and operational requirements within these regions.

The ITU recommendations [60] on communication channel design apply to the RF communication requirements of the equipments described in Table 2.9.

2.8 Satellite RF signal techniques

Communications with satellites requires consideration of a unique set of RF waveform problems. With issues such as communication link distance, lack of end-to-end line-of-sight, path effects, and atmospheric effects, there has been considerable research effort over the years to address these issues. The following sections describe and review the various commonly used techniques.

2.8.1 Satellite multiple access techniques

A key issue when first connecting to a system using a shared medium such as RF spectrum is to provide a means of initiating a connection without interfering with other transmitters that are attempting to achieve the same thing. The following sub-sections describe and review the common RF initial attachment protocols.

2.8.2 The ALOHA Protocol

The ALOHA protocol is very straightforward: nodes may transmit at any time, however, if a collision occurs, the node must apply a random back off time before re-transmitting (Figure 2.34).

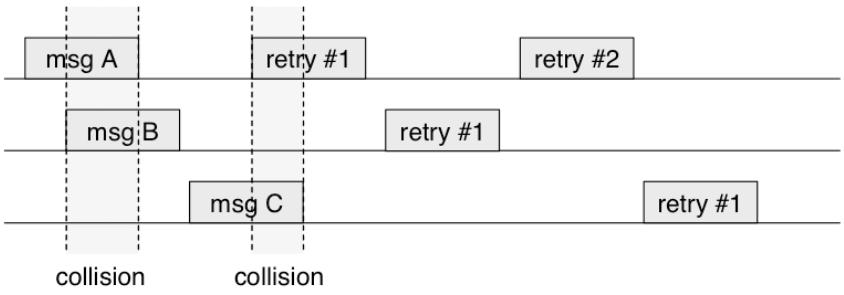

Figure 2.34 – Example ALOHA communication sequence with three nodes

To calculate the throughput of the ALOHA protocol we assume that the statistics are *Poisson* in nature, and that the back-off period following a collision is random. We consider that the messages take time *T* to send.

$$P[packet\ delivered\ correctly] = P[no\ other\ packets\ in\ period\ 2T] \quad (4)$$

Using a *Poisson* distribution where λ is the average number of packet transmissions in time *T* and *P(k)* is the probability that *k* packet transmissions occur in *T*, then,

$$P(k) = \lambda^k e^{\frac{-\lambda}{k!}} \qquad (5)$$

For each of *N* users transmitting with probability *p* in time period *T*, the average number of packets in *2T* is:

$$\lambda' = 2\,Np \qquad (6)$$

Then,

$$P[packet\ delivered\ correctly] = P(0) \qquad (7)$$

$$= \lambda'^0 e^{\frac{-\lambda'}{0!}} \qquad (8)$$

$$= e^{-2Np} \qquad (9)$$

Throughput is therefore,

$$Throughput = Np\, e^{-2Np} \qquad (10)$$

That is, *Np* attempts with probability e^{-2Np}

If we consider the optimum configuration for best throughput, which can be identified from the maximum, *d(Throughput)/d(Np)*, then throughput is highest when,

$$Np = \frac{1}{2} \qquad (11)$$

We can demonstrate this by substitution.

$$Throughput = \frac{1}{2} e^{-1} \qquad (12)$$

Which gives a maximum throughput of,

$$Maximum\ Throughput = \frac{1}{2e} \qquad (13)$$

$$= 18.4\% \qquad (14)$$

What this highlights is that in a pure random access satellite radio system there is a waste of 81.6% of the resource. This is not efficient, particularly if the system is to carry high data rates. However, random access as exemplified by the ALOHA

protocol is useful in cases where it is difficult to establish a distributed system-wide timing reference.

2.8.3 Timing beacons and the slotted ALOHA protocol

We can improve the throughput of such communication systems by introducing a common timing reference across the system. This can be achieved through the broadcasting of a timing 'beacon' signal that is used to mark out 'time-slots'.

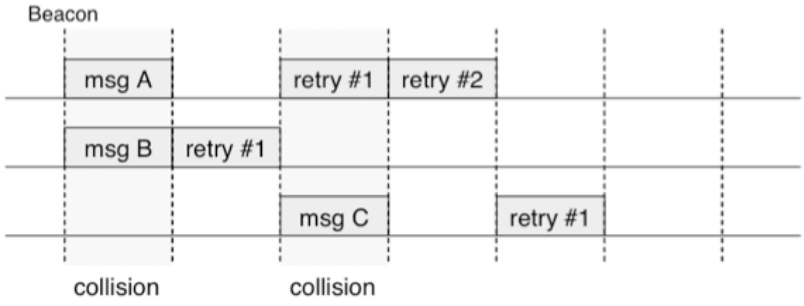

Figure 2.35 – Example Slotted-ALOHA communication sequence with three nodes

In the Slotted-ALOHA protocol, each node transmits at a slot boundary, then, as for the ALOHA protocol, if a collision occurs, apply a random back off and try again at another slot boundary (Figure 2.35).

To calculate the throughput of slotted-ALOHA we again assume a *Poisson* distribution queuing model and use a backlog approach. A backlogged packet is one that is ready to be transmitted but has been unable to be sent because a free slot has not yet been available. We also assume that if a new packet arrives it will attempt to transmit in the next slot; if there is a collision, it is only retransmitted after a random delay.

We assume the expected number of attempts per slot can be represented by a *Poisson* variable with a mean represented by η, where q_r represents the probability that a backlogged packet is re-transmitted in the next slot, and k is the number of backlogged packet:

$$\eta = \lambda + kq_r \qquad (15)$$

We assume the 'attempt-rate' of d packets per slot, and m attempts to find an available slot, which gives us,

$$P(m\ attempts) = \eta^m e^{\frac{-\eta}{m!}} \qquad (16)$$

We can then define the three states of a slot as,

$$P(idle) = P(no\ attempts\ in\ a\ slot) = e^{-\eta} \qquad (17)$$

$$P(success) = P(only\ one\ attempt\ in\ a\ slot) = \eta e^{-\eta} \qquad (18)$$

$$P(collision) = P(two\ or\ more\ attempts\ in\ a\ slot) = 1 - P(idle) - P(success) \qquad (19)$$

We define that maximum throughput occurs when the throughput equals the external arrival rate:

$$\frac{d}{d\eta(k)}\,\eta(k) = e^{-\eta} - \eta e^{-\eta} = 0 \qquad (20)$$

Which therefore shows as maximum when $\eta = 1$. Substituting into *P(success)* gives,

$$P(success) = \eta e^{-\eta} = \frac{1}{e} \qquad (21)$$

$$= 36.8\% \qquad (22)$$

Therefore, provided the incoming rate and outgoing rate remain stable, slotted ALOHA protocol achieves twice the throughput of the ALOHA protocol.

2.8.4 Advanced multiple access attach protocols

There are further advances that can be made in performance based on so-called 'splitting algorithms' and 'tree algorithms'. These tend to be specific to the problem being solved; they are not described further in this literature survey but can be used in satellite communication systems to enhance performance.

2.8.5 Time Division Multiple Access (TDMA) Protocol

It is also possible to simply allocate slots to individual users (Figure 2.36). This is Time Division Multiplexing (TDM). Time Division Multiplexing provides slots that

can be used by pre-assigned messages. Pre-assigning users or transmission nodes to each slot at a receiver creates Time Division Multiple Access (TDMA).

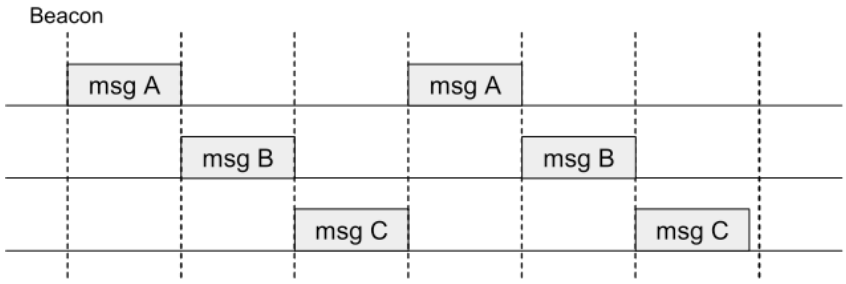

Figure 2.36 – Example of Time Division Multiplex (TDM) showing three nodes, or one node with three message streams

Though TDMA is deterministic, latency increases linearly with the number of users. This is not the case with ALOHA and related protocols, because they scale based on the packet rate and the collision rate. However, ALOHA and slotted ALOHA are unstable protocols and require supporting algorithms to prevent degradation of performance.

2.8.6 Demand Assigned Multiple Access (DAMA) protocol

TDMA can be inefficient if the users are not continuously transmitting, leaving the shared medium (or receiver) unused during these slots. A method of allocating TDMA slots on demand was developed for satellite communication in order to make better use of the shared media: in this case the RF spectrum handled by the satellite.

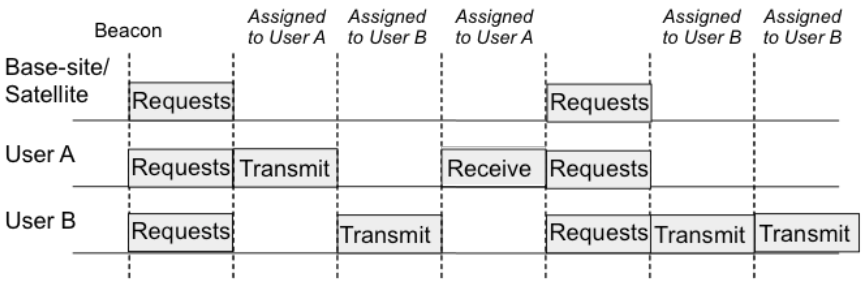

Figure 2.37 – Example of Demand Assigned Multiple Access (DAMA)

To implement DAMA, one of the slots is marked as a controller (the first slot in Figure 2.37). In this slot, sub-slots are typically created that allow nodes to demand access. The sub-slots where this occurs typically use some form of slotted ALOHA to register their requests.

A central algorithm at the receiver then decides which TDMA slots are to be allocated to which users/nodes, and transmits that mapping information to all users/nodes. This information may be sent in the remainder of the controller slot sub-slots.

2.8.7 Satellite MIMO

The requirement for increased data rate, particularly in the mobile communication market has been inexorable over the past decade. However, it is clear that there are few additional data-rate or performance gains that can be made by changing to new modulation schemes, and that no higher performance modulation scheme has been identified for many years. And of those implemented, their application specific and channel optimisations have taken them close to the Shannon limit of the channel. The alternatives are to use more bandwidth, or to provide more RF connectivity from transmit to receive. The latter approach is broadly termed MIMO (Multiple Input, Multiple Output). MIMO solutions have been explored for improved performance of satellite communication systems.

2.8.8 Types of MIMO

Multiple antenna techniques have become attractive, particularly with recent increases in processing power supporting the complex algorithms that are required. Multiple antenna techniques are classified using a taxonomy that begins with Single-Input (transmit) Single-Output (receive) (SISO) antenna systems and moves through SIMO and MISO to Multiple-Input Multiple-Output (MIMO). It is possible to compare MIMO techniques with diversity techniques, and here is demonstrated how an extension to the taxonomy can illustrate this (Table 2.10).

Spatial Diversity	MIMO *(Illustrated with three spatial layers)*
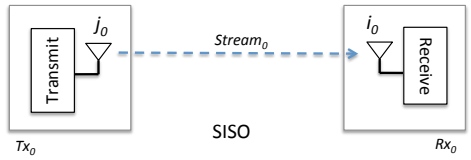	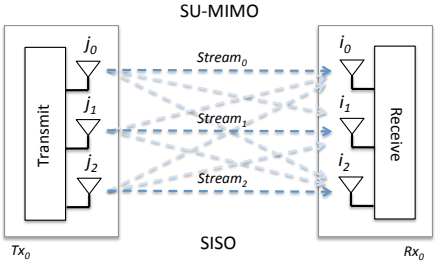
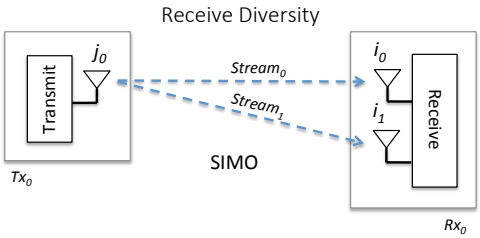	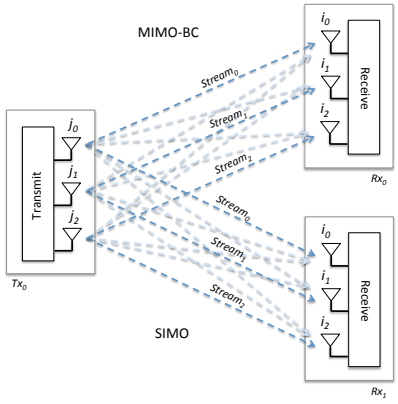
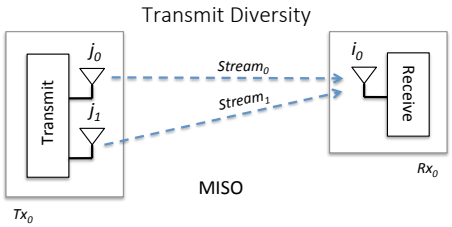	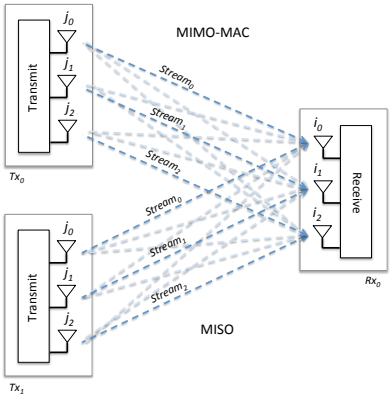
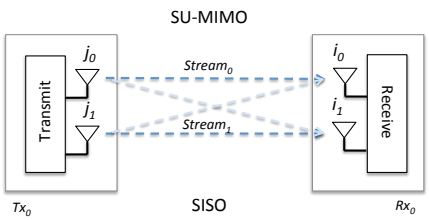	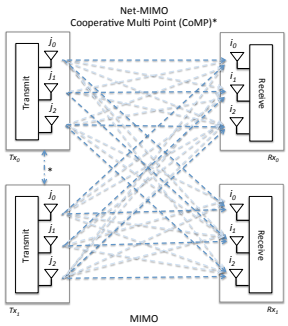

Table 2.10 (i. top left, then by column to viii. bottom right) – Illustration of the relationship between diversity and MIMO techniques

In MIMO systems, it is assumed that multi- and cross-path signals exist. It is the purpose of the algorithms to extract as much useful information from these signals and use them to pass additional data. This increases the overall capacity and throughput. There are a number of degrees of freedom in MIMO implementations. For example:

1. The channel can be coded:

   - At the transmitter (e.g. Tomlinson-Harashima pre-coding, Dirty Paper Coding);
   - At the receiver (e.g. matrix Decision Feedback Equalisation – DFE, or Minimum Mean Square Error – MMSE);
   - Or split between transmit and receive (e.g. Singular Value Decomposition – SVD).

2. The techniques used can be linear (e.g. linear pre-equalisation), or non-linear (e.g. matrix DFE).

3. The approach used can be open-loop, or closed-loop:

   - In 'open-loop' (sometimes referred to as direct-mapped) MIMO, information about the channel (H) is not available at the transmitter, resulting in an assumption of shared transmit power being applied to signals mapped to each transmit antenna.

   - In 'closed-loop' MIMO, channel information (H) is available to the transmitter, which allows the optimisation of the transmitted powers and signal phases to take advantage of knowledge of the signal paths across all possible channels.

4. Since multiple antennas can be fitted to individual nodes, there is also a differentiation for those MIMO implementations that connect multiple nodes with multiple antennas - these are described below:

- The case of a single node with multiple antennas connecting to another similar node is termed Single User MIMO (SU-MIMO).
- The case of multiple nodes with multiple antennas connecting with each other is termed Multi-User MIMO (MU-MIMO).
- Broadcast MIMO (MIMO-BC) refers to the case of a central transmission node with multiple antennas transmitting to multiple other nodes, all of which have multiple antennas. This is unidirectional transmission.
- Finally, in the case of bidirectional transmission with multiple nodes all having multiple antennas, there is Multiple-Access MIMO (MIMO-MAC).
- Lastly there is the case where multiple antennas act as though they are part of a single transmit or receive node, but are separated in space and only act cooperatively. This is termed Cooperative MIMO or Cooperative Multi-Point (CoMP). Systems with ad-hoc and multiple connections between such nodes are termed Net-MIMO.

2.8.9 Spatial diversity and Alamouti encoding

A well-studied and commonly used coded channel approach to provide diversity across multiple channels is Alamouti encoding. It is designed to provide tolerance to fading in a (2x2) antenna SU-MIMO system.

The (2x2) version of Alamouti encoding provides the only full-rate coding (i.e. 1 symbol out for 1 symbol in). There are diminishing returns for further increase in number of antennas, with a limit of (4x4) being considered the point where additional gains are minimal. This is because as the number of antennas and channels increase it becomes harder to maintain the orthogonality required between the signals in order to recover them at the receiver.

The process of Alamouti encoding the transmit signal provides a method of recovering the original transmitted stream at the receivers in the case where there is more than one pair of transmit and receive paths, and where exists multi-path and cross-path interference. Alamouti typically only allows the encoding of a single data stream across the MIMO channel.

Space Time Block Codes, such as Alamouti encoding, are one form of symbol coding for transmission across multiple channels. Since the invention of Alamouti encoding there have been attempts to improve the basic approach by introducing Space-Time Trellis Coding (STTC) and Space-Frequency Block Coding (SFBC): there are many variants. Alamouti encoding across two antennas at two frequencies, rather than across two antennas in time, is an example of SFBC.

2.8.10 Cyclic delay diversity

In addition to pre-coding the signals as illustrated by Alamouti encoding, modifying the phase allows for a degree of 'beam steering'. By adding a cyclic delay to the transmitted signals it is possible to cause the transmitted signal to propagate constructively in a given direction. This is termed cyclic delay diversity.

2.8.11 Closed-loop codebook feedback and pre-coded MIMO

As noted above there are other forms of pre-coding the signal that may or may not use channel state information (CSI) feedback from the receiver. One such feedback technique is Tomlinson-Harashima pre-coding, though a better solution might be Dirty Paper Coding; many approaches have been addressed.

In a closed loop system that measures the Channel State Information (CSI) at the receiver, it is possible to use this information to code for known interference at the transmitter: this is the concept of pre-coding. The bandwidth and latency that would be introduced by feeding back complex receiver measurements to the transmitter is overcome by using a codebook.

This method relies on the transmitters and receivers containing the same codebook: as such either the codebooks must be pre-placed on each node, or a central node must broadcast the codebook to all nodes. The codebook consists of an indexed table of the pre-coding values for each antenna port and for the number of spatial diversity layers supported (Table 2.11).

Codebook index	Number of layers	
	1	*2*
0	$\frac{1}{\sqrt{2}}\begin{bmatrix}1\\1\end{bmatrix}$	$\frac{1}{\sqrt{2}}\begin{bmatrix}1 & 0\\0 & 1\end{bmatrix}$
1	$\frac{1}{\sqrt{2}}\begin{bmatrix}1\\-1\end{bmatrix}$	$\frac{1}{2}\begin{bmatrix}1 & 1\\1 & -1\end{bmatrix}$
2	$\frac{1}{\sqrt{2}}\begin{bmatrix}1\\j\end{bmatrix}$	$\frac{1}{2}\begin{bmatrix}1 & 1\\j & -j\end{bmatrix}$
3	$\frac{1}{\sqrt{2}}\begin{bmatrix}1\\-j\end{bmatrix}$	—

Table 2.11 – An example of a MIMO pre-coder selection codebook (after *Wang, Wu and Zheng* [136])

2.8.12 Multi-User MIMO (MU-MIMO)

An extension to SU-MIMO is to apply coding to optimise transmission to multiple users simultaneously (MU-MIMO), as noted above. This can be achieved, for example, by decomposing the MU-MIMO channels to SU-MIMO channels. The following example illustrates a linear receiver approach in a three spatial layer pre-coded MU-MIMO configuration used as a downlink transmission system with a MISO topology to four receiver nodes (Figure 2.38).

To achieve cancellation of the interference caused by the signals from other nodes the technique is to pre-code the signals and reduce the interference by multiplying by a pre-coding matrix *M(k)*, where *M* is the number of transmit antennas, and *k* the number of receivers (Figure 2.39).

M(k) transforms symbol *b(k)* for the *kth* receiver before it is mixed with other symbols at the transmit antenna. When combined with the channel *H(k)* for the k^{th}

user, the received signal for receiver k becomes $r(k)$, with $n(k)$ additive white Gaussian noise (AWGN).

$$r(k) = H(k) \sum_{i=1\ to\ K} M(i)b(i) + n(k) \qquad (23)$$

Thus, the effective channel matrix can be represented as H_sM_s with each receiver suffering interference from signals intended for others receivers, represented by:

$$H(k) \sum_{i=1\ to\ K}^{i \neq k} M(i)b(i) \qquad (24)$$

Then, in order to cancel the interference of each stream, a pre-coding matrix $M(i)$ is defined such that:

$$H(k) \sum_{i=1\ to\ K}^{i \neq k} M(i)b(i) = 0 \qquad (25)$$

$M(i)$ consists of two components, the first represents the intersection of all the channel matrices that achieve diagonalisation of the effective channel matrix, and the second, a term to achieve the required characteristic of the communication in terms of quality of service or to compensate for the receiver, for example. See also codebook pre-coding, described above.

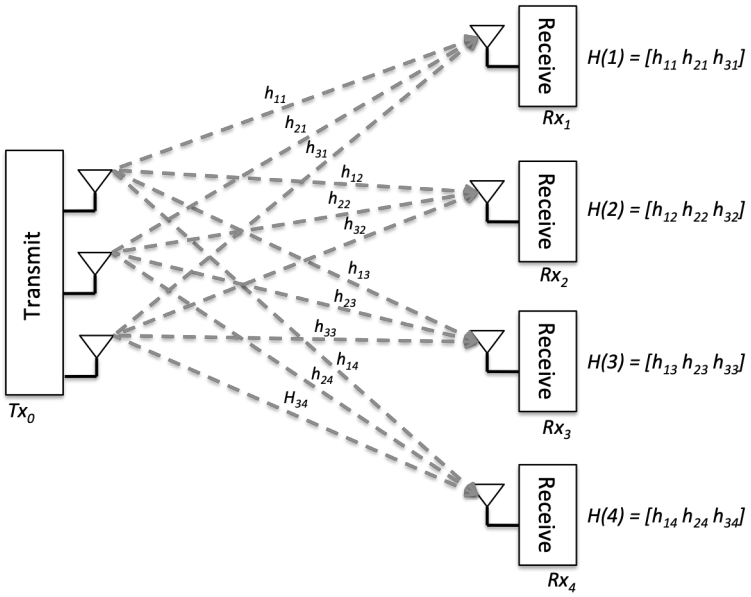

Figure 2.38 – Example MU-MIMO configuration for downlink communication with four receiver nodes (after *Kurve* [137])

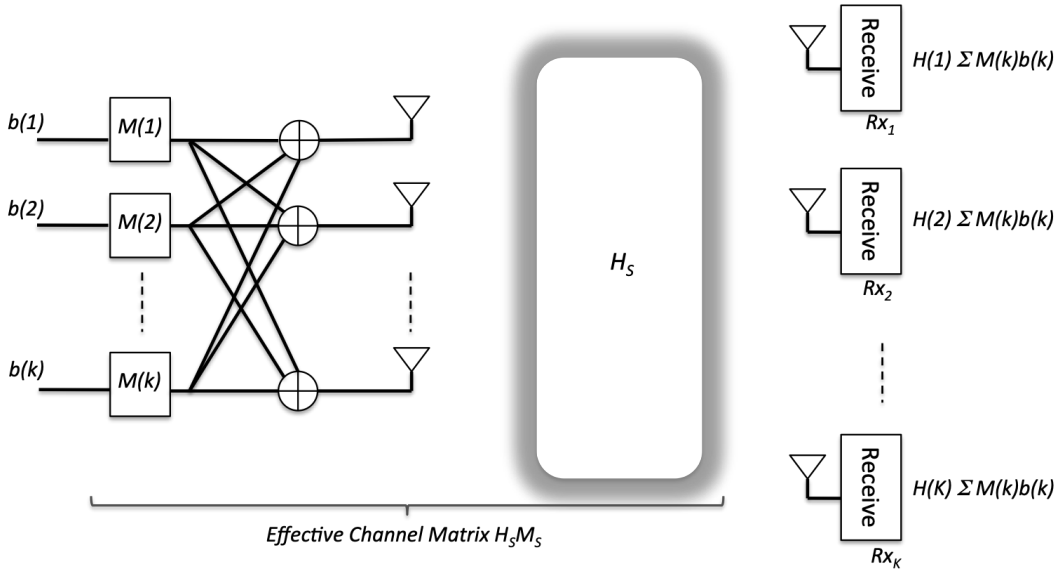

Figure 2.39 – Illustration of linear pre-coding of the signals to compensate for the MIMO channel (after *Kurve* [137])

The effect of the pre-coding matrix is to allow each receiver to consider the received signal as a single user channel MIMO (SU-MIMO) channel; a much more straightforward problem.

2.8.13 Multiple Access MIMO (MIMO-MAC)

On the uplink from multiple nodes to a central receiver, MIMO can be used though there is of course only a shared channel for each transmitting node, regardless of the number of layers being transmitted by each. Therefore, a Media Access Control (MAC) protocol must be established to ensure that each transmit node does not interfere with others.

Since individual transmit nodes are still transmitting multiple layers, it is still considered MIMO. A number of MAC protocols can be applied, including slotted-ALOHA and variants, TDMA and DAMA. The overall approach is termed MIMO-MAC.

2.8.14 Discussion of the application of MIMO to satellite communication

Based on a thorough literature search, there appear to be only a few papers on the topic of using satellites for multi-channel communication. *Arapoglou et.al* [110] discusses the use of two satellites for 2x2 MIMO to a ground terminal, but there are no papers that could be found that consider utilising the accurate timing of satellites, such as that demonstrated by GNSS, to allow their combined use as a cooperative sparse antenna system. Consequently there is no published literature on the capability of using beam-forming or MIMO techniques using accurately timed satellites. However, there are many papers describing these techniques for ground-based systems, such as mobile phone systems and sensor networks. This is useful as they act to de-risk many of the techniques and technologies that could be read across to a sparse antenna approach using co-timed satellites.

The published literature is similarly quiet on the topic of creating layered correlation regions through the use of time synchronised sparse antenna arrays. There is published work on digital beam-forming, and coded signals for radar, but none on the concept of spatially formed, or layered data communication using correlation or similar techniques.

2.8.15 Discussion of the Arapoglou satellite MIMO review paper

The thorough review paper by *Arapoglou et.al* [138] includes a reference to the use of dual satellites for MIMO connectivity in line-of-sight (LOS) with land mobile systems, as analysed by *Schwarz* et.al. [139]. Variations of this two satellite MIMO model have been explored by C.-I Oh, et.al. [140] that include Rayleigh flat fading and rain fading, rather than, as Arapoglou et.al point out, the AWGN satellite channel typically used in research models. In discussion of multiple satellite MIMO, *Arapoglou* et.al. make clear that the downlink channel from the satellites can be modelled as a broadcast MU-MIMO system and list the benefits as:

- *"more immune to LOS [loss of signal] or antenna correlation"*
- *"allow for spatial multiplexing gain without necessitating [fixed satellite terminals] with multiple antennas"*

- *"This is especially significant from a commercial point of view, since no modification is necessary to conventional [fixed satellite terminal] receivers."*

The issue of multiple satellites is addressed in terms of the physical implementation constraints and the need for synchronised satellites.

"The space restrictions inherent when using a single satellite turned research to the investigation of dual satellite configurations as a means of profiting by MIMO technology in [single user] [fixed satellite] communications. Similarly to [site diversity], [orbital diversity], i.e. the reception by a single earth station equipped with two directional antennas of the same information-bearing signal from two geostationary satellites at a certain angular separation, has been known for long as an [fading mitigation technique] against rain fading. Its main drawbacks are the waste of the limited satellite bandwidth for the transmission of the same signal and the need for synchronization of transmission from the two satellites."

The potential improvement in performance provided by MIMO is shown by *Perez-Neira* et.al. [141] in the following chart (Figure 2.40). In all cases it can be demonstrated that dual satellite MIMO, particularly with polarization diversity, provides increased performance over single satellite, single channel communication.

Interestingly, *Perez-Neira* also demonstrated that received samples may be simply expressed as:

$$\underline{y} = \left[\underline{\underline{H}}_{sat1} \quad \underline{\underline{H}}_{sat2} \right] \underline{s} + \underline{n} \tag{26}$$

Which can be conveniently developed into a combination of the Log Normal channel and a Rayleigh fading channel for satellite *i* transmitting to mobile receiver *j*. This is a useful decomposition for extending results from free space path loss to multi-path.

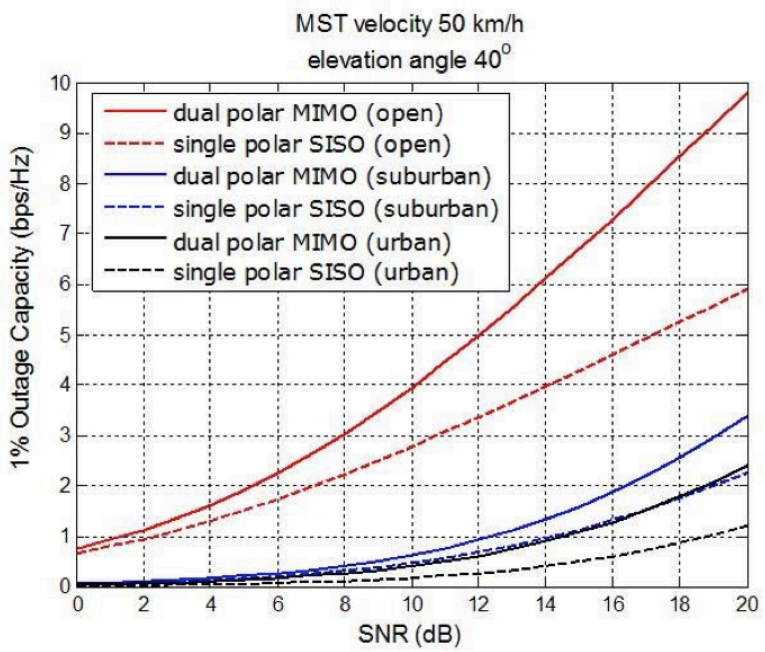

Figure 2.40 – 1% outage capacity performance of a dual satellite to mobile satellite terminal communication system (after *Perez-Neira* [141])

$$\underline{\underline{\boldsymbol{H}}}_{sati} = \begin{bmatrix} h_{11}^{i} & h_{12}^{i} \\ h_{21}^{i} & h_{22}^{i} \end{bmatrix} = \begin{bmatrix} \bar{h}_{11}^{i} & \bar{h}_{12}^{i} \\ \bar{h}_{21}^{i} & \bar{h}_{22}^{i} \end{bmatrix} + \begin{bmatrix} \tilde{h}_{11}^{i} & \tilde{h}_{12}^{i} \\ \tilde{h}_{21}^{i} & \tilde{h}_{22}^{i} \end{bmatrix} \tag{27}$$

$$\underline{\underline{\boldsymbol{H}}}_{sati} = \underline{\underline{\bar{\boldsymbol{H}}}}_{sati} + \underline{\underline{\tilde{\boldsymbol{H}}}}_{sati} \tag{28}$$

Based on this work it is possible for a synchronized satellite system using GNSS Stratum-1 referenced timing to provide the synchronization necessary at low cost to allow two or more satellites to operate as a broadcast MU-MIMO (BC-MIMO) system and that this could then be developed to extend the Coordinated Multi-Point (CoMP) MIMO architecture to multi-satellite operation.

This is a novel application of CoMP MIMO identified in this thesis and its use is expanded in later Sections.

The main issue with MIMO, as described in the *Arapoglou* paper, is that there is only multi-path at ground level, and that the bulk of the gains are diversity related.

2.8.16 Discussion of the Warty satellite MIMO paper

The paper by *Warty* [142] on cooperative satellite communication takes a different approach to many of the others that are published in that it discusses the set of MIMO relay techniques as a means of cooperatively distributing and transmitting data to an end point. This method potentially avoids the need for global time synchronisation and provides a method for coordinating transmission from multiple satellites. There are however, timing and sequencing constraints that impact performance.

2.8.17 Discussion of the European Space Agency MIMOSA programme

The European Space Agency (ESA) has developed a programme of research to address the topic of the "*characterisation of the MIMO channel for mobile satellite systems*". The objective of the project is stated as: "*to study the characteristics of fading from satellite systems taking into account MIMO technology with the goal to design and implement a software model of the satellite MIMO channel."*

The results are published by *Eberlein et.al.* [143] and *Moraitis et.al* [144], the latter of which developed a capacity evaluation method based on a propagation model for SIMO which could be of interest in the development of an extended model for MIMO.

2.9 Literature survey summary

In this wide ranging literature survey the following conclusions can be summarised.

Atmosphere: Atmospheric effects have a significant impact on RF propagation and need to be modelled for any communication channel that operates in the high altitude low orbit region of the Earth.

Standards: Existing satellite systems, generally, follow published standards for protocols, from ECSS and CCSDS standards for TM/TC control signals, to ETSI GMR standards for voice and data services, VSAT and satellite broadband standards

for Internet connectivity services to ground or aircraft, to satellite television standards. Very nearly all current communication satellites follow one or more of these standards.

There is a very comprehensive standard RF model of the atmosphere that can be used to maintain consistency in designing and testing RF systems operating in the high altitude low orbit region. However, there is currently no identified standard for laser optical communications in the space environment.

Communications satellites: For good ground coverage and for service resilience, all communications systems, at whatever orbital altitude, are effectively constellations. The only metric that is variable is in the tightness of the coupling of the individual space segment satellites to each other and to the ground segment. LEO satellite constellations benefit from close coupling via inter-satellite links, and this appears to be a trend followed by all new constellation proposals currently being developed. As a result, the majority of, in particular LEO, satellite constellations use a Walker orbital topology.

Waveforms: As highlighted in the literature survey, the majority of communication systems use low order modulation schemes; PSK, BPSK, GMSK, QPSK, combined with, in some cases, DSSS CDMA with various chip rates, with OFDM being not particularly common beyond broadcast services.

Data rates: User data rates, though trending towards higher data rates, are currently less than 1 Gbps.

Spectrum: Spectrum usage is a constraint leading to use of higher frequencies and wider bandwidths in the Ka-band, and with a trend towards Q/V and W-band in future.

Size, Weight and Power: Satellite generated power, typically from solar, is still a limiting factor, trending towards 5kW for LEO/MEO satellites, and to over 20kW for GEO satellites. Spacecraft volume and mass in terms of launcher fairing size and mass capability are also a limiting factor, which though trending to larger volume

and mass is also limited by the Assembly, Integration and Test (AIT) facilities, in which the satellites are built and tested. It seems unlikely, currently, that launchers and AIT facilities will provide support for satellites exceeding 6-7m height and 6-7 tonnes mass for the near future.

Applications: What is apparent is that each satellite constellation has specific data rate, antenna type, and particular standards for each targeted market, with a trend towards satellite cost and performance optimised for niche service requirements and not as one might expect targeting and optimising towards generic satellites.

High altitude aircraft comms: In the literature it is clear that high altitude aircraft are subject to the same 'rules of the air' as other atmospheric craft, and as such operate with very similar equipments; particularly if those aircraft must traverse commercial or controlled airspace to reach operating altitude. And although there are cases where use of restricted (that is military) airspace, or uncontrolled airspace (Class-G for example), can be used to reach altitude, there are still requirements in terms of radar visibility and communication that must be adhered to in order to meet safety requirements for those other airspace users. The summary, therefore, is that high altitude communications systems not only need to consider payload communications, such as satellite to aircraft or vice cersa, but also the performance envelope of the the more mundane communications (and navigation) services that must be supported.

MIMO: Initially considered to be a major next step in increasing performance of satellite communication, particularly for space-ground links, a review of the literature suggests that MIMO is only beneficial for the case where the ground terminal is subject to close-in multi-path, or when multiple satellites are used to increase signal to a single receiving terminal. Though in this latter case it is pointed out in the literature that the channel is closer to supporting a diversity or beam-formed-like transmission capability rather than a multi-channel MIMO capability. The only exception to this might be in the context of capabilities provided by MIMO-CoMP, which introduces the concept of time synchronised satellite transmissions, though again, this is very close to low-order beam-forming.

Multi-user access: As anticipated, the literature survey confirmed the poor performance of multi-access techniques, and strongly points to the need for implementation of less statistical and more prescriptive multi-user spectrum allocation. However, as the literature also points out, improvements require the imposition of an 'outside actor' typically in the form of an overall imposed timing reference, and even then, with current multiuser access algorithms, it is difficult to exceed 50% efficiency. There is clearly a problem here that could perhaps be better considered in the wider system context for satellite systems, and making use of 'outside actors' such as GNSS. Currently, however, these approaches and potential improvements do not appear to have been addressed in the literature.

Availability: The initial consideration of comparing ground communications (for example, backbone fibre-optic communication) availability and space segment availability was considered to be an issue since, based on the literature, the ground communication networks met 6-nines availability level (that is, only 32 seconds of downtime per year), whereas the space segment is designed to only meet 3-nines availability (that is, 9 hours of downtime per year). When put in that way, the difference seems tolerable, however, as data rates in the space segment are tending to increase, the data loss that is incurred across a year as a result of availability issues can be substantial.

For example, based on the literature, current highest data rates in the space segment are of the order of 1.8Gbps per link (with higher bisection bandwidths for the satellite switch core itself shown to be trending towards Tbps capacity). Then, over a year, the space segment will lose around 58Tbits of the transmitted data, purely as a result of availability, whereas the fibre-optic ground communications would only lose 57Gbits for the same data rate.

Based on the literature, though ground communications can be designed to the level of 6-nines availability, the main factor for the space segment, in particular the Earth-space communications link, is that availability is primarily atmospheric weather dependent. For RF systems, particularly in the Ku-band, rain is a particular issue, but more insidious, based on the literature, is the availability impact of clouds on laser optical communications for Earth-space links.

Spectrum: Based on the literature, it is clear that spectrum usage, and in particular the need for reducing interference between satellite systems, and between satellite systems and ground systems, as well as reducing interference to communications services used by aircraft, is a key issue for both operators and legislators. The consequence of caution and pragmatism results in limited spectrum being available for satellite communications systems, particularly in the lower frequency bands, which compete heavily with ground based user services.

There is a trend in the literature that is looking at new and novel methods to spectrum share, and in general, manage the spectrum more effectively to increase the number of users, particularly if in geographically separate regions. However, and currently, the published techniques to achieve this are cellular, but only at the Earth surface level.

UHF band allocations, for example, are typically globally unique, as are most mobile phone bands (typically L-band), and WiFi (S- and C-bands). From the literature it is clear that all satellite spectrum allocations are unique, and this results in the need for highly compressed bandwidths per satellite, and complex spectrum re-use techniques using beam forming or multiple antennas, hence forcing an upper limit on potential data rates, and resulting in a limit to the number of satellites that could use the available spectrum.

As the literature review highights, more efficient spectrum sharing techniques are required. One approach is to geographically divide the coverage area into smaller coverage areas with rfrequency re-use (addressed with increased numbers of ‘beams’), and to manage handover as a user transitions between these small coverage areas. An alternative is to manage the interference between the coverage areas using bespoke antenna designs (O3b and OneWeb antennas, for example). OneWeb has the additional issue of needing to not interfere with GEO satellites operating on the same frequency.

Technique	Approach	Example
Small Coverage Areas with Frequency Re-use	Use of multiple antennas (O3b)	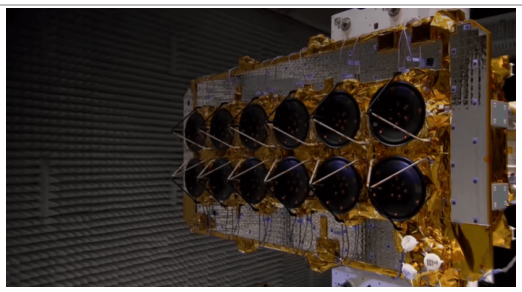 O3b (Image credit: O3b, Thales Alenia Space) O3b's satellite system architecture originally utilised hubbed ground stations from which signals were distributed. The multi-antenna approach is typical of high data rate ground hub satellite architectures where interconnect between hubs is provided in space.
	Use of beam forming antennas (Iridium, IridiumNext, OneWeb, O3b-NG)	 Iridium (Image credit: Iridium, Motorola) 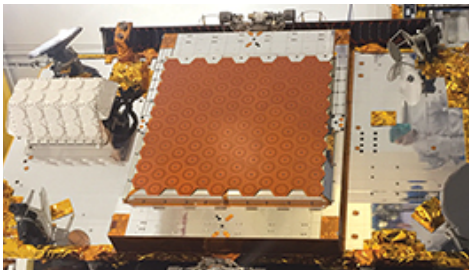 IridiumNext (Image credit: Iridium, Thales Alenia Space, OrbitalATK)

		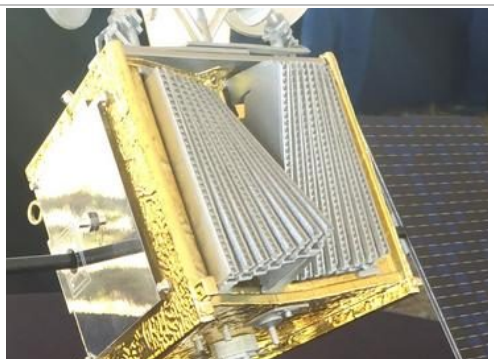 OneWeb (Image credit: OneWeb, Airbus)  O3b mPower (Image credit: O3b, Boeing) Improvement in the number of beams has been dramatic since the 1980s: Iridium satellites provided 48 small coverage areas per satellite with frequency re-use, whereas the latest O3b satellites are aiming to provide, based on early press releases, 30,000 shapeable and steerable beams.
Feeder Links	Use of links to ground, and links to GEO satellites	All satellites require additional antennas for their 'feeder links' to ground hubs, or up to GEO repeater satellits. For example those on OneWeb and Iridium:  OneWeb (Image credit: OneWeb, Airbus)

Handover management	Use of inter-satellite links	 IridiumNext (Image credit: Iridium, Thales Alenia Space, OrbitalATK) Satellite-to-satellite cross links are used to connect user traffic between satellites back to ground hub feeder locations, and are also used to pass coordination and handover information between satellites.
Interference management	Use of multiple frequencies	All satellite systems with multiple beams provide interference management by using spectrum frequency re-use patterns across the beams; in direct analogy to frequency re-use techniques used in mobile phone communications system.
	Satellite system coordination	Coordination to prevent interference at the satellite footprint edge can be provided by design, or by coordination using inter-satellite links.
	By agreement	Interference between satellites using similar frequencies at different orbits is typically resolved by geographical separation, or by using an agreed transmission level (that is, an agreed energy level) to reduce the impact on the ground or satellite.

Table 2.12 – Summary of frequency re-use and capacity improvement techniques

From the literature review in it can be seen that the above technology has been applied to solve the spectrum re-use, improve efficiency and provide capacity increase (Table 2.12). There are, however, opportunities to apply new technologies to improve spectrum re-use, efficiency and capacity: these are explored in this thesis.

References

[1] de Selding, P., "Test Data Indicate Possible Ka-band Weakness for UAV Links", SpaceNews, April 11, 2011

[2] "Aireon Space Based ADS-B performances model", Integrated Communication, Navigation and Surveillance Conference, April 2015, pp.1-28, 2015

[3] "SwiftBroadband-Safety: The Future of Aircraft Communications", White Paper, Inmarsat, 30 September 2016

[4] "Global Demand for In-Flight Broadband Hits new heights Amongst Airline Passengers", IFExpress article, airfax.com, May 24, 2016

[5] Virgin Orbit, "Launcher One service guide", Aug 2017

[6] Rocket Lab, "Electron: payload user's guide", Dec 2016

[7] "The potential role of small satellites, cubesats, constellations, and hosted payloads in designing the future Earth observing system architecture", Committee on Earth Science and Applications from Space (CESAS), Sept 17-19, 2014

[8] Clausen, I., Miller, E., A., "Intelligence revolution 1960", Center for the Study of National Reconnaissance, April 2012

[9] Hall, R. C., "SAMOS to the Moon: the clandestine transfer of reconnaissance technology between government agencies", Center for the study of National reconnaissance, October 2001

[10] Woods, R. O., "A cable to shrink the Earth", Mechanical Engineering, 2011, Vol.133 (1), p.40-45

[11] Glover, B. “History of the Atlantic Cable & Undersea Communications from the first submarine cable of 1850 to the worldwide fiber optic network: Atlantic Cables: 1856-2012”, on-line published data: atlantic-cable.com

[12] “United Nations Register of Space Objects”, A/AC.105/INF.1-419,421 and ST/SG/SER.E/1-629, Thirteenth edition, December 2011, and online updates to 2016

[13] “EDRS: European Data Relay System: The space data highway - Factsheet”, European Space Agency, 11 January, 2016

[14] “High growth continues for submarine fiber-optic systems in Asia”, Lightwave, 1998, Vol.15 (7), p.126-126

[15] Davis, C. C., “Fiber optic technology and its role in the information revolution”, http://www.ece.umd.edu/~davis/optfib.html

[16] Cornwell, D., “Space-based laser communications break threshold”, Optics & Photonics News, May 2016

[17] Bhatia, M., Davidson, J., et.al., “VoIP: An In-Depth Analysis”, Voice over IP Fundamentals, 2nd Edition, Cisco, October 2006

[18] Hastings, D. E., Putbrese, B. L., la Tour, P. A., “When will on-orbit servicing be part of the space enterprise?”, Acta Astronautica, Volume 127, October–November 2016, Pages 655–666

[19] Karafolas, N., Armengo, J. M. P., Mckenzie, I., “Introducing photonics in spacecraft engineering: ESA’s strategic approach”, IEEE Aerospace conference, 2009

[20] Pelton, J. N., et. al. editors, “Handbook of satellite applications”, Volume 1, Springer, 2013, ISBN 978-1-4419-7670-3

[21] “Mazar, H., “An analysis of regulatory frameworks for wireless communications, societal concerns and risk: the case of radio frequency (RF) allocation and licensing”, PhD Thesis, Middlesex University, August 2008

[22] Collis, C., “The geostationary orbit: a critical legal geography of space’s most valuable real estate”, The Sociological Review, 2009, Vol.57(1_supplement), pp.47-65

[23] “LEO satellite constellations: The microsatellite constellation in the New Space era”, Asia-Pacific Satellite Communications Council Newsletter, 2017

[24] Carpenter, M., et.al., “The stock market and innovative in the New Economy: the optical networking industry”, Industrial and Coroporate Change, Volume 12, Number 5, pp. 963-1034

[25] Flores-Abad, A., Ma, O., et.al., “A review of space robotics technologies for on-orbit servicing”, Progress in Aerospace Sciences, Volume 68, July 2014, Pages 1-26

[26] King, M. D., et.al., “Spatial and Temporal Distribution of Clouds Observed by MODIS Onboard the Terra and Aqua Satellites”, IEEE Transactions on geoscience and remote sensing, Vol 51, No 7, July 2013

[27] Richard, M., et. al., “Optical up-conversion enables capture of millimetre-wave video with an IR camera”, 13 August 2012, SPIE Newsroom. DOI: 10.1117/2.1201208.004406

[28] “Ionospheric propagation data and prediction methods required for the design of satellite services and systems”, ITU-R P.531 (01/2012)

[29] Kraus, J. D., “Radio astronomy”, 1986

[30] Emerson, D., “Attenuation at VHF in propagation through the Ionosphere”, online article, June 1998: https://www.cv.nrao.edu/~demerson/ionosphere/atten/atten.htm

[31] Tinsley, B.A., "Influence of solar wind on the global electric circuit, and inferred effects on cloud microphysics, temperature, and dynamics in the troposphere", Space Science Review 00:1-28, 2000

[32] Gadsden, M. "Noctilucent Clouds", Journal of the British Astronomical Association, 99, No. 5, pp. 210-214, 1989

[33] Harris, R., “Satellite remote sensing: an introduction”, Taylor and Francis, 1987

[34] Smith, D. J., Griffin, D. W., “Stratospheric microbiology at 20km over the Pacific Ocean”, Aerobiologica, 26, pp. 35-46, 2010

[35] Aguado, E., Burt, J. E. "Understanding Weather and Climate", 3rd Edition

[36] Wait, J., “The relation between VLF propagation and D-layer characteristics”, IEEE Transactions on Antennas and Propagation, Vol 12, Iss 2, pp. 239-240, 1964

[37] Damazio, D.O.; Takai, H., “A radio detector system for ultra high energy cosmic showers”, IEEE Nuclear Science Symposium Conference Record, Vol 1, pp. 134-138, 2003

[38] Pavlov, A. V., “Ion Chemistry of the Ionosphere at E- and F-Region Altitudes: A Review”, Survey Geophys, Vol 33, pp.1133–1172, 2012

[39] Max, C.; Avicola, K.; Bissinger, B., et.al., “Description Of An Adaptive Optics System Using A Sodium-layer Laser Guide Star”, IEEE Lasers and Electro-Optics Society, LEOS '92, Conference Proceedings, pp. 614-615, 1992

[40] Pancheva, D., Mukhtarov, P., “Global Response of the Ionosphere to Atmospheric Tides Forced from Below: Recent Progress Based on Satellite Measurements: Global Tidal Response of the Ionosphere”, Space Science Review Vol 168, pp. 175–209, 2012

[41] Luque, A., Ebert, U., “Sprites in varying air density: Charge conservation, glowing negative trails and changing velocity”, Geophysical Research Letters, Vol. 37, 2010

[42] Wescott, E. M, Sentman, D. D, et.al.’ “Blue Jets: their relationship to lightning and very large hail fall and their physical mechanisms for their production” Journal of Atmospheric and Solar Terrestrial Physics Vol 60, pp 713-724, 1998

[43] Rius, A.; Ruffini, G.; Romeo, A., “Analysis of ionospheric electron density distribution from GPS/MET occultations”, IEEE Transactions on Geoscience and Remote Sensing, Vol 36, Iss 2, pp 383-394, 1998

[44] Larin, I. K., “The Effect of Galactic Cosmic Rays on the Chemical Composition of the Atmosphere, Greenhouse Effect and Ozone Layer of the Earth”, Russian Journal of General Chemistry, Vol. 81, No. 13, pp. 2634–2640, 2011

[45] Lefohn, A. S., Wernli, H., “The importance of stratospheric-tropospheric transport in affecting surface ozone concentrations in the western and northern tier of the United States”, Atmospheric Environment Vol. 45, 2011

[46] “Altitude above the earth's surface with or without manoeuvres of the aerospace craft: 112.01 km”, Brian Binnie, SpaceShipOne, 10 April 2004, FAI Record file number #9881

[47] Yamagami, T., “Research balloons to float over 50km altitude”, JAXA Special Feature Report, 2011

[48] Greer, D., Harmony, P., Krake, K., Drela, M., “Design and predictions for a high-altitude (low Reynolds number) aerodynamic flight experiment”, NASA report NASA/TM-1999-206579, 1999

[49] Fleming, W. A., Kaufman, H. R., et.al., “Turbojet performance and operation at high altitudes with Hydrogen and JP-4 fuels”, NACA Research Memorandum E56E14, 1956

[50] Cojuangco, A. L. C., “Orbital lifetime analysis of pico- and nano-satellites”, Masters Thesis, University of Florida, 2007

[51] Owens, J.K.; Vaughan, W.W.; Niehuss, K.O.; Minow, J., “Space weather, Earth's neutral upper atmosphere (thermosphere), and spacecraft orbital lifetime/dynamics”, IEEE Transactions on Plasma Science, Vol 28, Iss 6, pp 1920-1930, 2000

[52] Ginet, G.P.; Dichter, B.K.; Brautigam, D.H.; Madden, D., "Proton Flux Anisotropy in Low Earth Orbit", IEEE Transactions on Nuclear Science, Vol 54, Iss 6, pp.1975-1980, 2007

[53] Curtis, H. J., "Limitations on space flight due to cosmic radiations", Science Vol.133, pp.312-6, 1961

[54] "Overview of Space Communications Protocols: Information Report", CCSDS 130.0-G-3, Green Book, July 2014

[55] "Radio Frequency and Modulation Systems – Part 1: Earth Stations and Spacecraft – Recommended Standard", CCSDS 401.0-B, Blue Book, February 2015

[56] "GEO-Mobile Radio Interface Specifications (Release 1); Part 5: Radio interface physical layer specifications; Sub-part 5: Radio Transmission and Reception; GMR-1 05.005", ETSI TS 101 376-5-5 V1.3.1

[57] "GEO-Mobile Radio Interface Specifications; Part 1: General specifications GMR-2 01.004", ETSI TS 101 377-1-1 V1.1.1

[58] "GEO-Mobile Radio Interface Specifications; Part 1: General specifications; Sub-part 3: General System Description; GMR-1 01.202", ETSI TS 101 376-1-3 V1.1.1

[59] "GEO-Mobile Radio Interface Specifications (Release 3); Third Generation Satellite Packet Radio Service; Part 5: Radio interface physical layer specifications; Sub-part 2: Multiplexing and Multiple Access; Stage 2 Service Description; GMR-1 3G 45.002", ETSI TS 101 376-5-2 V3.3.1

[60] "Prediction of path attenuation on links between an airborne platform and Space and between an airborne platform and the surface of the Earth", Recommendation ITU-R P.2041

[61] "Propagation data and prediction methods required for the design of Earth-space telecommunication systems", Recommendation ITU-R P.618

[62] "Rain height model for prediction methods", Recommendation ITU-R P.839

[63] “The radio refractive index: its formula and refractivity data”, Recommendation ITU-R P.453

[64] “Ionospheric propagation data and prediction methods required for the design of satellite services and systems”, Recommendation ITU-R P.531

[65] “Attenuation by atmospheric gases”, Recommendation ITU-R P.676

[66] “Water vapour: surface density and total columnar content”, Recommendation ITU-R P.836

[67] “Topography for Earth-to-space propagation modelling”, Recommendation ITU-R P.1511

[68] “Characteristics of precipitation for propagation modelling”, Recommendation ITU-R P.837

[69] “Specific attenuation model for rain for use in prediction methods”, Recommendation ITU-R P.838

[70] “Water vapour: surface density and total columnar content”, Recommendation ITU-R P.836

[71] “Reference Standard Atmospheres”, Recommendation ITU-R P.835

[72] “ESARAIN_PR6_v5”, “ESARAIN_MT_v5”, “ESARAIN_BETA_v5”, ITU-R Recommendation datasets available on-line

[73] “Water vapour: surface density and total columnar content”, Recommendation ITU-R P.836

[74] “Reference Standard Atmospheres”, Recommendation ITU-R P.835

[75] “ESARAIN_PR6_v5”, “ESARAIN_MT_v5”, “ESARAIN_BETA_v5”, ITU-R Recommendation datasets available on-line

[76] “ITU-R reference ionospheric characteristics”, Recommendation ITU-R P.1239

[77] “Guide to the application of the propagation methods of Radio communication Study Group 3”, Recommendation ITU-R P.1144

[78] “Choice of Indices for Long-Term Ionospheric Predictions”, Recommendation ITU-R P.371-8

[79] “Propagation curves for aeronautical mobile and radio navigation services using the VHF, UHF and SHF bands”, Recommendation ITU-R P.528

[80] “Attenuation due to clouds and fog”, Recommendation ITU-R P.840

[81] “Prediction method of fade dynamics on Earth-space paths”, Recommendation ITU-R P.1623

[82] “Propagation data required for the evaluation of interference between stations in space and those on the surface of the Earth”, Recommendation ITU-R P.619

[83] “Calculation of free-space attenuation”, Recommendation ITU-R P.525

[84] “Propagation data required for the design of Earth-space aeronautical mobile telecommunication systems”, Recommendation ITU-R P.682

[85] “Propagation data required for the design of Earth-space land mobile telecommunication systems”, Recommendation ITU-R P.681

[86] “Propagation data required for the design of Earth-space maritime mobile telecommunication systems”, Recommendation ITU-R P.680

[87] “Propagation data required for the design of broadcasting-satellite systems”, Recommendation ITU-R P.679

[88] “Definitions of Terms Relating to Propagation in Non-Ionised Media”, Recommendation ITU-R P.310-9

[89] “The Concept of Transmission Loss for Radio Links”, Recommendation ITU-R P.341.5

[90] “Characterisation of the variability of propagation phenomena and estimation of the risk associated with propagation margin”, Recommendation ITU-R P.678

[91] “Propagation by diffraction”, Recommendation ITU-R P.526

[92] “Digital Video Broadcasting (DVB); Second generation framing structure, channel coding and modulation systems for Broadcasting, Interactive Services, News Gathering and other broadband satellite applications; Part 2: DVB-S2 Extensions (DVB-S2X)”, ETSI EN 302 307-2 V1.1.1

[93] “IP Over Satellite (IPoS) - The Standard for Broadband Over Satellite”, Hughes Network Systems, January 2004

[94] “Understanding Satellite Broadband: Quality of Experience – Final Report”, Ofcom Report No: 72/11/R/193/R July 2011 - Issue 1

[95] Henry, C., “ViaSat Embarks on Global Triple Satellite Network”, ViaSatellite online magazine, December 2015

[96] “DVB Fact Sheet: DVB-S2X - S2 Extensions - Second Generation Satellite Extensions”, May 2014

[97] “Space engineering: Space data links - Telemetry synchronisation and channel coding”, ECSS-E-ST-50-01C, 31 July 2008

[98] “Space engineering: Ranging and Doppler tracking”, ECSS-E-ST-50-02C, 31 July 2008

[99] “Space engineering: Space data links - Telemetry transfer frame protocol”, ECSS-E-ST-50-03C, 31 July 2008

[100] “Space engineering: Space data links - Telecommand protocols synchronisation and channel coding”, ECSS-E-ST-50-04C, 31 July 2008

[101] “Space engineering Radio frequency and modulation”, ECSS-E-ST-50-05C Rev. 1, 6 March 2009

[102] “Space engineering Communications”, ECSS-E-ST-50C, 31 July 2008

[103] Sturza, M. A., Ghazvinian, F., “Teledesic satellite system overview”, Proc. Ka Band Utilisation Conf., Rome, Italy, Oct. 1995

[104] “The Teledesic Network: Using Low-Earth-Orbit Satellites to Provide Broadband, Wireless, Real- Time Internet Access Worldwide”, Daniel Kohn, Teledesic Corporation, USA

[105] Pratt, S. R., et. al., “An operational and performance overview of the Iridium Low Earth Orbit satellite system”, IEEE Communications Surveys, Second Quarter 1999

[106] “ICAO Technical specification for the aeronautical mobile satellite (route) service (AMS(R)S) Provided by Iridium satellite system”, IRD-SWG03-WP02

[107] Maine, K., Devieux, C., Swan, P., “Overview of IRIDIUM Satellite Network”, ISBN 0-7803-2636-9

[108] “What Is Iridium NEXT?”, presentation of Argo group at University College of San Diego

[109] “Iridium Communication Processor”, SEAKR Engineering Inc.

[110] Mazzella, M., et. al., “Multiple access techniques and spectrum utilisation of the Globalstar mobile satellite system”, Fourth IEE Conference on Telecommunications, 1993, Manchester, UK

[111] Dietrich, F., J., et. al., “The Globalstar Cellular Satellite System”, IEEE Transactions on antennas and propagation, Vol 46, No 6, June 1998

[112] Ilcev, S., D., “Orbcomm Space Segment for Mobile Satellite System (MSS)”, Conference: Telecommunication in Modern Satellite Cable and Broadcasting Services (TELSIKS), 2011 10th International Conference on, Volume: 2

[113] Ilcev, S., D., “Orbcomm Ground Segment for Mobile Satellite Communications”, International Siberian Conference on Control and Communications SIBCON, 2011

[114] “FCC FORM 442 – Federal Communications Commission application for new or modified radio station under Part 5 of FCC rules – experimental radio service (other than broadcast)”, Applicant'sName (company): SpaceExplorationTechnologiesCorp. FileNo.: 0356-EX-PL-2015

[115] Maine, K., Anderson, P., Bayuk, F, “Communication Architecture for GPS III”, IEEE Aerospace Conference Proceedings 2004

[116] Allain, D., J., “Ionospheric delay correction for single-frequency GPS receivers”, PhD Thesis, University of Bath, 2009

[117] Rose, J., A., R., “Ionospheric Imaging to Improve GPS Timing”, PhD Thesis, Bath University, 2011

[118] “Stratum levels defined”, Raltron Inc. Technical Note, 2012

[119] Langley, R., B., “The mathematics of GPS”, GPS World, July-August, 1991

[120] Meng, T., H., “Low-power GPS receiver design”, IEEE Workshop on Signal Processing Systems, pp. 1-10, 1998

[121] Dale, S., A., Daly, P., “The Soviet Union’s GLONASS navigation satellites”, IEEE AES Magazine, pp13-17, 1987

[122] Burbidge, G., “The Galileo IOV [In Orbit Validation] Satellite Payload Architecture”, IEE Aerospace Conference, 2005

[123] Nurmi, J., Lohan, E., S., Sand, S., Hurkanen, H., (editors), “GALILEO Positioning Technology”, Signals and Communications Technology Vol 182, Springer, 2015. ISBN 978-94-007-1829-6

[124] Hongwei, S., Zhigang, L., Feng, P., “Development of Satellite Navigation in China”, IEEE International Frequency Control Symposium, 2007 Joint with the 21st European Frequency and Time Forum, pp 297-300, 2007

[125] Sun, J., Jiao, W., Wu, H., Shi, C., (editors) “China Satellite Navigation Conference 2013 Proceedings: BeiDou/GNSS Navigation Applications. Test and Assessment Technology. User TerminalTechnology”, Lecture Notes in Electrical Engineering, Vol 243, Springer, 2013. ISBN 978-3-642-37397-8

[126] Teles, J., Samii, M. V., Doll, C., E., “Overview of TDRSS”, Advances in Space Research, Vol 16, No. 12, pp. (12)67-(12)-76, COSPAR, Pergamon 1995

[127] Muhonen, J., “SGLS/TDRSS Waveform Comparison”, IEEE Milcom, 1995

[128] Dornheim, M., A., “Improper Antenna Deployment Threatens Galileo Jupiter Mission”, Aviation Week & Space Technology, pp.25, Apr 22, 1991

[129] “TDRS-L Tracking and Data Relay Satellite”, Media Kit, NASA, 2014

[130] “EDRS (European Data Relay Satellite) Constellation”, ESA eoPortal Directory (on-line), 2016

[131] Gottfert, T., et. al. “The Link Management System for the European Data Relay System”, American Institute of Aeronautics and Astronautics AIAA, SpaceOps Conferences, 16-20 May, 2016

[132] “EDRS: European Data Relay System: The Space Data Highway”, ESA Factsheet, January 2016

[133] McKinney, M., M., “Transformational Satellite (TSAT) Communications Systems: Falling short on delivering advanced capabilities and bandwidth to ground-based users”, Wright Flyer Paper No. 27, US Air Command and Staff College, Research Report, Maxwell Air Force Base, Alabama, 2006. ISBN 978-1-479-38303-0

[134] “The Rules of the Air Regulations 2015”, UK CAA, 2015

[135] “Convention on International Civil Aviation”, ICAO Doc 7300/9, 2006

[136] Wang, J., Wu, M., Zheng, F., “The Codebook Design for MIMO Precoding Systems in LTE and LTE-A”, 6th International Conference on Wireless Communications Networking and Mobile Computing, Sept. 2010, pp.1-4

[137] Kurve, A., “Multi-user MIMO systems: The future in the making”, IEEE Potentials, November-December 2009, Vol.28(6)

[138] Arapoglou, P-D, et. al., “MIMO over Satellite: A Review”, IEEE Communications Surveys & Tutorials, First Quarter 2011, Vol.13(1), pp.27-51

[139] Schwarz, T. C., et. al., “Optimum-capacity MIMO satellite link for fixed and mobie services”, International ITG Workshop on Smart Antennas, Feb. 2008, pp.209-216

[140] Oh, C-I, et. al., “Analysis of the Rain fading channel and the system applying MIMO”, International Symposium on Communications and Information Technologies, Oct. 2006, pp.507-510

[141] Pérez-Neira, A., et. al., “Performance study of multiuser interference mitigation schemes for hybrid broadband multibeam satellite architectures”, EURASIP Journal on Wireless Communications and Networking, 2012, Volume 2012(1), pp. 1-19

[142] Warty, C, “Cooperative Communication for Multiple Satellite Network”, IEEE Aerospace Conference, March 2010, pp.1-7

[143] Eberlein, E., et. al., “Statistical evaluation of the MIMO gain for LMS channels”, Proceedings of the 5th European Conference on Antennas and Propagation, April 2011, pp. 2695-2699

[144] Moraitis, N., Horváth, P., Constantinou, P., Frigyes, I., “On the capacity of a SIMO land mobile satellite system at C-band: polarized and depolarized received field”, EURASIP Journal on Wireless Communications and Networking, 2012, Vol.2012(1), pp.1-12

Chapter 3

System Design Framework

3.1 Derivation of Spectrum and Altitude Datasets

In considering the spectrum issues of the high altitude low orbit environment, there are multiple free variables. To allow for a sensible analysis of the problem, and building on the data in the literature survey in Section 2, this Section considers a typical scenario and derives the values of the free variables. The values will then be used in the comparison of techniques in Section 5 that may provide enhanced spectrum performance. The values derived in this Section are represented as sets of data capturing the full limits of the free variables as identified in the literature and in published frequency spectrum allocations, with sufficient density based on these data sources to provide support for analysis later in this thesis (Section 6). The derived data sets are represented as value arrays.

3.2 Scenario

Communication with aircraft can be carried out in one of a number of ways. Such as, ground to aircraft, or ground to satellite to aircraft. Ground to aircraft communication assumes line-of-sight (LOS) once above building height, and is limited by the behaviour of the atmosphere. Ground to satellite to aircraft links are more typical, and these will be used as the foundation of a basic scenario which includes an aircraft or UAV/RPAS communicating via a satellite repeater.

3.2.1 Ground to satellite to aircraft

When a satellite flies at an orbit of altitude h_S, the distance at zenith between the ground station and the satellite will be d_{GS}.

The distance to an aircraft flying at an altitude represented by h_A depends on the slant angle between the satellite (tangent to orbit) and the aircraft, represented by θ_{SA}, and given by:

$$d_{SA} = (h_s - h_A) / Sin (\theta_{SA})$$

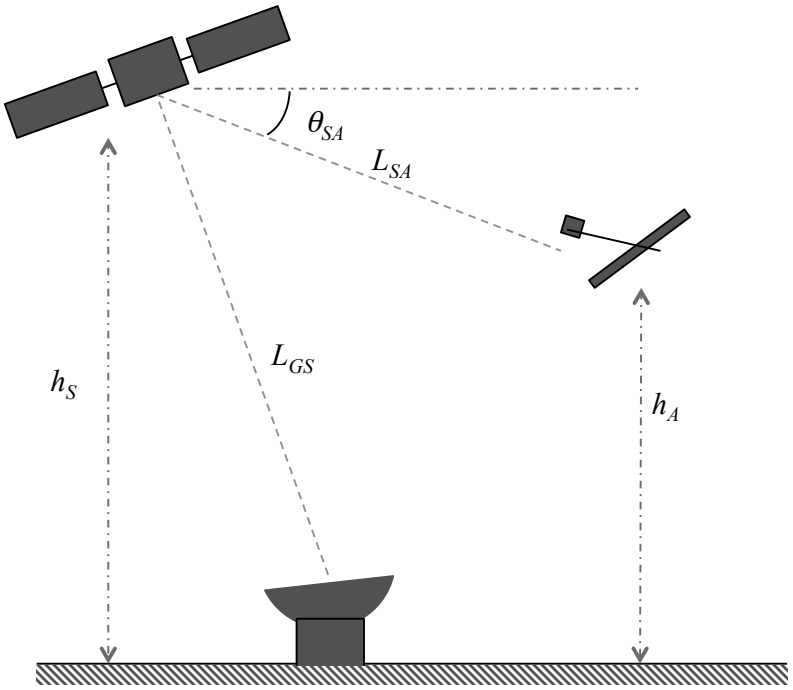

Figure 3.1 – The basic scenario

Assuming at this stage a free space path loss (FSPL) model and a perfect, lossless repeater in the satellite at zenith with no relative motion, we have a path loss (Figure 3.1) defined by:

$$L_{GSA} = (20Log_{10}(d_{GS}) + 20Log_{10}(f_1) + 32.45) + (20Log_{10}(d_{SA}) + 20Log_{10}(f_2) + 32.45) \quad (29)$$

$$L_{GSA} = 20Log_{10}(d_{GS.}\, d_{SA.}\, f_{1.}\, f_2) + 64.9 \quad [\text{dB}] \quad (30)$$

With free variables, $h_{S\,[km]}$, $h_{A\,[km]}$, $\theta_{SA\,[^o]}$, $f_{1\,[MHz]}$, $f_{2\,[MHz]}$. Let us now determine the range of these free variables.

3.2.2 Height of Satellite around the Earth (h_S)

The following chart (Figure 3.2), based on data from the United Nations (UN) Registry of Space Objects [1], illustrates the orbital altitude spread (apogee) of the more than 4,000 satellites in LEO.

The next chart (Figure 3.3), also taken from the UN Registry of Space Objects, shows the orbital altitude spread (apogee) for Medium Earth Orbit (MEO), and Geosynchronous Earth Orbit (GEO) satellites. The preponderance of satellites at GEO orbits is clear, the large number of GNSS satellites around 20,000km in MEO also evident.

We can process the data to show only those orbits used for communications satellites, and present the information as a distribution based on the number of satellites at a given orbital apogee for each satellite type (Figure 3.4), or more useful for this study, as a distribution of satellites by orbital apogee (Figure 3.5).

Figure 3.4, then, shows that there is a majority of communications satellites in LEO, confirming the findings of the literature study, however, there is an 'outlier' in the data in that Intelsat and other operators have, over the years, launched a comparable number of satellites to GEO (see also Figure 1.3 in Section 1).

Based on the data in Figure 3.5 the value of h_S can be constrained to the following values, ignoring those value where only one satellite is represented, and adding the O3b constellation altitude (7,825km), which is missing from the raw dataset.

$$h_S = \{35768, 7825, 1400, 930, 825, 750, 630\} \quad \text{[km]} \quad (31)$$

Indicating that there is currently only one communication satellite constellation in MEO orbit, which agrees with the data in the literature review, Section 2.3.10.

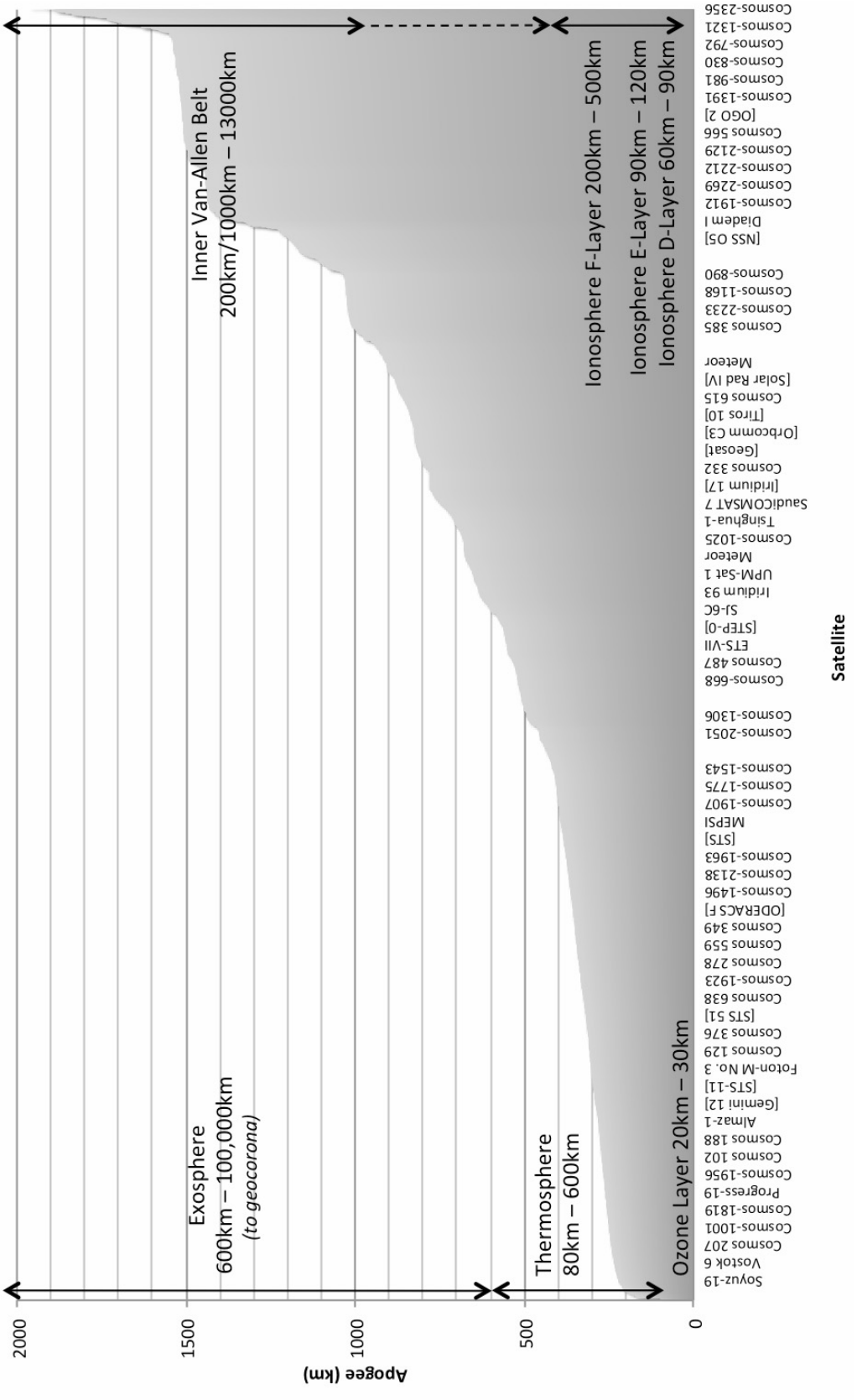

Figure 3.2 – Satellite distribution in LEO

(data sourced from *UN* [1], not all satellites labelled on axis)

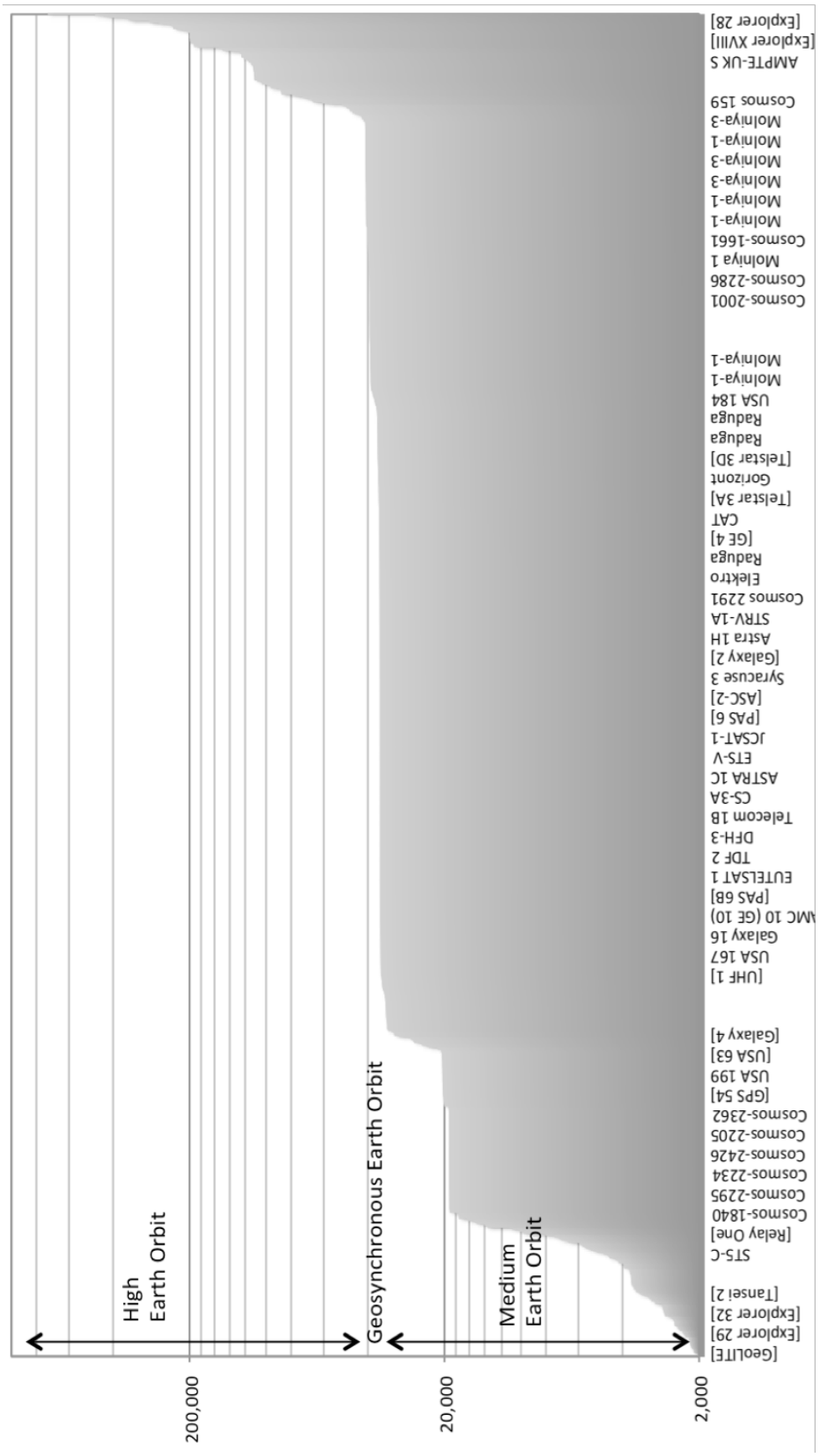

Figure 3.3 – Satellite distribution in MEO, GEO and HEO orbits

(data sourced from *UN* [1], not all satellites labelled on axis)

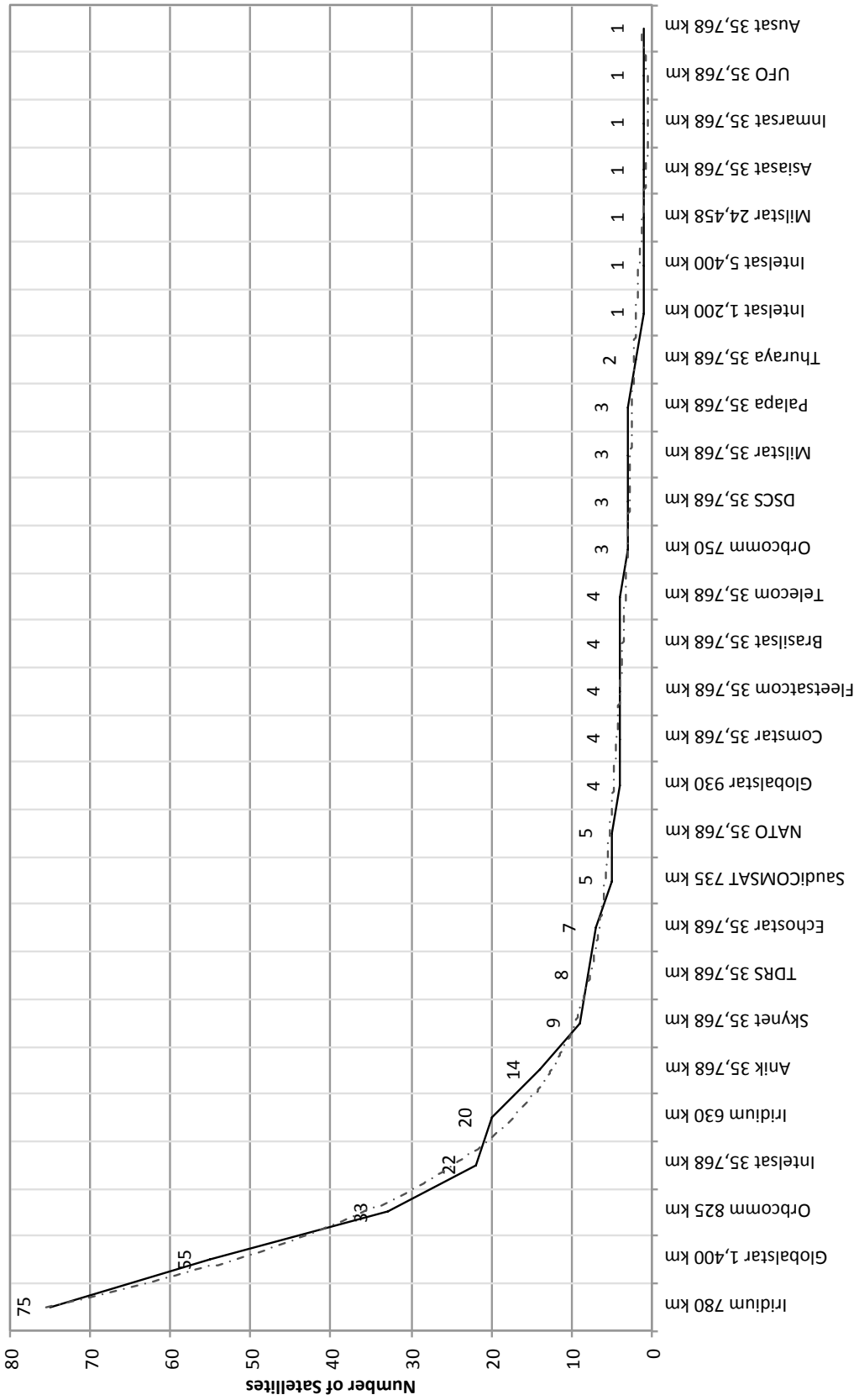

Figure 3.4 – Cumulative distribution of number of satellites by altitude

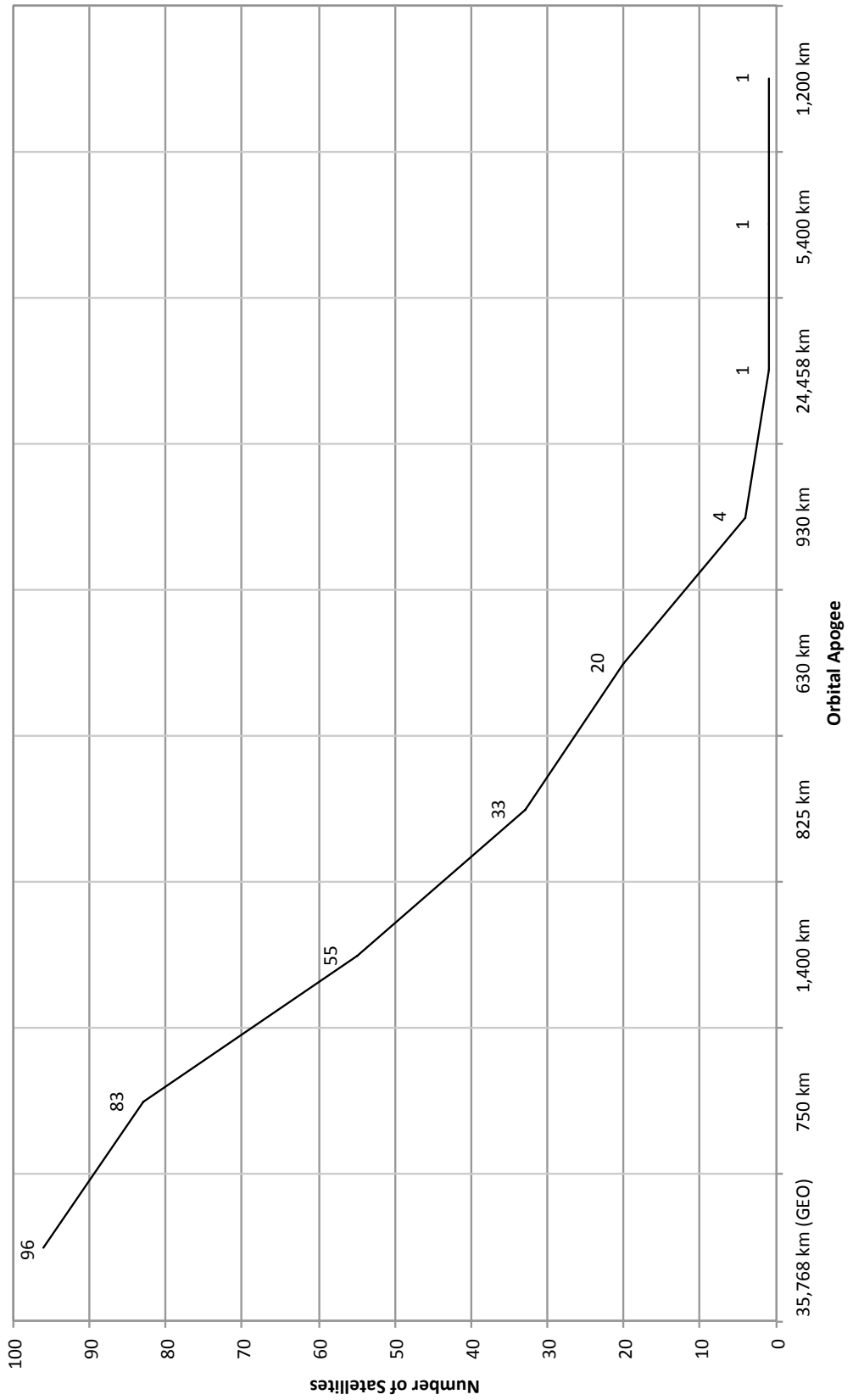

Figure 3.5 – Cumulative distribution curve of comms satellite types by apogee

3.2.3 Height of Aircraft above the Earth (h_A)

The height that aircraft fly (including manned, unmanned aerial vehicles, UAVs, and Remotely Piloted Aircraft Systems, RPAS) is illustrated in the following chart (Figure 3.6). The chart is based on data from multiple sources collected over many years from journals and published information. Also illustrated are the accepted altitudes of the atmospheric regions.

It is interesting to note that there is a significant layer of the atmosphere, between around 20km (highest aircraft flight) and 86km (lowest orbit), where it is not possible to sustain a continuous presence, and that many scientifically interesting atmospheric phenomena occur.

Figure 3.7 details the ceiling altitudes of a range UAV and RPAS aircraft. There are inflections in the graph of altitude ceiling performance of these craft, which perhaps indicates some commonality between designs.

The ceiling altitude data for UAV/RPAS can be converted, using a +/-2km range, to show the cumulative number of UAV/RPAS types by ceiling altitude (Figure 3.8).

Analysing the ceiling altitude of these UAV/RPAS aircraft the values of $h_{A(UAV)}$ can be defined:

$$h_{A(UAV)} = \{27, 20, 12, 5, 1\} \quad \text{[km]} \qquad (32)$$

We can draw a correspondence to the industry terms, HALE (High Altitude, Long Endurance) {27, 20} km, MALE (Medium Altitude, Long Endurance) {12, 5} km, and Tactical/Hobby UAVs around {1} km.

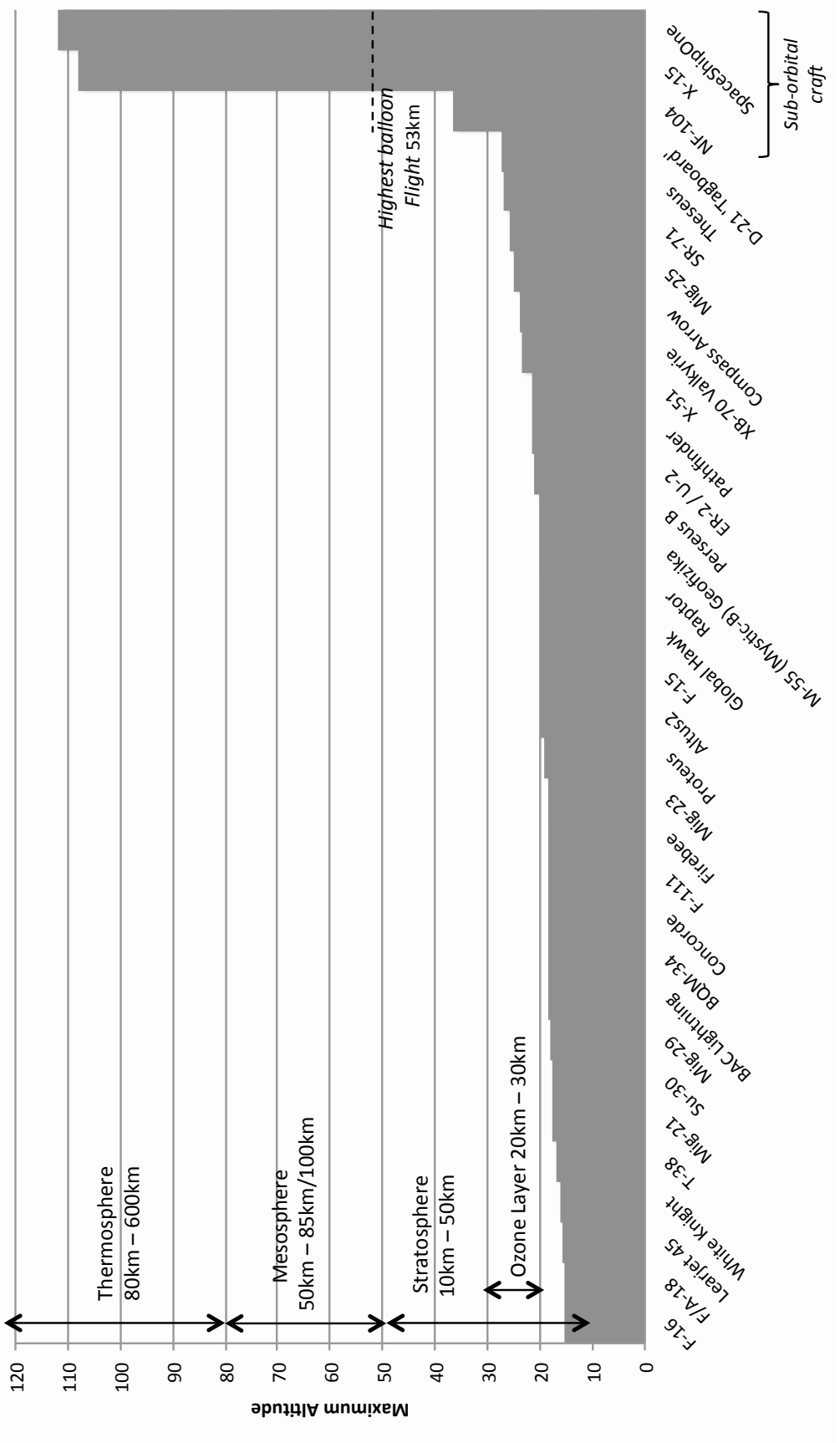

Figure 3.6 – Distribution of aircraft (manned and unmanned) and suborbital craft by altitude, alongside typical atmospheric effects and layers

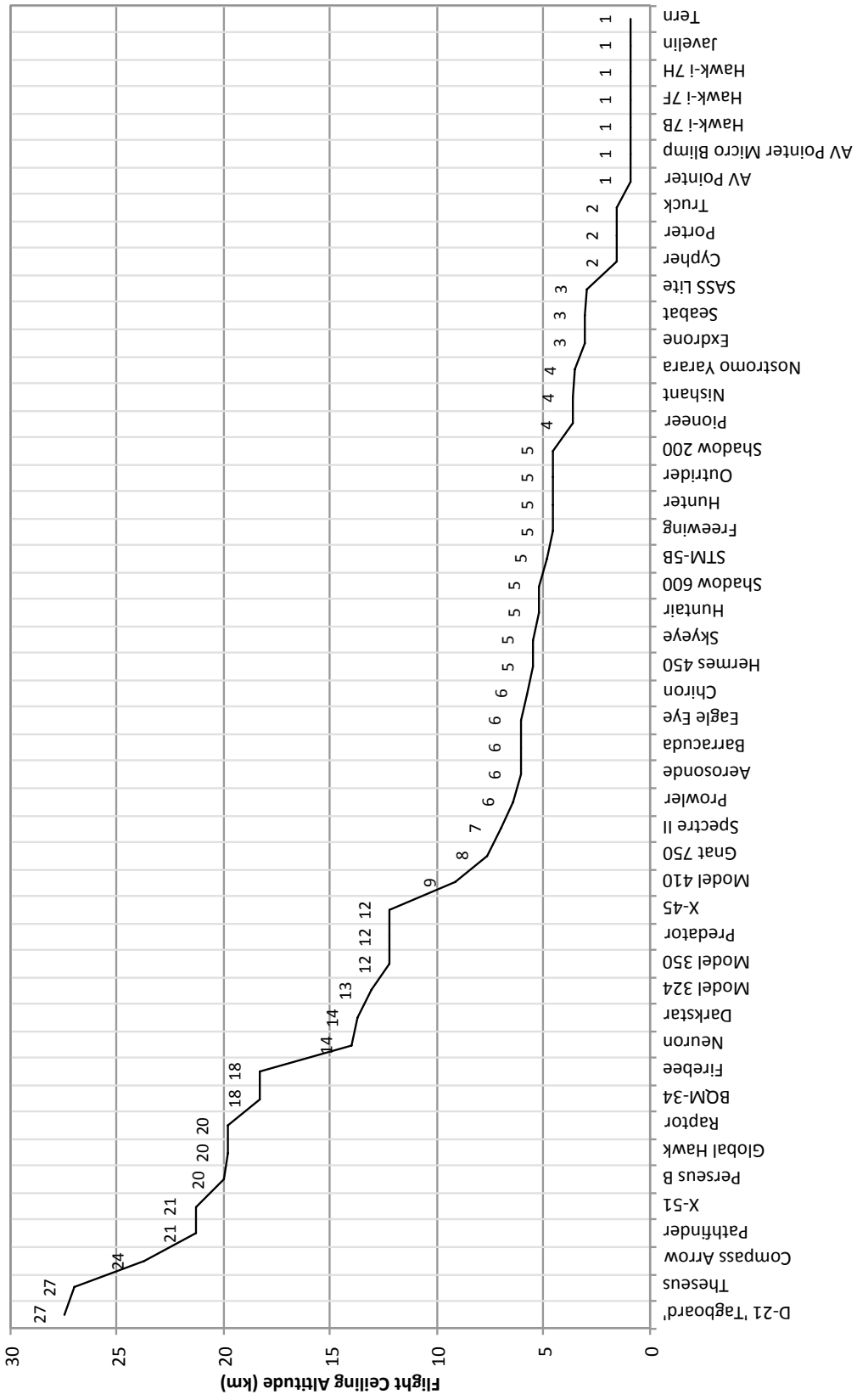

Figure 3.7 – Ceiling altitudes of UAV/RPAS by type

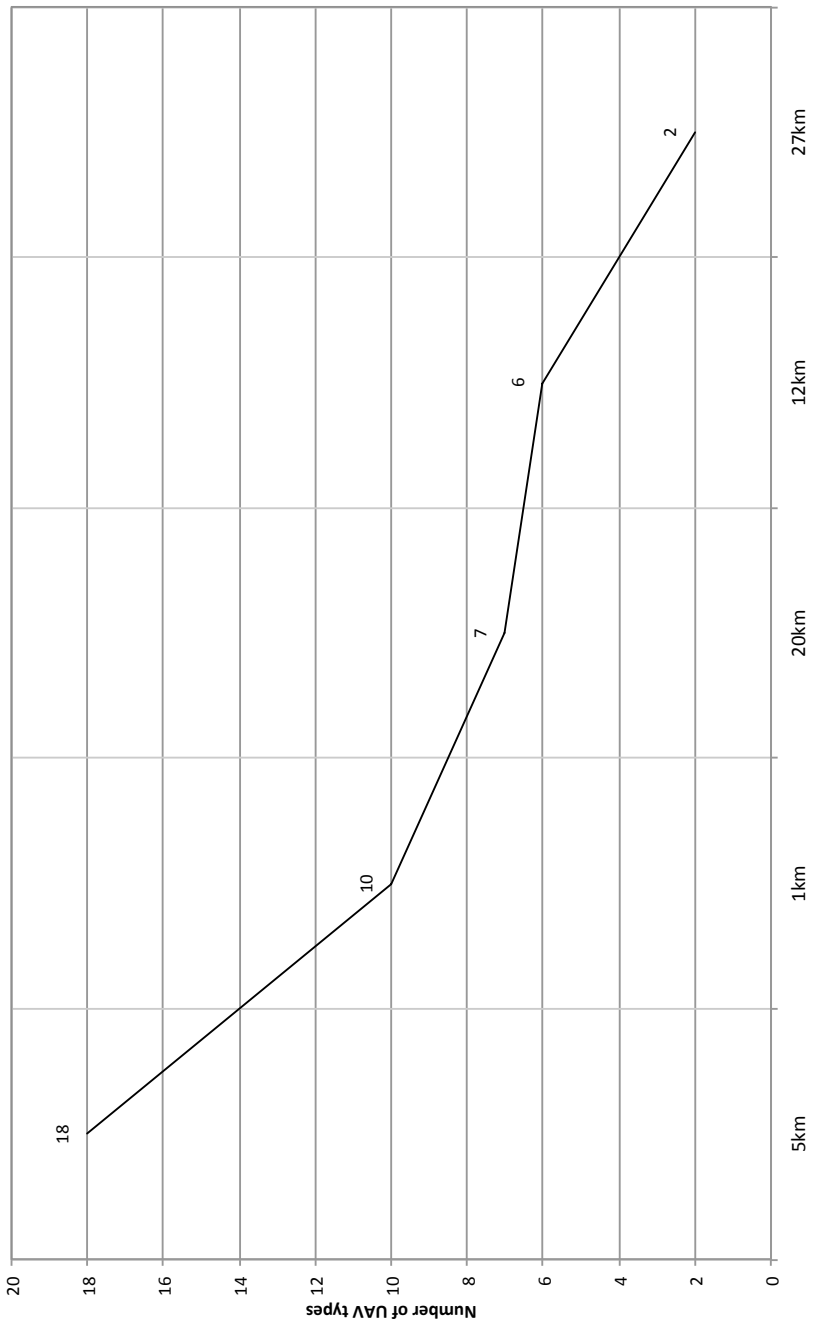

Figure 3.8 - Cumulative number of UAV/RPAS types by altitude ceiling

For manned aircraft, the data is shown below (Figure 3.9). Unlike spacecraft and UAV/RPAS, the number of aircraft types, and lack of published data on most, prevents a full detailed analysis.

In order to draw some conclusions, only aircraft capable of 35,000ft service ceiling or higher are considered, and in the case of the 30,000ft to 40,000ft commercial jet

aircraft cruise altitude, a sampling of types from the main manufacturers only is included. Below 35,000ft there are aircraft that operate from 'ground effect' all the way to this ceiling altitude, with many jet and propeller types; these are not included in the dataset here.

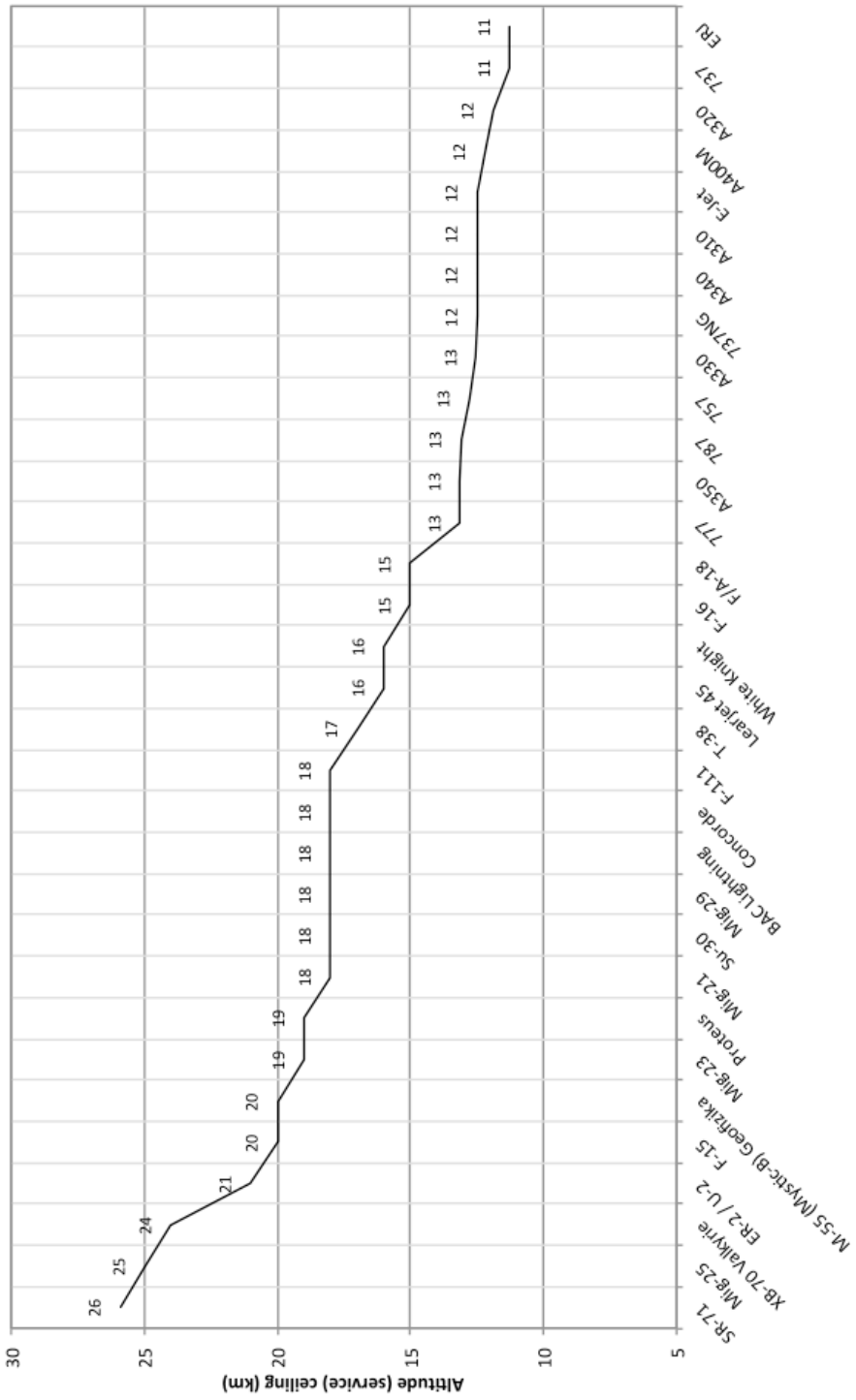

Figure 3.9 – Cumulative chart of altitude of aircraft by type

At lower altitudes, the cruising altitude is controlled by the 'airways in the sky' (typically Class-A airspace airways). Class-A typically begins at the transition altitude of 18,000 ft (5.5 km) in the US, and down as far as 3,000 ft (0.9 km) in Europe.

The transition altitude varies depending on atmospheric pressure. Since entering an airway is difficult without a turboprop or jet engine aircraft, we can assume that commercial aircraft fly above 3,000 ft (0.9 km) (in the cruise), with propeller driven craft more typical below 3,000 ft (0.9 km).

In summary, there are aircraft of all types operating up to 18,000 ft (5.5 km), but a smaller set of turboprop and jet engine aircraft that operate above this, typically with a service ceiling of around 40,000 ft (12.2 km).

Even with a limited dataset it can be seen that the following general values of $h_{A(Aircraft)}$ can be determined. Along with these values we add 18,000 ft (5.5 km) and 3,000 ft (0.9 km) as the bounds of the transition level for typical commercial (instrument) flight.

$$h_{A(Aircraft)} = \{25, 20, 18, 16, 15, 13, 12, 11, 3\} \text{ [km]} \quad (33)$$

Combining:

$$h_A = h_{A(UAV)} \, U \, h_{A(Aircraft)} \text{ [km]} \quad (34)$$

Then:

$$h_A = \{27, 25, 20, 18, 16, 15, 13, 12, 11, 5, 3, 1\} \text{ [km]} \quad (35)$$

3.2.4 Available frequencies (f_1, f_2)

Each country controls its RF spectrum allocation and this usually has the force of law. Where harmonisation of RF spectrum is required across country boundaries, transnational bodies such the United Nation's ITU (International Telecommunications Union) and other geographic bodies, such as CEPT in Europe

for example, define the standards. If agreed by these bodies, standards are then typically incorporated within country spectrum planning.

Since Aircraft and Spacecraft are 'transnational' by nature of the range of their operation, air systems are typically subject to ITU regulation for spectrum use. Frequency allocation is dependent both on geo-political and physical constraints.

The purpose of ITU spectrum regulation is defined in ITU Constitution Article-44 [2]: the key metric being managed by ITU spectrum agreements is *interference reduction*.

Based on the UK Ofcom consolidation of the ITU recommendations (which are accessible in an on-line database on the Ofcom website), the following charts illustrate the main frequencies available solely for satellite communications. That is, excluding amateur bands, military bands, and those bands subject to coordination constraints. The chart (Figure 3.10) shows the available bandwidth at each of the key frequency bands. This is then broken down into Earth to space frequencies (Figure 3.11), and space to Earth frequencies (Figure 3.12). These spectrum bands are licensed.

Much of the spectrum for satellite communications is discontiguous, but there are discrete regions of spectrum that can be grouped together for the sake of simplifying analysis.

We define these regions as frequency pairs representing the start of band, and end of band, respectively. The values align with the findings of the literature survey given in the description of satellite systems throughout Section 2.

$$f_{x(Earth\text{-}Space)} = \{ (1.427,1.429), (1.616, 1.6265), (1.785, 1.88), (2.025, 2.11), (7.145, 7.235), (10.7, 11.7), (12.5, 12.75), (17.3, 18.4), (19.3, 19.7), (28.5, 30), (40, 40.5), (47.5, 47.9), (48.2, 48.4), (49.44, 50.2) \} \text{ [GHz]} \quad (36)$$

$f_{x(Space\text{-}Earth)}$ = { (0.137, 0.143), (1.525, 1.535), (2.2, 2.29), (8.025, 8.175), (8.4, 8.5), (10.7, 11.7), (12.5, 12.75), (14.4, 14.47), (17.3, 18.4), (19.3, 19.7), (25.5, 27.0), (37.0, 40.5), (47.5, 47.9), (48.2, 48.54), (49.44, 50.2), (74.0, 84.0) } [GHz] (37)

The bands for 'space-to-space' communication appear to be application dependent but include cross-links for radio navigation (GNSS), Low and Medium Earth Orbit (LEO/MEO) communications satellite constellations, and LEO/MEO cross connection to Geosynchronous Earth Orbit (GEO) satellites.

There are other communication cross-links used for constellation and experimental satellites, and for science and interplanetary satellites. Some specific examples can be used to populate a list of typical space-to-space frequencies. For example, the Iridium satellite constellation uses 23.18 GHz to 23.38 GHz for cross-link communication. NASA's TDRS (Tracking and Data Relay Satellite) system constellation uses cross-links, but the frequency is not published. The European Alphasat satellite has an experimental Q/V-band (33.0 GHz to 50.0GHz and 40.0 GHz to 75.0 GHz respectively) communication transponder intended primarily for satellite constellation feeder and cross-link applications.

For the analysis carried out here, typical cross-link frequencies are defined as:

$f_{x(Space\text{-}Space)}$ = { (8.0, 12.0), (23.18, 23.38), (33.0, 75.0) } [GHz] (38)

It can be seen that the limitations of Earth based spectrum interference mitigation through licensed spectrum may not apply in space-to-space communications, provided there is no Earth vicinity interference and no interference with ITU agreed frequencies for other satellites. For example, NASA's Deep Space Network (DSN) uses X-band (8.0 GHz - 12.0 GHz) for satellite to Mars rover communication [3]. This is then relayed back to Earth to NASA's DSN ground stations on frequencies ranging from S-Band (2.0 GHz – 4.0 GHz) to Ka-Band. (26.5 GHz – 40.0 GHz). Though the X-band links overlap with Earth licensed spectrum bands, the distance means that there is no Earth interference impact.

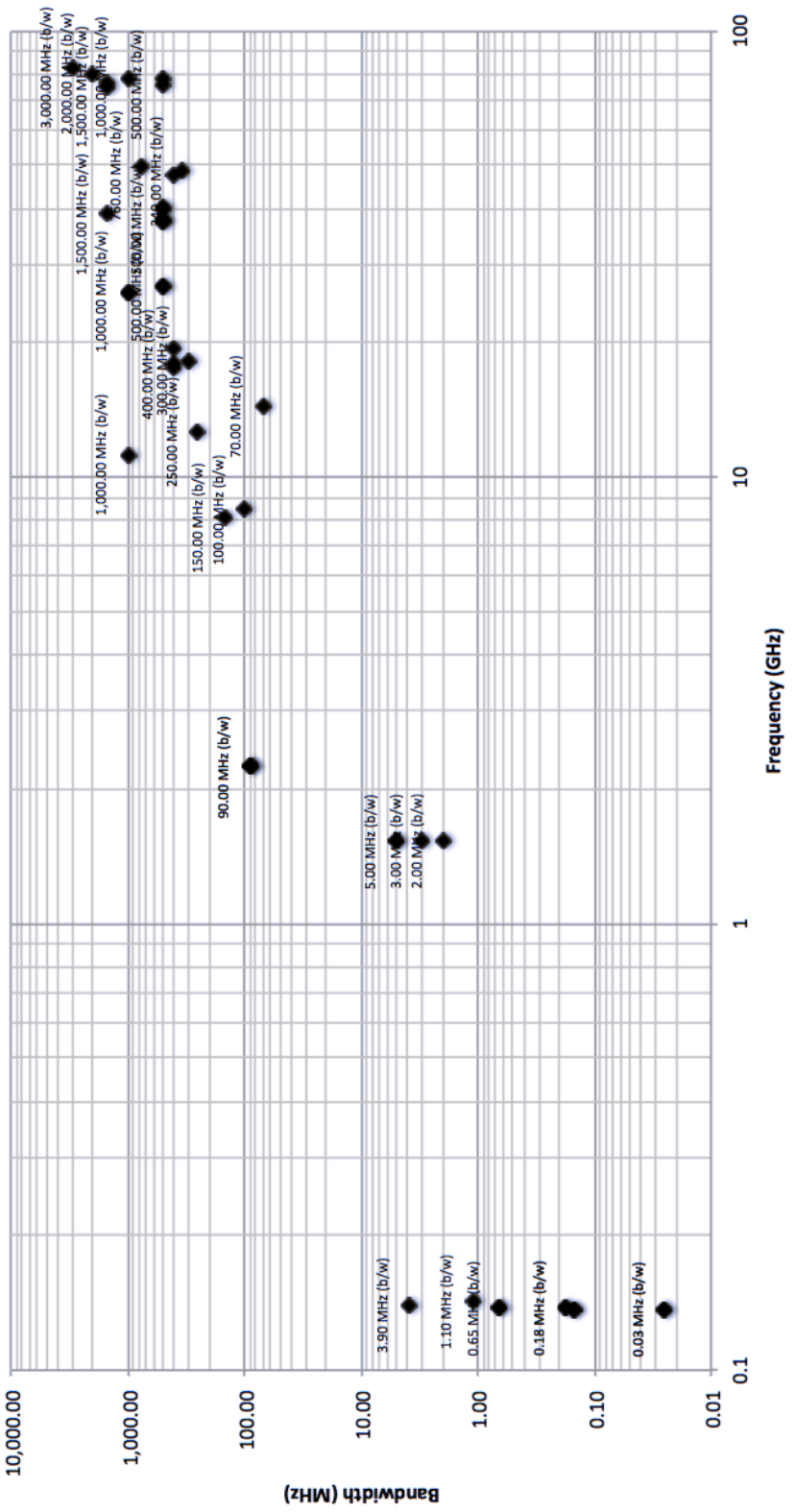

Figure 3.10 - Allocated spectrum for satellite communication
(excluding amateur, military, and those bands with coordination constraints)

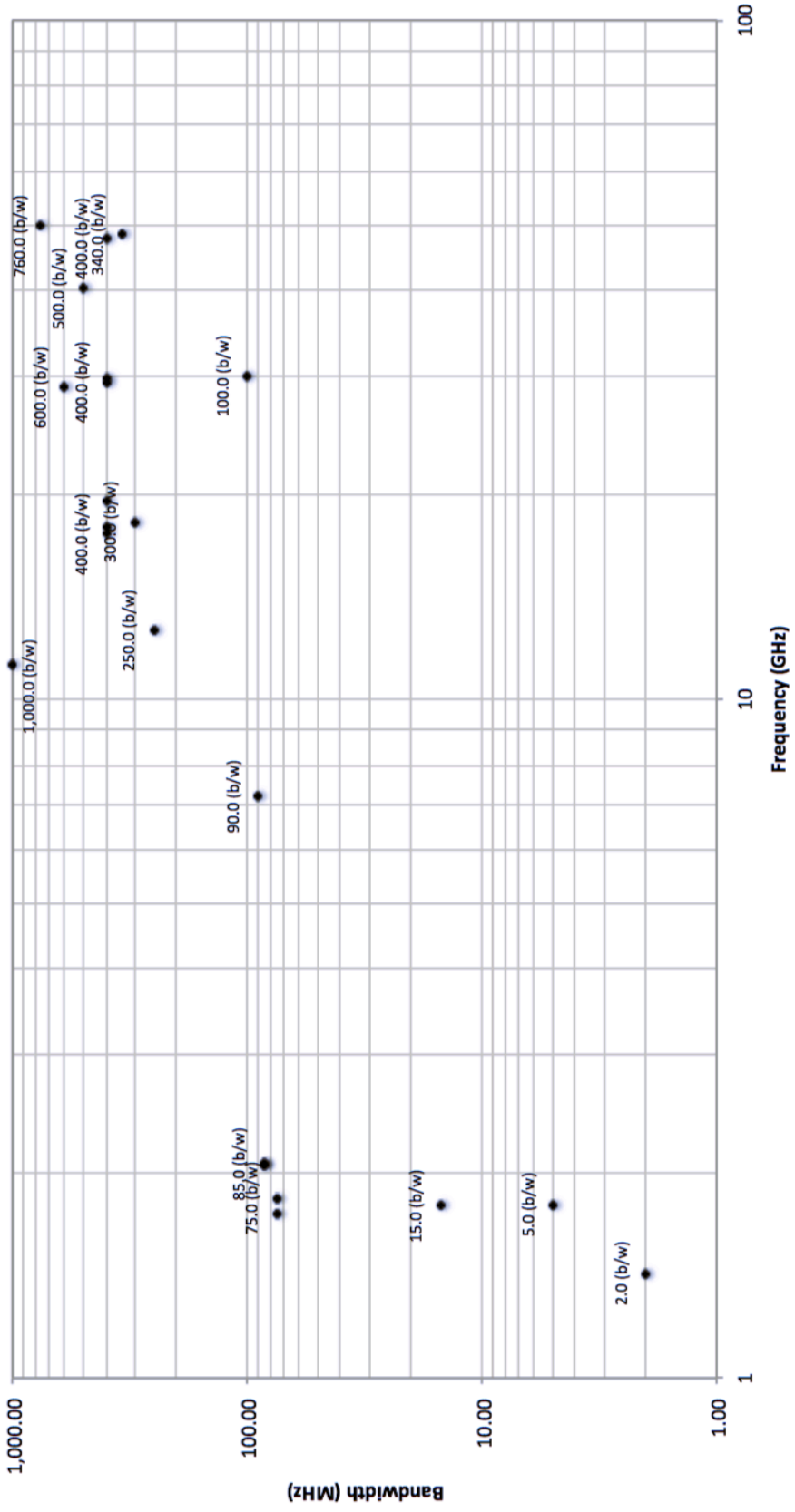

Figure 3.11 - Allocated spectrum for Earth to space communication (excluding amateur, military, and those bands with coordination constraints)

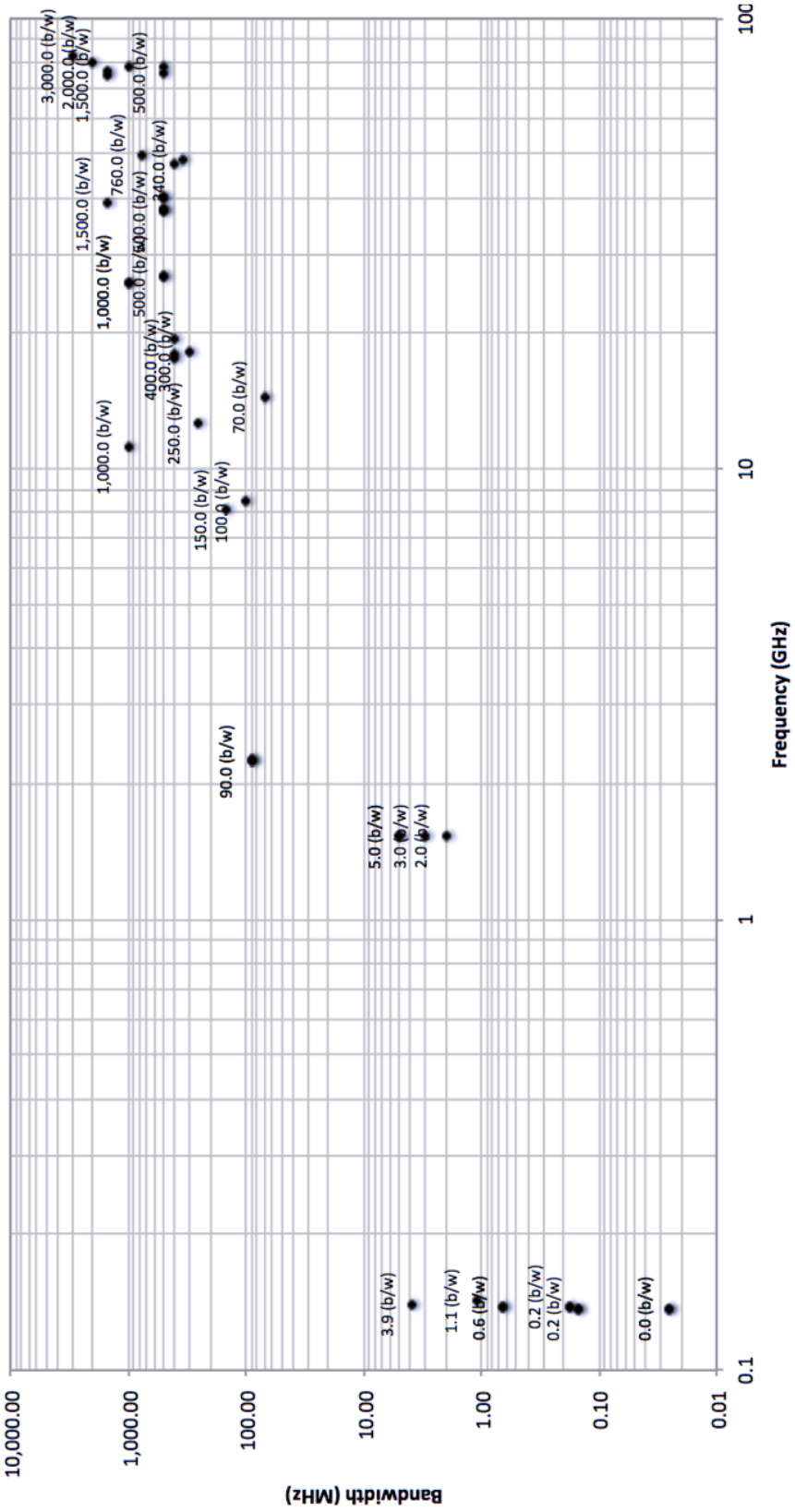

Figure 3.12 - Allocated spectrum for space to Earth communication (excluding amateur, military, and those bands with coordination constraints)

Even with this planning, there is still the possibility of satellite-to-satellite interference, and as such any cross-link RF communication spectrum allocation must be agreed by the ITU: as such, if ITU agreement can be negotiated, there is much scope for extremely wide-band RF cross-links for space-to-space communication in future.

3.3 Summary

In this Section is defined a scenario and its associated free-variables. Through the data collected in the literature review in Section 2, and additional data referenced in this Section, data sets for typical altitudes, orbits, and spectrum usage have been defined.

These datasets will be used in the performance analysis of proposed solutions to the spectrum problem, which is covered in Section 6.

3.4 Atmospheric RF propagation and channel model

In order to consider the performance of RF solutions in the high altitude and low-Earth orbit environment, a consistent model of the atmosphere is required. Following the literature survey, the standard ITU-R P.2041 [4] was chosen as the basis of the model, it references out to ITU-R P.618 [5] which covers many of the other standards. Unfortunately, there are no implementations of the standard that are easily available, therefore an implementation of the standard was developed as part of work for this thesis. The code is provided in Appendix A to this thesis. Since the model was bespoke for this thesis, additional features specific to the high altitude and low orbit nature of the problem could also be included.

3.5 ITU-R standards based model

To provide a repeatable and accurate model requires taking into account the effects of Earth's atmosphere, and the electromagnetic environment surrounding the Earth. A standardised procedure to do this is described in ITU-R-P.2041: Section 5 describes the '*attenuation between an airborne platform and space*". The related

standard, ITU-R P.618, describes the model for attenuation from Earth to space. ITU-R P.618 is referenced from within ITU-R P.2041. In the ITU.2041 standard, path loss attenuation is based on the contributing factors of:

- Gaseous attenuation
- Cloud attenuation
- Rain attenuation
- Tropospheric and ionospheric scintillation
- Refraction

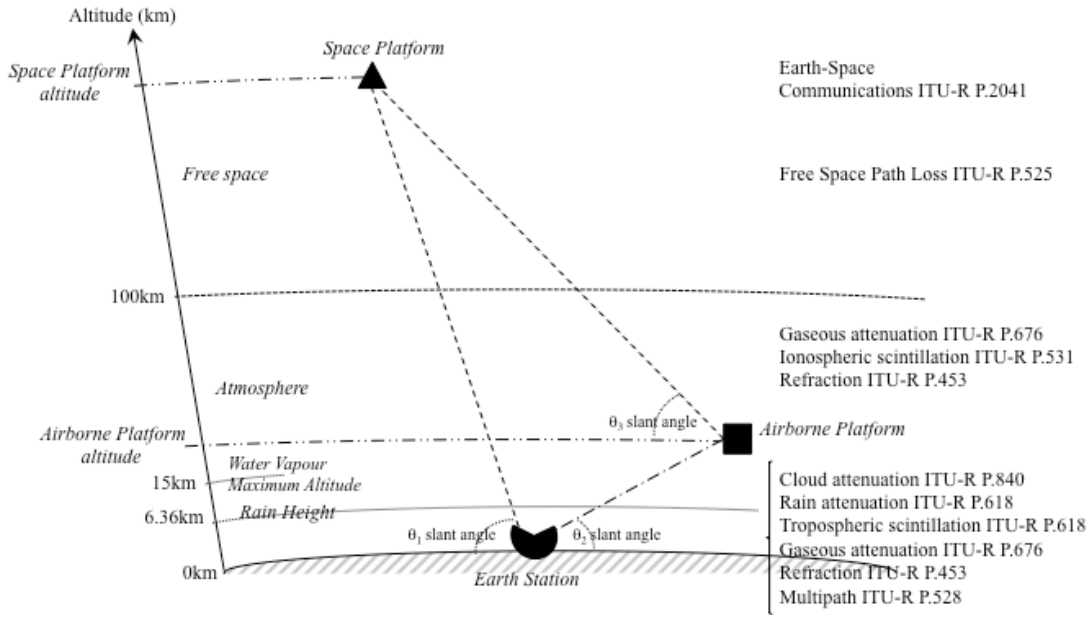

Figure 3.13 – Diagram of the scenario model with associated RF path loss standards showing the layer limits derived in this Section

The above diagram (Figure 3.13) illustrates the scenario in relation to the ITU standards, as identified in the literature survey in Section 2.2.4, and for each segment of the RF path of the basic scenario defined in Section 3.2.

Unfortunately, the ITU standards do not provide a straightforward generic model implementation. They are, as one would expect, designed to cover every possible scenario. For the sake of the analysis being developed here, a more generic model is

required. To achieve this the standards have been implemented as a set of re-usable C-code library modules with the following generalising approach.

- Where standards provide measurement for precise locations on the Earth, the generic model developed for this thesis calculates sensible representations of these values for full Earth calculation. Where this procedure is followed, the method used is described, and any constraints noted.

- Where standards describe atmospheric conditions at different altitudes, and with varying slant path angles, analysis has been performed to consider the range of values that result from such models, and provides a summary set of values along with narrative on the accuracy of these values.

By implementing the software library in this way, the output is a generic ITU.2041 path loss model that can be used to compare performance across a wide range of geographic locations, in-atmosphere and out-of-atmosphere positions, differing orbits, altitudes, and conditions, without the need to calculate and post-synthesise data for every potential point on Earth, or in the atmosphere and space, that relate to a particular calculation.

It should also be noted that the standards are, in some places, quite vague as to application and implementation, and much work has been required to untangle the descriptions to provide an accurate model implementation.

3.6 Total path loss attenuation

The total path loss attenuation (A_T^{AS}) between airborne and space platforms space is defined as the gaseous absorption plus the contribution of rain, clouds, and tropospheric scintillation through the geometric slant path, if the platform is below or equal to the 'rain height', as specified in ITU-R P.839 [6].

$$A_T^{AS}(p) = A_G^{AS}(p) + \sqrt{(A_R^{AS}(p) + A_C^{AS}(p))^2 + (A_S^{AS}(p))^2} \qquad (39)$$

Where:

p	represents a fixed probability
A_G^{AS}	represents gaseous attenuation due to absorption by water vapour and oxygen [dB]
A_R^{AS}	represents attenuation due to rain [dB]
A_C^{AS}	represents attenuation due to clouds [dB]
A_S^{AS}	represents attenuation due to tropospheric scintillation [dB]

If the platform is above the 'rain height', the path loss attenuation simplifies to:

$$A_T^{AS}(p) = A_G^{AS}(p) + A_C^{AS}(p) \qquad (40)$$

3.7 Rain height

'*Rain height*' above sea level is defined in ITU-R P.839 [6] as being 0.36 km above the 0° C isotherm height for the specific longitude and latitude information in the ITU-R P.839 supplied database. The data for the 0°C isotherm height is plotted in the standard, as reproduced below in Figure 3.14.

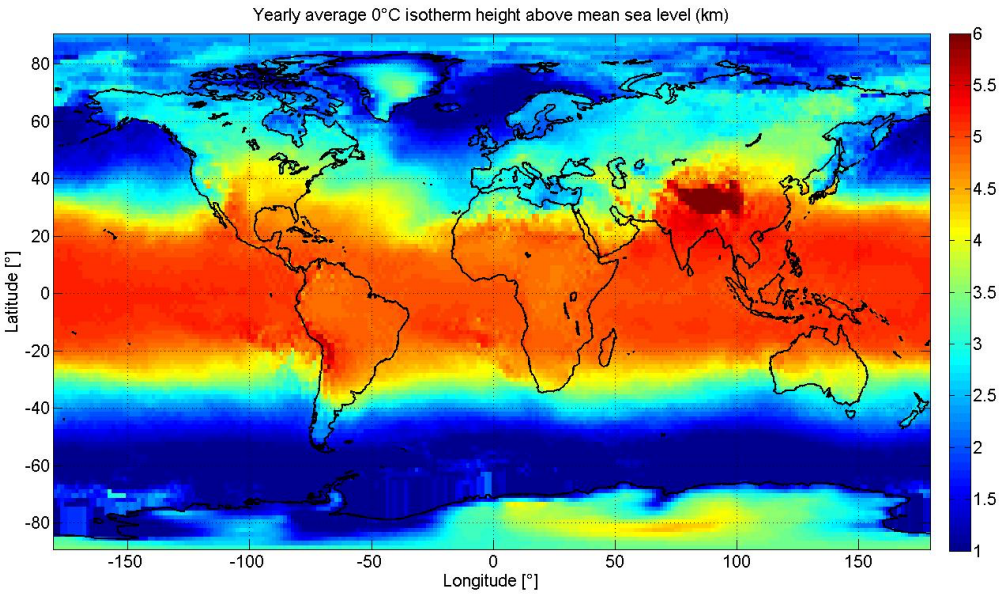

Figure 3.14 – Global 0°C isotherm height (after ITU-R P.839 [3])

For analysis in this thesis we will assume the worst-case condition of 0.36 km above the 0° C isotherm, giving:

$$RainHeight = 6.36 \text{ [km]} \quad (46)$$

Comparing this with the aircraft altitude heights (h_A) derived in Section 3.2.3, only the {5, 3, 1} km altitudes are affected. For reference, 6.36 km is approximately 21,000 ft.

3.8 Atmosphere gaseous attenuation

Gaseous attenuation (A_G^{AS}) is defined in ITU-R P.676 [7] for space to aircraft RF channels by two methods: a line-by-line measured spectrum method, and a curve fit approximation method. The former method has a frequency limit of 1,000 GHz and is as accurate as the molecular measurements, whereas the latter has a limit of 350 GHz and though a simpler calculation it is an approximation. The approximation has an error stated as approximately 0.1 dB/km at 10 GHz and approximately 0.7 dB/km at 60 GHz.

For this work, given the limit in ITU-R P.2041 of <55GHz (less than the 350GHz in ITU-R P.676) as the upper frequency for the approximate gaseous attenuation calculation, the line-by-line method for ITU-R P.676 will be implemented. Though more complex to calculate, this provides values for gaseous attenuation up to 1,000 GHz.

To make use of the equations in ITU-R P.676 requires knowledge of the local atmospheric temperature, pressure and water vapour profiles at a given time. These are typically found by radiosonde measurement. For general calculations, the recommended procedure in ITU-R P.676 is to use the "Reference Standard Atmosphere" defined in ITU-R P.835 [8]. The "Reference Standard Atmosphere" describes the atmosphere to an altitude of 100 km.

The Reference Standard Atmospheres in Annex 1 of ITU-R P.835 [8] are in thesis mathematically averaged for latitude, and plotted in the following charts: Figures 3.15, 3.16, and 3.17. Averaging creates a generic temperature, pressure and water vapour model of the Reference Standard Atmosphere with reasonable fit to all conditions, as can be seen in Figures 3.15, 3.16, and 3.17.

The software algorithm implemented in this thesis to calculate gaseous attenuation using the line-by-line method is as follows:

Step 1: Retrieve the temperature (*T*), pressure (*p*), and water vapour density (*d*) values from tables of the pre-processed averaged Reference Standard Atmosphere for the given frequency and altitude

Step 2: Calculate the underlying continuum attenuation

Step 3: Calculate Oxygen attenuation (using the line-by-line method)

Step 4: Calculate Water Vapour attenuation (using the line-by-line method)

Step 5: Sum the attenuation values

The software library module interface is defined as follows.

```
double attenuationGaseousFunction (double altitude, double frequency, int
testMode)
{
    // PARAMETERS
    // altitude            (km)
    // frequency           (GHz) (f)
    // testMode            = 1 (on) for standard values,
                           = 0 (off) for normal calculation
    // Returns:
    //   gaseous attenuation (dB/km)
```

The reference to 'testMode' above enables standard constants (as highlighted in ITU-R P.676 [7]) that produce the values of the familiar gaseous attenuation plot reproduced in many papers and RF literature. The values used with 'testMode' enabled are: temperature = 288K, pressure = 1013hPa, water vapour density = 7.5 g/m^3. The code should be modified if required to use a value of 0 g/m^3 to simulate the standard graph with dry air (0 % Relative Humidity).

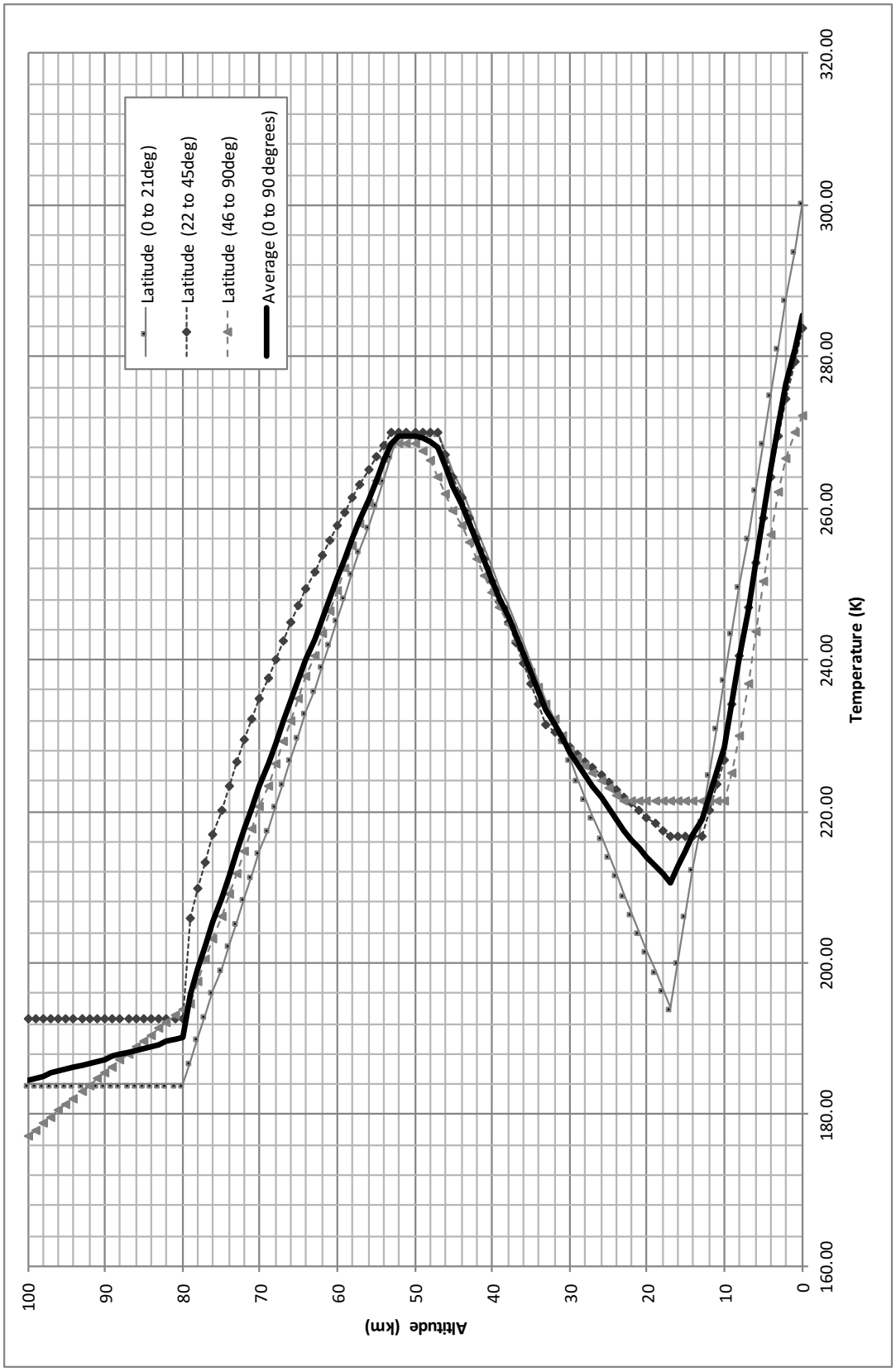

Figure 3.15 – Average across all latitudes of ITU-R P.835 [8] Annex 1 temperatures for the Reference Standard Atmosphere

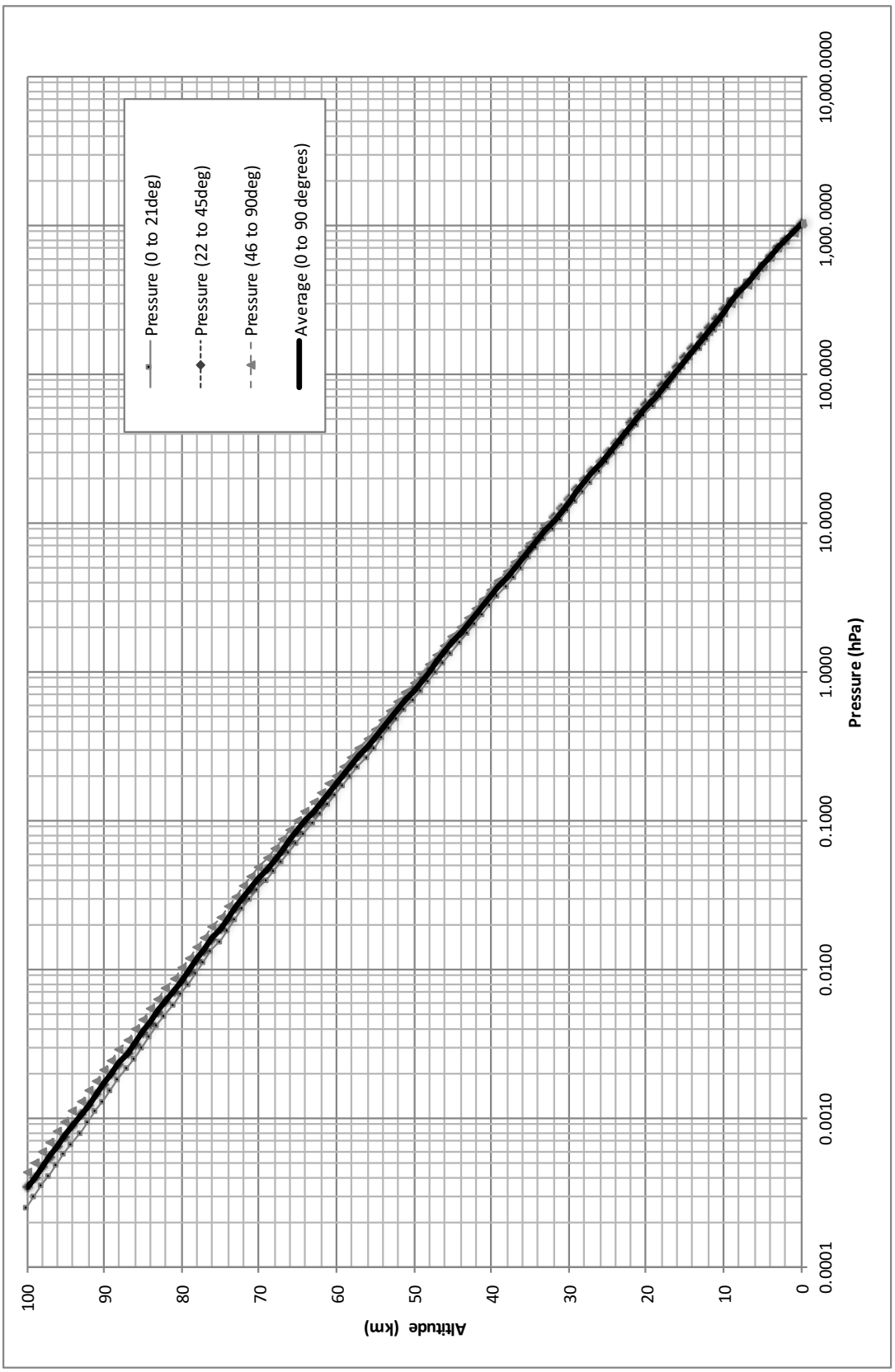

Figure 3.16 – Average across all latitudes of ITU-R P.835 [8] Annex 1 pressures for the Reference Standard Atmosphere

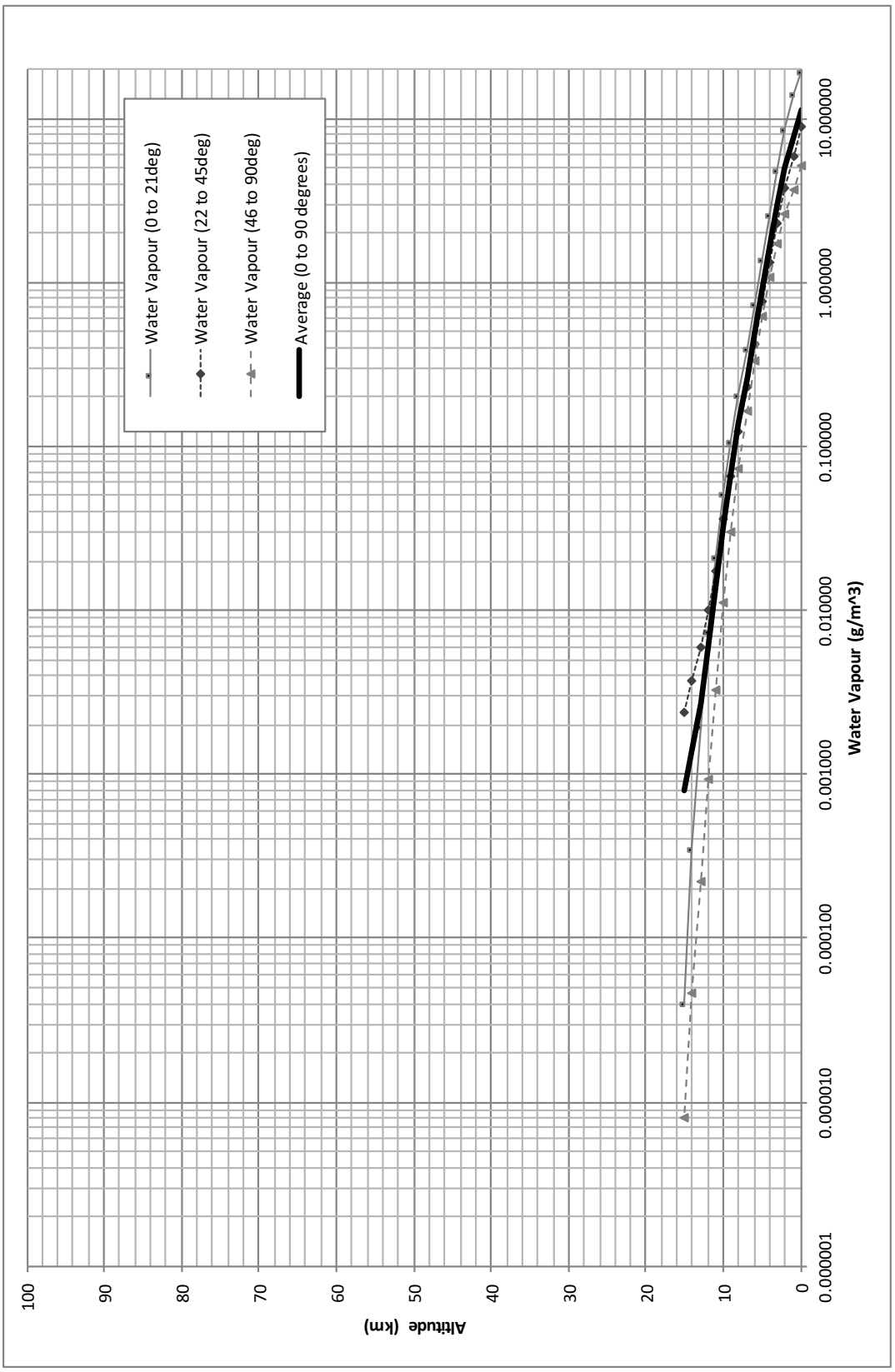

Figure 3.17 – Average across all latitudes of ITU-R P.835 [8] Annex 1 water vapour density for the Reference Standard Atmosphere (altitudes above 15 km are $0 g/m^3$)

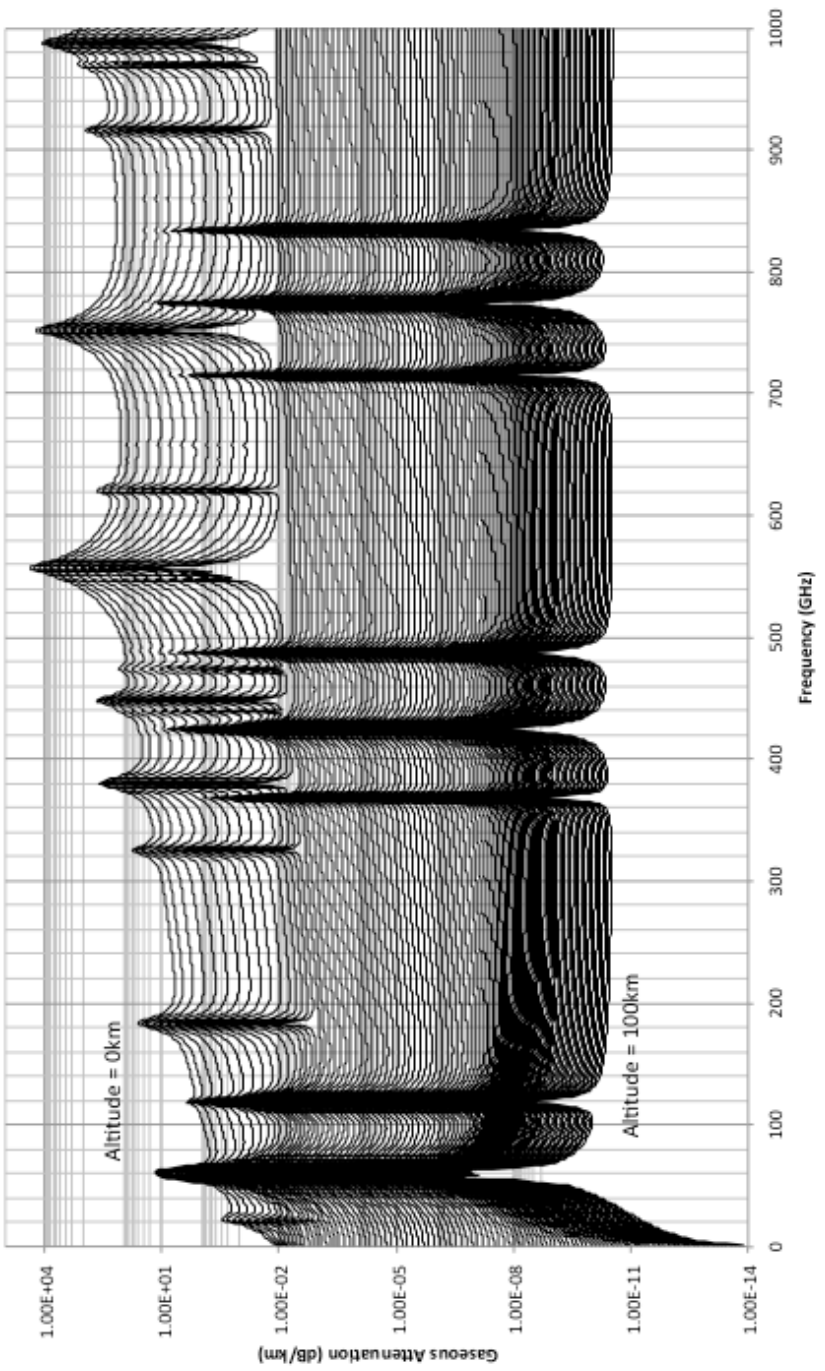

Figure 3.18 – Gaseous attenuation across 1 GHz to 1,000 GHz, from 0 km to 100 km altitude in 1 km steps, using averaged atmospheric conditions, and the 'line-by-line' spectrographic method indicating the transition at the atmospheric water vapour limit, and llustrating the range of values across the 0 to 100 km range

Using the software model and with the averaged values of Reference Standard Atmosphere, the following chart (Figure 3.18) can be calculated. The chart shows the calculation of gaseous attenuation across 1 GHz to 1,000 GHz, from 0 km to 100

km altitude in 1 km steps, using averaged atmospheric conditions, and using the ITU-R P.676 [7] Annex 1 'line-by-line' spectrographic data calculation.

The lack of water vapour above 15 km, as defined in ITU-R P.676 [7], and the change in absorption species with increased frequency and altitude, are clearly visible in the plot (Figure 3.18).

3.9 Confirming correct implementation of the algorithm

Unfortunately, there is no confirmatory dataset with which to confirm correct implementation of the ITU standards and it is left to the implementer to determine if the algorithm is implemented correctly. As far as can be determined for this thesis, the only option is to demonstrate correct implementation by graph comparison. It would be helpful if future ITU standards developments provided datasets for implementers to check their implementations.

Following a graph comparison approach, the following chart overlays the results from the implementation of the gaseous attenuation algorithm developed in this thesis with that of previously published results (after *Richard et.al.* [9]) there is good correlation at the 50% relative humidity line (Figure 3.19). The correlation is not accurate across all frequencies and this is likely to be a result of different selection of the values for the Reference Standard Atmosphere since *Richards* [9] only provides reference to the relative humidity.

3.10 Observations related to the gaseous attenuation results

The graph of gaseous attenuation illustrates an interesting observation that in the 'dry-air' above 15 km (approximately 49,000 ft) there is very little increase in the base attenuation up to 1THz frequency. The implication of this is that a high altitude long endurance (HALE) unmanned or manned vehicle's communication to or from a satellite is not increasingly limited by atmospheric absorption as the frequency increases.

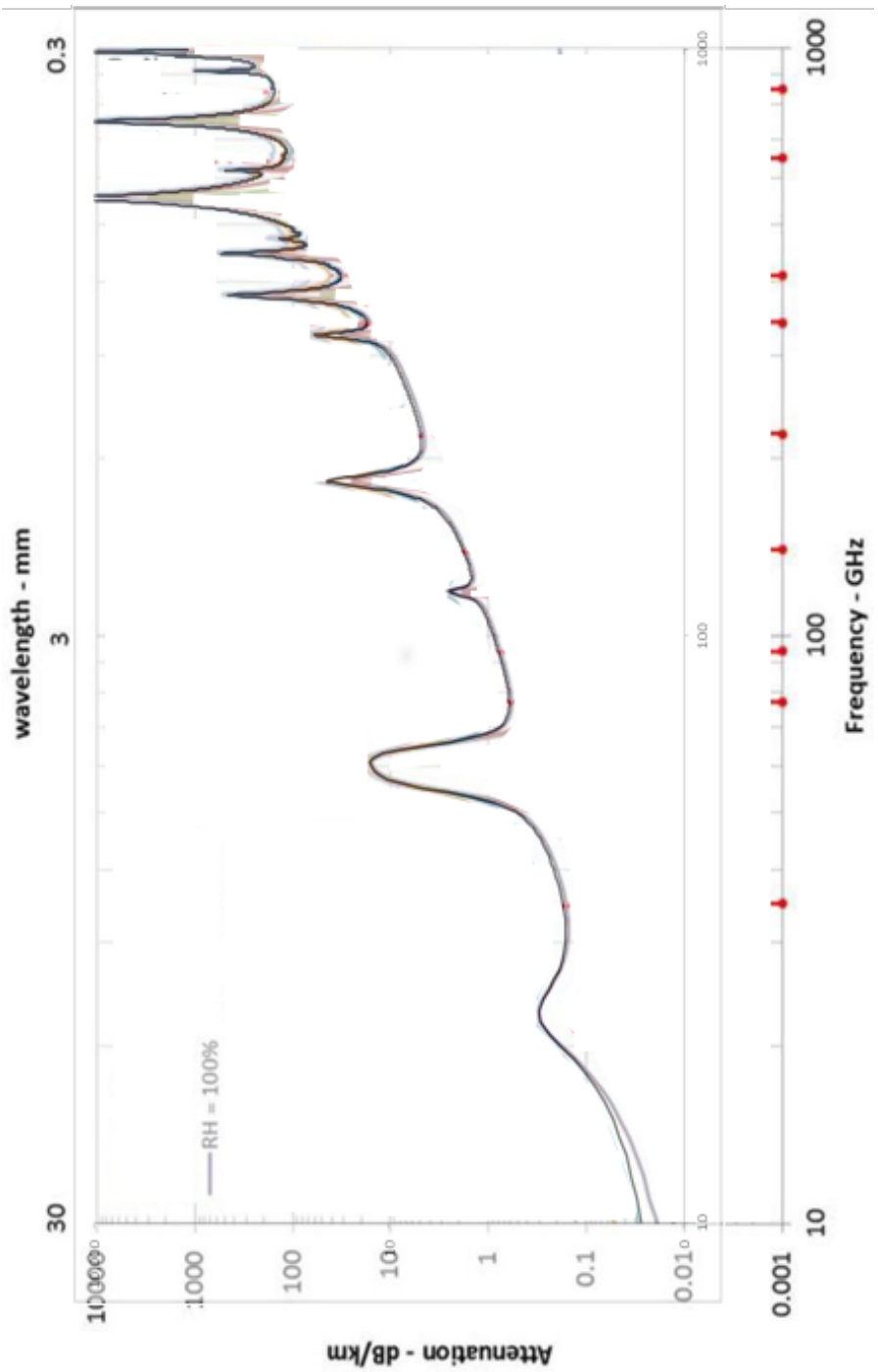

Figure 3.19 – Gaseous attenuation [dB/km] from the calculation in this study, overlaid and aligned with the gaseous attenuation chart after *Richard et.al.* [9]; showing good correlation to the 100% RH line, all other lines removed

The software library code developed in this thesis to produce these charts can be used to demonstrate other datasets. For example, Figure 3.20 shows the attenuation through the averaged Reference Standard Atmosphere at zenith for all frequencies from 1 GHz to 1,000 GHz.

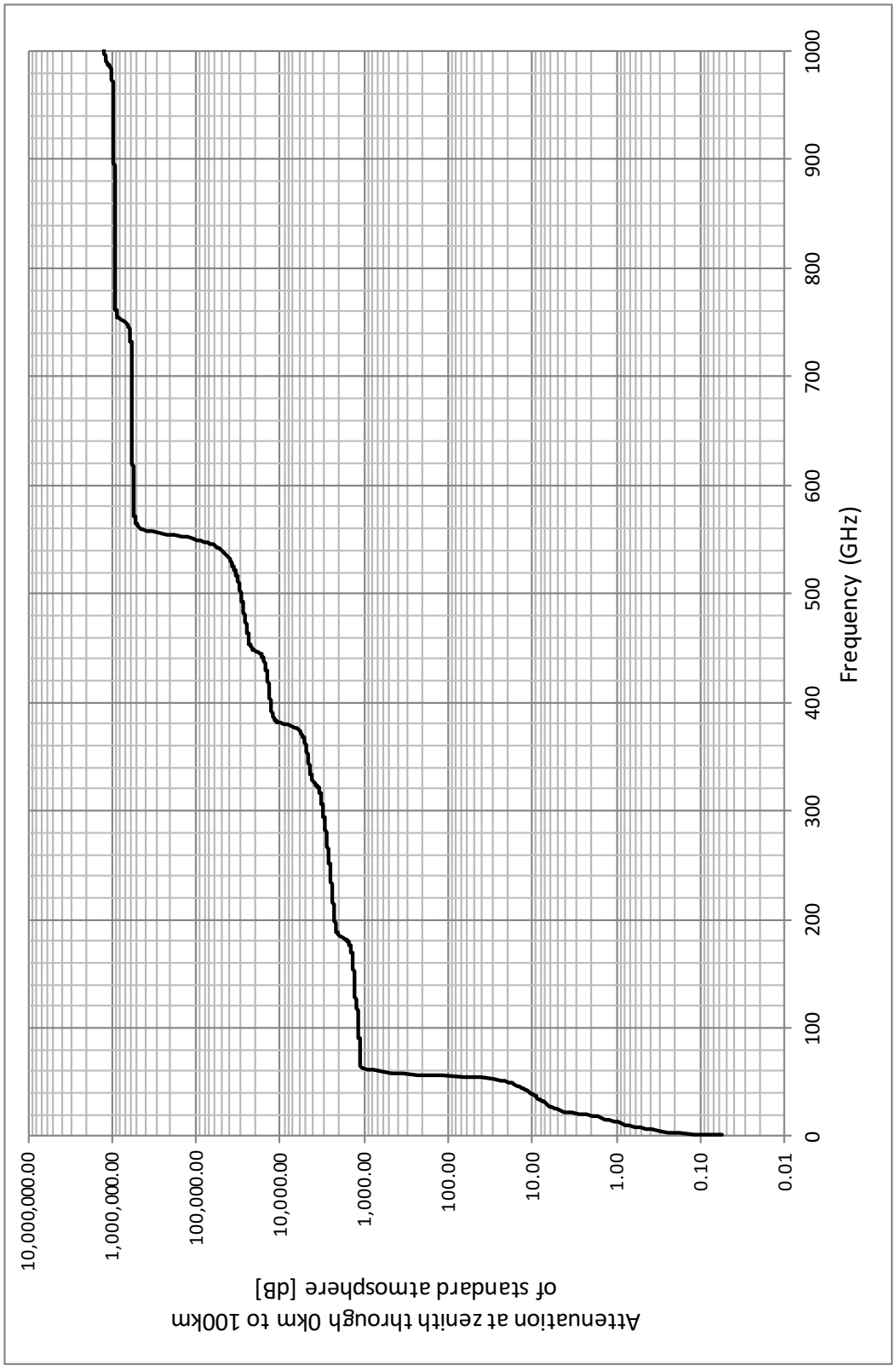

Figure 3.20 – Gaseous attenuation [dB] through 0 km to 100 km atmosphere for averaged Reference Standard Atmosphere across 1 GHz to 1,000 GHz

From the chart, it is clear that space-Earth satellite communication benefits from utilising frequencies below 63 GHz. Current satellite gateway and feeder technologies in Ka-, Q-, and (lower) V-bands all fall within this frequency range. The next progression for gateway and feeder links is clearly a move to W-band.

Interestingly, between 63 GHz and approximately 177 GHz there is very little difference in attenuation, and further, out to 370 GHz the increase in attenuation is relatively small in comparison to the dramatic difference between 1 GHz and 63 GHz.

This observation suggests that there are large regions of the higher frequency spectrum where the attenuation increase across the band is limited and may be conducive to the implementation of very wide bandwidth, very high data rate communications using technologies from the field of millimetre-wave radiometers, for example, and providing a practical growth path beyond W-band.

3.11 Free space path loss

Above 100 km the ITU-R P.2041 [4] standard assumes Free Space Path Loss (FSPL), as defined in ITU-R P.525 [10]. The following software library module interface is provided here. The equation is:

$$FSPL(dB) = 20Log_{10}Freq(MHz) + 20Log_{10}Dist(km) + 32.45 \qquad (47)$$

```
double freeSpacePathLossFunction (double pathLength, double frequency)
{
    // PARAMETERS
    //
    //  pathlength (km)
    //  frequency (GHz)
    //  Returns:
    //    free space path loss (dB)
```

3.12 Atmospheric attenuation due to clouds and fog

Calculating the value of atmospheric attenuation due to clouds and fog is difficult within a static model due to the dynamic nature of the atmosphere. An approach to

providing a consistent and comparable calculation is therefore described in ITU-R P.2041 [4]:

"*It is difficult to predict cloud attenuation from an airborne platform to space since different cloud types are at different altitudes with different vertical extents. However, a conservative approach is to assume the cloud base is at the rain height specified in Recommendation ITU-R P.839* [6] *and the cloud top is at 6* km.

Compute the cloud attenuation per Recommendation ITU-R P.840 [11] *as follows: use 100% of the total columnar content of cloud liquid water for altitudes below the rain height, 0% of the total columnar content of cloud liquid water for altitudes above the cloud top, with a linear transition of total columnar content of cloud liquid water between the cloud base and the cloud top.*"

However, this approach makes the definition of a generic model difficult as there is still a need to define or estimate the depth and altitude of clouds.

As such, the model coded in this thesis assumes clouds from the rain Height of 6.36 km (from ITU-R P.839 [6] and as described above in this Section) all the way to the ground; this being a conservative but not too restrictive estimate that can be scaled if required by likelihood of rain or fog (probability of exceedance – see Figure 3.21) and by the percentage of the path that is within cloud.

The other parameter required for the calculation of cloud attenuation is the columnar content of liquid water. In the ITU standard the probability of exceedance (Figure 3.21) defines the probability of an amount of columnar water content being exceeded over the length of a year. This is then used as the basis of the columnar water content value, which is used as described in the approach in ITU-R P.2041 [4], and noted above.

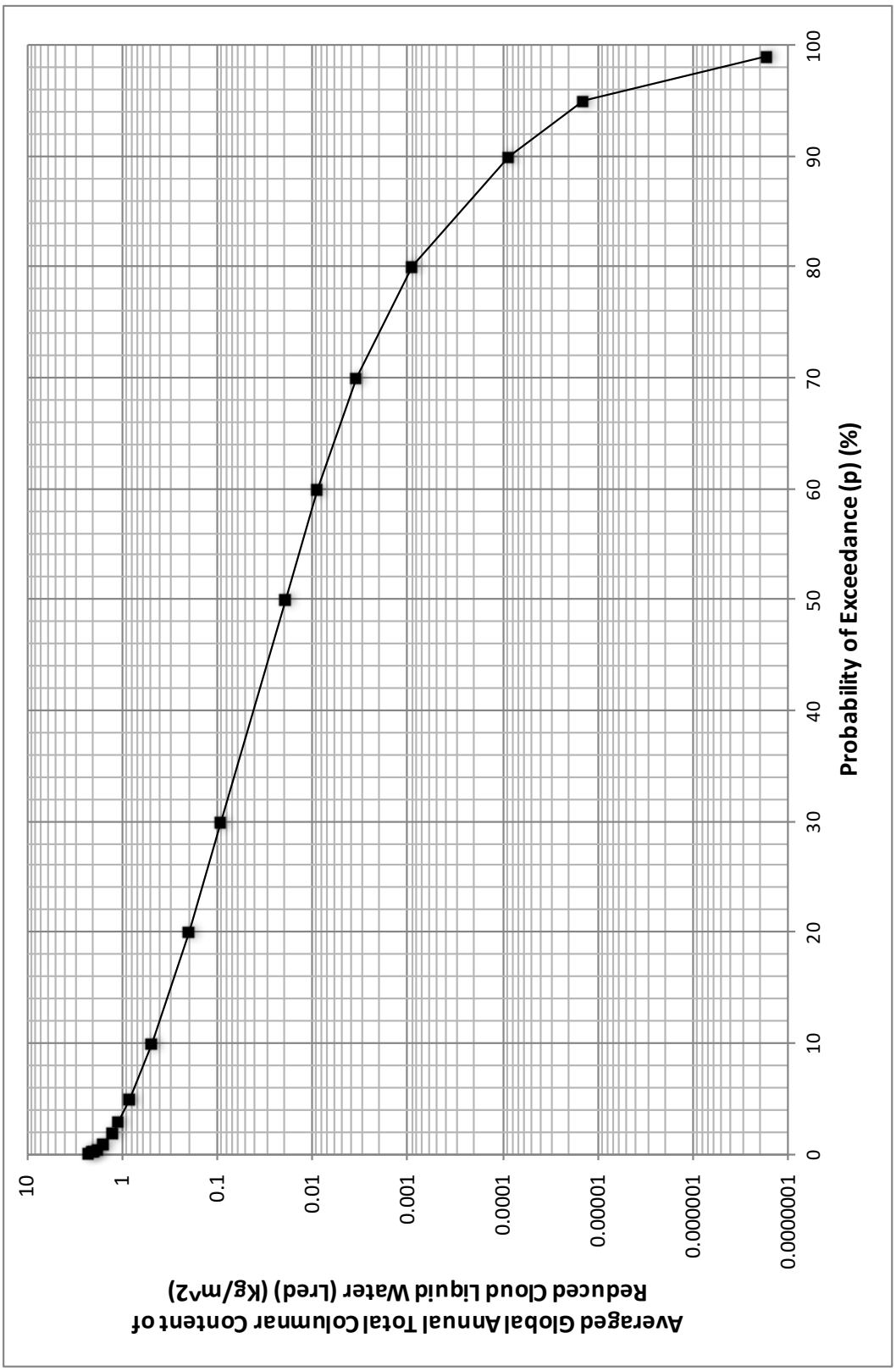

Figure 3.21 – Averaged probability of atmospheric attenuation due to clouds

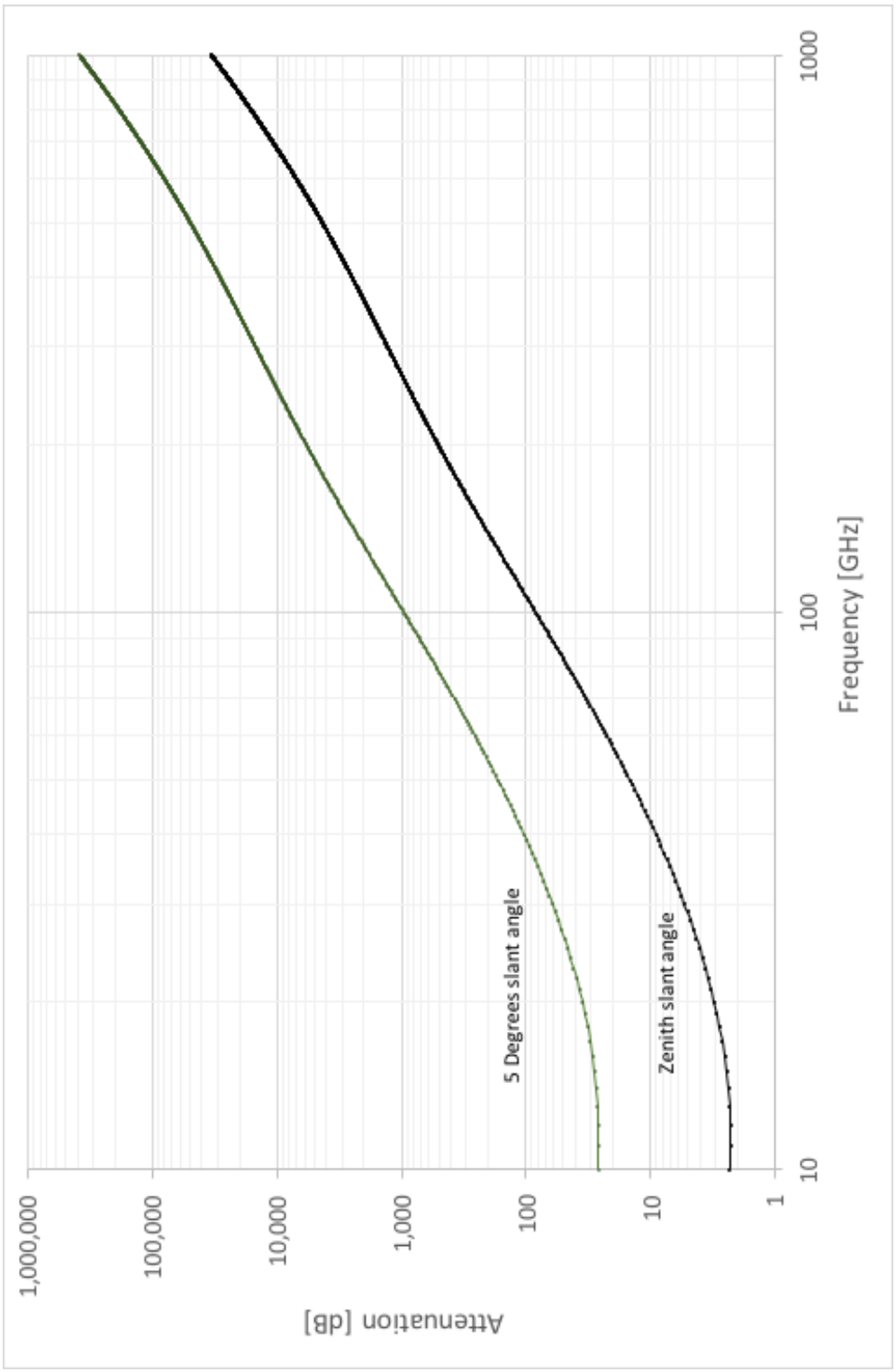

Figure 3.22 – Attenuation through clouds and fog to the rain height through 5º and zenith slant angles from Earth's surface across frequencies from 1 GHz to 1 THz at 0.1 % probability of exceedance

The basis of the calculation of attenuation due to clouds and fog is a resonance attenuation calculation caused by transmissions of a given frequency through ellipsoid dipole resonators representing the water vapour in clouds and fog. To perform the calculation defined in ITU-R P.840 [11] requires the calculation of a value '*Lred*'. This is provided in global tables of values accompanying the standard. For this thesis, the values of '*Lred*' have been mathematically averaged for the global dataset.

From these values, and implementing the mathematical models described in ITU-R P.840 [11], the following software library module was developed. The interface to this software model is shown below. It provides the value of attenuation due to clouds and fog across the frequency range 10 GHz to 1,000 GHz, for any RF path length below the rain height. The rain height is the maximum altitude at which rain will occur and is defined above as 6.36 km, it is not the same as the height at which the air is considered 'dry'; this lies above 15.0 km.

```
double attenuationCloudsAndFogFunction (int altitude, int frequency, double
slantAngle)
{
    // PARAMETERS
    //
    //  altitude     (km)
    //  frequency    (GHz)
    //  slant angle  (degrees)
    //  returns: cloud and fog attenuation (dB)
    //
```

The above chart (Figure 3.22) plots the attenuation through clouds and fog to the rain height through 5º and zenith slant angles from Earth's surface across frequencies from 1 GHz to 1 THz at 0.1 % probability of exceedance. The chart clearly shows the potentially large attenuation effects of clouds and fog.

3.13 Calculating the slant path

Calculation of the slant path from a point in space above the Earth's surface to a point on an arc representing an altitude or orbit (Figure 3.23) can be derived using the Sine rule.

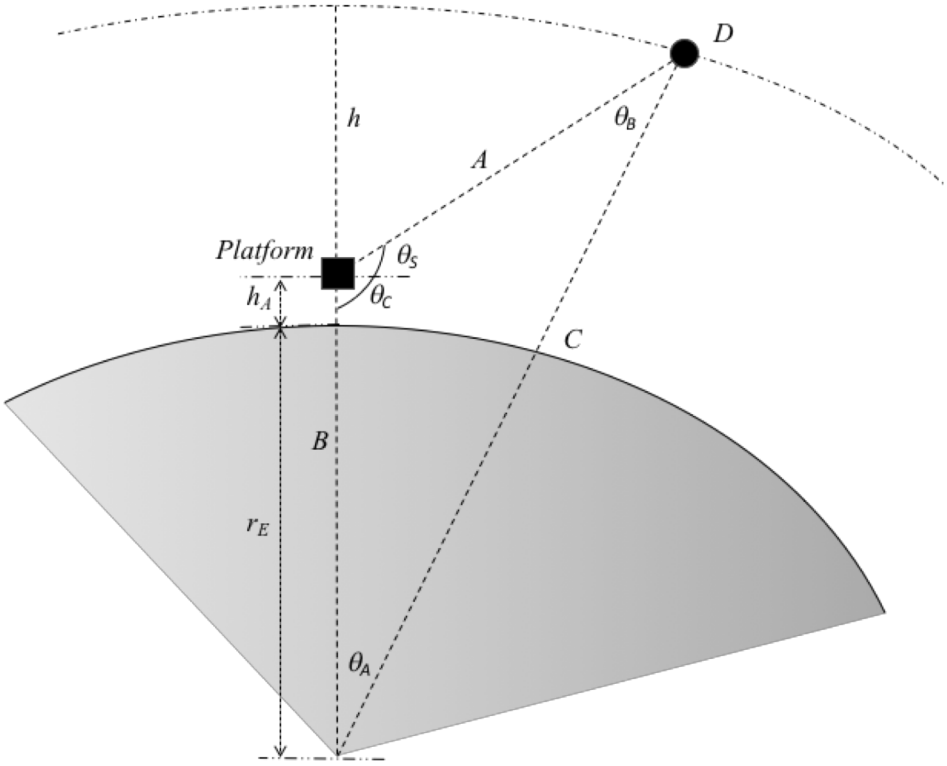

Figure 3.23 – Scenario model redrawn for the calculation of the slant angle

The slant path can be calculated using the Sine rule, with substitution of the sum of internal angles of a triangle equal to 180º :

$$\frac{A(Slant\ Path)}{Sin\ \theta_A} = \frac{r_E + h_A(Platform\ Altitude)}{Sin\ \theta_B} = \frac{C}{Sin\ \theta_C} \qquad (48)$$

Where r_E is the average radius of the Earth in kilometres (6371 km). The software module interface for this function is defined as follows.

```
double slantPathFunction (double h, double hA, double thetaS)
{
    // Parameters:
    //
    // h        altitude of altitude/orbit/satellite above the Earth (km)
    // hA       altitude of the transmitting platform (km)
    // thetaS   slant angle (deg)
    //
    // Returns:
    //    slant path (km)
    //
    // Calculation based on Sine rule
    //
```

3.14 Atmospheric attenuation due to rain

Implementing a model of atmospheric attenuation due to rain relies on data from a large number of standards and their associated datasets:

- ITU-R P.618 [5] Propagation data and prediction methods required for the design of Earth-space telecommunications systems
- ITU-R P.837 [12] Characteristics of precipitation for propagation modelling (and dataset)
- ITU-R P.838 [13] Specific attenuation model for rain for use in prediction methods
- ITU-R P.1511 [14] Topography for Earth-space propagation modelling
- ITU-R P.1144 [15] Guide to the application of methods
- ESARAIN_PR6_v5, ESARAIN_MT_v5, ESARAIN_BETA_v5 datasets [16]

As described in ITU-R P.2041 [4];

"*Rain attenuation is predicted from Recommendation ITU-R P.618* [5] *which computes the slant-path length, Ls, from hs, the height of the Earth station above mean sea level. For a path between an airborne platform and space, hs is replaced by the altitude of the airborne platform above mean sea level with the constraint that if hs is greater than or equal to hR* [the rain height]*, then the rain attenuation is 0 dB."*

The rain height *hR* - that is, the maximum altitude at which rain can occur - is defined above as *6.36 km*.

The calculation of attenuation due to rain in the ITU-R P.618 [5] standard is based on a probabilistic estimate of rainfall using global estimated rainfall datasets using the following steps. The ITU-R P.618 calculation only covers 7 GHz to 55 GHz. For the software implemented module defined for this thesis, the transmitter location is assumed to be at 45^{o} latitude.

Step 1: determine the rain height

Step 2: calculate the slant path length

Step 3: calculate the horizontal projection of the slant path

Step 4: obtain the rainfall rate exceeded for 0.01% of an average year from ITU-R P.837 [12]

Step 5: obtain the specific attenuation using the frequency dependent coefficients in ITU-R P.838 [13]

Step 6: calculate the horizontal reduction factor

Step 7: calculate the vertical adjustment factor

Step 8: calculate the effective path length

Step 9: calculate the predicted attenuation exceeded for 0.01% of an average year

Step 10: calculate the estimated attenuation

The following software library module interface provides the value of attenuation due to rain.

```
double attenuationRainFunction (int altitude, int frequency, double
slantAngle)
{
    // PARAMETERS
    //
    // frequency       = frequency (GHz)
    // altitude        = altitude of airborne platform (km)    (hS)
    // slantAngle      = elevation angle (degrees)
    // returns: Ap     = average annual fade exceeded at given percentage
(dB)
    // limits: valid only between 7GHz to 55GHz
    //
```

The following chart (Figure 3.24) plots attenuation through rain to the rain height through 5º and zenith slant angles from Earth's surface across frequencies from 7 GHz to 55 GHz.

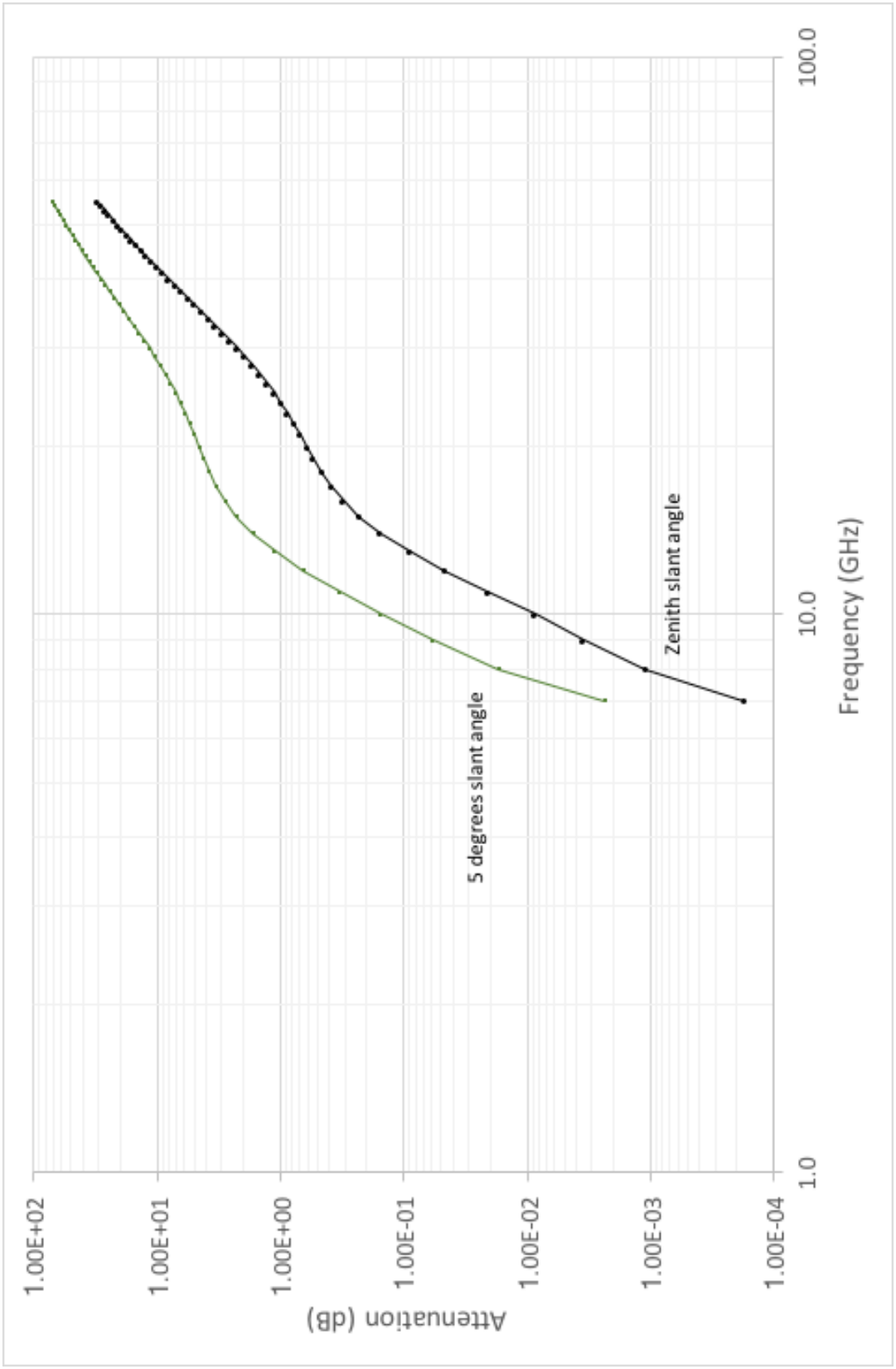

Figure 3.24 – Attenuation through rain to the rain height through 5° and zenith slant angles from Earth's surface across frequencies from 7 GHz to 55 GHz

3.15 Atmospheric attenuation due to tropospheric scintillation

Tropospheric attenuation is due to scintillation of signals traversing the turbulent tropospheric layer. Turbulence results in changes of signal refraction. The calculation of tropospheric attenuation consists of 9-steps as defined in ITU-R P618 [5]:

Step 1: For free-space elevation angles >= 5°, and for the value of *t* (the average surface ambient temperature (°C) at the site for a period of one month or longer) calculate the saturation water vapour pressure *es* (hPa) (ITU-R P.453 [17])
Step 2: Compute the wet term of the radio refractivity, *Nwet*, corresponding to es, the average surface temperature (*t)* and the average surface relative humidity (*H)* (N-units) (ITU-R P.453 [17])
Step 3: Calculate the standard deviation of the reference signal amplitude
Step 4: Calculate the effective path length
Step 5: Estimate the effective antenna diameter
Step 6: Calculate the antenna averaging factor
Step 7: Calculate the standard deviation of the signal for the applicable period and propagation path
Step 8: Calculate the time percentage factor, *a(p)*, for the time percentage, p, in the range between 0.01 % < *p* <= 5 0%
Step 9: Calculate the fade depth

The calculation has the limitation of 7 GHz to 14 GHz frequencies only. There is an assumption in ITU-R P.618 [5] that the turbulence height is 1,000 m. The following software library module interface provides the calculation.

```
double attenTropoScintillationFunction (int frequency, double slantAngle,
double earthAntennaDiameter)
{
    // PARAMETERS
    //
    //  frequency               (GHz)
    //  slantAngle              (degrees)
    //  earthAntennaDiameter    (metres)
    //  Returns:
    //    tropospheric scintillation fade depth (dB)
    // limits: valid only between 7GHz to 14GHz
    //
```

The software calculation in this thesis implements the standard, which is only valid for frequencies between 7 GHz and 14 GHz, and for slant angles greater than 5° (Figure 3.25).

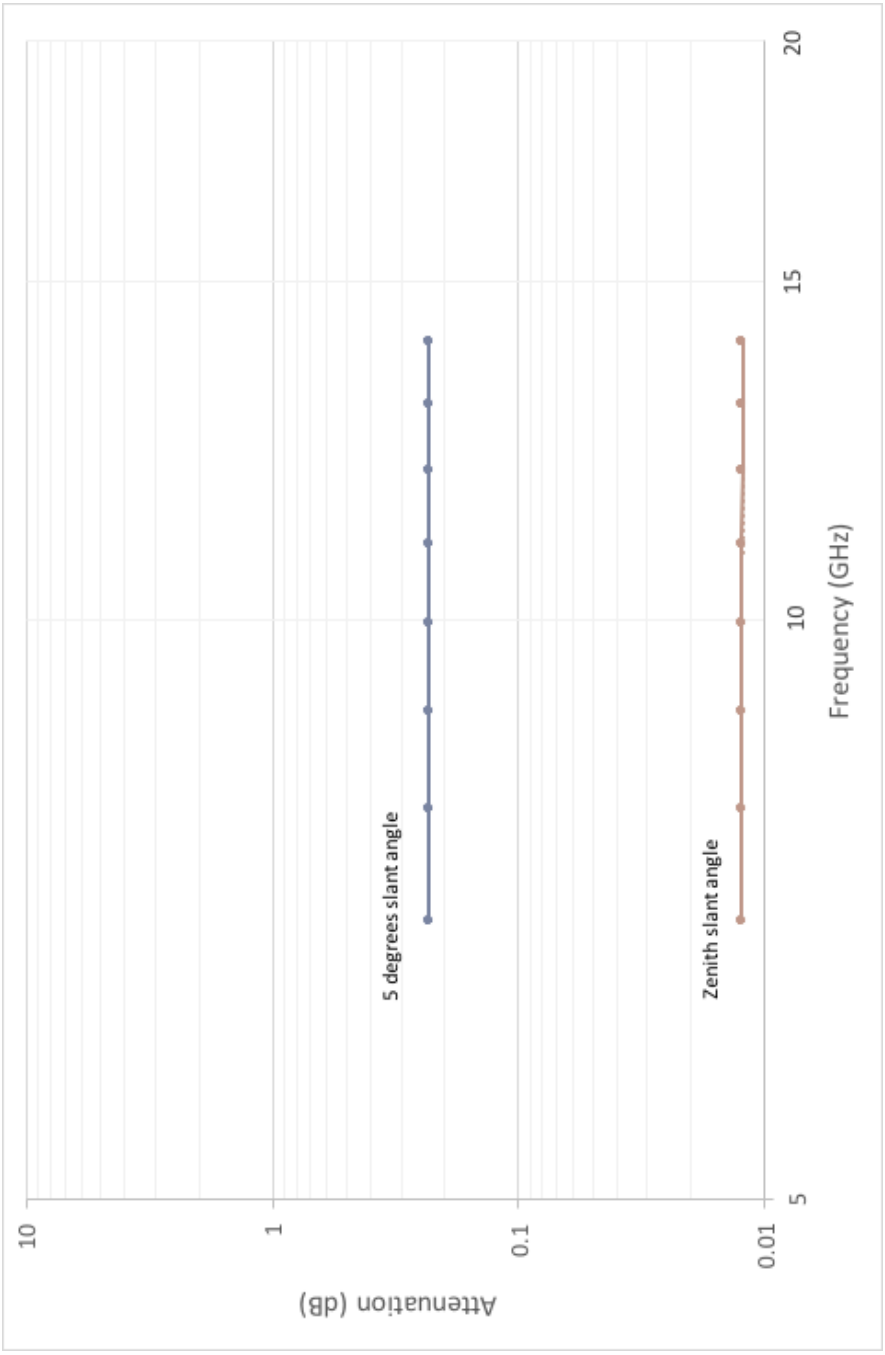

Figure 3.25 – Attenuation through the tropospheric scintillation to the turbulent height through 5° and zenith slant angles from Earth's surface across frequencies from 7 GHz to 14 GHz

3.16 Atmospheric attenuation due to Ionospheric effects

The ionosphere contains layers of ionised gases that act as reflectors and diffractors to RF signals at certain frequencies. The ionosphere covers the atmospheric regions of the upper mesosphere, the thermosphere, and the lower exosphere as described in Section 2.1. Historically, the ionospheric layers have been given the following characteristics (Table 3.1).

Label	**Altitude**	**Frequency**
D Layer	60 – 90 km	Mainly 10 MHz and below
E Layer *(Kennely-Heaviside layer)*	90 – 160 km	Mainly 10 MHz and below
Es Layer *(sporadic E layer)*	~ 100 km	Up to 50 MHz and occasionally above
F Layer *(Appleton-Barnett Layer)*	150 – 800km	Split into two layers, F1 and F2, below
F1 Layer	150 – 220 km (only during daylight. Merges into the F2 layer at night)	Mainly 10 MHz and below
F2 Layer	220 – 800 km	Mainly 10 MHz and below

Table 3.1 – Summary of the ionosphere layers and characteristics

An RF signal traversing the ionosphere encounters the effects of attenuation (due primarily to absorption), scintillation (and scattering), Faraday rotation, and delay (including propagation and group delay). The method for estimating these values is provide in ITU-R P.531 [18]. The method chosen for the calculation is described in the standard at *Section 5* on Absorption, and at *Section 4* on scintillation:

"*When direct information is not available, ionospheric absorption loss can be estimated from available models according to the (sec i)/f^2 relationship for frequencies above 30 MHz, where i is the zenith angle of the propagation path in the ionosphere. For equatorial and mid-latitude regions, radio-waves of frequencies above 70 MHz will assure penetration of the ionosphere without significant absorption.*

Measurements at middle latitudes indicate that, for a one-way traverse of the ionosphere at vertical incidence, the absorption at 30 MHz under normal conditions is typically 0.2 to 0.5 dB. During a solar flare, the absorption will increase but will be less than 5 dB. Enhanced absorption can occur at high latitudes due to polar cap and auroral events; these two phenomena occur at random intervals, last for different periods of time, and their effects are functions of the locations of the terminals and the elevation angle of the path."

"[Below 3 GHz, but occasionally up to 12 GHz] *scintillations are created by fluctuations of the refractive index, which are caused by inhomogeneities in the medium. At the receiver, the signal exhibits rapid amplitude and phase fluctuations, and modifications to its time coherence properties. Principally through the mechanisms of forward scattering and diffraction, small-scale irregular structures in the ionization density cause scintillation phenomena in which the steady signal at the receiver is replaced by one which is fluctuating in amplitude, phase and apparent direction of arrival. Depending on the modulation of the system, various aspects of scintillation affect the system performance differently. The most commonly used parameter characterizing the intensity fluctuations is the scintillation* [activity] *index S_4*"… which represents the peak to peak scintillation intensity fluctuation. As such the scintillation is represented as a fading effect. S_4 varies between the values 0 (minimum) and 1 (maximum) and is typically measured for the frequency of interest.

For simplicity, as described in the standard, S_4 falls into three categories: weak (<0.3), moderate (0.3 – 0.6), and strong (>0.6). For the model implemented here, a moderate value of 0.5 is used.

From ITU-R P.531 [18], the fade value (P_{fluc}) can be calculated for values of S_4 using the following relation:

$$P_{fluc} = 27.5\, {S_4}^{1.26} \quad \text{[dB]} \qquad (49)$$

For an S_4 value of 0.5 this corresponds to scintillation fading of P_{fluc} = 11dB. This value would be applied to all paths traversing the ionosphere below 4 GHz; where 4

GHz is the highest measured frequency in ITU-R P.531 [18], and is representative of an average value compared to application of the value out to 12 GHz, which is noted as being only an occasional situation. To manage the 4 GHz to 12 GHz region, the value of P_{fluc} is treated as reducing a *1/freq* in the model. Though this is not in the standard, it seems a reasonable approximation based on the time varying nature of the value of S_4 and the limited range of measurements over frequency.

The effects of auroral events add additional absorption of approximately 0.01 dB for events lasting <1 % of the time at mid latitudes. This based on a frequency of 1 GHz and relates only to traversal of the D and E layers of the ionosphere. The effect of auroral absorption is not captured in the library module developed here.

Polar cap absorption [18] has a similar level of attenuation, around 0.04 dB at 1 GHz, and falling roughly as $1/frequency^2$ beyond that. Again, this is not included in the library module calculation.

Scintillation causes additional attenuation and is added to the overall attenuation value based on the average peak-to-peak flux variation and assuming a frequency dependent reduction with increasing frequency.

Atmospheric propagation delay [18] adds up to approximately 250nsec to the propagation time, reducing with $1/frequency^2$ above that. Faraday rotation relates to the amount of polarisation rotation that occurs as the RF signal passes through the ionosphere.

The following software library module interface is provided for calculation of these values.

```
void attenIonosphericEffectsFunction (double frequency, double
*ionosphericAttenuation, double *faradayRotation, double *groupDelay)
{
    // PARAMETERS
    //  frequency (GHz)
    //  Returns:
    //    ionosphericAttenuation (dB)
    //    faradayRotation (degrees)
    //    groupDelay (seconds)
    // limits: applies to paths traversing 60km to 800km altitude
    //
```

The ionospheric attenuation (absorption and scintillation fading) across the frequency range 100 MHz to 100 GHz is illustrated below (Figure 3.26).

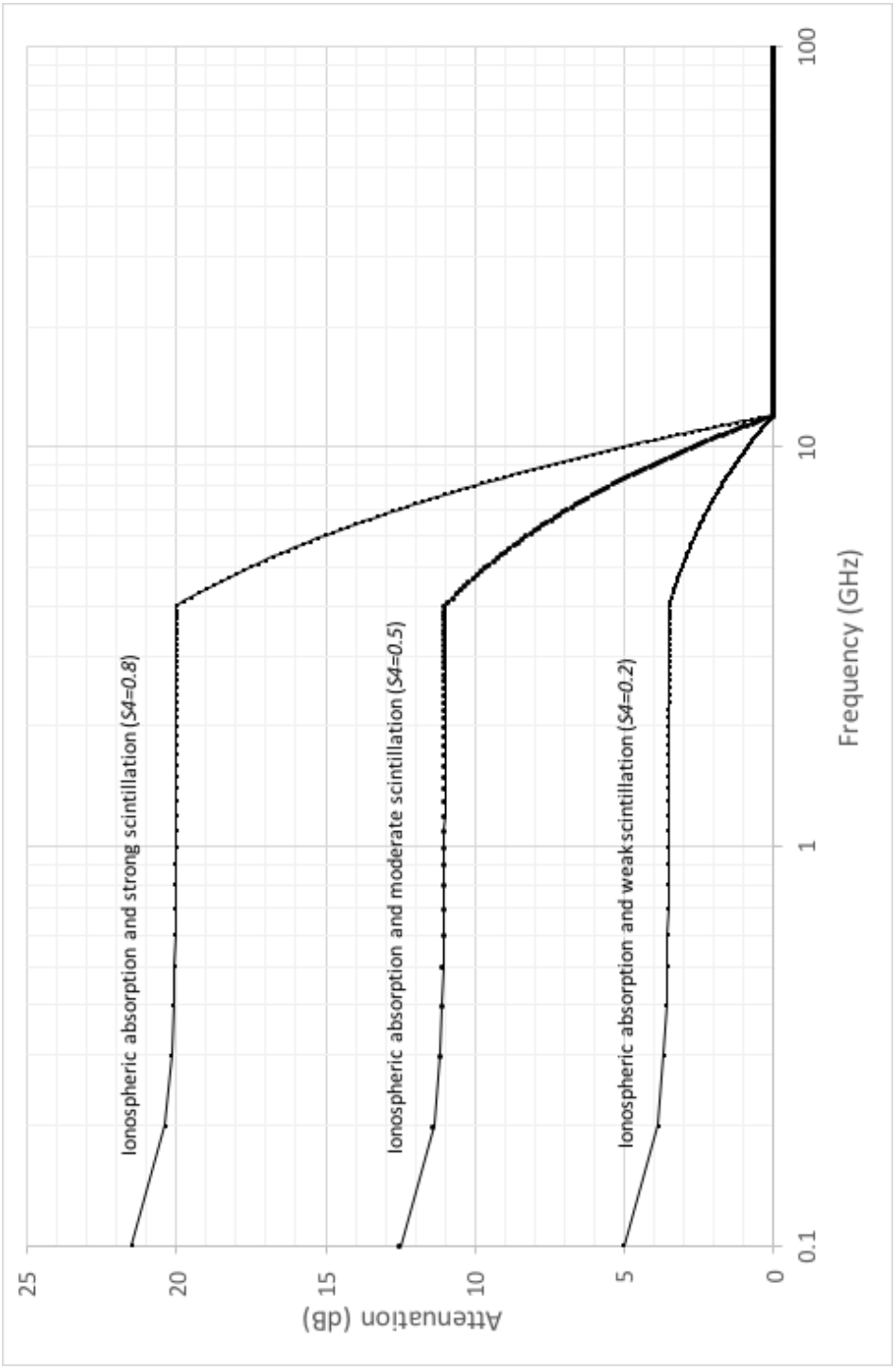

Figure 3.26 – Ionospheric attenuation from 100 MHz to 100 GHz

3.17 Effects of atmospheric refraction

Atmospheric refraction is dependent on the temperature and the pressure of the atmosphere at points through the atmosphere from ground to space. The required calculation is described in ITU-R P.453 [17], and utilises the averaged temperature and pressure (dry and wet) values determined above for whole Earth coverage and based on the tabular values from ITU-R P.835 [8].

```
double attenuationRefractionFunction (int altitude)
{
    // PARAMETERS
    //
    //  altitude    (km)
    //  Returns:
    //      radioRefractivity    (N-units)
```

The following chart (Figure 3.27) illustrates the reduction in refraction the further away from the surface the RF signal propagates: as the refractive index reduces, the signal will bend towards the surface. As the launch angle reduces to around 3^{o} above the surface, refraction can cause capture within the atmosphere.

3.18 Beam spreading loss

There are two effects that lead to spreading of the beam.

The first is caused by differential ray bending from opposite ends of an antenna as the signal wavefront propagates through the atmosphere. This problem becomes more acute at low signal elevation above the ground.

The second is that in turbulent atmospheric conditions, the rapidly changing refractive index can lead to beam spreading and scintillation. This spreading can lead to a reduction of the received energy and is hence considered as a path loss effect.

For the model developed in this thesis, neither of the two beam spreading loss effects are included; the former issue has less impact as the signal propagation angle increases from the surface, and the latter issue is dealt with in terms of refraction.

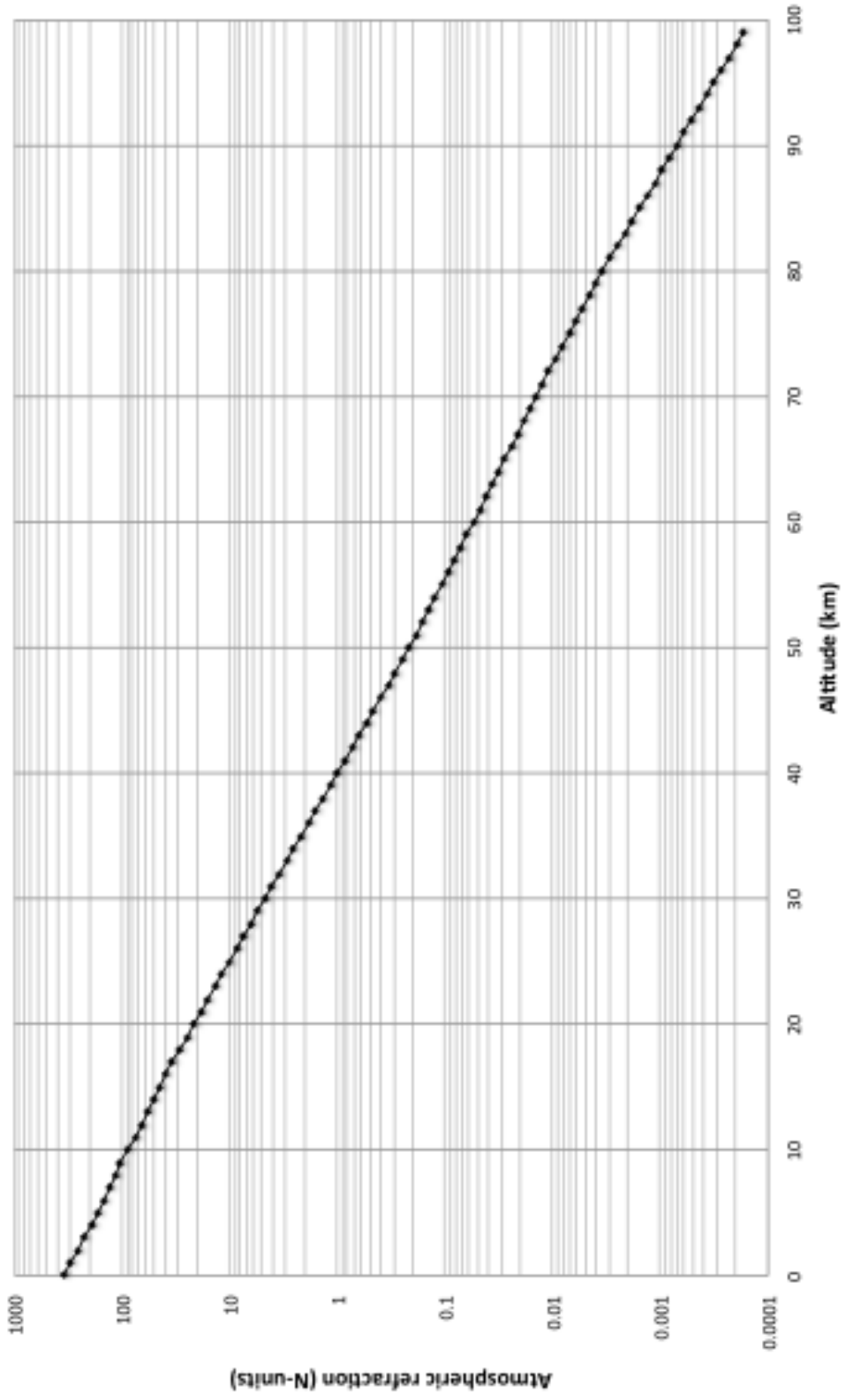

Figure 3.27 – Atmospheric refraction with altitude

3.19 Rain and ice depolarisation

Below the rain height, and at various frequencies, cross-polarisation of RF signals can occur due to the fact that rain and ice droplets aren't round. This effect occurs with rain in tropospheric RF transmission, and for microwave and mm-wave communication links, for example. The effect is important to acknowledge, but is not included in the RF modelling in this study.

3.20 RF interference due to spacecraft Electrostatic Discharge

Electrostatic discharge (ESD) events on spacecraft are caused by differential charge accumulating on surfaces as the satellite passes through the plasma surrounding the Earth, or as a result of radiation [19]. As a known problem, the effects of ESD on communications payloads are mitigated by design. The effects are therefore not included in the RF modelling in this study.

3.21 Ground multi-path

When a ground based receiver is pointing at low elevation angles, signals from aircraft or spacecraft can suffer multi-path fading due to a ground reflected signal subtracting from the direct signal at the receiver. The effect can be mitigated in many ways, including utilisation of higher elevation angles, baffles, directional antennas, and diversity antenna configurations, for example.

At higher mm-wave frequencies, the wavelength begins to match that of the structure of the material, or of debris and misalignments of the material surface. This has an effect on the attenuation model for reflection and also impacts polarisation loss due to randomisation of rotation.

Effects of this form of ground multi-path are not included in the RF model developed in this study.

3.22 Doppler

For GEO satellites the Doppler effect on the frequency is small due to the minimal differential motion. However, in the LEOP (Launch and Early Operations) phase, where the satellite has been launched to a geosynchronous transfer orbit (GTO), and is engaged in orbit raising to GEO, the RF signal Doppler can be relatively high. At LEO and MEO orbits, the Doppler relative to a ground station is similarly high.

The frequency shift due to Doppler can be calculated as:

$$\Delta f = \frac{\Delta v \times f_0}{c} \qquad (50)$$

Where:

Δf = measured Doppler frequency [*Hz*]

Δv = relative velocity between transmitter and receiver [m/s]

f_0 = transmit frequency [*Hz*]

c = speed of light [$3x10^8$ *m/s*]

From the work on available frequencies, the uplink, downlink and cross-link frequencies are known, the relative velocity can be arrived at by considering the orbital mechanics.

In a straightforward elliptical orbit around Earth (with no perturbations, for example), the orbit can be described using Kepler's Third law.

$$a^3 = \frac{\mu}{\rho^2} \qquad (51)$$

Where:

a = Semi major axis distance between the two bodies [*km*]

μ = Earth geocentric gravitational constant [3.986005 x10^{14} m^3/s^2]

ρ = Mean motion of the satellite [*radians/s*]

To calculate the mean motion of the satellite for GEO, substitute the GEO altitude of 35,786km plus the radius of the Earth at an average of 6,378km into the equation of Kepler's Third Law.

$$\rho = \sqrt{\frac{\mu}{a^3}} = \sqrt{\frac{3.986005\times10^{14}}{(35786+6378)^3}} = 7.292 \times 10^{-5}\ [radians/s] \qquad (52)$$

Alternatively, this can be calculated using Newton's Laws of Motion to derive the scalar value of satellite orbital velocity *v*.

$$v = \sqrt{\frac{G.M_E}{a_m}} \qquad (53)$$

Where:

v = Satellite orbital velocity [m/s]

G = Gravitational constant [6.67x10^{-11} Nm^2/kg^2]

M_E = Mass of the Earth [5.98 x10^{24} kg]

a_m = Semi major axis distance between the two bodies [m]

Which, for a median LEO orbit of 1,000km, gives the requirement for a satellite to maintain a velocity of:

$$v = \sqrt{\frac{6.67\times10^{-11} \times 5.98\times10^{24}}{(6378+1000)\times1000}} = 7{,}352.65\ [m/s] \qquad (54)$$

Given the orbital velocity *v* and assuming that the angle from the receiver to the transmitter is proportional to $\cos(\theta)$, then we can relate the Doppler frequency to the orbital velocity as:

$$\Delta f = \frac{v \times f_0}{c} \times \cos(\theta) \qquad (55)$$

Which can be plotted (Figure 3.28) for typical uplink frequencies (for example 2 GHz C-band), and for typical median orbital altitudes of LEO (1,000 km) and MEO (18,893 km).

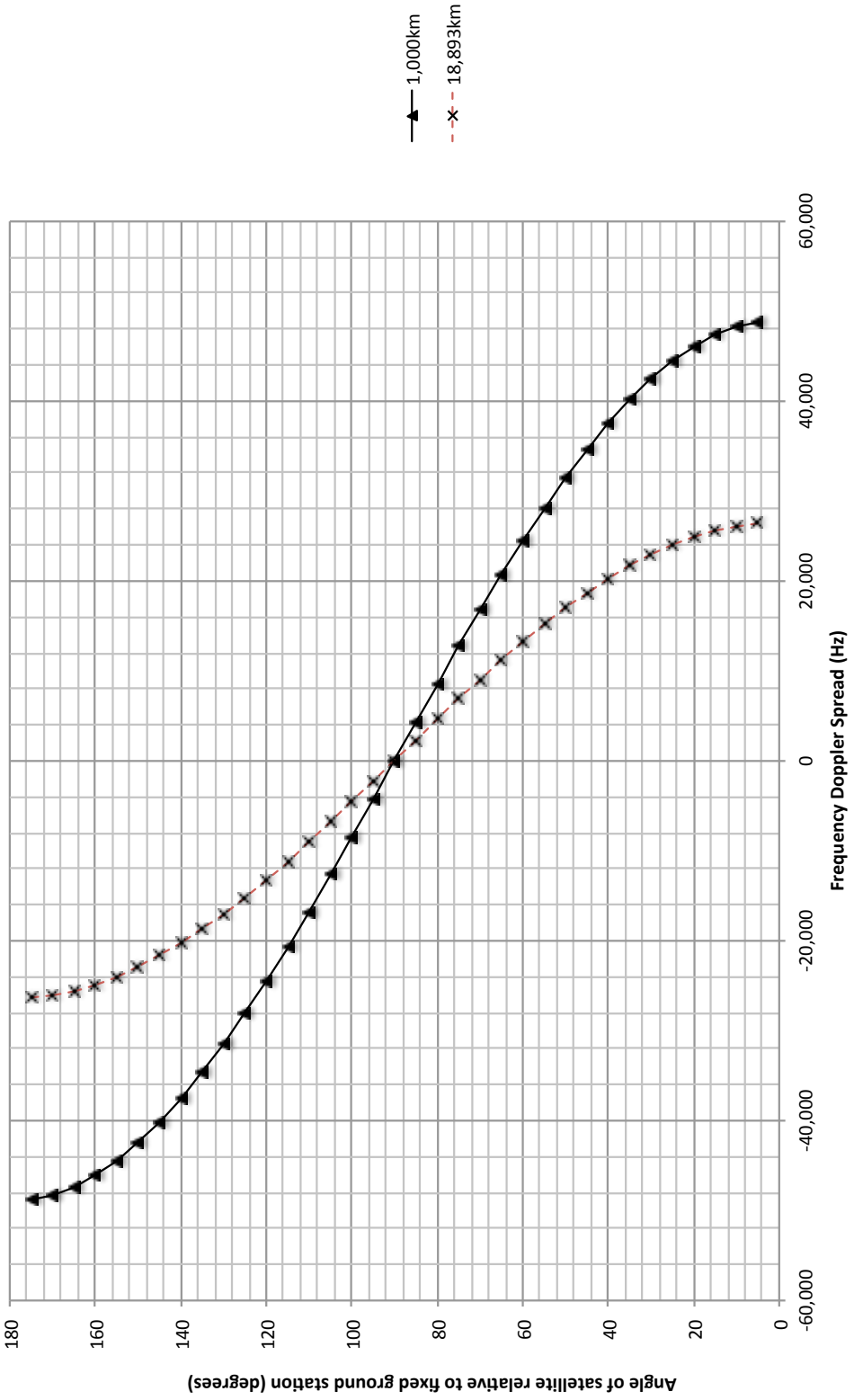

Figure 3.28 – Frequency Doppler spread for satellite operating at 2 GHz at median orbital altitudes of LEO and MEO

3.23 RF Channel Model

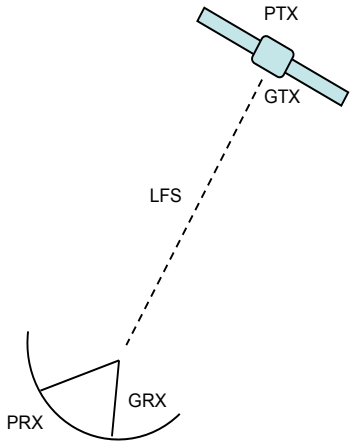

Figure 3.29 – Diagrammatic view of the satellite to ground RF channel

The power at the receiver in the above illustration (Figure 3.29) is expressed as (*Dalgleish* [20]):

$$P_{RX} = P_{TX} + G_{TX} - L_{TX} - L_{FS} - L_M + G_{RX} - L_{RX} \qquad (56)$$

Where:

P_{RX} = Received power [dB]

P_{TX} = Transmit power [dB]

G_{TX} = Transmit antenna gain [dBi]

L_{TX} = Transmit losses [dB]

L_{FS} = Path loss (typically Free Space Path Loss) [dB]

L_M = Losses (fading, shadowing, polarisation, …) [dB]

G_{RX} = Receive antenna gain [dBi]

L_{RX} = Receive losses [dB]

To illustrate this and consider some of the issues around the channel model, consider a typical Ku-band GEO satellite downlink transponder. For this example, assume a frequency of 11.7 GHz with a transponder output power (from the amplifier: usually a Travelling Wave Tube Amplifier TWTA or Solid State Power Amplifier SSPA) of 25 W. Further suppose that the satellite has a 20 dBi antenna gain with 2 dB feeder losses. With a ground station, 38,000 km from the satellite, and with a 15 m diameter receive antenna with 55 % efficiency, and a low noise receive amplifier with a noise temperature of 100 K.

In this example assume the path has Free Space Path Loss. In such a scenario, what would be the available Signal (Carrier) -to-Noise (C/N) at the receiver? Such a calculation is shown below.

$$Transmit\ power\ (P_{TX)}) = 10\ Log_{10}25W = 14\ dBW \quad (57)$$

$$Equivalent\ Isotropically\ Radiated\ Power\ (EIRP) = 14dBW + 20dB - 2dB \quad (58)$$

Then EIRP is:

$$EIRP = 32dBW = 62dBm \quad (59)$$

Converting frequency to wavelength:

$$\lambda = \frac{3 \times 10^8\ m/s}{11.7 \times 10^9\ Hz} = 0.0256m \quad (60)$$

Calculating the Free Space Path Loss (FSPL):

$$FSPL = 20Log_{10}\frac{(4\pi d)}{\lambda}\ [dB] \quad (61)$$

Where:

d = Distance between the transmitter and receiver [m]
λ = Wavelength [m]

Substituting values:

$$FSPL = 20Log_{10}\frac{(4\pi\ 38 \times 10^6)}{0.0256} = 205.4\ dB \quad (62)$$

To calculate the received power we use the equation for the gain of an antenna.

$$G_{RX} = \frac{4\pi}{\lambda^2}A_e.E_{ff} \quad (63)$$

Where:

A_e = Effective aperture area [m^2]
E_{ff} = Antenna efficiency [%]

Using,

$$A_e = \frac{\pi(diameter)^2}{4} = \frac{\pi 15^2}{4} = 176.715\ m^2 \quad (64)$$

And substituting above, the receive antenna gain can be determined.

$$G_{RX} = \frac{4\pi}{(0.0256)^2}\ (176.715).(0.55) = 62.7\ dB \quad (65)$$

Combining the values calculated above, the received power (P_{RX}) is given by,

$$P_{RX} = Transmit\ EIRP - Path\ loss + Receiver\ gain \quad (66)$$

Which is,

$$P_{RX} = 62dBm - 205.4\ dB + 62.7\ dB = -80.7\ dBm \quad (67)$$

The receiver thermal noise is calculated from the equation below,

$$N_{RX} = Boltzmann's\ Constant\ .Temp \quad (68)$$

Which gives,

$$N_{RX} = 1.38 \times 10^{-23}\ .100K = -208.6\ dBW/Hz \quad (69)$$

Converting to dBm,

$$N_{RX} = -178.6\ dBm/Hz \quad (70)$$

Therefore, the available margin for the data signal is given by,

$$C/N = Signal\ [dB] - Noise[dB] \quad (71)$$

Which is,

$$C/N = -80.7\ dBm - (-178.6\ dBm/Hz) = 97.9\ dB\ Hz \quad (72)$$

Note that the result is bandwidth dependent. If we now want to calculate the available modulation margin, we subtract the required energy per bit as a ratio to the noise in that bandwidth (E_b/N_o) for that modulation scheme. In our example, let us assume that the required E_b/N_o to provide a data rate of 36Mbps is 20dB for 16-QAM modulation and ¾ coding. We then calculate the maximum channel noise that the system can tolerate as shown.

For an E_b/N_o= 20dB, the margin is reduced, leaving the following maximum channel noise.

$$Maximum\ channel\ noise = Signal\ margin - Required\ E_b/N_o$$

$$= 97.9\ dB\ Hz - 20dB = 77.9\ dB\ Hz$$

Since, no bandwidth has been defined for this example, the result is bandwidth dependent.

Finally, if we assume an 8dB fade margin and a typical wideband -90dB receiver threshold we can calculate the link margin, and the link margin with fade margin as follows.

$$Link\ margin = Receive\ power - Receive\ sensitivity \tag{73}$$

We have that,

$$Link\ margin = -80.7dBm - (-91dB) = 10.3dBm \tag{74}$$

Including the fade margin, we have,

$$Link\ margin = 10.3dBm - 8dB = 2.3\ dBm \tag{75}$$

For the RF channels in the satellite systems described in this study, the fade margin and path loss can be replaced by values calculated using the software implemented ITU-R P.2041 model. The above example, therefore, illustrates a generic RF satellite channel example on which other calculations can be constructed.

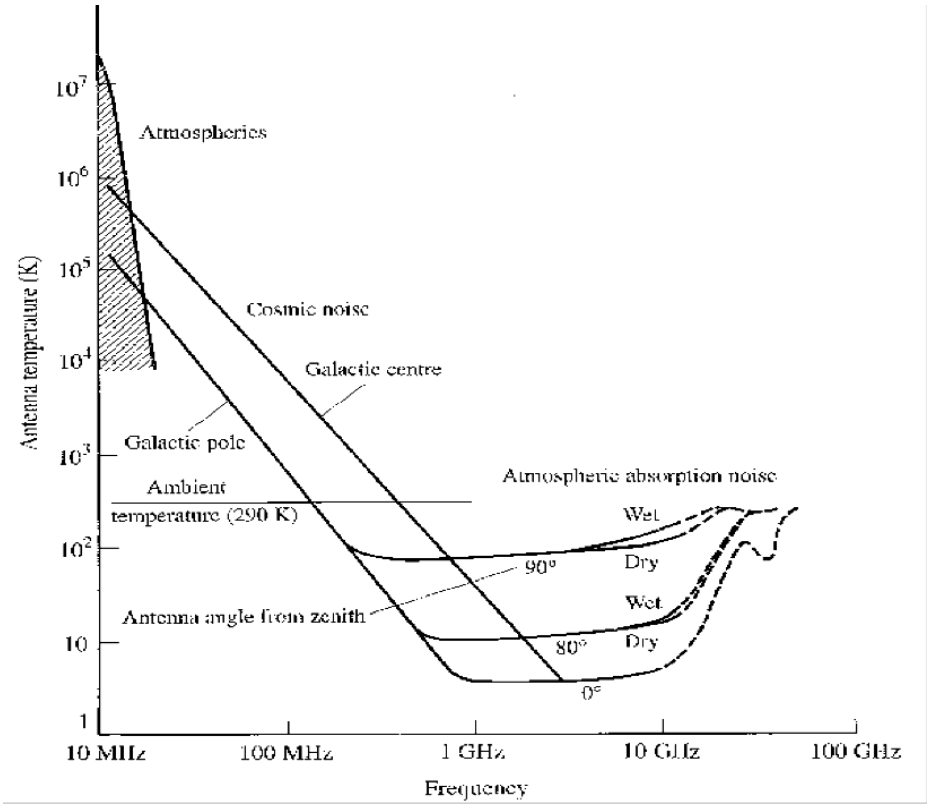

Figure 3.30 – Chart illustrating noise from galactic sources, cosmic rays and other sources (after *Kraus* [21]).

The antenna noise temperature is defined as any noise that is within the 'view' of the antenna beam. For antennas pointed at the Earth or planets, this results in additional noise from the 273K (average) Earth temperature. For antennas pointed at space, there are a number of other noise sources that must be taken into account in the antenna temperature (Figure 3.30).

3.24 G/T

A useful measure of performance for satellite communications, and in particular in understanding the performance of transponders, is defined as gain over noise temperature, or G/T. Defined as follows [17].

$$\frac{G}{T} = \frac{\left[\frac{G_{RX}}{L_R L_{FRX} L_{POL}}\right]}{\frac{T_A}{L_{FRX}} + T_F\left(1 - \frac{1}{L_{FRX}}\right) + T_R} \quad [K^{-1}] \qquad (76)$$

Where:

G_{RX} = Receive antenna gain

L_R = Antenna and cable losses at the receiver

L_{FRX} = Approximately, the front end receiver loss

L_{POL} = Receiver polarisation loss

T_A = Antenna noise temperature [K]

T_F = Ambient temperature of the RF front end [K]

T_R = Ambient temperature of the receiver [K]

The value of T_A is the sum of T_{Sky}, T_{Ground} and $T_{Atmosphere}$. T_{Sky} is typically between 20 K to 100 K for S band up to K band. T_{Ground} is approximately *10K* for signal receive elevations of 10° *to* 90° above the horizontal. And $T_{Atmosphere}$ is typically rain dominated, which for temperate climates is around 10 K, and for clear skies is treated as 0 K. In general, then define T_A = 50+10+0 = 60 K

Since the antenna noise temperature includes the noise aperture of everything in the field of view of the antenna, this can include the sun (as high as 12,000 K) and moon (270 K at around 4 GHz). It can also include ground noise picked up in the antenna side lobes (as noted in the above calculation).

In general, we can simplify the G/T equation by expressing it in dB, and using typical values of L_{FRX} = 1 dB, T_A = 60 K, T_F = 290 K, T_R = 290 K.

$$G/T = G_{RX} - L_R - 10\text{LOG}_{10}(290/10^{0.1} + 290.(1\text{-}1/10^{0.1})\text{+}290) \quad \text{[dB/K]} \qquad (77)$$

$$G/T = G_{RX} - L_R - 27.63 \quad \text{[dB/K]} \qquad (78)$$

Then, for the example described previously, the value of G/T is given as follows.

$$G/T = 62.7 - 3 - 27.63 = 32 \quad \text{[dB/K]} \qquad (79)$$

3.25 Discussion

One of the main criticisms that can be levelled at this Section is that there is no formal proof that the implementations defined in this Section, and the software provided in Appendix A are accurate and complete. This is an issue for the ITU-R standards since there is no pro-forma test suite to show correct implementation.

In an attempt to show some level of accuracy of implementation of the equations and algorithms, a comparison between the modelled gaseous attenuation (using the software code in Appendix A) was made against a published version of the same calculation (after *Richard* [6]) as illustrated in overly in Figure 4.7.

The remainng implementations, for fog, rain, clouds, tropospheric and ionospheric scintillation have been checked line-by-line between the code and the textual descriptions of the algorithms in the ITU-R standards.

3.26 Discussion of model accuracy

The lack of pro-forma test data to confirm an implementation of the ITU-R standards is a considerable oversight by the standards working group, and although WG3 (Working Group 3) does publish a dataset for gaseous absorption, there is not enough information in the dataset to make a comparison to an implementation of the ITU-R standard. The situation for the other atmospheric modelling standards, such as

those for clouds, fog, rain, ionospheric and tropospheric scintillation is equally frustrating with no datasets available. In the literature, it was found that ESA (European Space Agency) had sponsored work to derive pro-forma datasets for confirmation of implementation of the ITU-R standards, but these results appear to no longer be supported and were not accessible. The only method to provide at least some level of confidence in the implementation of the ITU-R standard was to overlay plots of the generated data with those produced by others, this is the method used to demonstrate correct implementation of the gaseous absorption standard in the thesis, though it was quickly found that many authors in the literature do not include sufficient detail of the parameters used to create their results. Differences in pressure, density, water vapour etc. all play a part, and comparison is not possible if these values are not given in the literature. In conclusion therefore, the implementation of the ITU-R standards for space-Earth communication provided in this thesis is as accurate as can be given these constraints. The main purpose of the standards in this thesis is to provide consistent results for comparison of techniques, and the implementation achieves this with realistic results being produced.

3.27 Summary and conclusion

The first part of this section derived data sets for the typical altitudes and orbits of satellites and high altitude platforms, along with the regulator defined frequencies for upink (to the platform) and downlink (from the platform).

The RF model described in this Section covers a frequency range of 100 MHz to 1 THz for gaseous absorption, and with limits as described in the standards, provision of attenuation for clouds, fog, rain, tropospheric and ionospheric absorption and scintillation, for the region from 5^{o} above the horizon to zenith, for Earth based, aircraft or satellite RF systems.

The following software library functions (Table 3.2) have been developed. The implementation software code is provided as Appendix A to this thesis.

Free Space Path Loss	`double freeSpacePathLossFunction (double pathLength, double frequency)`
Gaseous attenuation	`double attenuationGaseousFunction (double altitude, double frequency, int testMode)`
Attenuation due to clouds and fog	`double attenuationCloudsFunction (int altitude, int frequency, double slantAngle)`
Attenuation due to rain	`double attenuationRainFunction (int altitude, int frequency, double slantAngle)`
Tropospheric scintillation	`double attenTropoScintillation FunctionWithAltitude (int frequency, double slantAngle, double earthAntennaDiameter)`
Ionospheric attenuation, scintillation, polarisation rotation, and group delay	`void attenIonosphericEffectsFunction (double frequency, double *ionosphericAttenuation, double *faradayRotation, double *groupDelay)`
Atmospheric refraction	`double attenuationRefractionFunction (int altitude)`

Table 3.2 – Summary of software library function for Earth-space RF calculations

As a result of this work a model has been formed upon which to test concepts.

References

[1] "United Nations Register of Space Objects", A/AC.105/INF.1-419,421 and ST/SG/SER.E/1-629, Thirteenth edition, December 2011, and online updates to 2016

[2] "Collection of the basic texts of the International Telecommunication Union adopted by the Plenipotentiary Conference", ITU, Edition 2015

[3] Edwards, C., "Mars Network: An Orbital Relay Infrastructure for Mars Exploration", DESCANSO seminar, 17 September 2003

[4] "Prediction of path attenuation on links between an airborne platform and Space and between an airborne platform and the surface of the Earth", Recommendation ITU-R P.2041

[5] “Propagation data and prediction methods required for the design of Earth-space telecommunication systems”, Recommendation ITU-R P.618

[6] “Rain height model for prediction methods”, Recommendation ITU-R P.839

[7] “Attenuation by atmospheric gases”, Recommendation ITU-R P.676

[8] “Reference standard atmospheres”, Recommendation ITU-R P.835

[9] Richard, M., et. al., “Optical up-conversion enables capture of millimetre-wave video with an IR camera”, 13 August 2012, SPIE Newsroom. DOI: 10.1117/2.1201208.004406

[10] “Calculation of free-space attenuation”, Recommendation ITU-R P.525

[11] “Attenuation due to clouds and fog”, Recommendation ITU-R P.840

[12] “Characteristics of precipitation for propagation modelling”, Recommendation ITU-R P.837

[13] “Specific attenuation model for rain for use in prediction methods”, Recommendation ITU-R P.838

[14] “Topography for Earth-to-space propagation modelling”, Recommendation ITU-R P.1511

[15] “Guide to the application of the propagation methods of Radio Communication Study Group 3”, Recommendation ITU-R P.11449

[16] “ESARAIN_PR6_v5”, “ESARAIN_MT_v5”, “ESARAIN_BETA_v5”, ITU-R Recommendation datasets available on-line

[17] “The radio refractive index: its formula and refractivity data”, Recommendation ITU-R P.453

[18] “Ionospheric propagation data and prediction methods required for the design of satellite services and systems”, Recommendation ITU-R P.531

[19] “Space engineering: Calculation of radiation and its effects and margin policy handbook”, European Space Agency, ECSS-E-HB-10-12A, 17 December 2010

[20] Dalgleish, D., I., “An introduction to satellite communication”, IEE, Peter Perigrinus, 1991, ISBN 0 86341 132 0

[21] Kraus, J. D., “Radio astronomy”, 1986

Chapter 4

Non directional Low Earth Orbit System Deployment

4.1 Improving spectrum efficiency and capacity

Building from the literature review, the derived information in Sections 2 and 3, and using the modelling software developed in Section 4, in this Section is explored techniques that could improve spectrum efficiency and capacity in the high altitude low orbit environment.

Several experimental models were constructed using standard modelling tools in order to test the hypothesis that some form of 'layered' frequency re-use could be contrived in the high altitude low orbit region.

The first experimental model considered the basic RF environment, and the suitability of simulation tools to progress an analysis of more complex ideas and implementations.

The second experimental model developed a correlation approach by recasting GNSS in signal timing terms rather than the more common position timing approach. Then, along with utilising a little-known approach from radar technology, combining them in what can loosely be termed 'reverse GPS'.

The third experimental model built on the 'reverse GPS' technique with the identification of the need for directional antennas. This succeeded in being able to produce spatial cellular patterns with spectrum re-use; an improvement over the initial aim of the investigation which was to provide increased spectrum efficiency and capacity using only layered spectrum re-use.

Then, based on the findings in the experimental models, and using information from Section 2 and Section 3, a number of approaches to the problem of multiple access

and the problem of managing spectrum re-use of these spatial cells was identified and compared in a trade-off study: comparing performance against a set of metrics.

The best candidate solution identified in the study was further tested by modelling of the antenna pattern and consideration of the system design. The major benefit of which is being able to completely re-use spectrum at ground level with minimal interference. This unique finding is then further explored.

Finally, a description of the derived spectrum re-use solution is described and summarised in preparation for Section 6 where the model is simulated against the values derived in Section 3 and the path loss model implemented in Section 4 as part of the discussion and summary of the work.

4.2 Discussion of potential approaches and initial work

As noted in the literature review of Section 2.8, though being part of the same spectrum, there are only two techniques that can realistically be used to transmit information. These are identified as RF and the various wavelengths of light.

RF communication is long established as a key technology for Earth-space and space-aircraft communication. The benefits of RF are:

- mature technology (components and mechanisms are available in nearly all the usable bands);
- largely weather independent;
- one-to-one or one-to-many (broadcast) link capable;
- foliage, building and platform structure penetrating at some frequencies.

Optical communication, in particular laser optical inter-satellite links (OISL) and laser optical links to ground, are a relatively new technology in comparison to RF, though research in the field has been continuing for many years and is rapidly advancing. The benefit of laser optical communication is the very high data rate it can support due to the high energy density compared to RF. However, there are

many issues that make the approach less attractive than RF in the context of spectrum capacity improvement, particularly for high availability communications. The main issues with optical communication are:

- acquisition time (though research efforts in this field are improving the performance);
- weather dependence and subsequent availability of communications (it is clear that 3-nines availability of signal for communications is not feasible for laser space-Earth communication due to the large diversity distances imposed by the statistical nature of cloud cover);
- limited suitability for broadcast (there is no published broadcast capable solution to date);
- direct line of sight only;
- unable to penetrate foliage, buildings (excluding windows perhaps) or structures.

A typical approach for communication to an aircraft from a satellite is to use a relatively wide-beam high-power RF connection. In the reverse direction, and to achieve high data rates within the limited physical envelope of the aircraft, directional antenna systems are used. Directional antenna systems generally take the form of gimballed dishes, or one/two axis hemispheric lens antennas, or phased array patch antennas with gimballed or phase controlled beam positioning.

Though directionality at the aircraft provides improved gain back to the satellite, it does not improve the spectrum capacity, since the spectrum typically cannot be re-used by other aircraft, or by users on the ground. Typically, the spectrum is licensed, allocated and shared. With multiple access techniques and large footprint coverage cell patterns (all the way to the ground) used to accommodate multiple aircraft in the system.

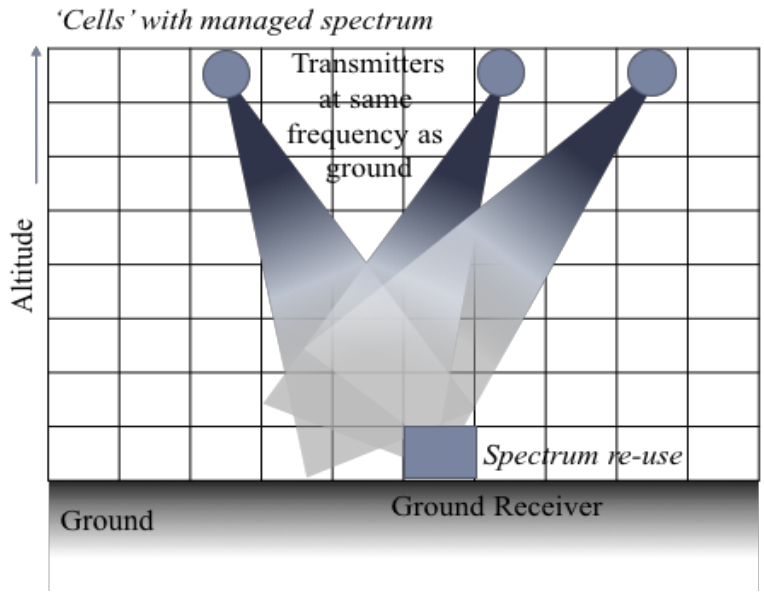

Figure 4.1 – Illustration of the general approach explored in this Section of improving spectrum capacity through managed spectrum re-use on the ground

If there were a way to create shared spectrum 'in the sky', it would need to provide isolation of spectrum to individual areas of the 'sky'. In other words, there must be a form of spatial segmentation of the medium; perhaps analogous to that achieved with ground cellular communication systems.

What would be beneficial for improved spectrum efficiency and capacity, and increased data rates for satellite-aircraft communication for example, would be the concept of a 'cells in the sky' solution where the propagation decays into the noise floor by the time it reaches the ground, facilitating full spectrum re-use at ground level (Figure 4.1).

But how to achieve this, given that the analogous ground cellular systems must have a transmitter placed centrally in each cell, will be explored in this Section.

4.3 Experiment 1 - An Initial Approach

The initial approach for this Section was to research the sort of RF environments that could be created in the high-altitude low orbit region with satellites as transmitters using models constructed in Matlab. It was clear, initially, that any form of

synchronised transmission from satellites in orbit would appear as a sparse beam-formed array and, depending on the frequency, could perhaps be 'phased' at some points in the region between the satellites and the Earth, as one might expect, to create the required spatial layers or cells.

The first experimental model developed was designed to consider the RF interaction between several satellites as they transmitted signals towards the ground.

4.3.1 Simulation model

The purpose of the first experimental model was to consider the effect of several satellite transmitters above a flat ground non-reflecting surface with transmission using free space path loss (FSPL). The signals were assumed to be orthogonal and are summed at each spatial location to provide the total received power, as though they were perfectly processsed. This was plotted to provide a view of what might be achievable with multiple satellite transmissions. The aim was to conclude whether such a coordinated set of satellite transmissions could produce a 'layered'spatial effect, as discussed in Section 1.

To support multiple simulations, and for multiple datasets to be collected, a Matlab model was coded with the following free variables (the Matlab code is provided in Appendix B):

- number of satellites
- satellite transmission frequencies
- satellite spatial positions
- receiver (nominally aircraft or UAV/RPAS) positions
- satellite transmit power
- receiver sensitivity (receiver nominally aircraft or UAV/RPAS located)

The Matlab model used a spatial partitioning approach to the simulation, dividing the simulation space into 1 km x 1 km squares.

The Matlab model was run multiple times, varying the free variables on each run. An analysis of the results is given below.

4.3.2 Results and analysis

The first set of experiments considered three satellites in orbit, 200 km apart and at 475 km orbital altitude. The Matlab model was used to calculate and summed the orthogonal signals at each point in space. The resulting RF signal strength results were plotted based on the 1 km grid basis. The Matlab code is provided in Appendix B.

For the following result (Figure 4.2) the transmit power was defined as 20 W and the frequency as 2.4 GHz. There is no added white Gaussian noise (AWGN). The plot is contoured at 10 dBm intervals.

Figure 4.2 illustrates that a tenuous 'horizontal layering' effect might be achieved in the vertical in consideration of 'bands of equal signal strength'.

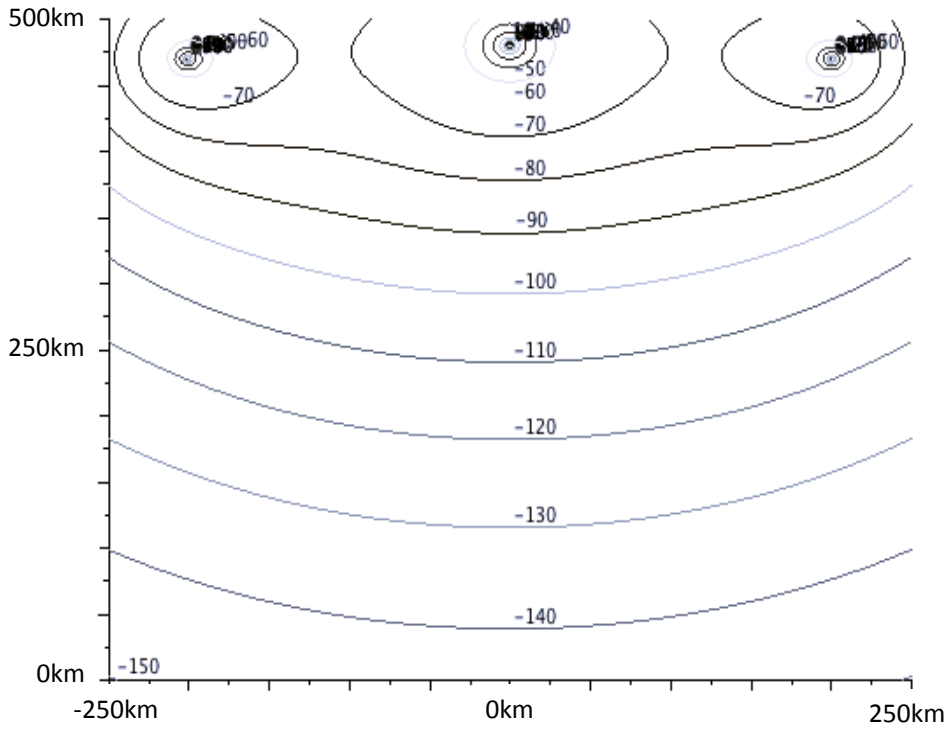

Figure 4.2 – Signal strength of three satellites at 475km altitude and 200km apart

Adding more satellites – increasing the number of transmitters in the sparse beamforming array - increases the effect in the far field, as might be expected for a non-coherent transmission array.

By observation it is clear that using this to create a 'moving-cells-in-the-sky' structure is not directly possible. However, there may be the possibility of creating a 'layer in the sky' by differentiating receive signals based on signal strength. The problem of course is how to attach information to the wavefronts so that there are differences as the signal distance increases.

To address this question, consideration was given to methods of carrying information on the transmitted signals in order to allow decoding at different distances from the transmitters.

4.3.2.1 Amplitude modulation

Trivially, one could amplitude modulate the signals from the three satellites such that they coherently combine at a receiver. However, this does not resolve the problem of transferring different information to different points in the space, but simply provides areas with signal availability, and areas without. This would provide, in effect, a crude form of beamforming but with little application for the requirement being explored here.

4.3.2.2 Phase/frequency modulation

Adding phase control to the signals converts the situation into a sparse phased array transmitter which would create regions of phase summation and regions of phase cancellation. Again, however, this does not easily resolve the problem of concurrently transferring different information to different points in the space, since it achieves creation of different regions of phase coherence proportional to the number of antennas, but not transmission of multiple data transfers to different locations in the space.

To do so would require multiple frequencies with separate phase control for each frequency. Although this technique has been implemented many times, as illustrated in the discussion of the satellites in the literature review of Section 2 (Iridium Next, O3b, etc.), it does not provide the ability to create layers or 'cells' because in practical implementations to date there is no coordination between the satellites to provide the required additional degrees of signal combination.

4.3.3 Discussion and summary

It is clear that modifying the signals can transfer information, but does not support the transfer of different information to a significant number of different spatial locations.

From this rather simplistic experiment, to create 'cells' using this approach requires a large number of satellites, with a large number of antenna apertures, with a large number of frequencies, with independent phase control, and coordination between transmitters (that is, satellites) to provide the signal combination.

As noted above, though beam forming is quite common in current satellite systems, the technique of coordination between satellites, as found in the literature survey at Section 2.8, it does not exist beyond communication cross-links (typically user plane data) for constellations, and as such the creation of 'cells' in the vertical space has not been explored.

In the context of signal combination beyond that offered by existing satellite beamforming solutions, it may be possible to recast the problem in a novel modulated wavefront way. This was explored in the next experimental model.

4.4 Experiment 2 - The concept of 'reverse GPS'

In a Global Navigation Satellite System (GNSS), such as Navstar GPS, Galileo or Glonass, for example, as described in Section 2.4.2, the fundamental principle is,

minimally, the trilateration of position based on known time of flight from known positions in space. In practice, this means known RF propagation timing from multiple satellites flying with precisely known ephemeris.

The propagation time is calculated from an estimate of the local time at the receiver and coded timing information in the transmitted signals, as measured at the local time estimate. Calculation can then be used to refine the local time, based on multiple signal sources – a minimum of four. Then, knowing the propagation distances (pseudo ranges) based on the timing deltas the local position can be geometrically derived.

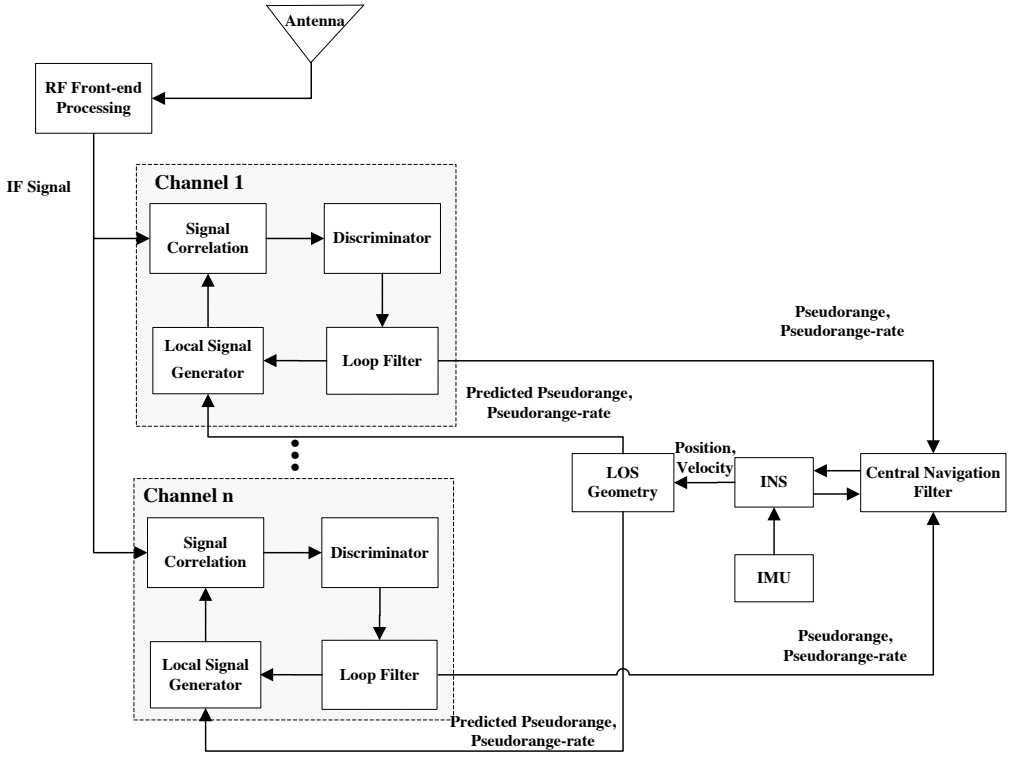

Figure 4.3 – Block diagram of a GNSS receiver with signal correlation for each channel, fed-back rate timing, and pseudo-range recovery (after *Qin et.al.* [1])

In the GPS version of GNSS, signals are coded using direct sequence spread spectrum. The signal is spread using known codes, typically Gold codes, for each satellite. The correlated (or match filter recovered) signals for each satellite are despread at the receiver and the delta between the known transmission time and the

correlated signal received time is used, along with the satellite position data from ephemeris, to calculate the pseudo range to each satellite (Figure 4.3).

If the receiver is stationary, correlation across multiple satellite's direct sequence spread spectrum signals, provides local time measurement to derive multiple pseudo-ranges, which permits calculation of the receiver position.

If the receiver moves, the correlation position moves in local time, which changes the derived pseudo-ranges and thus the calculated position.

If we now imagine a GNSS-like system where the Gold code is replaced by a long PRN sequence with good autocorrelation properties. At the satellite, the transmitter can continually send this long sequence. At the ground receiver, the correlation problem becomes more complex because the receiver would need to correlate the incoming signal against all of the PRN sequence. The outcome of the correlation would be local timing reference as is the case for GPS Gold code correlation.

Although correlating with a long PRN sequence sounds inefficient it is a feature of spread spectrum mobile phone standards (3G UMTS [2] uplink scrambling codes have repeats of 16,777,216, for example).

If the receiver in this GNSS-like system is stationary and the transmitted signal is modified so that the transmitted spread code is moved in transmission time (ie. a different start point within the code), then the received signal would be despread to a different position indicating a different receiver local time assuming a different code to correlate with the time shifted signal.

Further, we can add that if the code were not a repeating spreading codes but instead was of different values - that is, reordered spreading code sequences in code book reference perhaps - then as the receiver moved, the receiver would decode different values depending on their position. A 'reverse' of the purpose of the Gold code in a GNSS system; a 'reverse GPS' if you will.

By contriving the location of the satellites, and the transmitted codes, it is here hypothesized that a 'layered communication' system could be constructed using this approach.

In the illustration shown in Figure 4.4, and given the scenario described above, when receiver *P* is at location *X*, pseudo-range distance d_1 can be calculated from measuring arrival t_k and knowing $L_k()$. d_2 can be similarly calculated. It is assumed for this example that the two satellites L_1, L_2 are stationary. In this scenario is considered a two-code approach.

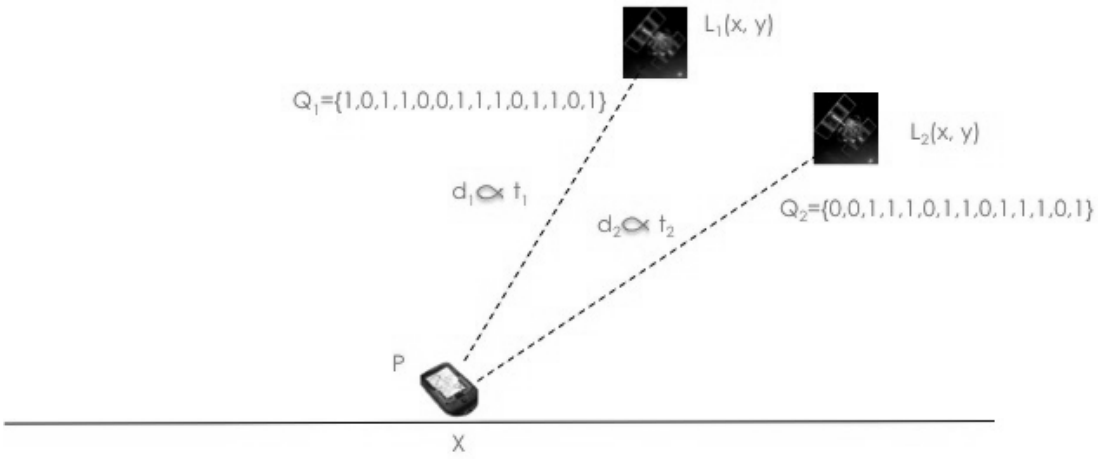

Figure 4.4 – Illustration of the relationship between
satellites, receiver and signals of the GNSS-like 'reverse GPS' scenario

When *P* is stationary it receives two coded signal sequences, Q_1 and Q_2, and, assuming orthogonal spreading between the satellites, is able to independently recover Q_1 and Q_2.

When *P* moves, the distances d_1 and d_2 change, and thus the relative start positions of Q_1 and Q_2 move in relation to one another from *P*'s perspective. That is, the receive time for each sequence differs by some delta time value *D* in each case. Which can be expressed as:

$$t_1 => t_1 + Dt' \qquad (80)$$

and

$$t_2 => t_2 + Dt" \qquad (81)$$

If the receiver at position P remains stationary, then changing the Q_1 and Q_2 sequence start positions amounts to moving the point at which the two sets of symbols Q_1, Q_2 arrive simultaneously at P. If the sequences Q_1 and Q_2 were contrived to cross-correlate or sum and thus produce a new sequence at the point when they arrive simultaneously then dynamically modifying Q_1 and Q_2 would allow data to be transferred to P at the intersection of the two received signals.

For example, for two positions of $P = (X_1, X_2)$:

$$Q_1 \text{ (Symbol position } X_1) \ . \ Q_2 \text{ (Symbol position } X_1) = A \text{ First Symbol,} \qquad (82)$$

Concurrently with,

$$Q_1 \text{ (Symbol position } X_2) \ . \ Q_2 \text{ (Symbol position } X_2) = A \text{ Second Symbol.} \qquad (83)$$

Then we can, in principle at least, selectively send a sequence of symbols to a receiver at *Position* X_1 that is different to receiver at *Position* X_2.

This leads to a number of areas for further work.

- Because Q_1 and Q_2 sequences sum, or correlate, at different positions in the symbol stream, is there a set of dynamically modifiable sequences that would allow for transmission of different data to different locations;

- would further satellites and transmitted sequences add more capability;

- and what sort of layered pattern could be created.

To explore these points a simulation model was constructed in Matlab (code is provided in Appendix B).

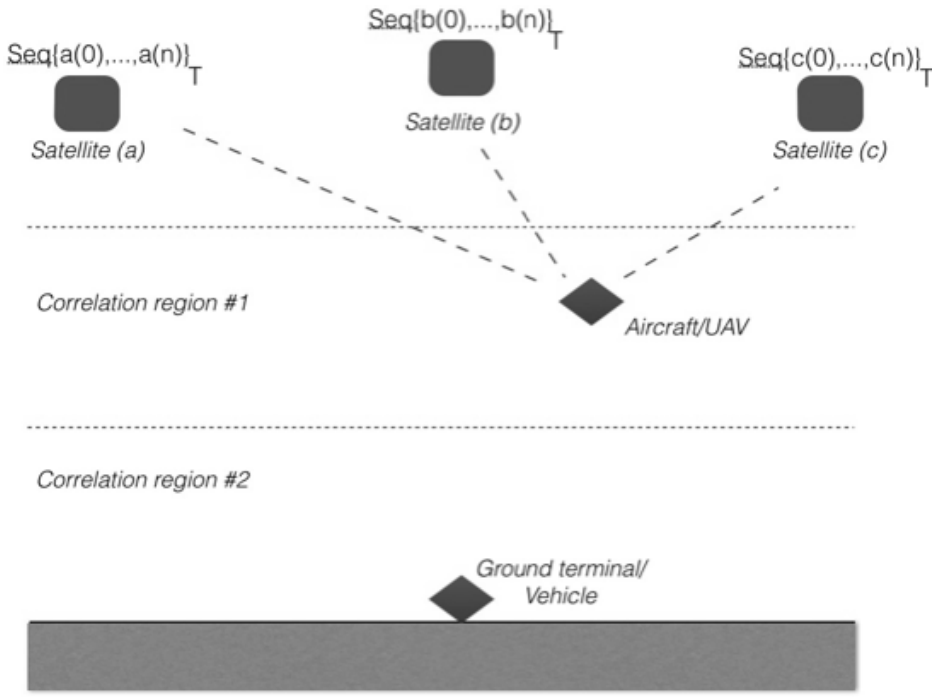

Figure 4.5 – Illustration of the use of summed, or correlated, signals for the spatial re-use of spectrum in the high altitude low orbit environment

In Figure 4.5, three satellites *(a ,b, c)* are transmitting sequences, *Seq*, of symbols over period *T* with the aim to dynamically modify the *Seq* symbols to provide correlation at the *Aircraft/UAV*.

It is clear that there is overlap in this technique with sparse element phased arrays, and correlated radar techniques, although the benefit in this case is the ability to potentially code different data to different spatial locations concurrently; more akin perhaps to multi-user MIMO, but different in that the signals are being combined in correlation rather than matrix decomposition.

4.4.1 Constructing the simulation model

If we imagine that we can arrange to transmit cross-correlating sequences modulated with data at the correct time from a number of satellites, then only at the point in space at which the signals exactly correlate would it be possible to decode the signal. For two given symbol sequences, *sm*, consisting of symbols *s*, and *q*, over time *T*,

where the time shifts are elements of Seq_n and Seq_m respectively, we can represent them as follows.

$$sm_1 = \{s_T, \ldots, s_{T+k}\}\big|_{\forall T \in \{Seq_m\}}$$
$$sm_2 = \{q_T, \ldots, q_{T+k}\}\big|_{\forall T \in \{Seq_m\}} \qquad (84)$$

Then, if the symbol sequence transmitted from satellite 1 is represented by sm_1, and that of satellite 2 as sm_2, and they are transmitted over the same period of time as the overarching transmitted spread spectrum sequence Seq_m, then there exists, if (s_{T+k}* q_{T+k}) cross-correlates, a point in time at which a subset of sm_1 and sm_2 result in transmission of information coded in $\{ s_{T+k}\ q_{T+k}\}$ to a point in space; and since time corresponds to position, this relates to information transfer to a specific location in space defined by that point in time relative to the transmitters.

Then, by contriving the sequences sm_1, sm_2 to provide transmission of different correlated values to different spatial locations, there is ability to create an effect similar to the construction of spatial 'cells', or in this case 'point locations'.

If, in addition, we lower the power of the transmitted signal in order to take advantage of spread spectrum coding gain, and in particular multiple signal correlated coding gain, then the uncorrelated signals themselves can be at low enough level to avoid creating interference elsewhere.

In essence if this were the case it would allow for the creation of spatial correlation regions where signals can be recovered and which are essentially unrecoverable elsewhere, and where signal transmissions in space would not interfere with signal transmissions on the ground.

As a next step, let us consider extending the experiment with a simple arrangement of two transmitters at right angles to each other in a region of space mapped with Cartesian coordinates. To illustrate this, let us first consider a diagrammatic sequence to demonstrate the concept (Figure 4.6).

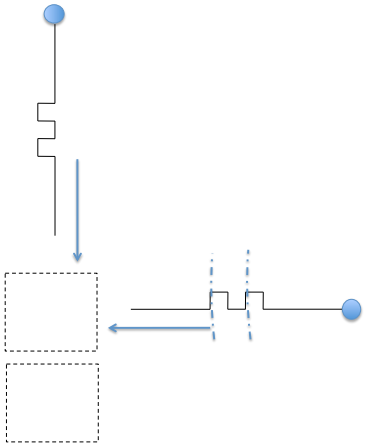

Figure 4.6-1 - Time T_0

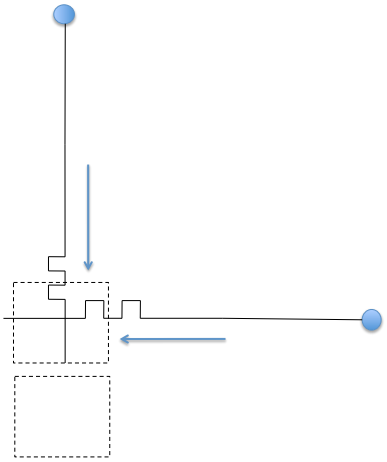

Figure 4.6-2 - Time T_1

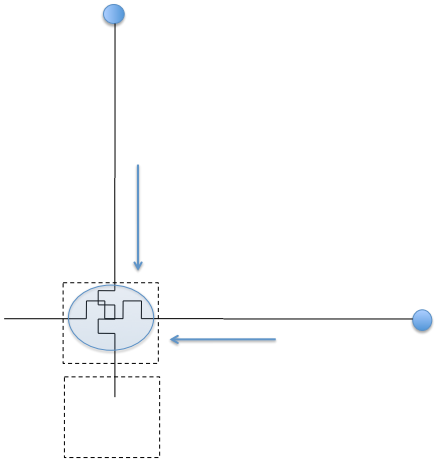

Figure 4.6-3 – Time T_3

As the wavefronts of the signals propagate from the transmitters (Figure 4.6-1, there is no correlation at receivers in marked regions of space. When the wavefronts meet at a receiver (Figure 4.6-2), if that receiver receives both of the correlating signals from which can then be recovered, then the transmitted symbol can be decoded (Figure 4.6-3).

In the following diagrammatic sequence, one of the transmissions is moved in time (Figure 4.7) compared to the previous example (in Figure 4.6). The diagram now illustrates two parts of the wavefront, represented as two copies of the transmission.

As the transmitted wavefronts meet within the marked regions of space, correlation now only takes place in one of the boundary areas, but not the other, illustrating the opportunity for transmission to two different locations in space using the correlation approach.

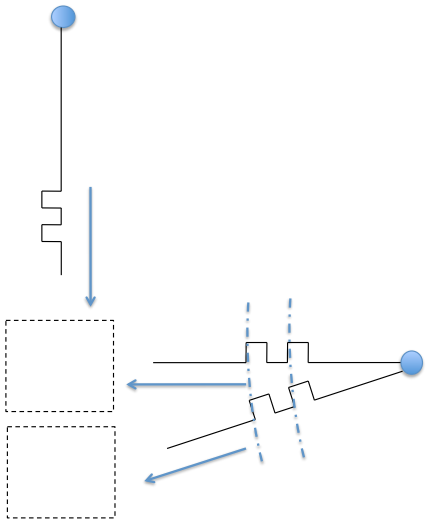

Figure 4.7-1 – Time T_0

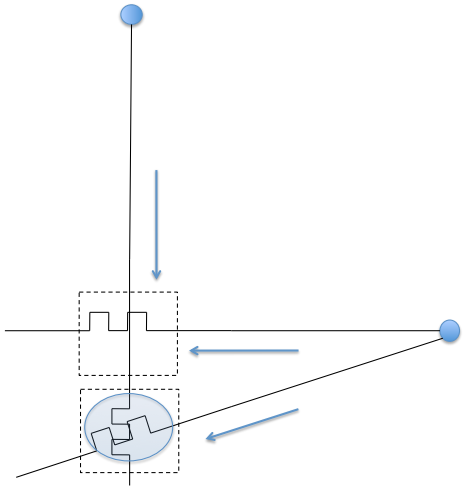

Figure 4.7-2 – Time T_1

To explore this approach in more detail a simulation model was created in Matlab (see Appendix B).

In the Matlab model (illustrated in Figure 4.8) it is assumed that $d_1 = d_2$. Then, at time T_k in area A, $Q_1(k).Q_2(k) = 1$ if the two signals arrive at the same time; demonstrating what would be the effect of correlation.

To consider all the space in the simulation, which is 500 km by 500 km, if we arrange that distance $[P(y_1) - P(y_0)]$ = symbol time T_s, and similarly in the x direction, then we can show that A => $Q_1(k).Q_2(k) = 1$ because symbols $Q_1(k)$ and $Q_2(k)$ correlate for the duration of a symbol. Thus, in the Matlab simulation code, any point where the transmitted signals correlate for the symbol period T_s, the point in space is marked.

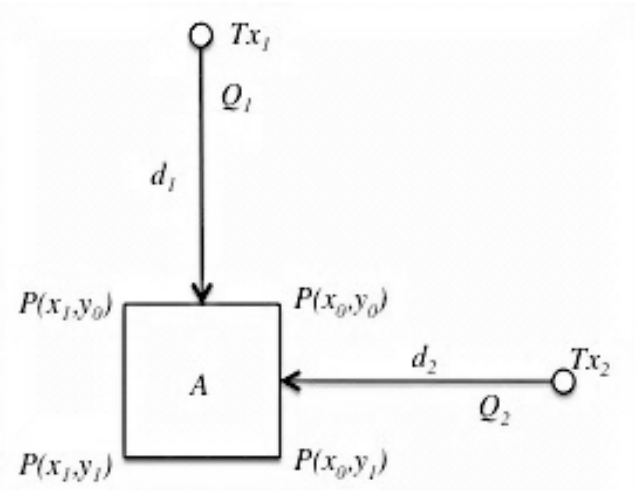

Figure 4.8 – Illustration of the mathematical model

The simulation is constructed as a time-step model with the space represented as an array. At each time-step, the transmitted symbols are propagated from the transmitters, T_{x1}, T_{x2}, following a spherical propagation pattern. As the simulation progresses, points on the array where correlation occurs within the symbol period are indicated in the array with a summation of the received signal strength at that location from the two transmitters. Path loss is modeled as Free Space Path Loss. There is no AWGN. Matlab code for this simulation model this is provided in Appendix B.

4.4.2 Discussion and analysis

The simulation was setup following the configuration in Figure 5.8, with two 10 W transmitters. To mimic the transmission of spreading codes, the length of the correlation region for each of the two transmitted signals was approximated and set to 50 km.

The following chart (Figure 4.9) plots the data captured from each time step and then presents them overlaid. This results in a sum of all the correlation points across the whole simulation region, and shows the ‘aftermath’ of the two wavefronts running through one another.

On running the simulation and collecting the results, although the 'square box' model (Figure 4.9) seemed straightforward, of course, it neglected the wider propagating wavefront, which not only results in correlation within area *A*, but also along the positions outside area *A* where the two wavefronts pass.

The reason for the diagram looking the way it does is that the box model in Figure 4.8 considers a perfectly Cartesian wavefront that is only projected across the width of the area *A*. That is, there is no omnidirectional propagating wavefront. With a realistic omnidirectional wavefront, the model shows exactly what one would expect; a line of correlation points as the wavefronts pass through each other (Figure 4.9).

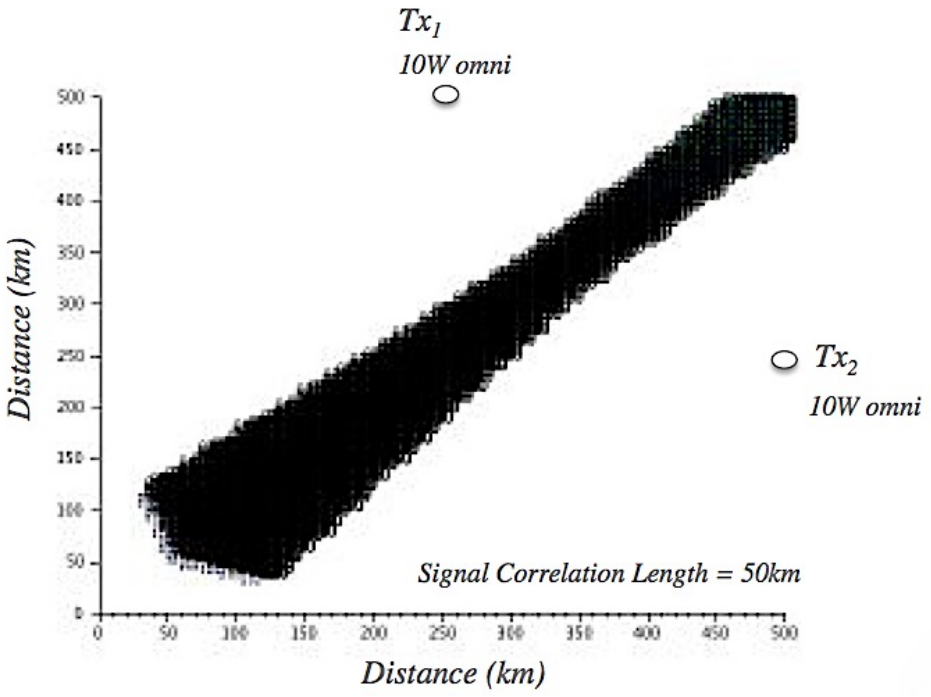

Figure 4.9 – Simulation result for the model of two correlating transmissions, with multiple time measurements superimposed

The 'line of correlation' (Figure 5.9) could be aligned with an orbit (Figure 4.10) to create a layered communication solution at defined altitudes above the Earth's surface, with transmission from two satellites operating in different orbits, but this is extremely contrived and not practical.

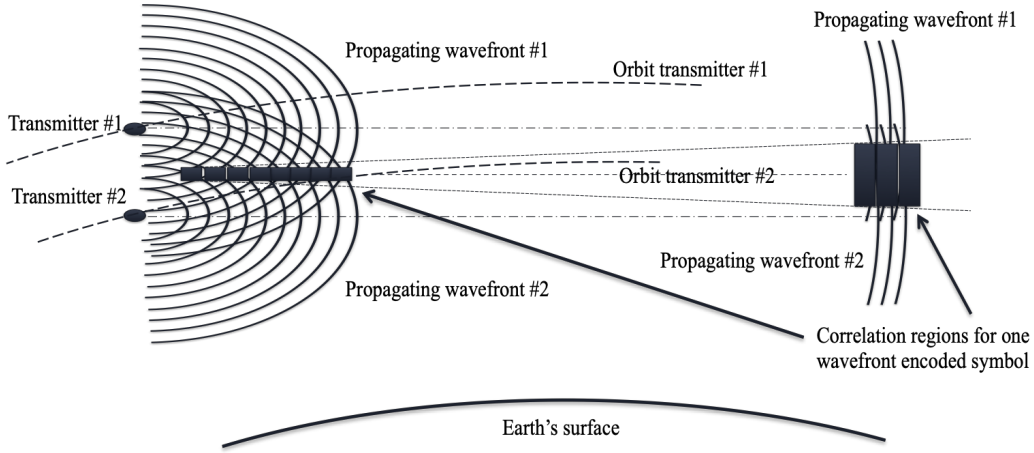

Figure 4.10 – Illustration of contrived correlation region for a single symbol as two wavefronts propagate from satellites in adjacent orbits

4.4.3 Discussion and summary

The 'reverse GPS' approach of using correlated wavefronts to create points in space where signals combine to form decodable 'peaks', and non-decodable 'troughs' has some merit, but suffers in the omnidirectional case from the correlation points being, over time, across all the region of direct overlap of the information carrying wavefronts as they propagate.

Several spatial configurations were considered and simulated, but all have the same problem of only providing a single point, or line of points, where the signal can be considered to impart information at a spatial location at a point in time. As with all techniques that rely on combining signals from multiple transmitters, as the number of transmitters increases, the locations in space where the 'peaks' occur becomes smaller and more focused.

However, the 'reverse GPS' wave front correlation technique, in extremis, has, it would appear, very close similarity to coded netted radar (for example, see *Paichard* [3]), and perhaps its use would be better explored for that application.

It was found during the modelling that Matlab, on a reasonably fast and modern computer, was incapable of scaling beyond a 500 km x 500 km space and providing 1 km x 1 km resolution for propagating wavefronts in reasonable time. Simulations

with larger spaces required less resolution, or larger steps in the propagating waves. It is recommended that modelling wave fronts with this time-stepped approach is not practical for a reasonable compute capability, and other, more direct implementations of the underlying mathematics should be explored if others wish to continue this approach in further work.

In conclusion, Experiments 1 and 2, having gone through the typical, and a few less obvious (for example, 'reverse GPS') methods of beam forming, amplitude, phase/frequency modulation, signal coding, and correlated wavefronts, have been shown to not progress significantly towards the goal of 'cells'; and although discrete areas of 'cells' were created, the approach was not extensible and required extremely contrived positioning of transmitters.

To extend towards a generic solution, a new approach was needed.

References

[1] Qin, F., Zhan, X., Du, G., "Performance Improvement of Receivers Based on Ultra-Tight Integration in GNSS-Challenged Environments", Sensors 2013, 13, 16406-16423

[2] Holma, H, Toskala, A., "WCDMA for UMTS: Radio Access for Third Generation Mobile Communications", Wiley, 2004. ISBN: 978-0-470-87096-9

[3] Paichard, Y., "Orthogonal Multi-Carrier Phased Coded Signal for Netted Radar Systems", International Waveform Diversity and Design Conference, Feb. 2009, pp.234-236

Chapter 5

Directional Low Earth Orbit System Deployment

5.1 Experiment 3 - Layered communication with directional antennas

Having exhausted the various methods of non-directed transmission in an effort to create ‘cells’. Attention was then turned to the application of directed transmissions. There are only a few ways in which beam forming can be implemented.

5.1.1 Antenna array beam-forming

Antenna array beam-forming (*Balanis* [4] for example) relies on geometric alignment of phases at a physical location based on the control of those phases from a series of transmitters. The benefit is the creation of a peak signal at a specific point in space. However, all cooperating transmitters must be contributing the same modulated signal in order to provide the correlated phase coherence at the receiver. There is also the need to know where the receiver is located in relation to the transmitters. Although there have been various attempts at ‘blind beam-forming’ over the years, the need for a ‘back-channel’ from the receiver to the transmitter is always required for good performance.

As described in Section 2, Multi-User MIMO (MU-MIMO) solves the classical beam-forming limitation of ‘many transmitters to one receiver’, allowing for ‘many to many’ user connections. However, the trade-off in this case is in the reduction in power for each additional user beam that is mathematically created in the MU-MIMO calculation. There is also a limit to the number of individual ‘beams’ that can be formed in this way, which at best requires $n+1$ antennas for n users. Eventually there is no benefit in adding more users as the power limits the range with increased users.

5.1.2 Directional antenna beam creation

Directional RF antennas are, as in optics, either reflective or refractive. Reflective antennas can be used to increase gain at the expense of beam-width.

To provide different communications channels to different cell positions ‘in space, there would need to be either (i) formation of multiple refracted directional beams, or (ii) multiple reflectors, to create a fan of beams that could then, perhaps, be used to support ‘moving-cells-in-the-sky’.

Multiple beams from a single reflecting antenna are not easy to arrange, particularly if they are required to have different characteristics, or to carry different modulation. Any form of grating leads to multiple identical beams, but with the power shared.

Multiple reflecting directional antennas could be used to form multiple beams (O3b satellite in Section 2, for example), but this requires considerable complexity and a large number of antennas.

A more compact solution was identified in the form of refractive optics, and in particular the lens antenna.

5.1.3 Lens antennas

The Luneburg lens antenna relies on a spherical refractive antenna element with radial gradient permittivity across the sphere. Similar to Maxwell’s ‘Fisheye’ and close analogue to Rotman lenses.

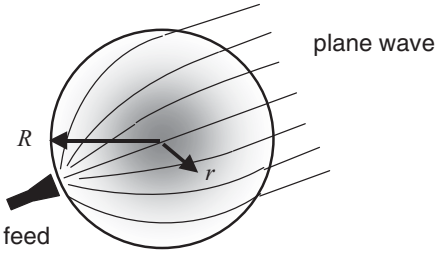

Figure 5.1 – Ray paths in a Luneburg lens (after *Thornton and Huang* [5])

The gradient permittivity causes the plane wave to refract to a point on or near the surface of the spherical lens (Figure 5.1). Where the dielectric constant (ε_r) drops radially from the centre of the sphere with a refractive index n:

$$n = \sqrt{\varepsilon_r} = \sqrt{2 - \left(\frac{r}{R}\right)^2} \qquad (85)$$

Feed structures can include horn antennas or polyrod RF launch structures. The Luneburg lens has the following features (after *James et. al.* [6]):

"*1) No gain loss on scan:*
2) No scan blindness:
3) The beam shape is invariant with pointing angle:
4) Inherently very wide band coverage:
5) Time-delay phase shifting:
6) Feed position not critical:
7) Multi-beaming capability:
8) Simplifies the signal path."

The Maxwell Fisheye and Rotman Lens antennas are similar to the Luneburg lens antenna in as much as the Luneburg lens is derived from the Maxwell Fisheye (Figure 5.2) lens, and the Rotman lens is based on a laminar structure that similarly converts plane waves to feed ports for each direction (Figure 5.3).

The Maxwell Fisheye lens uses the refractive paths to focus a signal from one point on the spherical lens to the opposite point on the sphere.

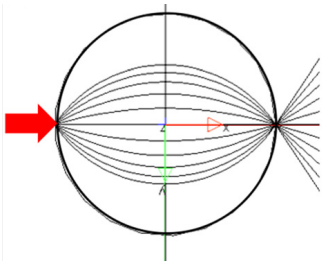

Figure 5.2 – Ray paths in a Maxwell Fisheye lens (after *Liu, Mendis et.al.* [7])

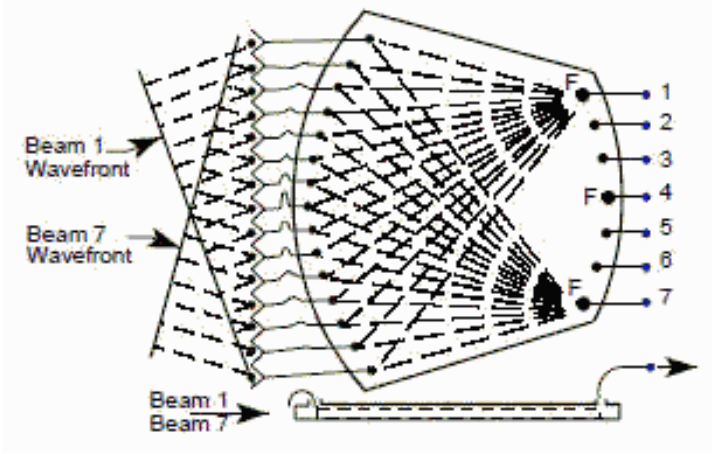

Figure 5.3 – Ray paths in a Rotman lens (after *Naval Air Warfare Center Weapons Division* [8])

The following is an example of a Q-band waveguide switched Luneburg lens for communication applications (Figure 5.4). Use of Luneburg lens antennas in space has been studied over many years (*Rudduck and Walker* [9]).

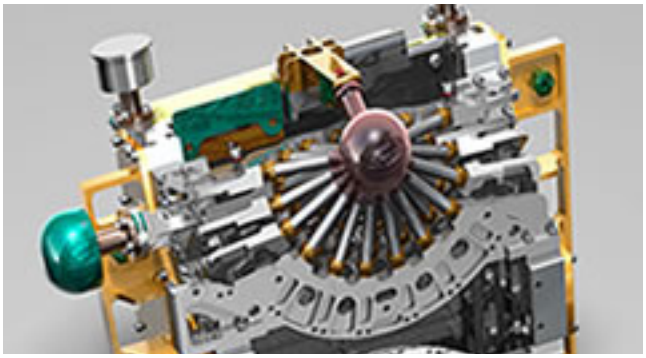

Figure 5.4 – Example of a Luneburg lens antenna system with waveguide feeds (after *Defence Update article* [10] *see also EMS Technologies Beam Forming Networks White Paper* [11])

Luneburg lens approaches have been suggested for use in creating ground based cellular mobile phone coverage from High Altitude Platforms (HAPs) by *Thornton and Huang* [5].

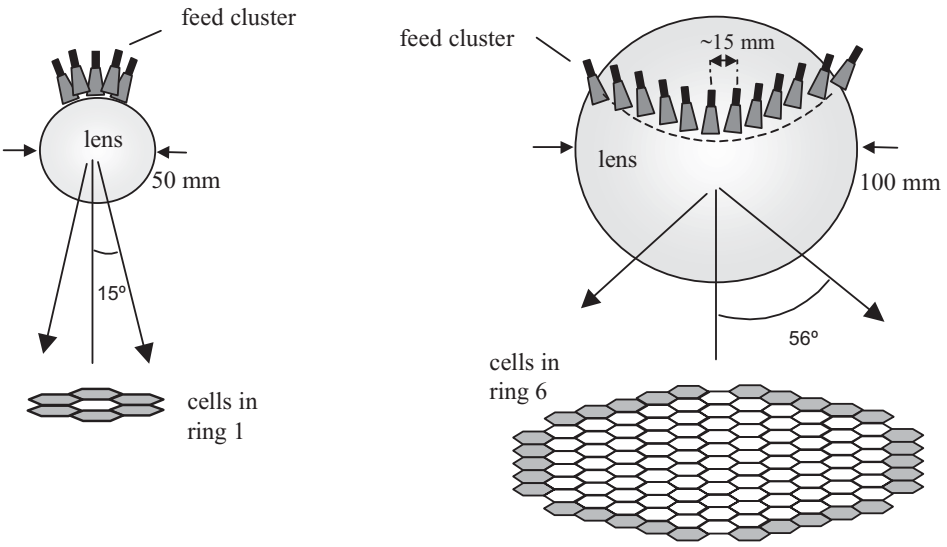

Figure 5.5 – Illustration of the Luneburg lens with multiple antenna feeds, providing a projected cellular (or in 2D terms, a 'wedge') pattern (after *Thornton and Huang* [5])

In a HAP solution, a Luneburg lens is fed from one antenna for each corresponding cell on the ground (Figure 5.5); with more antennas, the greater the coverage, and with each cell having its own antenna (and RF circuitry) it is the equivalent of providing each ground cell with its own, admittedly distant, transmitter. This spatial division approach resolves many of the problems that limit antenna arrays for such applications. It also circumvents the problem of producing multiple spot beams without the need for multiple reflectors, whilst removing the complexity and foibles of beam formed antenna arrays.

If we consider projecting a multi-beam pattern from two satellites with lens antennas, across a view that is limited to a vertical 2-dimensional representation, and visualise the beams 'in the air' as it were, then it is possible to create a mesh of intersecting beams (Figure 5.6).

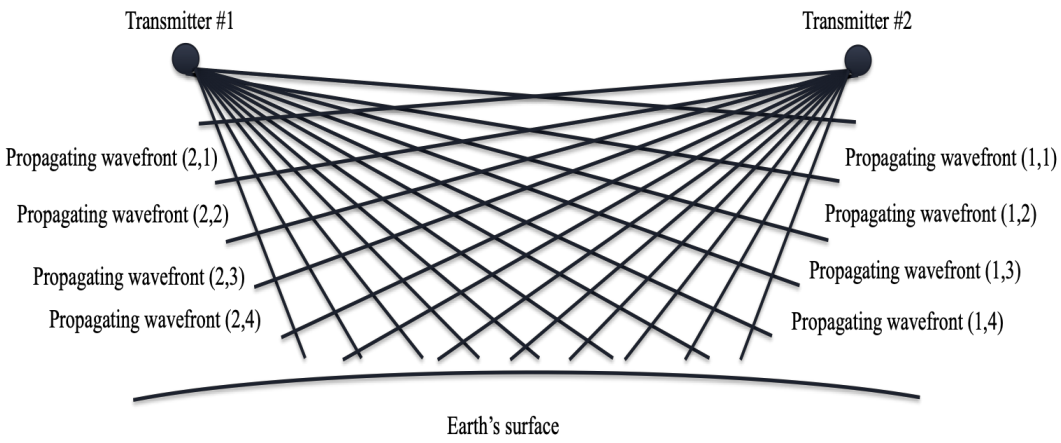

Figure 5.6 – A mesh of intersecting beams resulting from the transmission from two satellites using lens antennas with antenna feed clusters

Figure 5.6 shows the construction of 'wedge' partitioning of space, where each wedge corresponds to a transmission feed on the lens. Multiple satellites can therefore provide overlapping 'wedges' that divide the space into 'cells'. In principle, this provides a potential to create the 'cells in the sky' approach highlighted at the beginning of this work.

There is, however, still an issue of addressing each cell, since the transmitted wavefronts in each wedge have the same issue as identified in Experiment 1 in this Section, whereby different information cannot be projected at each cell because the wavefront contains only one set of information.

Fortunately, perhaps, the concept of 'reverse GPS' and correlation that was explored in Experiment 2 in this Section, may provide a means to provide different information in each cell by using correlation from multiple transmissions through multiple overlapping wedges. There are number of potential approaches. These are now explored.

5.1.4 Approach 1 – individual frequencies per wedge

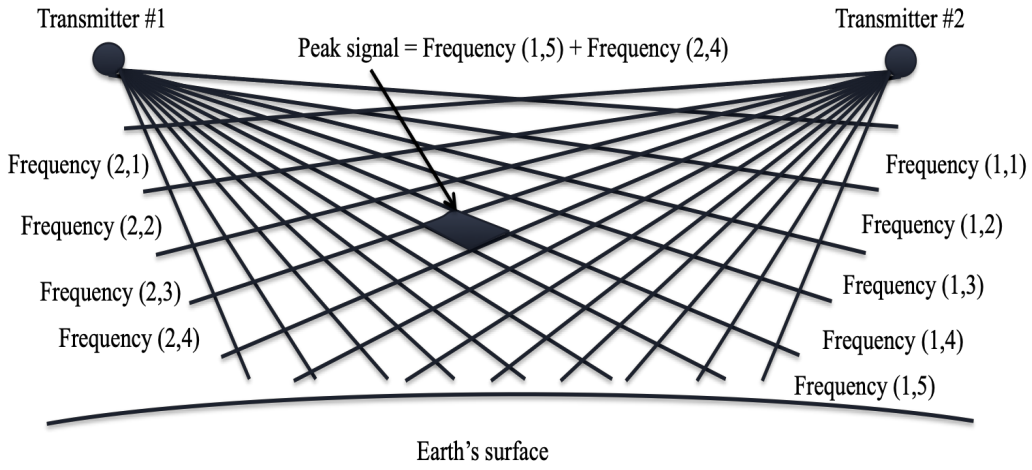

Figure 5.7 – Illustration of a straightforward technique for transmission to only one 'cell'

A simple scheme that would allow each cell in this in-air structure to be individually addressed for transmission and reception, would be to provide each beam with a different frequency (Figure 5.7): *Frequency ({1, ..., n}, {1, ..., m})*. It would, of course, and unfortunately, require a considerable number of frequencies: defeating the object of providing a spectrum efficient solution.

Alternatively, if we assume that all transmitted frequencies contain a 'pilot tone', which is detectable within each wedge of the in-air structure, then a cell at a specific location within the in-air structure may scan for the frequencies to use (Figure 5.8).

Reception would then be carried out using, for example, diversity combine of the two transmission frequencies' signals.
Transmission might be on a fixed frequency offset from the received frequencies, with transmit diversity, for example.

The problem with this technique is that if one cell is using a frequency in a wedge, then no other cell in the wedge can use that frequency. Another issue is that the required number of frequencies scales linearly with the number of satellites and

number of wedges as $(n_w \times N_{satellites})$, and is therefore not spectrally efficient. Improving the situation required the addition of a multiple access sharing scheme.

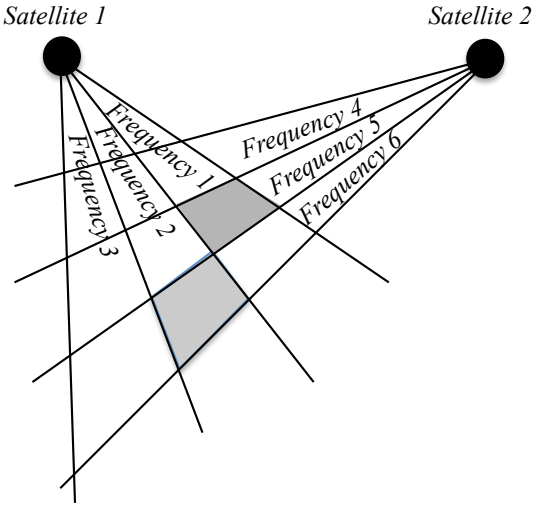

Figure 5.8 – Illustration of a multi frequency technique for transmission to only one cell

5.1.5 Approach 2 – individual frequencies with multiple access control

As described in Section 2.7, there are a number of multiple access techniques that could be applied, but they potentially resulted in a loss of performance due to the inefficiencies of collisions. For example, use of the ALOHA protocol would lead to a reduction in throughput to, statistically, 18.4 % of the full capacity, and slotted ALOHA, taking advantage of the pilot tone as a time-slot marker, would reduce throughput statistically to 36.8 % of maximum.

The use of TDMA would work, but is only efficient in the in-air structure if all cells in the wedge are occupied by user transmissions. Otherwise the approach is temporally inefficient.

An alternative approach using DAMA (Demand Assigined Multiple Access) (Figure 5.9) would appear to be the most efficient as this constrains the slotted-ALOHA inefficiency to a single time slot (contention slot). However, the consequence is that with a requirement for regular contention slots there is still a reduction in

performance proportional to the length of the time-slot and the number of time-slots between contention slots. This would need further analysis to optimise the trade-off and is not pursued further here.

The DAMA approach held the implication that the satellites would need to provide a centralised scheduler, requiring closed loop control following the DAMA protocol. Although this would not be a significant overhead, particularly when compared with ALOHA or TDMA.

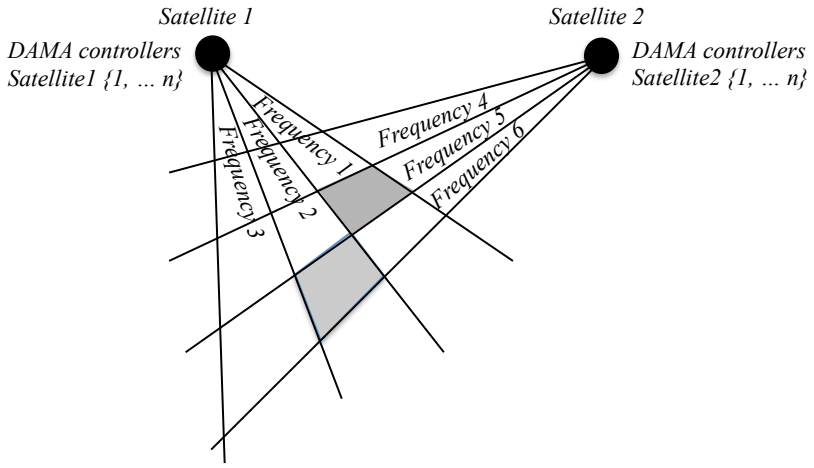

Figure 5.9 – Illustration of a multi frequency DAMA technique for transmission to only one cell

The problem of the number of frequencies increasing linearly with the number of satellites was not resolved using this approach. A more optimal approach would be one where there is the opportunity for frequency re-use.

5.1.6 Approach 3 – DAMA access with frequency re-use

In this approach, a user within a cell within a wedge, searches for the frequencies available in the cell using the pilot tones. The pilot tones provide beacons that could be used to identify time-slots, and to identify the DAMA contention slot. This process would need to be completed for each frequency identified in the overall search.

Unlike previous approaches described above, this approach and procedure would allow frequencies to be re-used across the wedges (Figure 5.10). Which, given the potential physical dimensions of the wedges, the frequency re-use could be as close as every other wedge. The only impact with this level of re-use is a possible issue of interference at, or example, the Luneburg lens; performance would depend on the isolation, and potential cross-talk between the wedges as seen by the multiple antennas around the lens.

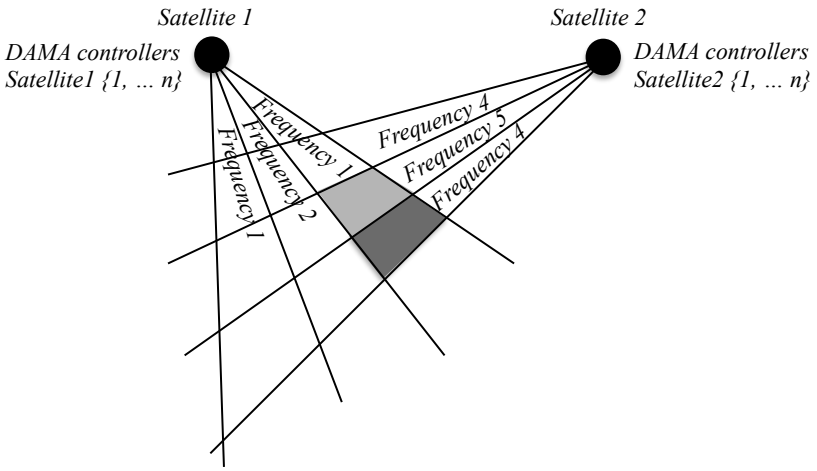

Figure 5.10 – Illustration of a DAMA technique with two frequencies per satellite re-use at each satellite for transmission to only one cell

With this approach, the number of frequencies scales as $(n_{re\text{-}use} \times N_{satellites})$ where 'n' would be three in the above example (Figure 5.10), which is an improvement compared to $(n_w \times N_{satellites})$ of the previous two approaches.

Though this technique was relatively efficient, and would be functional in a realistic implementation, a potentially more efficient approach was considered which involved replacing DAMA with DSSS-CDMA.

5.1.7 Approach 4 – DSSS-CDMA access with frequency re-use

As discussed in Section 2.3.8 with regard to the Globalstar satellite architecture, Direct Sequence Spread Spectrum (DSSS) has some benefits in satellite

communication, particularly in terms of reducing latency. In this approach, all cells in a wedge could be transmitting simultaneously using orthogonal spreading codes.

DSSS-CDMA replaces the issue of DAMA controlled frequencies within a wedge with those of orthogonal spreading codes within a wedge. The benefit of orthogonal codes is that they can be transmitted simultaneously since they combine as 'noise'. However, such codes are not perfectly orthogonal and, typically with system timing issues, the DSSS-CDMA approach will reach a point of being summed noise-level performance limited. In other words, we have traded frequency inefficiencies, for code inefficiencies.

In order for DSSS-CDMA to operate for the in-air structure, there needed to be a method of initial attachment and pilot tones as before, but the benefit of DSSS-CDMA was that, what was a contention slot taking up the whole frequency for a wedge, is now a contention slot on one orthogonal code within the wedge. And if there are no users transmitting in this orthogonal coded contention slot, there is no increase in the overall noise level, and there is no impact with concurrent orthogonal coded transmissions from other users in the wedge. Which is a significant benefit.

In comparison to previous approaches above, there is an improvement in latency, through the removal of time slots, and by moving the contention slot to an orthogonal code contention slot. There would also an improvement in throughput since all users in a wedge can transmit simultaneously on different orthogonal codes. The general approach here would be similar to that of the 3GPP UMTS standard as discussed in Section 2 in the context of GMR-3G.

The main issue raised with the use of DSSS and CDMA techniques for satellite is the the increased EIRP (to cope with the increased peak to average signal power for spread spectrum) and linearity requirements in comparison to the use of other schemes, such as FDMA. However, if the EIRP level is suitable and available, then DSSS-CDMA is a better solution than FDMA. And as discussed above, DSSS-CDMA showed considerable benefit over DAMA.

An improvement on this technique would be to combine the orthogonal coding scheme with gain from signals from wedges from other satellites.

5.1.8 Approach 5 – DSSS-CDMA access with frequency re-use and multiple satellite coding

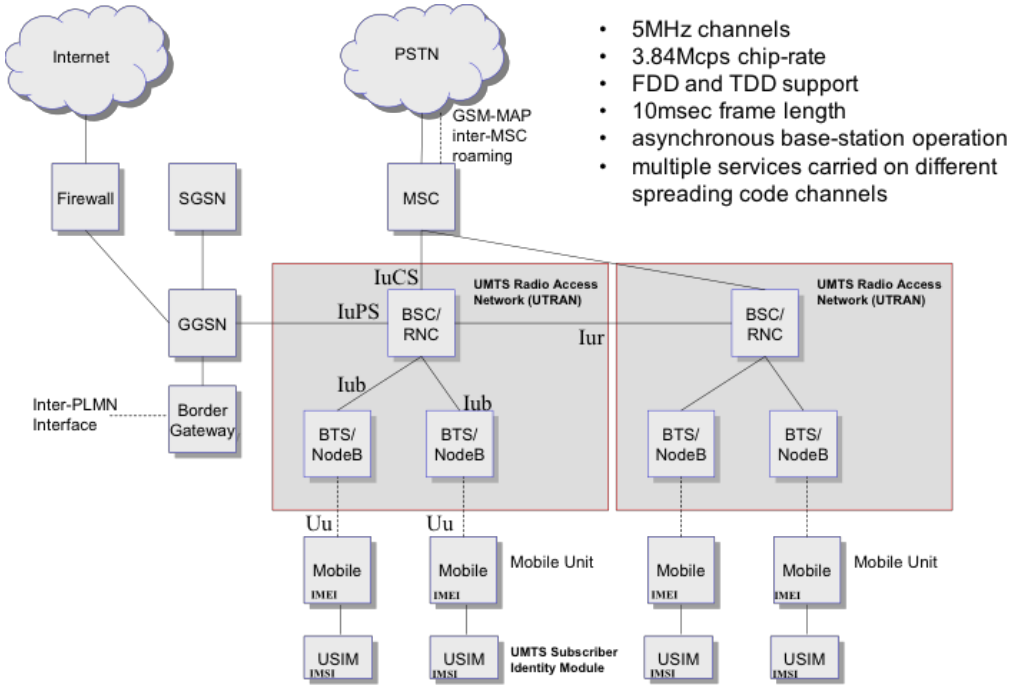

Figure 5.11 – 3GPP-UMTS architecture and characteristics illustrating the connectivity of the access network for soft-handover (*Iur*)

In the 3GPP-UMTS [2] spread spectrum standard, multiple base-stations (NodeB – Figure 5.11) are identified by a random orthogonal 'scrambling' code, typically a Gold code, which is applied to the transmitted signal for each base station. The benefit of such a code operating as a scrambling code is that when it is multiplied with the transmitted orthogonal code, there is no increase in bandwidth.

In this case, the benefit of additional frequencies could be, in extremis with all transmitters operating on the same frequency, removed. And a situation where all users were communicating with satellites on the same frequency could be achieved with identification of cells and satellites by orthogonal codes and scrambling codes.

This implementation could be enhanced by taking benefit of the lens antenna created wedge in-air structure. This being the case, the addition of Space Division Multiple Access (SDMA) could be of benefit.

5.1.9 Approach 6 – Use of SDMA techniques

As described by *Lotter and van Rooyen* [12]; "*A SDMA system is a multiple access technique which enables two or more subscribers, affiliated to the same base station, to use the same Time and Frequency and Code (T/F/C) resources on the grounds of their physical location or spatial separation.*"

Ilcev [13] discusses a similar set of issues to those described in the approaches given here but from the context of satellite borne smart antennas (that is, beam formed and switched beam antenna systems) for the creation of cellular mobile communications cells on the ground. The discussion in the paper does not, however, provide any quantitative conclusion beyond a qualitative endorsement of SDMA.

The previous approaches described above have all taken into account SDMA in that they describe methods of multiple access within a wedge. Although if the resources presented by two wedges from adjacent satellites are taken into account then a 'soft connection' approach can be made, akin to the soft-handover techniques described in the 3GPP UMTS standards.

In such an approach, each satellite would contribute to the signal at each cell so that a cell could achieve processing gain not only from DSSS-CDMA in a wedge from a first satellite, but increased gain from combined signal with DSSS-CDMA in a wedge from a second satellite. To achieve this, in an analogous manner to 3GPP-UMTS, a communication connection is required between the satellites to pass time synchronisation and spreading code information (analogous to the *Iur* interface in the 3GPP-UMTS standard).

Since this is now very close to the 3GPP–UMTS standard for DSSS-CDMA with SDMA, there was considered some benefit in progressing along the 3GPP-UMTS

development path to identify whether any of the 3GPP-UMTS techniques provide advantage for the cells approach explored here.

For clarity, it should be noted that unlike the 3GPP-UMTS standard, for the cells and in-air structure there is no transmitter at the centre of a cell, and there would be multiple users within each cell. So, although seeming very similar to the 3GPP-UMTS standard, there are large differences between what is being discussed here and typical implementations and architectures of 3GPP-UMTS.

5.1.10 Approach 7 – Use of DSSS-CDMA with SDMA techniques and 3GPP

As the 3GPP standards [14] body drives the technology forward, each standards release tries to achieve two things: higher data rates (per user), and better spectrum efficiency (measured in bits/sec/Hz).

There were dramatic increases in spectrum efficiency for 3GPP-UMTS standard Releases 10 and 11, which relied on MIMO (of which there is very little gain in free space satellite configurations – as noted in the discussion in Section 2), extremely wide spectrum (up to 100 MHz), and a move to Orthogonal Frequency Division Modulation (OFDM) downlink with SCDMA (synchronous CDMA) uplink to the satellite.

There are other features in the releases, typically as ‘options’, and these were also of interest as they are part of the core standards roadmap. One of these features is CoMP-MIMO [15] (as described in Section 2 and illustrated in Figure 5.12). Cooperative Multi-Point (CoMP) MIMO is considered to be a sparse transmission array technique with combined performance from multiple transmitters and receivers due to cross-linked synchronisation and message passing between nodes. In context here, that would be a cross-linked DSSS-CDMA with SDMA technique similar to the previous approach described above.

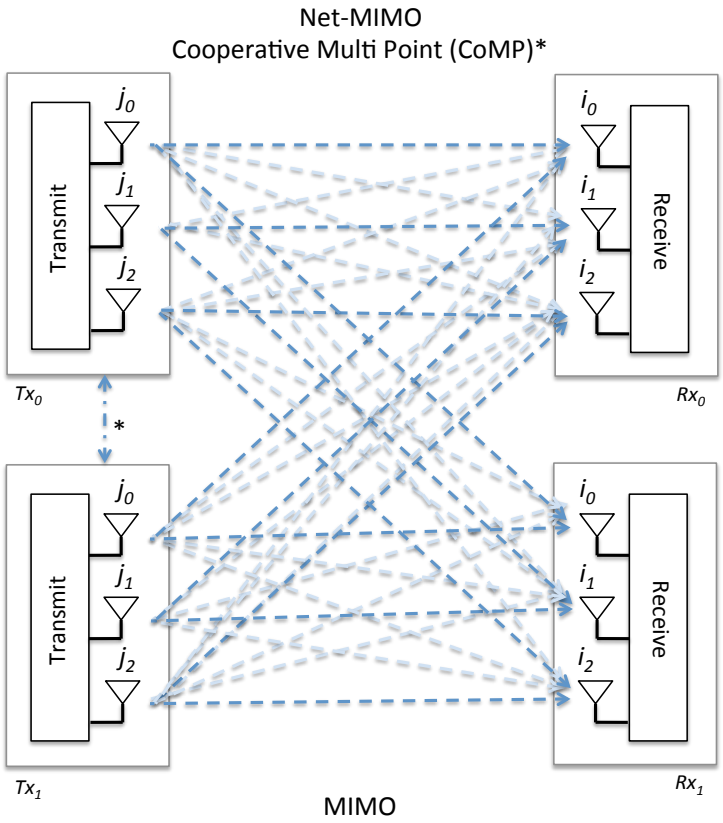

Figure 5.12 – Example showing 3GPP CoMP-MIMO (timing and signalling control connected MIMO transmission nodes) for the case of Net-MIMO with 3 spatial layers and two receive nodes

Although OFDM is more spectrally efficient, it is difficult to achieve processing gain from the combination of two signals because each requires their own frequency, whereas with spread spectrum techniques the same frequency can be re-used with only a trade for higher EIRP and summed noise-floor limitations. The latter of which is more easily attained, particularly in the wedges of an SDMA approach.

5.2 Synthesis and results

In the discussion above, the following approaches were considered (Table 5.1).

Approach	Summary
1	Individual frequencies per wedge
2	Individual frequencies with multiple access control

3	DAMA access with frequency re-use
4	DSSS-CDMA access with frequency re-use
5	DSSS-CDMA access with frequency re-use and multiple satellite coding
6	Use of SDMA techniques
7	Use of DSSS-CDMA with SDMA and discussion of the 3GPP roadmap

Table 5.1 – Summary of approaches

The following charts (Figures 5.13, 5.14, 5.15, 5.16) provide a comparison of the approaches discussed above based on the following metrics and assumptions.

- *Spectrum*: Assuming 120^{o} transmission with 6^{o} per wedge (20 wedges per satellite) and 1.25 MHz (typical mobile data bandwidth) per required frequency. Frequency re-use assumes a re-use factor of two (i.e. every other wedge has the same frequency). [MHz]
- *Latency*: Assuming 1 user accessing the system, the value is the worst-case number of time slots before the message is sent. The assumption is a not unusual 16 TDMA slots per wedge, or 16 orthogonal codes per wedge, with DAMA adding a contention slot at least every 32 slots. [Timeslots]
- *Data rate*: Assuming 2.88 bits/sec/Hz per received stream (a not unusual value for mobile systems), 1.25 MHz per frequency, and assuming up to 7 additional streams from the additional satellites. [Mbps]
- *Figure of Merit*: This is a synthetic metric constructed by calculating *((500.0-Spectrum) × (3000.0-Latency) × Data rate)*, which provides a larger value for a solution that more closely meets the requirements of the discussion of approaches above. The scaling factors (500 and 3000) are added based on the known limits of the contributing values, and to balance the relative contribution of each. This is, therefore, only a comparative, synthetic, figure of merit. [No units]

As a result of the analysis, and previous discussion of the benefits and issues of each approach to the problem, it could be seen that DSSS-CDMA with SDMA, with frequency re-use, and a system architecture using the connectivity features of CoMP-MIMO was the best option to take forward for further study.

Figure 5.13 – Comparison of spectrum usage for the approaches discussed in this section

Number of Satellites	1	2	3	4	5	6	7	8
individual frequencies with multiple access control	320	640	960	1280	1600	1920	2240	2560
DAMA access with frequency re-use	40	80	120	160	200	240	280	320
DSSS-CDMA access with DAMA frequency re-use	2	2	2	2	2	2	2	2
DSSS-CDMA access with DAMA, frequency re-use and multiple satellite coding	2	2	2	2	2	2	2	2
Use of SDMA techniques	2	2	2	2	2	2	2	2
DSSS-CDMA with SDMA, frequency re-use, and CoMP-MIMO	2	2	2	2	2	2	2	2

Figure 5.14 – Comparison of latency for the approaches discussed in this section

	1	2	3	4	5	6	7	8
Individual frequencies per wedge	3.6	7.2	10.8	14.4	18	21.6	25.2	28.8
individual frequencies with multiple access control	3.6	7.2	10.8	14.4	18	21.6	25.2	28.8
DAMA access with frequency re-use	3.6	7.2	10.8	14.4	18	21.6	25.2	28.8
DSSS-CDMA access with DAMA frequency re-use	3.6	7.2	10.8	14.4	18	21.6	25.2	28.8
DSSS-CDMA access with DAMA, frequency re-use and multiple satellite coding	25.2	50.4	75.6	100.8	126	151.2	176.4	201.6
Use of SDMA techniques	25.2	50.4	75.6	100.8	126	151.2	176.4	201.6
DSSS-CDMA with SDMA, frequency re-use, and CoMP-MIMO	25.2	50.4	75.6	100.8	126	151.2	176.4	201.6

Figure 5.15 – Comparison of data rate for the approaches discussed in this section

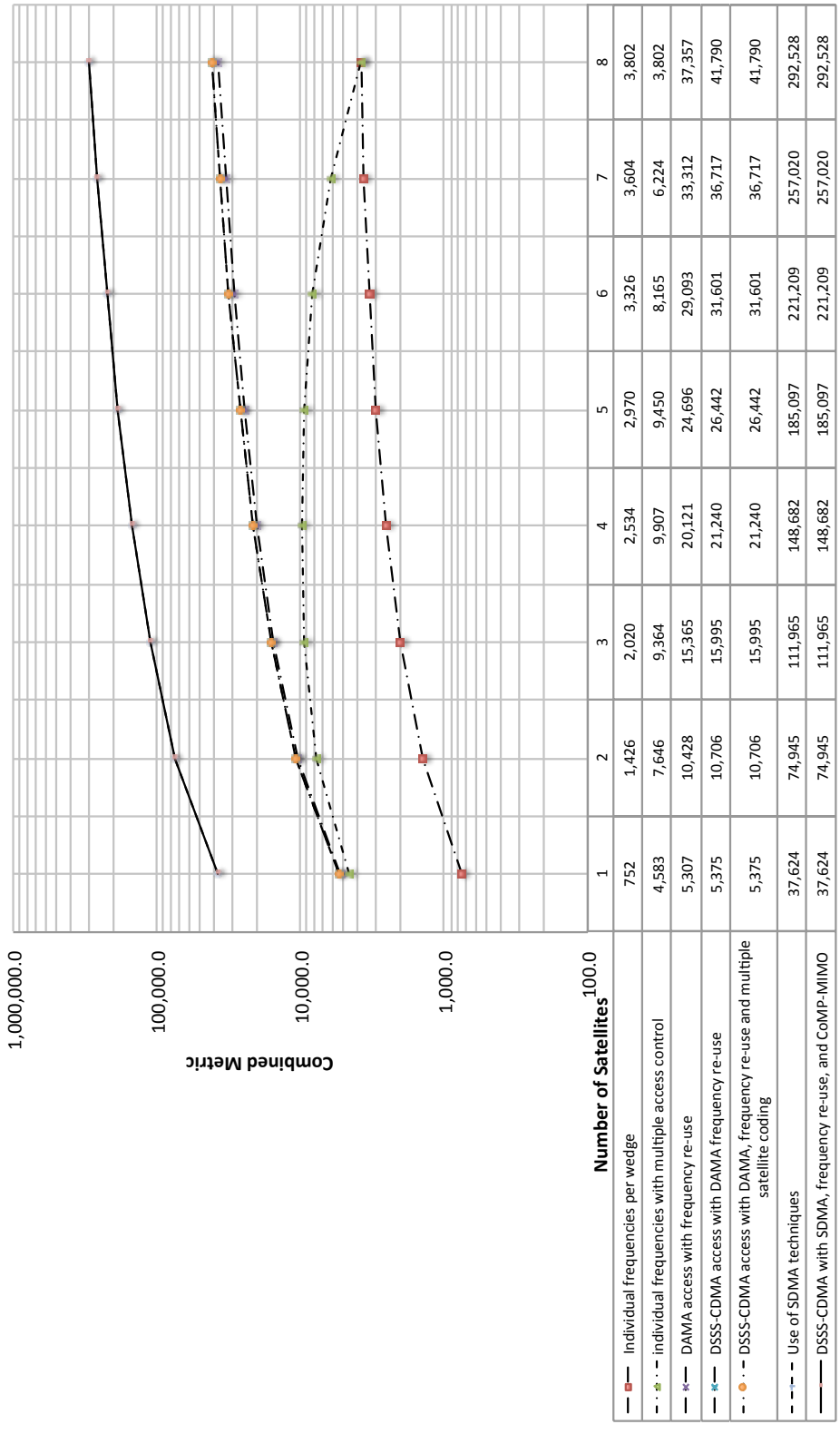

	1	2	3	4	5	6	7	8
Individual frequencies per wedge	752	1,426	2,020	2,534	2,970	3,326	3,604	3,802
individual frequencies with multiple access control	4,583	7,646	9,364	9,907	9,450	8,165	6,224	3,802
DAMA access with frequency re-use	5,307	10,428	15,365	20,121	24,696	29,093	33,312	37,357
DSSS-CDMA access with DAMA frequency re-use	5,375	10,706	15,995	21,240	26,442	31,601	36,717	41,790
DSSS-CDMA access with DAMA, frequency re-use and multiple satellite coding	5,375	10,706	15,995	21,240	26,442	31,601	36,717	41,790
Use of SDMA techniques	37,624	74,945	111,965	148,682	185,097	221,209	257,020	292,528
DSSS-CDMA with SDMA, frequency re-use, and CoMP-MIMO	37,624	74,945	111,965	148,682	185,097	221,209	257,020	292,528

Figure 5.16 – Comparison of a combined metric for the approaches discussed in this section (a larger value is preferred)

5.3 Further study of the selected approach

As described above, a novel concept for creating communication 'cells in the air' was identified. The basis of the concept is the use of multiple satellites with lens RF optics with multiple antenna feeds providing SDMA access for DSSS-CDMA users within a cell. The following sections consider the RF propagation issues around the concept, based on the data in Section 3 and the model developed in Section 4.

5.3.1 RF path loss and model for 'moving-cells-in-the-sky'

Following *Thornton and Huang* [6] the wave front produced by an RF launch structure at the surface of a gradient sphere Luneburg lens can be approximated by a function of the following form.

$$P(\theta) = \left(\frac{\sin\left(\pi \frac{D}{\lambda} \sin\theta \right)}{\pi \frac{D}{\lambda} \sin\theta} \right)^2 \qquad (86)$$

Where D is the antenna aperture diameter and θ is the beam angle.

Following *Thornton and Huang* (and *Morgan* [16]; from whom *Thornton and Huang* take their lead) the main lobe is approximated by nulling the side-lobes beyond the half power bandwidth (HPBW) (at -45 dB in the example) of the main beam (Figure 5.17). The frequency is 12 GHz and antenna diameter is 0.01m

Assuming that the HPBW is selected to allow the pattern to fill a cell, and that the cell is polygonal, produced by two satellite wedge transmissions, then the beam pattern across the cell can be plotted as the 2-dimensional combination of the truncated approximation of the main beam radiation pattern (Figure 5.18).

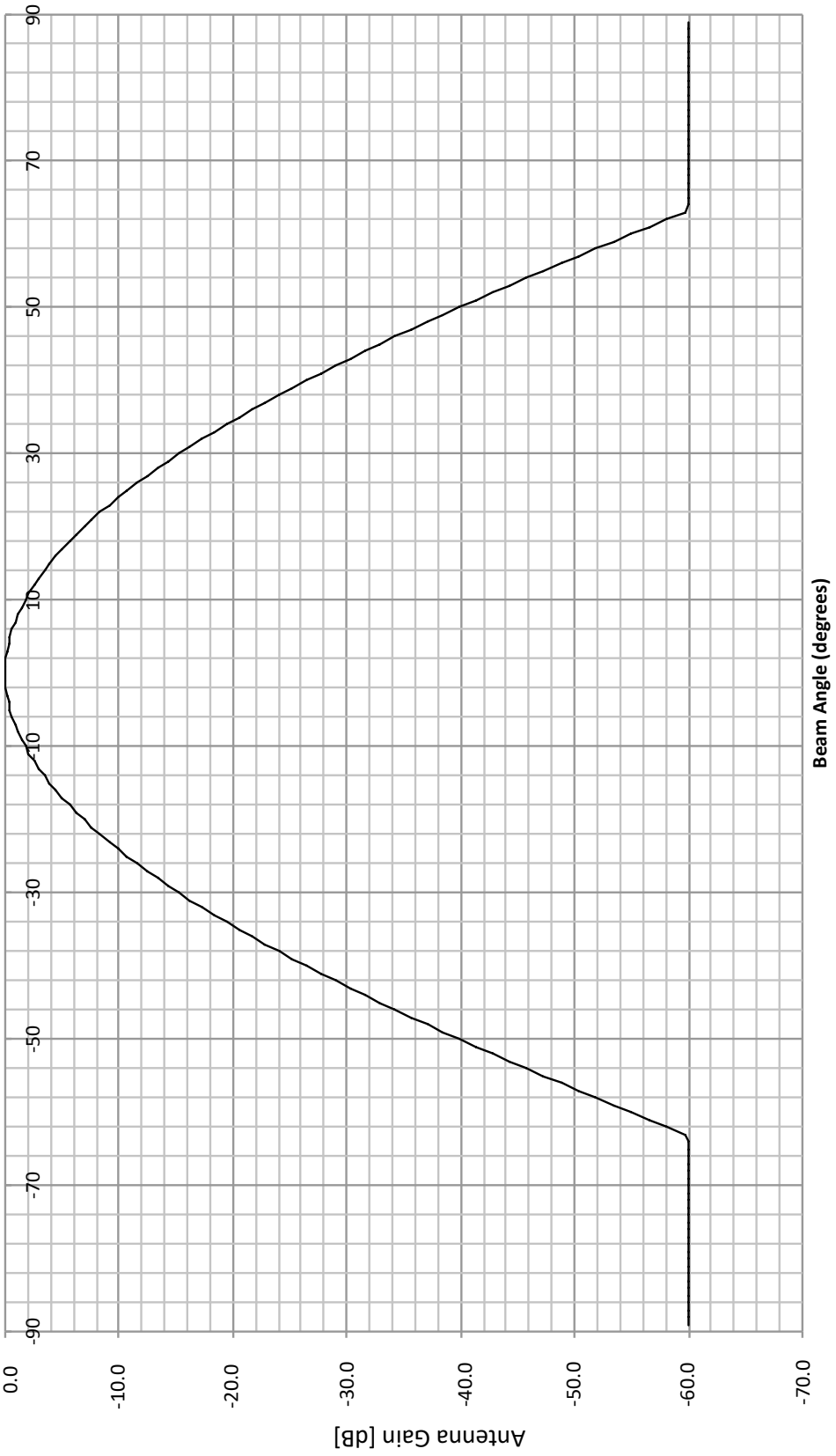

Figure 5.17 – Approximating the main beam of the radiation pattern of a 12 GHz transmission in the far field (following the approach described by *Thornton*)

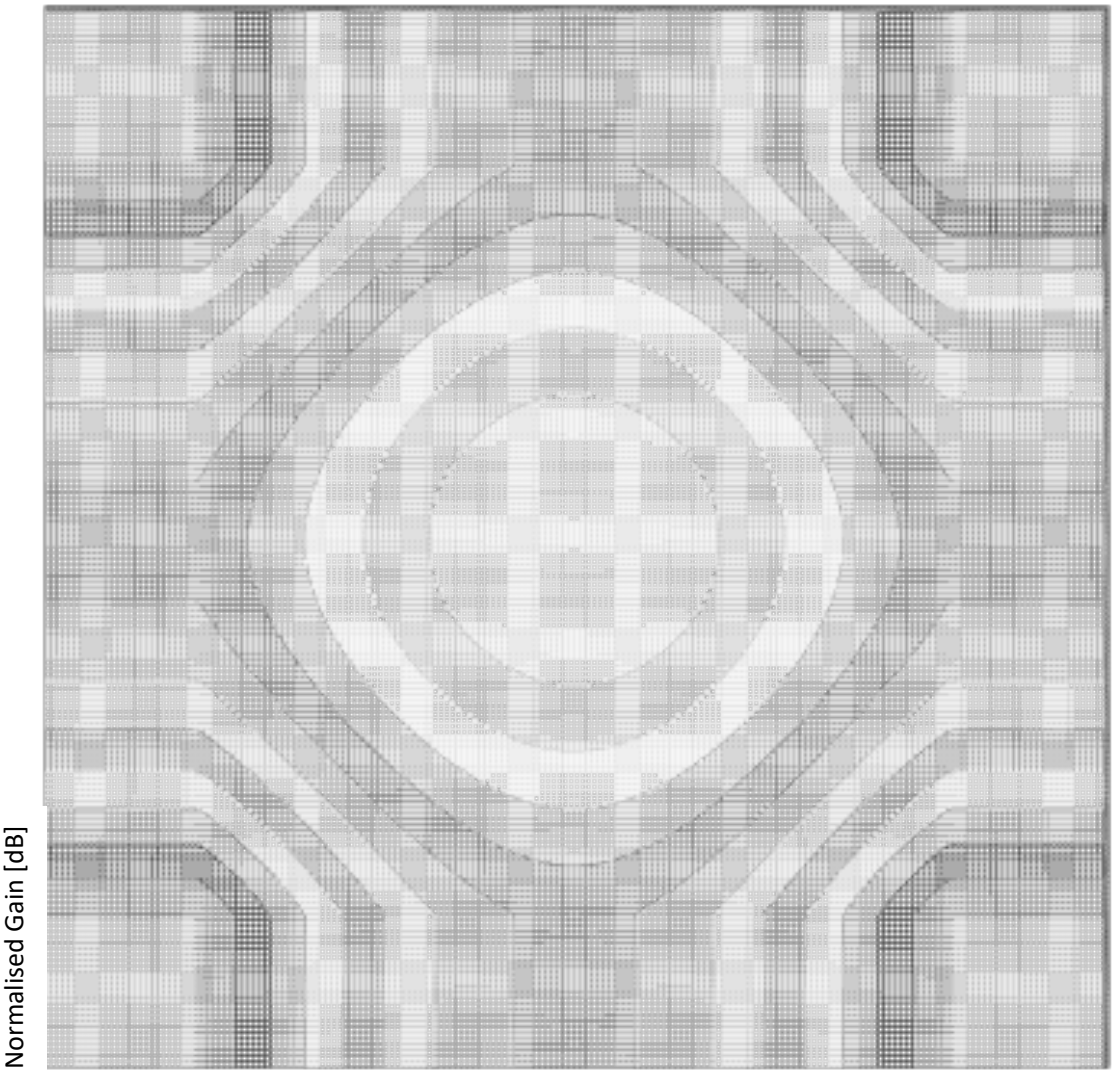

Figure 5.18 – Calculated projection, for illustration, of a 'cell' in which the receive power of two satellite orthogonal transmissions are summed (grey levels are summed antenna gain in dB, as shown in Figure 5.19)

Assuming that the horizontal and vertical beam pattern from the antenna is the same and projected orthogonally, then the summed power pattern can be projected across a two-dimensional cell (Figure 5.18). The data can be plotted as a 3-dimensional chart as shown in Figure 5.19.

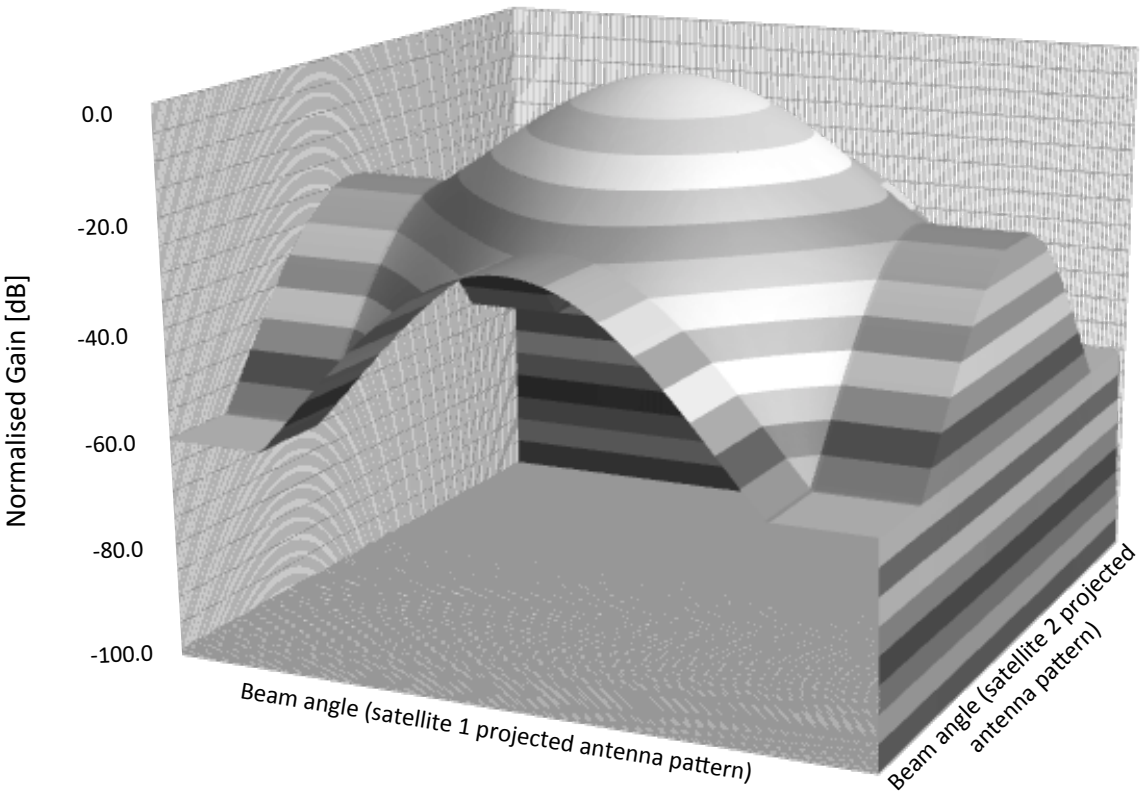

Figure 5.19 – 3-dimensional projection of a cell in which the receive power of two satellite orthogonal transmissions are summed

By extending this calculation to take into account additional transmissions from two satellites, retaining the assumption that all transmissions are cartesian and orthogonal, then the summed pattern across the space appears as in Figure 5.20. This can be plotted in 3-dimensions in order to show the overall structure (Figure 5.21).

With a demonstration of how a pattern of transmissions from two satellites can create spatial cells the next step was to project the transmitted signals across the non-orthogonal, non-uniform power distribution of the in-air structure shown in Figure 5.22.

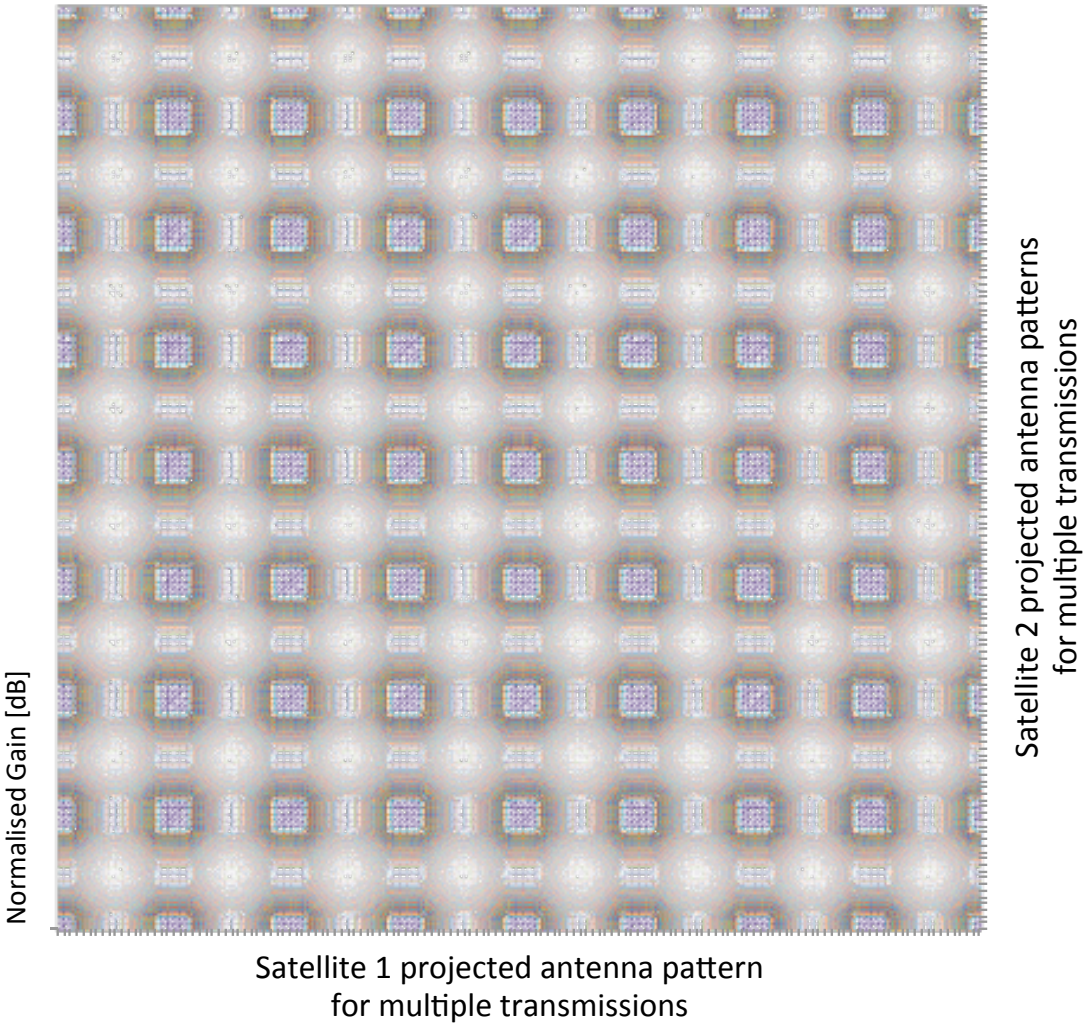

Figure 5.20 – Calculated projection of a multiple cells generated by transmission of multiple orthogonal wedges of uniform power to illustrate the pattern (grey levels are antenna gain in dB as in Figure 5.21)

Thus, the projected signal pattern should be generated within the constrained space of:

$$[(x1, y1), (x2, y2), (x3, y3), (x4, y4)] \qquad (87)$$

as illustrated (Figure 5.22).

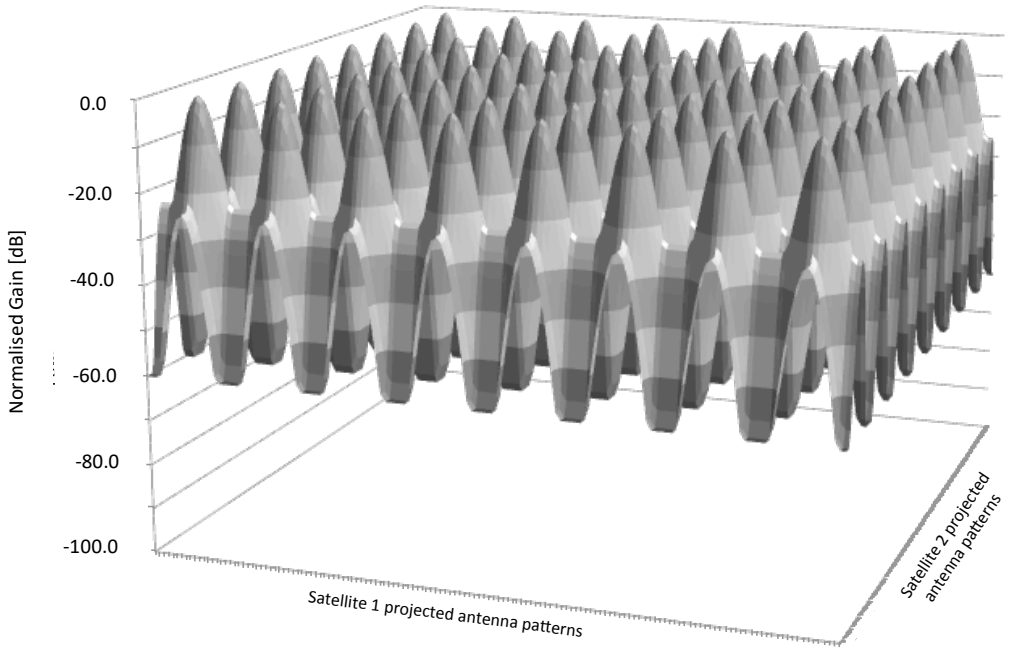

Figure 5.21 – 3-dimensional projection of multiple 'cells' generated by transmission of multiple orthogonal 'wedges' of uniform power

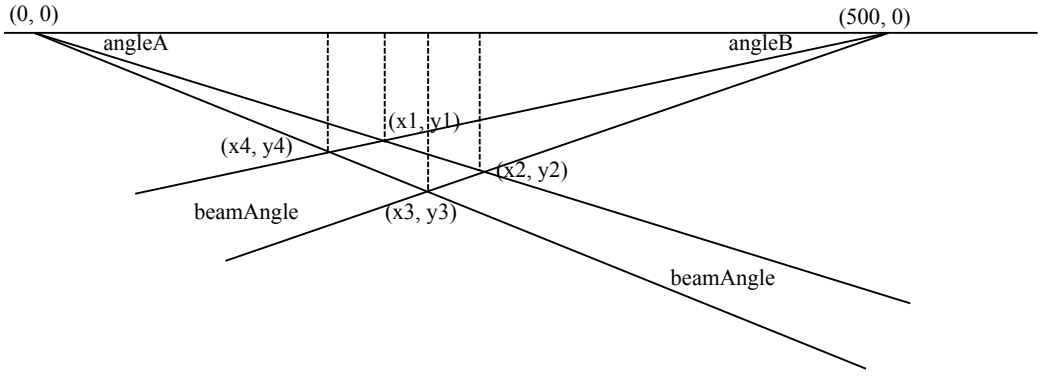

Figure 5.22 – Coordinates for an 'in-space cell' given two sources

It was assumed that a typical multi-antenna-fed Luneburg lens would be used at K-band, and choosing 6º wedges defines *angleA* and *angleB* in multiples of 6º.

For a two-source projection, the coordinates (x_k, y_k) are derived as follows, using an intermediary term, t_x that represents the ratio of the tangents of the two angles:

$$t_x = tan\ (angleB) / tan\ (angleA) \qquad (88)$$

And defining the coordinates of points *A* and *B* as:

$$A\ (A_x, A_y) \quad (89)$$

$$B\ (B_x, B_y) \quad (90)$$

Which are then used in the derivation of the two coordinate positions:

$$x_k = (|(A_x - B_x)| \times t_x) / (1 + t_x) \quad (91)$$

$$y_k = x_k \times tan\ (angleA) \quad (92)$$

Giving (x_k, y_k) for any point in the space.

For the case shown in Figure 5.22, with two satellites flying at *(0, 0)* and *(500, 0)* datum orbit positions (in Cartesian space above a flat Earth) and measured in km, with *angleA* of 36º, and *angleB* of 48º, and with 6º 'beam angle, the coordinates of the 'cell' would be:

$$(x1, y1) = (302.26, 219.61) \quad [km] \quad (93)$$

$$(x2, y2) = (327.25, 237.76) \quad [km] \quad (94)$$

$$(x3, y3) = (302.26, 272.16) \quad [km] \quad (95)$$

$$(x4, y4) = (276.13, 248.63) \quad [km] \quad (96)$$

From these coordinates, we can derive the path length to each of the coordinates from point A and point B.

$$pathLength\ A(x_k, y_k) = y_k / sin\ (angleA) \quad (97)$$

$$pathLength\ B(x_k, y_k) = y_k / sin\ (angleB) \quad (98)$$

Which for the example in Figure 5.26, and using the same assumptions as above, leads to the following table (Table 5.2).

	pathLengthA [km]	pathLengthB [km]
(x1, y1)	373.62	295.51
(x2, y2)	404.51	293.89
(x3, y3)	406.74	336.41
(x4, y4)	371.57	334.57

Table 5.2 – RF path lengths to the corner coordinates of the cell

The area of each cell varies with distance from the satellites, due to the beam width angle, and refraction (which in this model is not accounted for). The area, without refraction, can be calculated as follows.

$$cellArea = |((x_1.y_2 - x_2.y_1) + (x_2.y_3 - x_3.y_2) + (x_3.y_4 - x_4.y_3) + (x_4.y_1 - x_1.y_4))| / 2.0 \quad (99)$$

Which for the example above, and by way of illustration, leads to a cell area of *1343.29* km^2.

From the model derived in Section 4, any cell position with altitude beyond 100 km should only have FSPL applied. However, for lower altitudes the atmospheric RF channel model must be applied. This distorts the cells due to refraction, and introduces additional attenuation across the cell.

For the example described above, the lowest altitude is 219.61 km. As such the cell can be described using FSPL. Therefore, for a frequency of 12 GHz, and using the model for path loss in Section 4 with path lengths from Table 5.2, the coordinates of the cell have the following path loss from positions A and B (Table 5.3).

	pathLossA [dB]	pathLossB [dB]
(x1, y1)	165.48	163.45
(x2, y2)	166.17	163.40
(x3, y3)	166.22	164.57
(x4, y4)	165.43	164.52

Table 5.3 – RF path loss from the satellites to the corners of the ‘cell’

The central RF path loss can be calculated geometrically, or by averaging the values in Table 5.3. Which for the example gives a path loss to the centre of the cell of 164.91dB.

Given these values it is possible to geometrically project the main beam radiation pattern across each using calculated path loss values, from peak to edge.

5.3.2 Adjacent wedge interference

As noted in the discussion of waveforms in Section 5.3, the optimum waveform based on trade off analysis is a DSSS-CDMA modulation using SDMA with frequency re-use and a CoMP MIMO -like system architecture.

If we assume a wedge frequency re-use of two, and a further assumption that each satellite operates with two system-wide unique frequencies. Then adjacent cell interference is a consequence of the following:

1. Wedge beam alignment errors caused by antenna and Luneburg lens
2. Frequency accuracy at the cell;
3. Band-edge shape of the transmitted signal.

Assuming that (1) and (2) above can be optimised, then the main component of adjacent wedge interference would be band-edge shape of the transmitted signal, which will be dependent on the modulation and filter roll-off. The interference for on-ground RF cellular transmission systems is typically dependent on the distance from the adjacent cell transmitters, but in this case the transmitters are distant and as such the effects are related to (1) and (2). To consider this quantitatively requires definition of an implementation, but in general we can relate the adjacent wedge interference contributions as follows.

$$Interference_{Wedge} = f(beam\ alignment) + f(frequency\ accuracy) + f(band\ edge\ frequency\ roll\ off) \quad (100)$$

Where:

$Interference_{Wedge}$	Adjacent wedge interference [dB]
f(beam alignment)	Function determining interference due to beam alignment [dB]
f(frequency accuracy)	Function determining interference due to frequency overlap [dB]
f(band edge frequency roll off)	Function determining interference due to RF band edge roll off [dB]

5.3.3 Adjacent cell interference

Adjacent cells within a wedge suffer from interference due to wedge alignment from the second (or more) satellite transmitter wedge(s). Also, if the assumption is that there are the same number of spreading codes per wedge as the maximum number of potential cells within the wedge created by a second (or more) satellite transmitter (that is, Luneburg lens and feeds), then the adjacent cell interference can be related as described below. Noting that the cell spreading code can be a separate orthogonal scrambling code to the user orthogonal codes (for example, a Gold scrambling code for the cell, and an OVSF spreading code for users, following the 3GPP-UMTS approach, for example).

$$Interference_{Cell} = f(beam\ alignment) + f(frequency\ accuracy) + f(cell\ code\ orthogonality) \quad (101)$$

Where:

$Interference_{Cell}$	Adjacent cell interference [dB]
f(beam alignment)	Function determining interference due to beam alignment [dB]
f(frequency accuracy)	Function determining interference due to frequency overlap [dB]
f(cell code orthogonality)	Function determining interference due to code orthogonality [dB]

5.3.4 Adjacent user channel interference

Within each cell, individual users can be identified by a spreading code, which, following the 3GPP-UMTS approach, would lead to a user interference level described as follows. Noting that a similar level of interference can occur for the synchronisation (pilot tone) channel described previously.

$$\begin{aligned} Interference_{User} = {} & f(beam\ alignment) + f\ (frequency\ accuracy) \\ & + f(cell\ code\ orthogonality) \\ & + f(user\ spreading\ code\ orthogonality) \end{aligned} \quad (102)$$

Where:

$Interference_{User}$	Adjacent user interference [dB]
f(beam alignment)	Function determining interference due to beam alignment [dB]
f(frequency accuracy)	Function determining interference due to frequency overlap [dB]
f(cell code orthogonality)	Function determining interference due to code orthogonality [dB]
f(user spreading code orthogonality)	Function determining interference due to user spreading code orthogonality [dB]

5.3.5 Analysis of modulation options for the uplink return channel

Typically, return channel modulation is lower performing because of the multiple access requirement of a many to one receive architecture. However, in the system defined here with DSSS-CDMA, the return user channel can be a reverse of the user forward channel if at a different frequency: this as a direct analogy to 3GPP-UMTS, which similarly has a Frequency Division Duplex (FDD) DSSS-CDMA approach [138], but not for the reverse (uplink) channel.

The symmetry of the approach described here means that the channel model is identical for the forward (downlink) and reverse (uplink) channel, but the user transmission power may differ.

5.3.6 Power control

With the use of DSSS-CDMA modulation and access control comes the issue of dynamic range amplitude control at the receiver, generally known as the 'near-far' problem. This occurs when transmitters of the same power are at different distances from the spread spectrum receiver; in which configuration a closer transmitter might dominate the dynamic range of the receiver leaving only limited dynamic range for the distant transmitter. The typical solution is closed loop power control, which in this case would require closed loop control between the user and the satellite for each transmitted spreading code (which would be identical to how the downlink and uplink power control is managed in 3GPP-UMTS).

5.3.7 Consideration of the need to rotate the pattern

One of the unique problems with the system as described here is that because the satellites are below GEO, they have a velocity relative to the ground, and relative to lower orbits. This results in the wedge and cell structure moving relative to the ground and to lower orbit platforms.

If wedge/cell pattern is rotated at the satellite in an attempt to keep it stationary relative to one of the high altitude and low orbit platforms, it would, of course, not provide the same relative motion for other platforms.

The best approach to take, therefore, is to let the wedge/cell structure move, relative to high altitude and low orbit platforms, and rely on hand-over between cells to maintain connectivity (akin to the approach taken by Iridium and O3b as discussed in Section 2.2.19, for example).

5.3.8 'Reverse Handover' between cells

As a user or platform reaches the edge of a cell there is a need to handover to the next cell. Typical mobile communications systems achieve this using either user terminal managed handover (e.g. WiFi technology), or system managed handover (e.g. mobile phone technology). The former has some advantages in terms of simplicity of control algorithm, but the latter has the benefit of being able to coordinate and manage the resources needed to perform handover cleanly.

There are typically two methods for handover in system managed scenarios. The first uses a measure of the RSSI (Received Signal Strength Indication) to indicate when the user is close to the cell edge. The second uses BER (Bit Error Rate). RSSI is simple to measure and apply, but BER provides a more robust approximation of the distance from the transmitter.

For the 'moving-cells-in-the-sky' system considered here, there is the ability to use the position information, of within which cell a user is located, to provide additional hints to a system handover algorithm in terms of knowledge of cell size.
System or central handover control in this manner then becomes analogous to the 3GPP-UMTS standard, where handover decisions are made, in this instance, between satellites operating as RNCs (3GPP-UMTS Radio Network Controllers), communicating handover information between them on what 3GPP-UMTS terms the *Iur* interface, and with handover decisions based on BER measurements at user platforms being collated and fed back to the satellites' RNC function.

5.3.9 Expanding to multiple satellites

Thus far, for simplicity, only two satellites have been considered. In a realistic system, there would be many more, for example in perhaps a Walker constellation. The maths of the system described extends easily to multiple satellites, and the cells become higher order and three-dimensional polygons as a result. Each real-World lens produced wedge would be conical, and not the two-dimensional wedge used in this analysis for simplicity. However, the mathematics can easily be extended to describe intersection of conical transmissions.

The main issue that arises with multiple satellites is interference caused by re-use of spectrum and spreading codes. The issues are extensions of the problems described in the section on interference above (Section 5.3.2). A way to manage this re-use is to assign each satellite a small number of re-use frequencies (wedge frequency re-use of two, for example). Then, for an illustrative 5 MHz wide communications channel allocated as each 'frequency', and assuming an Iridium-like Walker constellation of around 66 satellites, the required spectrum would be 330 MHz for the whole constellation, which is large in commercial satellite terms, but not excessive.

Increasing the bandwidth to 20 MHz results in a requirement for an allocation of 1.32 GHz for the constellation, which could only be achieved practically in or above the current standard K, Q and V bands. A system at W-band would have the bandwidth to support this higher bandwidth, but could interfere with W-band mobile communication back-haul links on the ground. This would require consideration by ITU, for example, to resolve a usable part of the spectrum.

5.3.10 Interference avoidance on the ground

With the use of multiple satellites and DSSS-CDMA it is feasible for the 'moving-cells-in-the-sky' system to lower the transmission power from each satellite, such that the measured spread spectrum signal at ground level is negligible. The lowering of the power can be compensated in the cells by using processing gain provided by transmissions from multiple satellites.

The following calculation illustrates an example of this approach. The example (Table 5.4) shows two calculations, one from two satellites to a UAV/RPAS operating at 65,000 ft (circa 20km) altitude, and another for the signals at the surface of the Earth. There are two satellites at an altitude of approximately 250 km (ignoring slant angle and just assuming range). Transmission power is 10 W at 12 GHz with a 3 dB antenna gain at the transmit and receive locations. The receiver is assumed to be wideband with a receive threshold of -120 dB. Processing gain is assumed to be 30 dB for each received signal at the UAV/RPAS, and in this

example, is summed from each satellite. Noise is not included in this example, which focuses on the received signal level for illustration.

Satellite	Tx Power (dB)	Frequency [MHz]	Tx Antenna Gain [dB]	Distance Satellite to RPAS [km]	Distance Satellite to Earth [km]	Path loss (FSPL) [dB]	Rx Antenna Gain [dB]	Receive power [dB]	Processing gain [dB]	Summed processed gain [dB]	Receiver threshold [dB]	Margin [dB]	Processing gain margin [dB] (Sat. 1+2)
1	10	12,000	3	230	-	161.268	3	-145.268	30	-115.268	-120	4.732	9.464
2	10	12,000	3	230	-	161.268	3	-145.268	30	-115.268	-120	4.732	-
1	10	12,000	3	-	250	161.992	3	-145.992	0	-145.992	-120	-25.992	-
2	10	12,000	3	-	250	161.992	3	-145.992	0	-145.992	-120	-25.992	-

Table 5.4 – Example demonstration of interference avoidance on the ground

The results are shown in terms of received signal margin with summed gain (9.464 dB in this example) for the UAV/RPAS, and the signal margin at the surface of the Earth (-25.99 dB in this example). Illustrating that the UAV/RPAS can recover a signal that conveniently appears below the receiver's receive threshold at the Earth's surface. Further parameter contrivance can create a situation where the received signal would be below the receiver noise floor.

This unique approach allows the re-use of large sections of ground spectrum in the high altitude low orbit environment without creating interference on the ground. Thus, solving one of the problems identified earlier in this study.

5.4 Discussion and summary

In this Section, the work has led to the conclusion that a 'moving-cells-in-the-sky' solution is feasible, and that many of the features of standard cellular communications systems can be applied to provide an indication of how, perhaps, a realisation of the system could be achieved (Figure 5.17).

A mechanism for communications attachment will need to be expanded on in further work. The illustration in this section assumes that the user terminal also has a lens antenna system, such as a Luneburg lens, to direct signals back to the satellite. Technically this is not onerous as it is only a minor modification to the movable antenna feed hemispherical Luneburg lens systems currently employed for high data-rate satellite communications fitted to commercial aircraft (see L-3 Communications FFS-2402 Luneburg lens product [17] for example).

The main difference here is the requirement for one antenna per satellite wedge in which the user terminal sits. There is a trade-off to derive the number of Luneburg lens feeds required: the FFS-2402, for example, has four hemispheric Luneburg lenses, for transmit and receive to multiple satellites, and this may not be sufficient.

Overall the process of initial communication attachment (termed "camping on") would be similar to that for 3GPP-UMTS, but with additional variations in the procedure to cope with the wedge scrambling code assignment and user terminal location assessment. An example of the attachment process is described below.

1. The user terminal scans the available frequencies and known scrambling and spreading codes to identify the synchronisation ('pilot tone') channels for each wedge in which it sits. The user terminal then receives information from the identified satellites on characteristics of the transmission and reception in that wedge from the Radio Network Controller (RNC) (see also Figure 5.11) at each satellite.

2. The user terminal then announces its presence to each satellite via a known pre-defined DSSS-CDMA RACH (Random Access Channel) [14] for each wedge in which it sits.

3. The RNCs at each satellite, based on the received signals, now know which wedges to use to communicate with the user terminal. The RNC's can now communicate and coordinate with each other to determine scrambling and spreading code allocations within their wedges, which can then be passed by return message to the user terminal from each satellite. At this point, the user terminal can use the parameters to communicate with the satellite constellation and pass data.

Other benefits of adopting the 3GPP-UMTS [14] general approach and architecture are potential opportunities to utilise the security mechanisms, location registration (Home Location Register – HLR - for example), encrypted data link mechanisms,

handover mechanics, routing, and basics of the radio network management that are part of the standard.

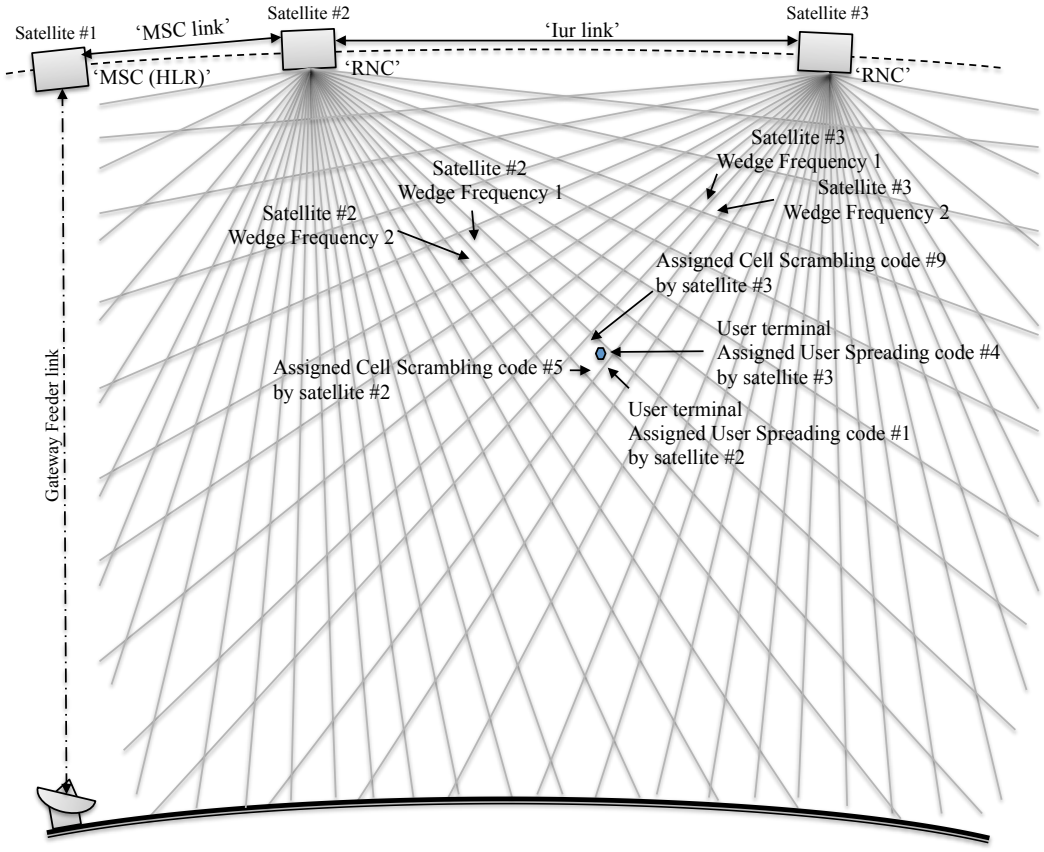

Figure 5.23 – Illustration of a single user terminal, representing a UAV/RPAS, and the values that are assigned to allow it to be uniquely identified and addressed – cells and satellites are in motion relative to the Earth

Based on this work an illustrative diagram (Figure 5.23) can be constructed that demonstrates the practicality of the approach.

The cells in the sky approach derived here provides many advantages compared to other techniques, such as diversity or MIMO. Compared to diversity, there is much improved spectrum reuse because the multiple beam approach based on a lens antenna allows for space division multiple access from multiple transmitters, which is not possible with a classic diversity approach. And MIMO in its various forms provides beam forming using optimisation of a combination of the H matrix and, for typical MU-MIMO, the pre-distortion of the signal, which limits the number of beams, and as noted by Arapoglu, reviewed in Section 2, without multipath that only

occurs close to the ground the available gain from multiple satellite MIMO is minimal: the moving-cells-in-the-sky approach does not have this limitation.

The next Section addresses the comparison of the performance of the approach identified here with common techniques such as other variants MIMO and beam forming techniques.

References

[4] Balanis, C., A., "Antenna Theory: analysis and design", Wiley-Interscience, 2005, ISBN: 0-471-66782-X

[5] Thornton, J., Huang, K-C., "Modern lens antennas for communications engineering", Wiley, 2013, ISBN: 978-1-118-01065-5

[6] James, G., Kot, J., Parfitt, A., "A Luneburg Lens Element for the SKA", CSIRO Telecommunications and Industrial Physics, 10 August 1999

[7] Liu, J., Mendis, R., Mittleman, D. M., "A Maxwell's fish eye lens for the terahertz region", Applied Physics Letters 103, 2013

[8] "Electronic Warfare and Radar Systems Engineering Handbook", Naval Air Warfare Center Weapons Division, Point Magu, California, October 2013

[9] Rudduck, R. C., Walter, C.H., "Luneberg *(sic)* Lenses for Space communications", IRE Transactions of Space Electronics and Telemetry, 1962

[10] "F-22 enters the network – Linking IFDL, TTNT, Link-16", Defence Update online magazine article, May 28, 2008

[11] "Beam Forming Networks", EMS Technologies Whitepaper, August 2004

[12] Lotter, P., M., van Rooyen, P., "An overview of Space Division Multiple Access techniques in cellular systems", Proceedings of the 1998 South African Symposium on Communications and Signal Processing COMSIG, 1998, pp. 161-164

[13] Ilcev, S., D., “Space Division Multiple Access (SDMA) applicable for Mobile Satellite Communications”, 10th International Conference on Telecommunication in Modern Satellite Cable and Broadcasting Services, October 2011, Volume 2, pp. 693-696

[14] “Technical Specification Group Services and System Aspects; General Universal Mobile Telecommunications System (UMTS) architecture (Release 13)”, 3GPP TS 23.101 V13.0.0, 2015

[15] Ming, D., Luo, H., “Multi-point cooperative communication systems: theory and applications”, Springer, 2013, ISBN 978-3-642-34948-5

[16] Morgan, S., P., “General solution of the Luneburg lens problem”, Journal of Applied Physics, Volume 29, No. 9, September 1958, pp. 1358–1368

[17] “L-3 Communications: Datron advanced technologies capabilities presentation”, on-line datasheet presentation, 2013

This page intentionally blank to aid printing.

Chapter 6

Consideration of the Performance of the System

6.1 Overview

The ‘moving-cells-in-the-sky’ approach defined in Section 5 demonstrates a solution to the problem of improving on limited spectrum capacity and efficiency in the high altitude low orbit environment, and provides a solution to the problem as highlighted in Section 1.

This Section focuses on the performance of the approach using the path loss model described in Section 4, with the frequency and altitude datasets identified in Section 3, and compares these results with the performance of point-to-point beams, beam forming and MIMO approaches.

In this Section the software model built for this thesis in Section 3 (with code provided in Appendix A) automatically takes into the ITU-R standards and parameters to include for the various altitudes, orbits, frequencies and signal slant angles as defined in the standards.

6.2 Boundaries of the problem – derivation of a satellite constellation

To demonstrate comparative results for the proposed solution described in Section 5, this sub-section focusses on the derivation of a typical satellite constellation that was used as a comparator for the ‘moving-cells-in-the-sky’ approach with point-to-point, beamforming and MIMO approaches.

In Section 3 were identified the typical values for spacecraft orbital altitude, aircraft/UAV/RPAS altitudes, and available frequencies. The following charts (Figure 6.1, Figure 6.2) illustrate the boundaries of the path loss attenuation for these typical values for Earth-to-space and space-to-Earth links. For the aircraft/UAV/RPAS/ground platform, an antenna diameter of 0.6 m is assumed. The

atmospheric model is as defined in Section 4 and includes all impairments -rain, clouds/fog, gaseous absorption, and tropospheric and ionospheric attenuation - for Earth averaged values across the frequency limits as described in detail in Section 4.

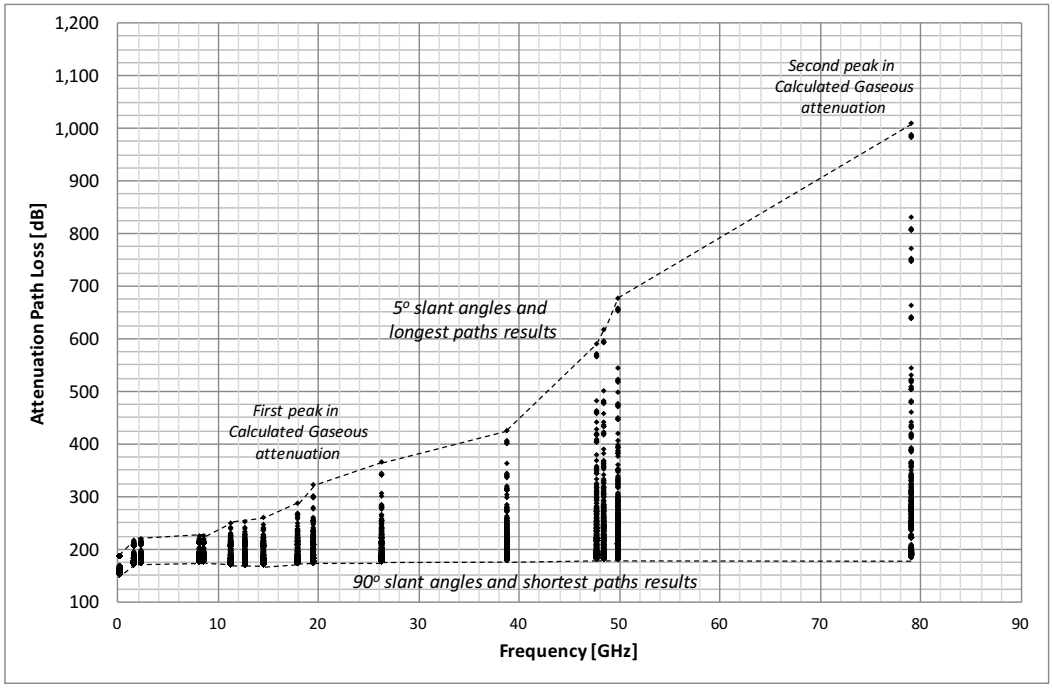

Figure 6.1 – Boundary of the path loss attenuation across typical spacecraft, aircraft/UAV/RPAS altitudes and available frequencies (Section 3) for space to Earth links including attenuation factors across the frequencies modelled by the ITU-R standards for atmospheric attenuation (Section 4)

Two things are clear from these results:

1. There is little difference in attenuation across the frequency range for zenith, or close to zenith slant angles for typical altitude and orbit values of platforms or cases with relatively short paths.
2. At low slant angles toward the horizon, or for slant angles up to zenith that have long path lengths to high orbits, attenuation increases dramatically with frequency.

The obvious approach would be, from these results, to have a configuration with ground and platform communication paths in which there were sufficient satellites to provide close-to-zenith paths to each satellite in order to reduce the path loss. And

since the ‘cells in the sky’ solution requires multiple satellites to take advantage of the available signal gain, this pushed towards a requirement for a constellation with a very large number of satellites.

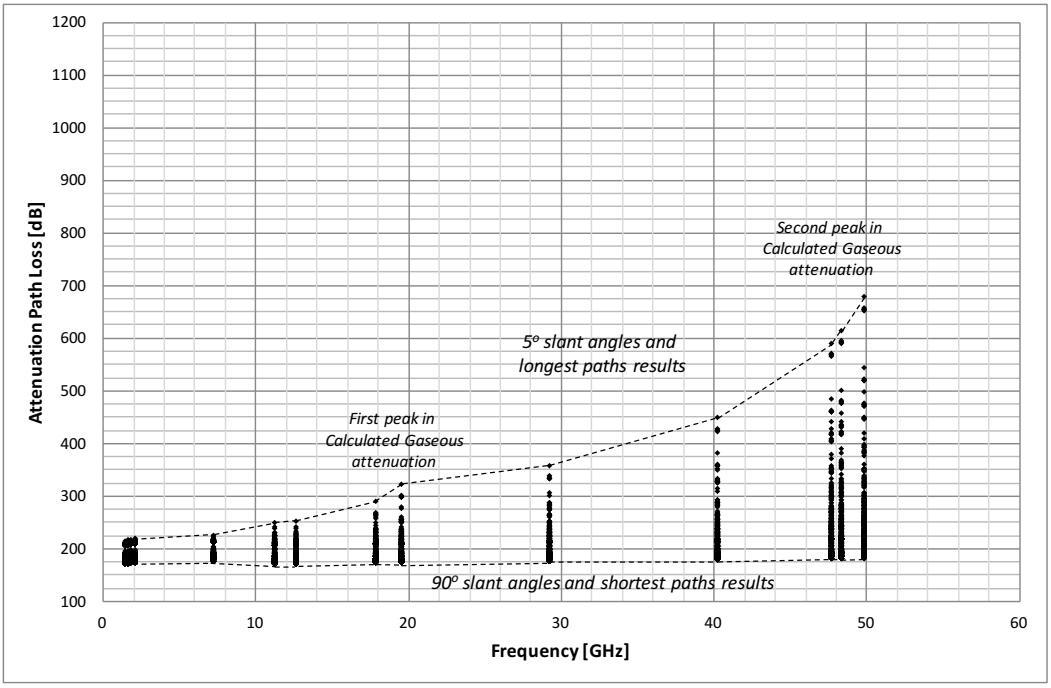

Figure 6.2 – Boundary of the path loss attenuation across typical spacecraft, aircraft/UAV/RPAS altitudes and available frequencies (Section 3) for Earth to Space links including attenuation factors across the frequencies modelled by the ITU-R standards for atmospheric attenuation (Section 4)

As noted in Section 2, in the discussion of existing satellite constellations, the higher the orbit the lower the number of satellites required to provide full Earth coverage. But then, as orbital altitude is increased there would be an increase in the path loss attenuation, particularly for low slant angle satellites. There is a trade off with respect to the most appropriate orbital altitude.

To consider this trade off a STK simulation model was constructed to visualise the effects of altitude and number of satellites in a constellation and the overpass opportunities for a fixed position on the Earth. For the simulation, Goonhilly Earth Station was chosen as a typical non-equatorial ground station.

Assuming an initial orbital altitude of 630km (defined as the lowest orbit in the list of orbital altitudes in Section 3), and assuming 3 satellites with the same orbital parameters of 630 km altitude, 95º inclination (to improve non collision statistics over the poles), 0º RAAN (Right Ascension of the Ascending Node), and with 10º true anomaly between them. This would require a constellation of 1,296 satellites for full Earth coverage, assuming 10º plane separation. This size of constellation is similar to those proposed by OneWeb and SpaceX, for example (see Section 2 for details of the various satellite constellations).

For a near overhead pass of the Goonhilly Earth Station, the three satellites would be visible as shown in Figure 6.3. The simulation was run from 1 January 2016 to 1 January 2020.

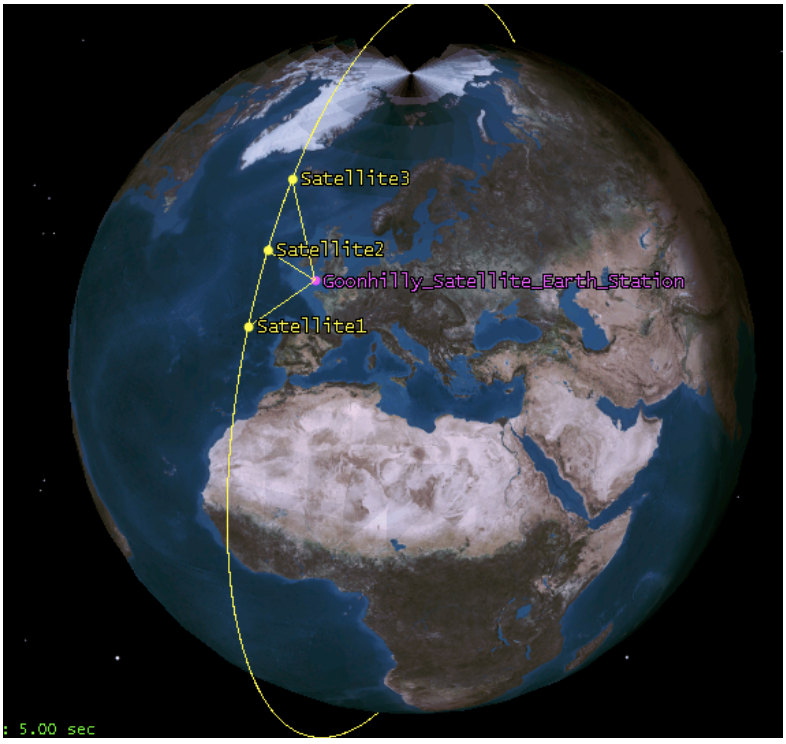

Figure 6.3 – STK simulation of three satellites at 630 km altitude, 95º inclination, 0º RAAN, and 10º along orbit separation (by true anomaly) connecting with a ground station at Goonhilly, UK

Global Statistics			
Min Duration	Pass #9120	27 Aug 2019 06:24:01.935	4.914 sec

Max Duration	Pass #8299	29 Apr 2019 00:47:29.625	797.828 sec
Mean Duration			620.274 sec

Table 6.1 – Simulation results for 630 km orbit (as described in the text)

The simulation results show that at 630 km altitude, there are 6 passes over Goonhilly Earth Station per day by each satellite, with a mean duration of 10.39 minutes in view of the receiver (Table 6.1).

The path lengths from Goonhilly Earth Station to the satellites at +/-10º along the orbit track can be calculated using the `slantPathLengthFunction()` (sine rule calculation of angle) from Section 4, and the corresponding *slantAngle* of 23.3º (that is, +/- 66.7º from Earth station Zenith), which can be found geometrically using the approach described in Section 4.

This does of course mean that there could be up to 5 satellites visible to the ground station however, these additional satellites would be below 5º above the horizon (4.95º), and thus out of the range of the simulation calculations.

Given that in a full simulation there would be adjacent orbital planes, the actual number of satellites visible would be nine. However, the case above refers to one orbital plane containing three satellites for illustration. The path lengths from a ground station are as shown in Table 6.2.

Satellite #1 *(630* km*)*	-10º along orbit	1323.79 km
Satellite #2 *(630* km*)*	0º (zenith)	630.0 km
Satellite #3 *(630* km*)*	+10º along orbit	1323.79 km

Table 6.2 – Path lengths to the three satellites in the 630 km orbit constellation

Figure 6.4 shows the attenuation path loss across the space to Earth frequencies, and Figure 6.5 for Earth to space, as calculated using the ITU-R model in Section 4, of the three satellites with path lengths as Table 6.2 and slant angles of -23.3º, +90.0º, +23.3º (that is -10º, 0º, +10º along the orbital track).

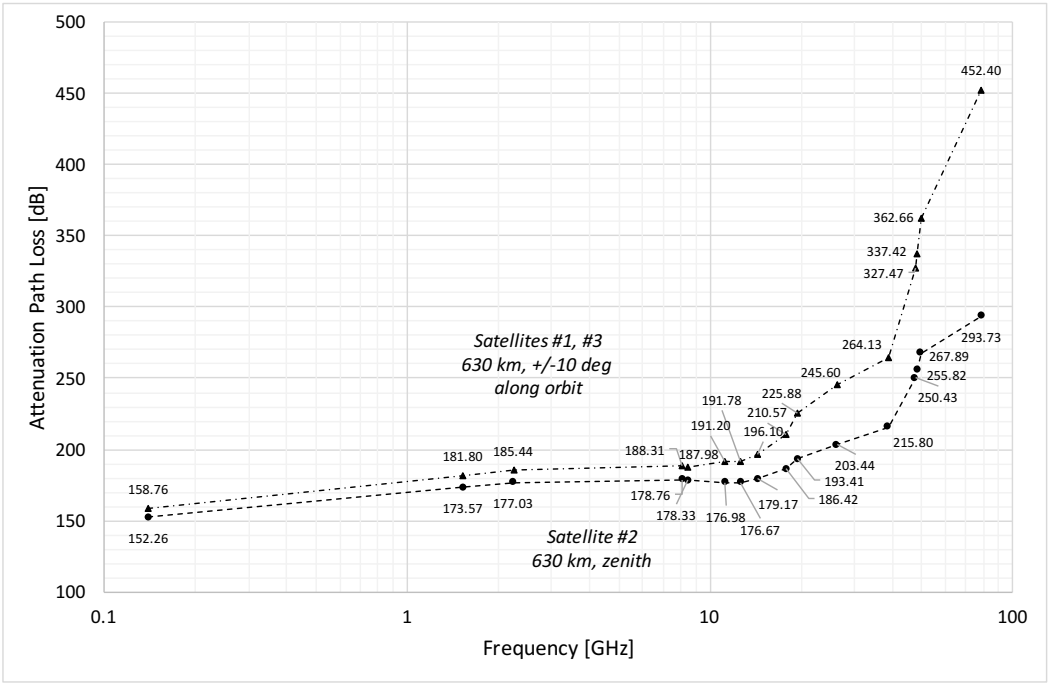

Figure 6.4 – Path loss simulation, with space to Earth frequencies (derived in Section 3), of the three satellites at 630 km altitude, 95º inclination, 0º RAAN, and 10º along orbit separation connecting with a ground station

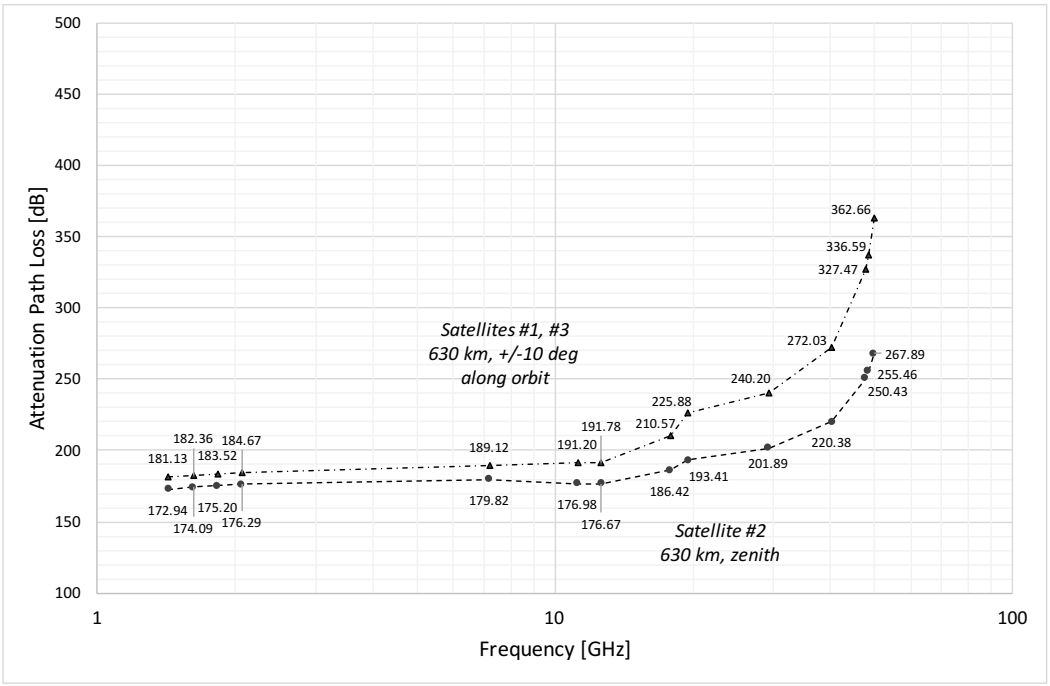

Figure 6.5 – Path loss simulation, with Earth to space frequencies (derived in Section 3), of the three satellites at 630 km altitude, 95º inclination, 0º RAAN, and 10º along orbit separation connecting with a ground station

The frequency selected for the performance comparison and trade-off was taken as the minimum attenuation path loss at the highest frequency for Earth to space and space to Earth path loss as identified in both Figure 6.4 and Figure 6.5. This occurs at 12.625 GHz in the lower Ku band. This is the centre frequency of the licensed 12.5 GHz to 12.75 GHz satellite band, which may be used for Earth to space, or space to Earth communication.

The path lengths in Table 6.2 were used, along with the model developed in Section 4, and the frequencies identified in Section 3, to derive the path loss attenuation for each path (Table 6.3).

Satellite #1 *(630* km*)*	-10^{o} along orbit	191.78 dB
Satellite #2 *(630* km*)*	0^{o} (zenith)	176.77 dB
Satellite #3 *(630* km*)*	+10^{o} along orbit	191.78 dB

Table 6.3 – Path attenuation to the three satellites in the 630 km orbit constellation

To support the trade-off, the simulation and calculations were re-run for the highest LEO orbit defined in the list of orbital altitudes in Section 3, at 1,400 km. Figure 6.6 shows the results for a near overhead pass of the Goonhilly Earth Station with three satellites visible at 10^{o} separation along the orbit path. The simulation was run from 1 January 2016 to 1 January 2020.

The simulation results show that at 1,400 km altitude, there are 10 passes over Goonhilly Earth Station per day by each satellite, with a mean duration of 15.6 minutes in view of the receiver (Table 6.4).

Global Statistics			
Min Duration	Pass #6293	11 Sep 2017 03:25:12.347	20.506 sec
Max Duration	Pass #10895	7 Dec 2018 02:14:56.849	1322.022 sec
Mean Duration			936.284 sec

Table 6.4 – Simulation results for 1,400 km orbit

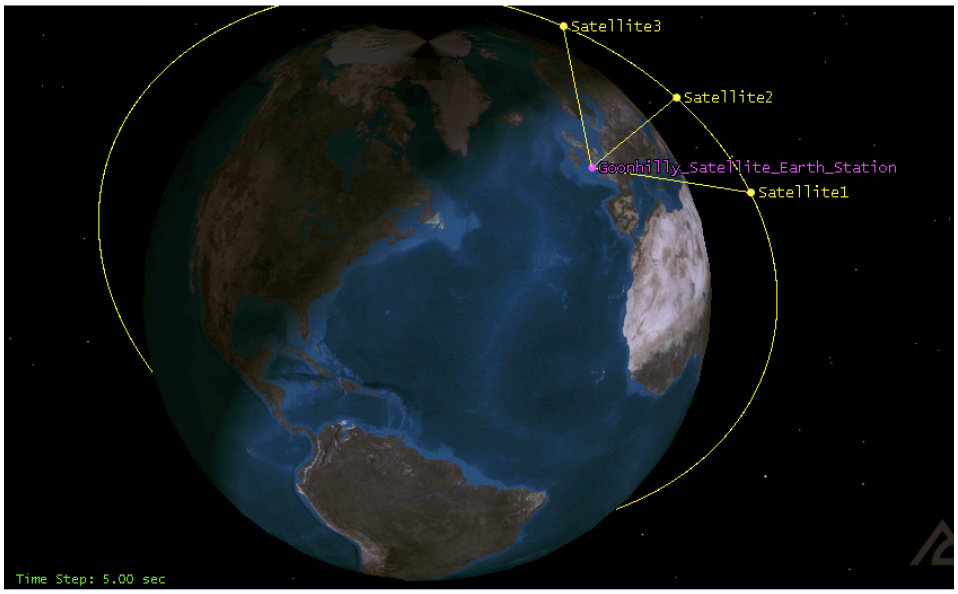

Figure 6.6 – STK simulation of three satellites at 1,400 km altitude, 95º inclination, 0º RAAN, and 10º along orbit separation connecting with a ground station at Goonhilly, UK

With a 1,400 km orbit, +/- 10º along orbit equates to a slant angle above the horizon of 43.5º, further, +/- 20º equates to 19.3º, and +/- 30º to 5.27º. It would therefore be possible, with similar plane separations of +/- 10º, 20º, 30º to be able to view 21 satellites from a ground station. A constellation with these parameters would require 1,296 satellites.

To keep the comparison straightforward between the 630 km and 1,400 km orbits, only the +/- 20º along orbit path satellites were considered at 1,400 km in the trade-off for orbital altitude. This results in the two orbital altitudes having similar slant angles of 23.3º at 630 km, compared with 19.3º at 1,400 km. The result is a constellation size of 324 satellites at 1,400km.

The path lengths from Goonhilly Earth Station to the satellites at +/-20º along the orbit track at the 1,400 km orbit can be calculated using the `slantPathLengthFunction()` (sine rule calculation of angle - from Section 4, for the corresponding *slantAngle* of 19.3º (that is, +/- 70.7º from Earth station zenith), which can be found trigonometrically using the approach described in Section 4.10.

Given that in a full simulation there would be adjacent orbital planes, the actual number of satellites visible would be nine. However, the case above refers to one orbital plane containing three satellites for illustration.

The path lengths are as shown in Table 6.5. Figure 6.7 shows the attenuation path loss for the space to Earth frequencies, and Figure 6.8 for Earth to space. Table 6.6 provides the calculated path loss attenuation.

Satellite #1 *(1,400* km*)*	-20^{o} along orbit	2,816.98 km
Satellite #2 *(1,400* km*)*	0^{o} (zenith)	1,400.0 km
Satellite #3 *(1,400* km*)*	+20^{o} along orbit	2,816.98 km

Table 6.5 – Path lengths to the three satellites in the 1,400 km orbit constellation

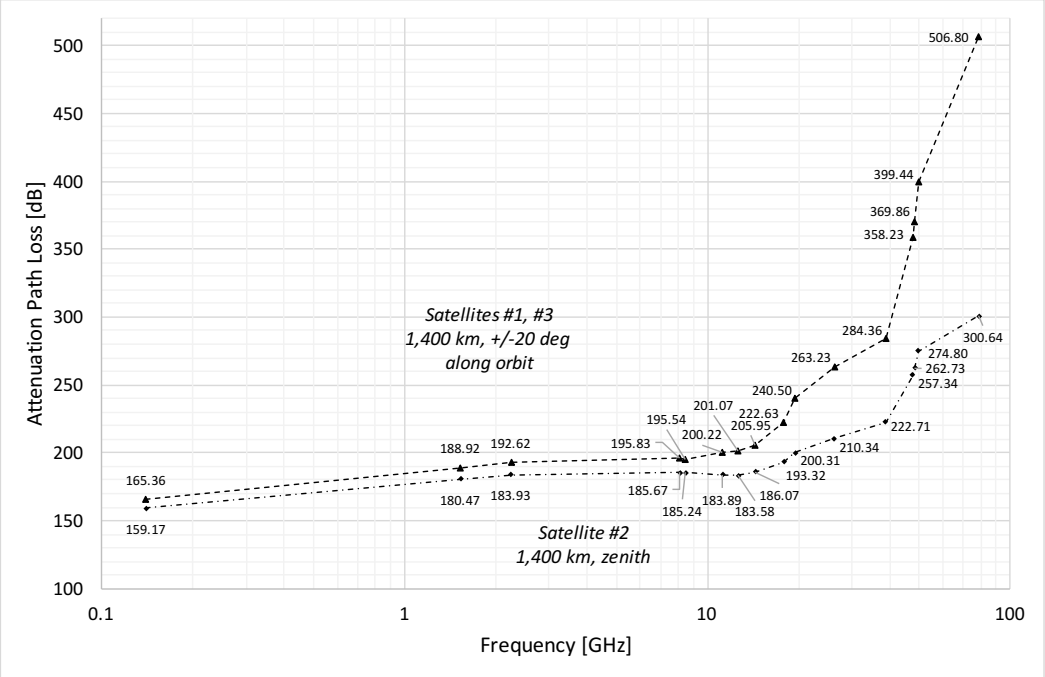

Figure 6.7 – Path loss simulation, with space to Earth frequencies (derived in Section 3), of the three satellites at 1,400 km altitude, 95^{o} inclination, 0^{o} RAAN, and 20^{o} along orbit separation connecting with a ground station

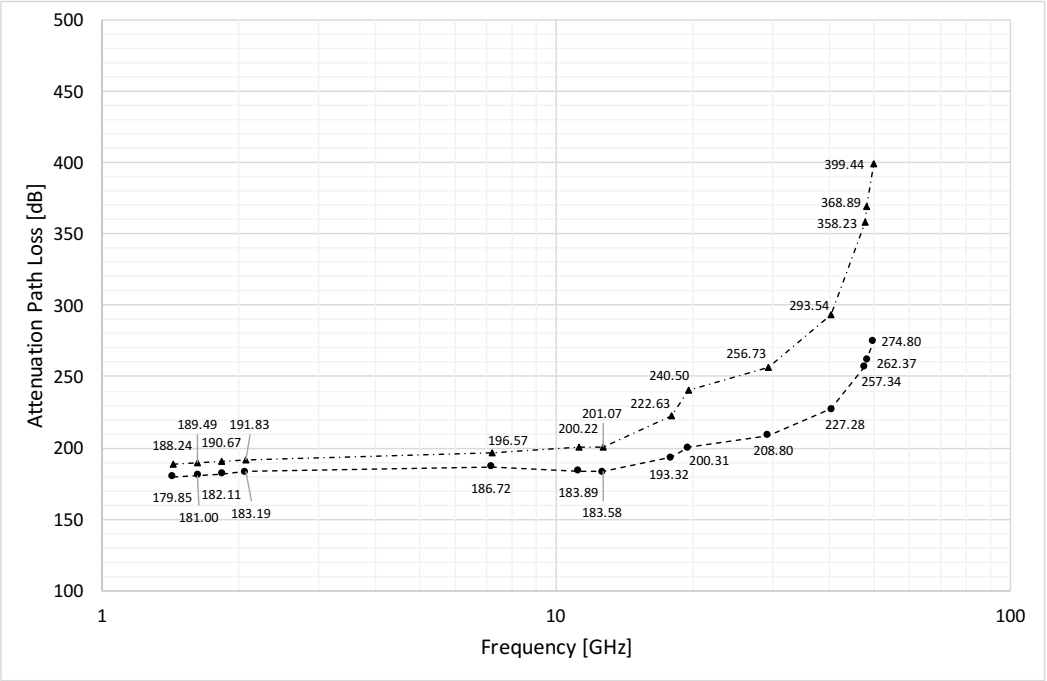

Figure 6.8 – Path loss simulation, with Earth to space frequencies (derived in Section 3), of the three satellites at 1,400 km altitude, 95^{o} inclination, 0^{o} RAAN, and 20^{o} along orbit separation connecting with a ground station

Satellite #1 *(1,400* km*)*	-20^{o} along orbit	201.07 dB
Satellite #2 *(1,400* km*)*	0^{o} (zenith)	183.58 dB
Satellite #3 *(1,400* km*)*	+20^{o} along orbit	201.07 dB

Table 6.6 – Path attenuation to the three satellites in the 1,400 km orbit constellation

6.3 Comparison of low versus high LEO for scenario constellation

As shown in Table 6.7, the difference in orbit altitude from low LEO at 630 km to high LEO at 1,400 km is a dramatic reduction in the number of satellites required to provide a constellation. Though this reduction leads to an increase in path length, the penalty in attenuation path loss is only 8 dB.

For the performance analysis following in this Section, the model constellation used for comparison consisted of 18 planes of 18 satellites with 20^{o} separation along the orbit path, and between the orbital planes.

Orbital Altitude [km]	Constellation #satellites	Satellite location along orbit [^{o}]	Slant angle above horizon [^{o}]	Path length [km]	Attenuation path loss [dB]
630	1,296	-10	23.3	1,323.79	191.78
		0.0	90.0	630.0	176.77
		+10	23.3	1,323.79	191.78
1,400	324	-20	19.3	2,816.98	201.07
		0.0	90.0	1,400.0	183.58
		+20	19.3	2,816.98	201.07

Table 6.7 – Comparison of the characteristics of low and high LEO orbits for the scenario constellation

6.4 Scenario for comparing performance of the 'moving cells-in-thee-sky' approach

To compare the 'moving cells in the sky' approach with point-to-point communications and MIMO solutions the satellite constellation model derived in Section 6.3 was used. Three satellites in a 1,400 km orbit with 20^{o} orbital path separation transmitting in the licensed 12.5 GHz to 12.75 GHz satellite Ku band.

The scenario for the performance comparison extended this model by adding from the dataset derived in Section 3 an aircraft at 11 km (~ 36,000 ft), and adding two UAVs; one at 20 km (~ 65,000 ft), and another at 5 km (~ 16,000 ft). Assuming that the three platforms are operating at, respectively, -19.3^{o} from zenith, zenith, and +19.3^{o} from zenith. Where zenith represents the ground location of an Earth station (Figure 6.9). The Earth station contains a user ground communication terminal.

For the communications links, bandwidths are assumed to be formed from 100 MHz allocated to downlink from the satellites (12.6 GHz to 12.7 GHz) and 100 MHz allocated to the uplink from the satellites (12.5 GHz to 12.6 GHz). Frequency re-use is assumed to be within the 100 MHz bandwidths. Transmission power from platforms is assumed to be 10 W (uplink to satellites), and from each satellite of up

to 25 W (downlink) for each transmitter; losses were assumed to be negligible. Issues of power management for large arrays at this power were not considered in the performance analysis.

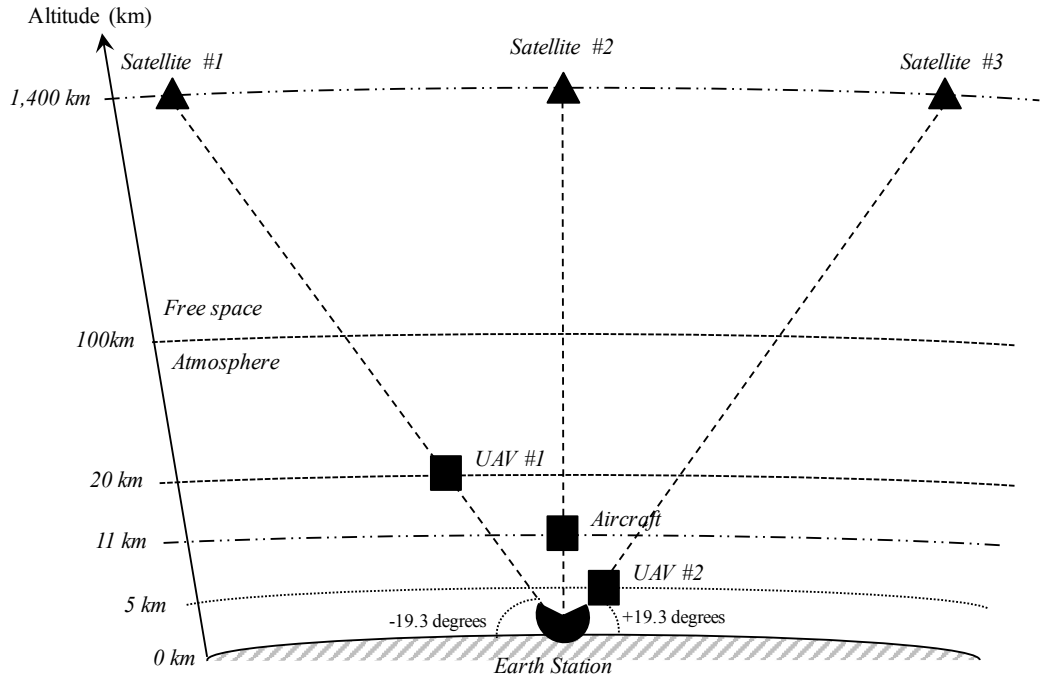

Figure 6.9 – Scenario for comparing performance

6.5 Performance of a point-to-point communications approach

In a point-to-point satellite communication system, the aircraft, UAV and user ground station would perhaps first listen out for beacons from each of the satellites in order to determine which satellites to communicate with. In order to identify each satellite, and given that in general there is no satellite to satellite communication, each satellite link would need to have its own frequency allocation.

For the scenario described above (Section 6.4) this results in each satellite of the 324 constellation being allocated 100 MHz / 324 = 0.309 kHz of bandwidth.

If we improve this by using frequency re-use across the constellation of 9 (that is, 3 satellites x 3 adjacent planes) as illustrated in Figure 6.10, the frequency allocation

per satellite increases to 100 MHz / 9 = 11.111 MHz. This value was used in the performance comparison.

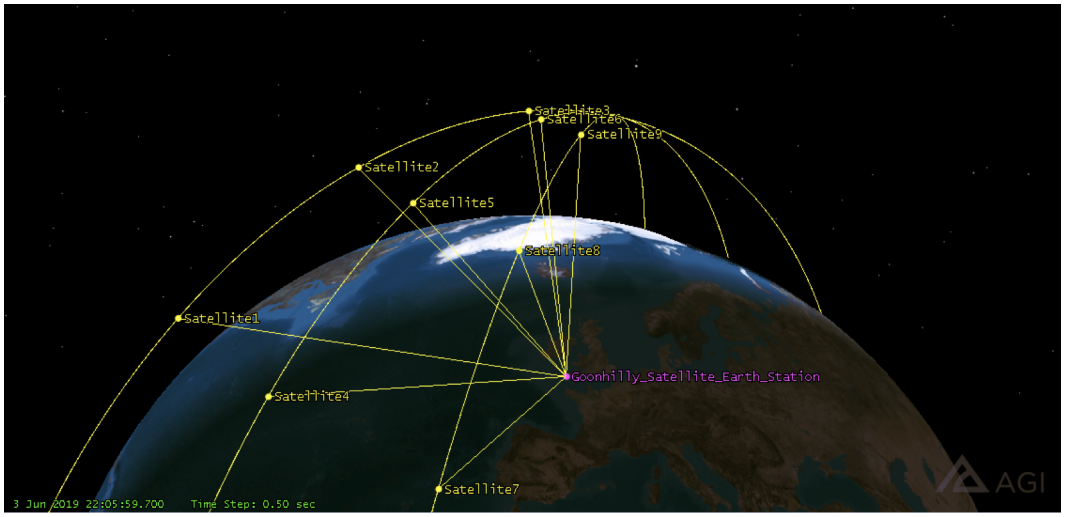

Figure 6.10 – Illustration of the paths of a nine satellite frequency repeat pattern as three satellites along each orbit with 20º separation, and 20º separation between planes (model in the text excludes polar convergence) with inclination of 95.0º and connected to a ground station (STK simulation)

As a real-World example of such a point-to-point satellite, consider the O3b satellite shown in Figure 6.11, described in detail in Section 2.3.10. The transmission dishes are approximately 0.45m in diameter. For the receivers, we can assume a similar dish antenna. This leads to a beam width of 3.7º. For uplink a noise temperature of 100K is assumed (based on *Kraus*, as described in Section 4.20), with 293K for downlink.

For each aircraft, UAV and user ground station identifying a particular satellite with which it can communicate there are in the best case, for the scenario being considered, three satellites independently connected to the three platforms (UAV #1, Aircraft and UAV #2) with UAV #2 and the ground station connected to one satellite (#3) (see Figure 6.9 above).

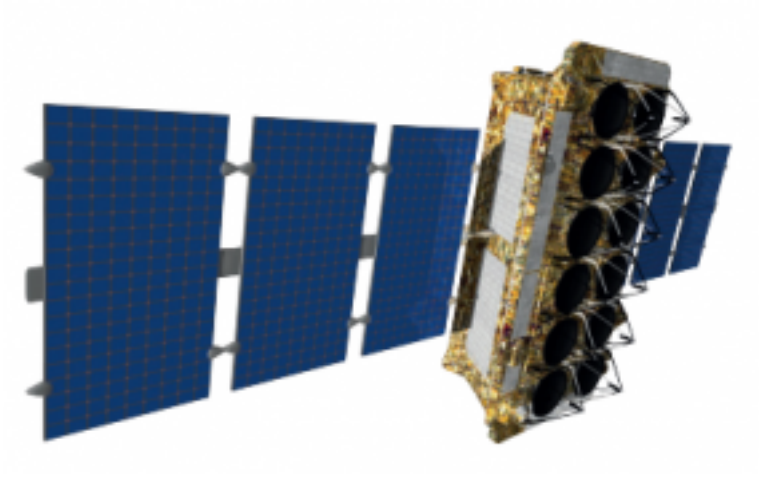

Figure 6.11 – Satellite with multiple steerable point-to-point beams
(credit: SES-O3b, Thales Alenia Space)

This requires that satellite #3 operate multiple access on transmit and receive (assuming 50/50 time division communication for two platforms' connections in this scenario). This would be true to a greater extent on the O3b satellite since overlapping the beams would require each to use different frequency allocation. In the scenario described here we assume one beam on one satellite handles the two platforms, as this makes a more realistic comparison scenario, and can be modelled by halving the data rate for those platforms.

Using these values, the path lengths and path loos attenuation values can be calculated (Table 6.8).

From	To	Path length [km]	Path loss [dB]
Satellite #1	UAV #1	2,787.22	183.45
Satellite #2	Aircraft	1,393.55	177.51
Satellite #3	Ground user terminal	2,816.98	201.07
Satellite #3	UAV #2	2,809.55	192.25

Table 6.8 – Path attenuation between each of the satellites and platforms for point-to-point communication at a centre frequency of 12.625 GHz

Using the values in Table 6.8 the data rate at each platform for a point to point link can be calculated using the channel model described in Section 4, with all

atmospheric attenuation impairments included, and assuming BPSK only modulation (Table 6.9). A noise temperature of 293K on the downlink, and 100K on the uplink is assumed.

From	To	Frequency [GHz]	Data Rate [Mbps]
Satellite #1	UAV #1	12.600,000	196.80
Satellite #2	Aircraft	12.611,111	262.9
Satellite #3	Ground terminal	12.622.222	0.69
Satellite #3	UAV #2	12.633.333	49.770
UAV #1	Satellite #1	12.500,000	202.93
Aircraft	Satellite #2	12.511,111	269.10
Ground terminal	Satellite #3	12.522,222	3.75
UAV #2	Satellite #3	12.533,333	52.83

Table 6.9 – Maximum data rate between each of the satellites and platforms for point-to-point communication in the scenario described in the text

Though in some cases there was enough margin for higher order modulation schemes, only the results for BPSK are presented to allow comparison with other techniques in this Section. Total spectrum usage for all satellites in a point-to-point constellation configuration does not exceed 200 MHz (100 MHz for uplinks. 100 MHz for downlinks).

6.6 Performance of a MIMO communications approach

In the case of MIMO from one satellite there is no performance gain beyond that described in Section 6. And as discussed in Section 2, MIMO has little advantage beyond diversity gain because the spatial multiplexing can only occur due to multipath between clutter at ground level.

However, as noted for the ‘moving-cells-in-the-sky’ approach, the introduction of communication between satellites allows for multi-user cooperative MIMO (called CoMP – Cooperative Multi-Point) which does provide the spatial separation needed

to make use of MIMO approaches. Details of the different forms of MIMO are described in Section 2.

For Multi-User MIMO, which could be utilised in the scenario, there is the issue of requiring closed loop knowledge of the channel in order to optimise the beam shaping through manipulation of the transmit parameters based on fed-back knowledge of the overall channel matrix (*H*); as described in Section 2.

Without closed loop control MU-MIMO becomes extremely difficult and the performance reduces for the open loop case. By comparison however, the 'moving-cells-in-the-sky' approach can operate open-loop.

6.7 Performance of a 'moving-cells-in-the-sky' communications approach

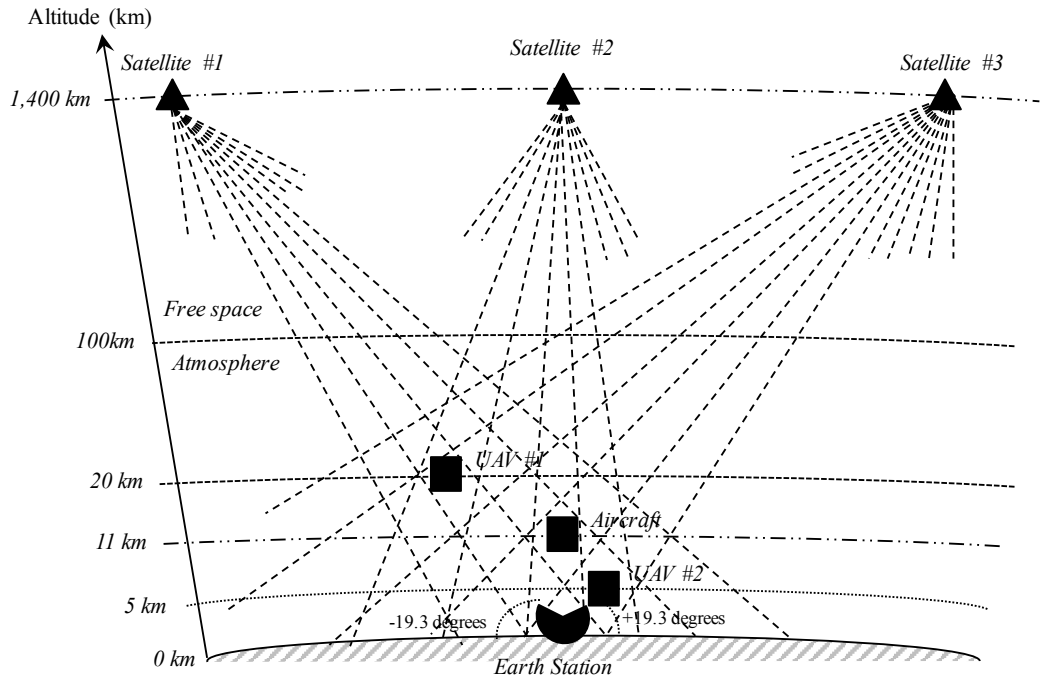

Figure 6.12 – Performance comparison scenario illustrating the lens antenna beams that form wedges which then combine to form 'moving-cells-in-the-sky'

The above diagram (Figure 6.12) recasts the performance comparison scenario diagram in Figure 6.9 with the addition of satellite transmission from lens antenna structures on an illustrative 3.7^{o} wedge angle, in order to simplify comparison with point-to-point communication and other techniques. The wedges intersect to form 'moving-cells-in-the-sky'.

The ‘moving-cells-in-the-sky’ approach is based on DSSS-CDMA with SDMA, with frequency re-use, and a system architecture using the connectivity features of CoMP-MIMO, as described in Section 5.

6.7.1 SDMA - Space Division Multiple Access

The space division structure is illustrated in Figure 6.12. If we assume 10^{o} from orbit tangent to 170^{o} from orbit tangent and assume the lens antenna has 3.7^{o} apertures, then each satellite has 43 beams. For the scenario, it is assumed that the nadir beam is central within a wedge.

Simplifying Figure 6.12 to show only the signal paths from each satellite to each platform results in Figure 6.13. Where each platform now has three communication paths. The path lengths have been calculated based on the geometry of the scenario (Table 6.10).

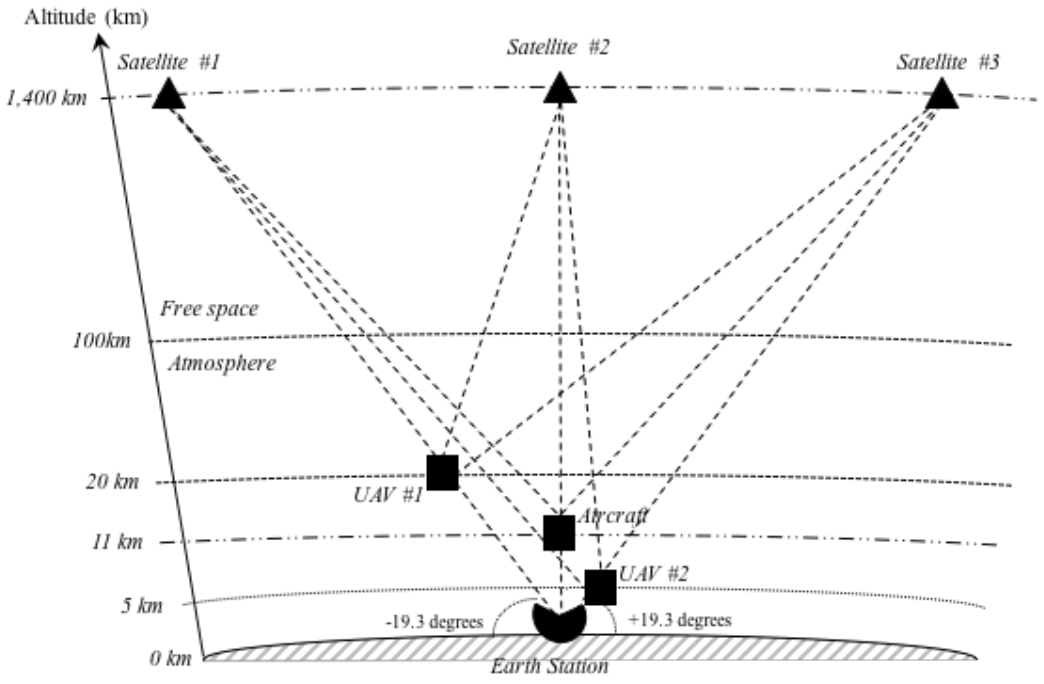

Figure 6.13 – Simplified scenario diagram with direct paths shown

From	To	Platform Altitude [km]	Slant Angle [^{o}]	Path length [km]
Satellite #1	UAV #1	20	19.3	2,787.22
Satellite #1	Aircraft	11	19.1	2,812.67
Satellite #1	UAV #2	5	19.2	2,815.57
Satellite #1	Ground station	0	19.3	2,816.98
Satellite #2	UAV #1	20	87.6	1,381.00
Satellite #2	Aircraft	11	90.0	1,389.00
Satellite #2	UAV #2	5	89.4	1,395.06
Satellite #2	Ground station	0	90.0	1,400.00
Satellite #3	UAV #1	20	18.8	2,817.44
Satellite #3	Aircraft	11	19.1	2,812.67
Satellite #3	UAV #2	5	19.3	2,809.55
Satellite #3	Ground station	0	19.3	2,816.98

Table 6.10 – Path length between each of the satellites and platforms

6.7.2 Frequency re-use

The process for attachment of each non-satellite platform to a satellite is described in Section 5.8. Following RACH attach and coordination of information between the network controller elements (c.f. RNC) of each satellite. If we assume a two frequency repeat across the wedges, and different frequencies for each satellite, then the 3 satellite scenario requires 6 frequencies, or 36 frequencies if the additional satellite planes are included (that is, 3 satellites, three planes, 2 frequencies per satellite; with satellites numbered #1 to #9). This results in each wedge being allocated 100 / 36 = 2.778 MHz. But since there are 43 beams per satellite that equates to an aggregate 43 x 2.778 = 119.454 MHz per satellite all accessible simultaneously through the lens antenna and its 43 multiple feeds, in the 3 satellite along orbital track case. Including the orthogonal direction would multiply this to a total of 1,849 beams per satellite.

The path loss for each communication between platform and satellite is given in Table 6.11 (downlinks) and Table 6.12 (uplinks).

From	To	Frequency [GHz]	Path loss [dB]
Satellite #1	UAV #1	12.600,000	183.44
Satellite #1	Aircraft	12.602,778	183.88
Satellite #1	UAV #2	12.602,778	192.30
Satellite #1	Ground station	12.600,000	201.02
Satellite #2	UAV #1	12.605,556	177.29
Satellite #2	Aircraft	12.605,556	177.50
Satellite #2	UAV #2	12.608,334	180.30
Satellite #2	Ground station	12.605,556	183.55
Satellite #3	UAV #1	12.611,112	183.54
Satellite #3	Aircraft	12.611,112	183.89
Satellite #3	UAV #2	12.613,890	192.24
Satellite #3	Ground station	12.613,890	201.05

Table 6.11 – Path loss between each of the satellites and platforms (downlink frequencies)

To	From	Frequency [GHz]	Path loss [dB]
Satellite #1	UAV #1	12.500,000	183.37
Satellite #1	Aircraft	12.502,778	183.81
Satellite #1	UAV #2	12.502,778	192.22
Satellite #1	Ground station	12.500,000	200.82
Satellite #2	UAV #1	12.505,556	177.22
Satellite #2	Aircraft	12.505,556	177.43
Satellite #2	UAV #2	12.508,334	180.23
Satellite #2	Ground station	12.505,556	183.43
Satellite #3	UAV #1	12.511,112	183.47
Satellite #3	Aircraft	12.511,112	183.82
Satellite #3	UAV #2	12.513,890	192.17
Satellite #3	Ground station	12.513,890	200.84

Table 6.12 – Path loss between each of the satellites and platforms (uplink frequencies)

The path loss values are calculated using the model developed in Section 4 and including all atmospheric impairments. Downlinks assume 293K noise temperature, and uplinks 100K.

6.7.3 CoMP-MIMO like connectivity

Now, since each platform can connect with multiple satellites, the aircraft platform, for example, has access to 9 x 2.778 = 25.002 MHz. For situations where there is more than one platform in a wedge; in the scenario of Figure 6.12, that includes most of the platforms, the DSSS approach results in a lowering of the overall data rate, but because of the spread spectrum nature of the signals there is no increase in latency, and no reduction in the accessible bandwidth. There is, of course, a reduction in the data rate, modelled here as a multiplier reduction by the number of platforms in the wedge.

6.7.4 Scenario performance calculation

As in the point-to-point case, and using the path loss values of Tables 6.11 and 6.12, the data rate at each platform can be calculated using the model described in Section 4, and assuming BPSK only. Total spectrum usage for all satellites in a 'moving-cells-in-the-sky' configuration does not exceed 200 MHz (100 MHz for uplinks. 100 MHz for downlinks). The data rate is calculated based on the sum of the signals that are available from multiple satellites, divided by the number of platforms within each shared wedge, in order to emulate a combined signal value for each platform (Table 6.13).

From	To	Frequency [GHz]	Data Rate [Mbps]
Satellite #1	UAV #1	12.600,000	32.979
Satellite #1	Aircraft	12.602,778	64.747
Satellite #1	UAV #2	12.602,778	41.356
Satellite #1	Ground station	12.600,000	8.561
Satellite #2	UAV #1	12.605,556	83.064
Satellite #2	Aircraft	12.605,556	41.251

Satellite #2	UAV #2	12.608,334	74.713
Satellite #2	Ground station	12.605,556	32.837
Satellite #3	UAV #1	12.611,112	65.723
Satellite #3	Aircraft	12.611,112	64.751
Satellite #3	UAV #2	12.613,890	20.783
Satellite #3	Ground station	12.613,890	8.545

Table 6.13 – Maximum data rate between each of the satellites and platforms for 'moving-cells-in-the-sky' (downlink) communication in the scenario described in the text

The overall data rate for the downlink to each platform is now calculated by summing the data rates from the three satellites to each platform. Since there are nine satellites in the frequency repeat cluster these values can be further multiplied by three representing additional data rate via wedges on the other satellites in the nine satellite cluster (Table 6.14).

From	To	Data Rate [Mbps] 3-satellites	Data Rate [Mbps] 9-satellite cluster
Satellites	UAV #1	181.766	545.299
Satellites	Aircraft	170.748	512.245
Satellites	UAV #2	136.852	410.555
Satellites	Ground station	49.943	149.829

Table 6.14 – Maximum data rate between each of the satellites and platforms for 'moving-cells-in-the-sky' (downlink) taking into account summation of data rates and including signals from other satellites in the 9-satellite cluster

Tables 6.14 and 6.15 provide the same calculations for the uplink data rate performance.

To	From	Frequency [GHz]	Data Rate [Mbps]
Satellite #1	UAV #1	12.500,000	27.259
Satellite #1	Aircraft	12.502,778	53.307
Satellite #1	UAV #2	12.502,778	29.917

Satellite #1	Ground station	12.500,000	2.841
Satellite #2	UAV #1	12.505,556	71.625
Satellite #2	Aircraft	12.505,556	35.532
Satellite #2	UAV #2	12.508,334	63.274
Satellite #2	Ground station	12.505,556	27.117
Satellite #3	UAV #1	12.511,112	54.284
Satellite #3	Aircraft	12.511,112	53.312
Satellite #3	UAV #2	12.513,890	15.063
Satellite #3	Ground station	12.513,890	2.826

Table 6.15 – Maximum data rate between each of the satellites and platforms for 'moving-cells-in-the-sky' (uplink) communication in the scenario described in the text

From	To	Data Rate [Mbps] 3-satellites	Data Rate [Mbps] 9-satellite cluster
Satellites	UAV #1	153.169	459.506
Satellites	Aircraft	142.151	426.452
Satellites	UAV #2	108.254	324.761
Satellites	Ground station	32.784	98.353

Table 6.16 – Maximum data rate between each of the satellites and platforms for 'moving-cells-in-the-sky' (uplink) taking into account summation of data rates and including signals from other satellites in the 9-satellite cluster

6.8 Performance of a beamformed communications approach

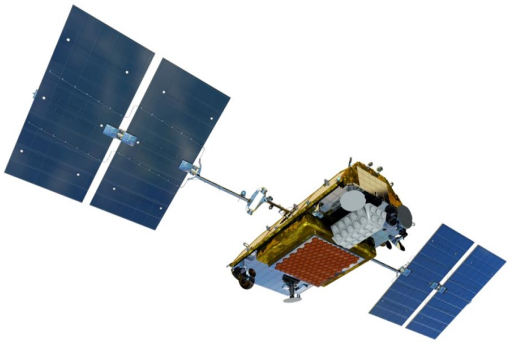

Figure 6.14 – Satellite with beamformed antenna array
(credit: Iridium, Thales Alenia Space)

The two types of beamforming were considered in the performance comparison. These being time domain and frequency domain beamforming. An example of a beamforming antenna satellite is the IridiumNext shown in Figure 6.14 and described in detail in Section 2.3.7.

6.8.1 Time-domain beamforming

Time domain beamforming is primarily a time domain phasing of signals across a set of antennas making up the aperture of an array in order to produce geometric pointing of the transmitted signal in the far field (Figure 6.15).

For the performance scenario illustrated in Figure 6.9 such a beamforming system would provide only one beam per satellite, and without coordination between satellites would require a time division multiplexing of the beam to different platforms in a single beam.

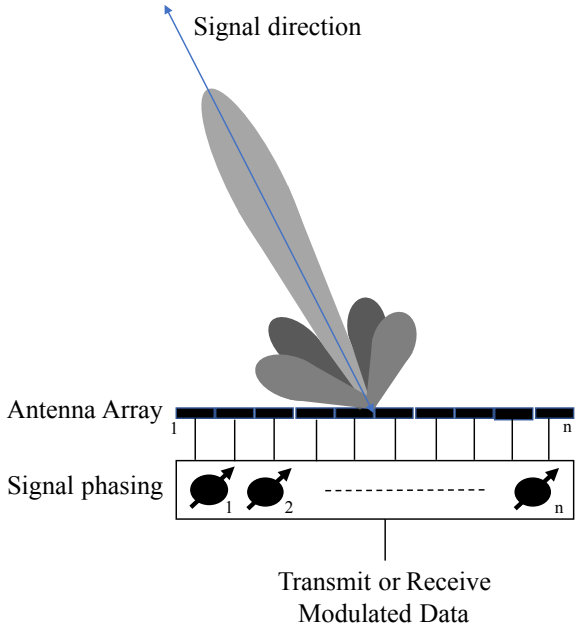

Figure 6.15 – Beamformed antenna array beams

An issue with beamforming is that the transmitter needs to know the location of the receiver in order to point the beam. This is extremely difficult to achieve unless there

is a closed loop connection between the receiver and the transmitter. The 'moving-cells-in-the-sky' approach on the other hand is able to operate open loop.

For more complex scenarios the beam would need to time multiplex between different pointing directions. It is clear that the mechanics of this approach are identical in nature to the point-to-point approach described above in Section 6.5 and therefore has similar performance.

6.8.2 Frequency domain beamforming

Unlike time domain beamforming, frequency domain beamforming treats the problem of creating steerable beams as a transformed problem in the frequency domain using Fourier transforms. An example architecture for a frequency domain beamforming system is shown in Figure 6.16.

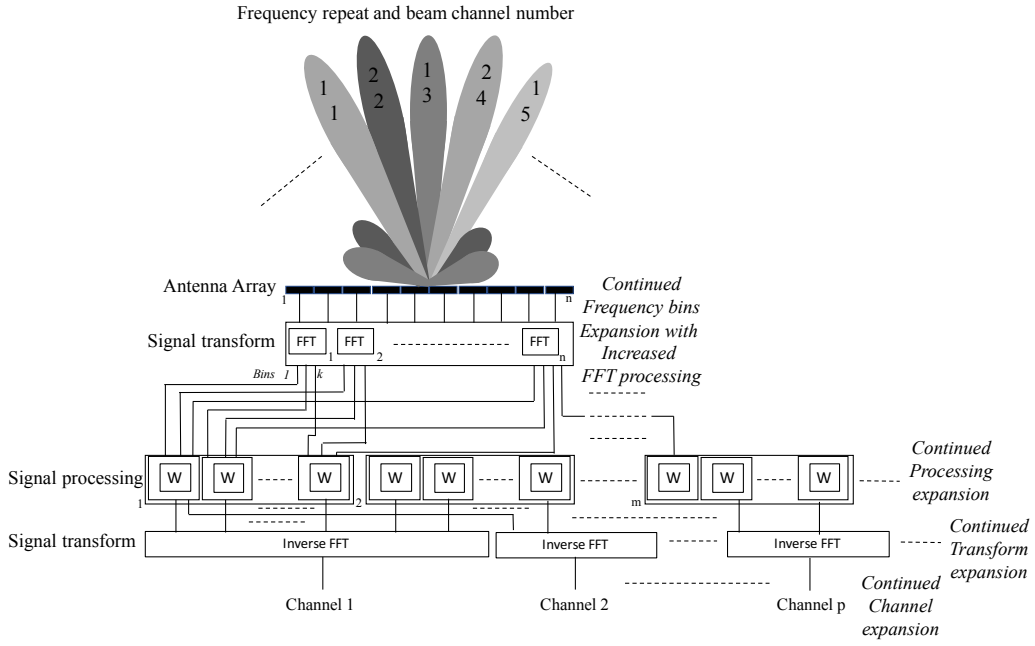

Figure 6.16 – Multi-beam beamformed antenna array

Frequency domain beamforming, therefore, is primarily a frequency domain parameter (twiddle) manipulation and transform to and from the frequency domain of signals across a set of antennas making up the aperture of an array in order to produce geometric pointing of the transmitted signal in the far field.

The key difference with frequency domain beamforming is that it effectively creates the beams ‘virtually’ in processing and as such the processing can be extended by adding more copies to provide capacity to support multi-beam and multi-frequency beamforming (Figure 6.16).

This is a very flexible technique and is scalable. For the 43 x 43 apertures of the ‘moving-cells-in-the-sky’ approach above, however, it would require a large FFT and inverse FFT processing capability to be added.

The frequency domain beamforming processing can provide a fan of beams with repeat frequency of two, as in the ‘cells-in the-sky’ approach, but with the need for significantly higher complexity in processing. By creating these fixed position fans, or wedges, the need for closed loop beamforming is not required. However, the general increase in processing for frequency domain beamforming adds significantly to the system architecture complexity.

By comparison, in the case of a lens approach, such as a Luneburg for ‘moving-cells-in-the-sky’, the beams are created structurally and do not require complex processing.

6.9 Performance of moving-cells-in-the-sky approach with coding gain

A feature of the ‘moving-cells-in-the-sky’ approach is that it enables signals from multiple satellites to combine at each cell. As such there was the possibility to explore whether various processing gain approaches would provide benefit. In Section 5.8 was described an approach in which the transmit power of the satellites was reduced so that the signal, when combined in the cell could be easily recovered, but the individual satellite transmissions were low enough that at ground level they would fall within the noise floor.

The signal is difficult to recover at ground level because, as in the scenario example in this Section, it would require the ground station to be within or have access to the signals from the same three wedges that cross at the cell.

Additionally, transmission power could be further reduced by making use of coding gain in the DSSS waveform. This would make the signal power outside the cell lower and create opportunities for further spatial spectrum efficiency.

The benefit of spatial spectrum efficiency can be exploited in a number of ways, including the re-use of spectrum spatially with non-cooperative electromagnetic spectrum users. And offers the ability to selectively 'enable' communication with a ground station, for example, by controlling the processed receive power in a cell that includes the ground station. These are interesting topics to explore, but are left for further work.

6.10 Performance comparison

The following charts (Figures 6.17 and 6.18) collate and plot the values from this Section both for the point-to-point and 'moving-cells-in-the-sky' approaches, noting that time domain beamforming has similar performance to the point-to-point approach, frequency domain beamforming has similar performance to 'moving-cells-in-the-sky'.

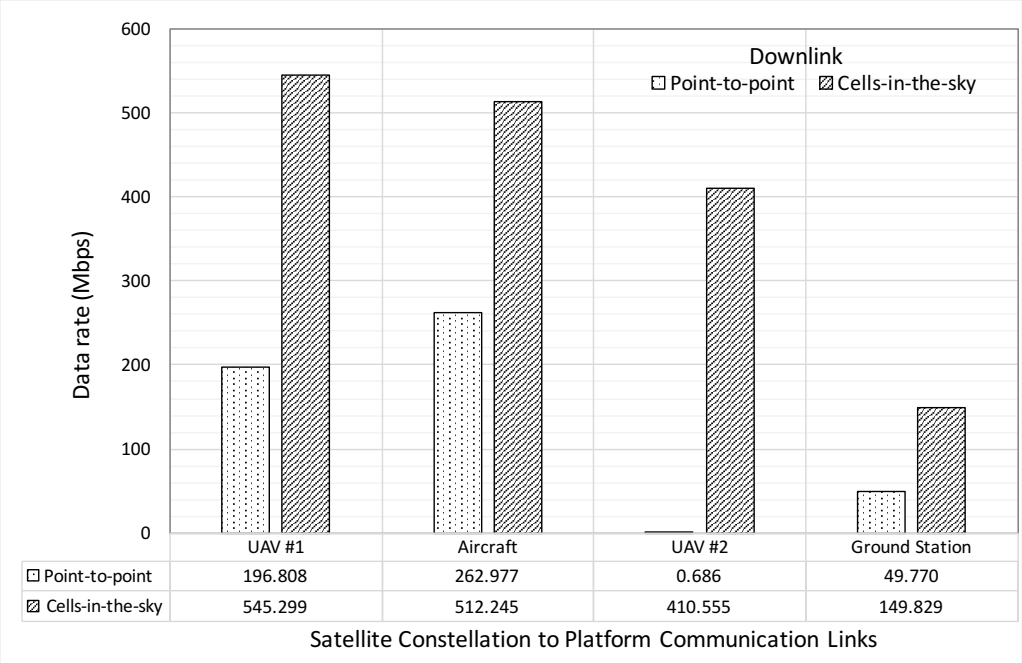

Figure 6.17 – Downlink data rate performance comparison

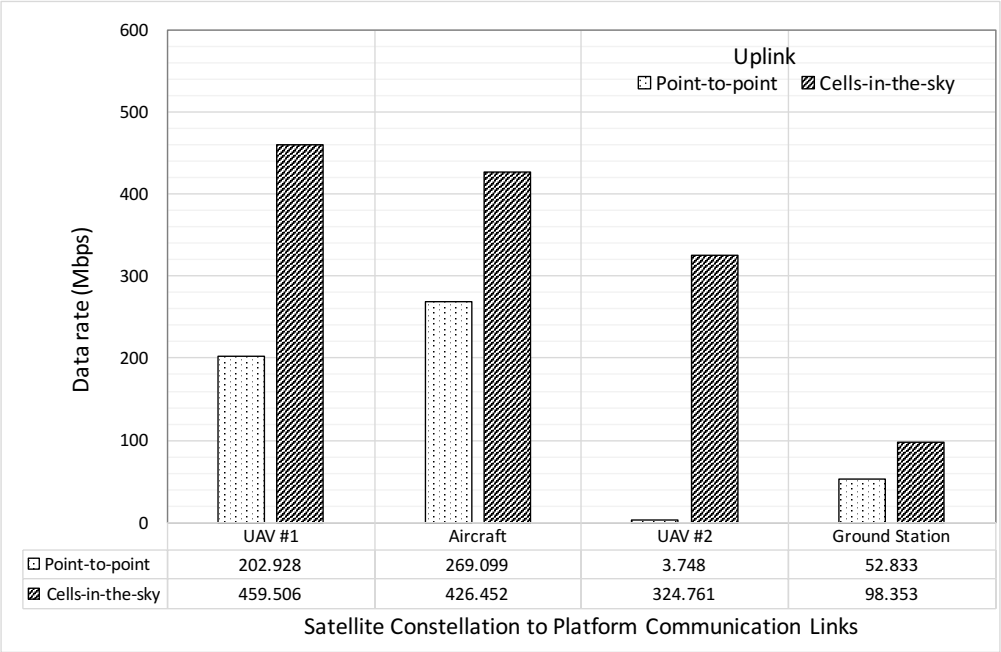

Figure 6.18 – Uplink data rate performance comparison

The data for each approach is presented in Table 6.17, where the constellation bi-section bandwidth metric equals the constellation size of 324 multiplied by the downlink data rate of the nine satellite frequency repeat, divided by two to get the bi-section value.

Approach	Donwnlink data rate to aircraft [Mbps]	Uplink data rate from aircraft [Mbps]	Constellation bi-section bandwidth [Gbps]	System Architecture Complexity	Spectrum Efficiency [bits/sec/ Hz]
Point-to-point	262.977	286.099	4.734	Low	47.336
'Moving-cells-in-the-sky'	512.245	426.452	9.220	Medium	92.204
Time domain beamforming	See text	---	---	---	---
Frequency domain beamforming	512.245	426.452	9.220	High	92.204
MIMO	See text	---	---	---	---

Table 6.17 – Performance comparison scenario results by metric

Spectrum efficiency was computed using the constellation size of 324 multiplied by the downlink data rate of the 9 satellite frequency repeat divided by the 200 MHz overall available bandwidth for the scenario.

Now, if it assumed that a synthetic metric is used to measure the system architecture complexity of Low = 3, Medium = 2 and High = 1, a figure of merit for performance of each approach (which, for clarification, is a different measure than that in Section 5.6) can be provided by multiplying system architecture complexity by spectrum efficiency (Table 6.18).

MIMO particularly is only able to beamform effectively with closed loop feedback of the channels, as is the case for time domain beamforming, and since this is extremely difficult to achieve, compared to the simplicity of the the 'moving-cells-in-the-sky' open loop approach, the two are not included in the performance comparison. For reference however, at best, and with feedback, the performance of both time domain beamforming and MIMO (in particular MU-MIMO with CoMP) could only match that of point-to-point for the scenario in this Section.

Approach	System Architecture Complexity	Spectrum Efficiency (bits/sec/ Hz)	System Arch. Figure of merit
Point-to-point	Low (3)	47.336	142.008
'Moving-cells-in-the-sky'	Medium (2)	92.204	184.408
Time domain beamforming	See text	---	---
Frequency domain beamforming	High (1)	92.204	92.204
MIMO	See text	---	---

Table 6.18 – Performance comparison scenario approaches by metric

From the performance analysis it is clear that the 'moving-cells-in-the-sky' approach provides higher performance and better spectrum efficiency at lower system complexity than other solutions.

6.11 Discussion and summary

In this Section a scenario was constructed to allow performance comparison of a number of techniques highlighted in the literature review of Section 2. The scenario was developed by first concluding a suitable frequency, based on simulation of the path loss attenuation across the frequencies of aircraft, ground and satellites and at altitudes as identified in Section 3.

This work concluded in the selection of 12.625 GHz as the centre frequency for the scenario, with 100 MHz spectrum allocated to uplink and 100 MHz spectrum allocated to downlink, and with a 1,400 km orbital altitude for the satellites.

Determining the satellite orbital altitude involved the use of channel path loss modelling, and data rate calculations based on reasonable assumptions for the antennas, transmitters and receivers when using DSSS waveforms. And that 1,400 km was the highest identified satellite orbit within the dataset of Section 3 that was within LEO; an arbitrary restriction, but a realistic one given the introduction of large constellations as illustrated in the literature review of Section 2.

The number of satellites in the scenario was determined from a ground station visibility perspective and concluded on a 20^{o} along track, and 20^{o} between planes polar constellation structure that results in a not unreasonable 324 satellite constellation at 1,400 km orbital altitude.

To reduce the complexity of the performance analysis, and to allow demonstration of performance in a realistic scenario, frequencies within the two 100 MHz allocations were repeated across the constellation based on a nine satellite (three along track, three planes) repeat pattern. And finally, to further simplify the scenario, calculations were made based on the three along-track satellites then expanded to the nine satellite repeat, and finally scaled to the full constellation.

A mixture of platform altitudes was introduced in the form of two UAVs; one at high altitude, the other low. An aircraft, and a ground station. And located in contrived

positions to allow for performance assessment not only of a point-to-point communication nature, but also of a shared spectrum nature.
Simulations using STK were run to illustrate the constellation configuration, and were also used in its determination through trade-off.

Performance results were derived for point-to-point satellite communication, the 'moving-cells-in-the-sky' approach, both time domain and frequency domain beamforming, and MIMO, both in the form of SU-MIMO and MU-MIMO including CoMP.

The metrics used for performance comparison included uplink and downlink data rates, constellation bi-section bandwidth, spectrum efficiency, system architecture complexity, and a synthetic metric of spectrum efficiency and system architecture complexity as a figure of merit.

The results demonstrated that both MIMO (in particular MU-MIMO with CoMP) and time domain beamforming could not easily operate open loop, and since the 'moving-cells-in-the-sky' approach could successfully do so, there was larger benefit in the latter solution.

This becomes more obvious when comparing the potential uplink and downlink data rates, which for both of these approaches would be comparable at best, and closed loop, to the point-to-point approach results.

Because of the flexibility of the frequency domain approach, a phased array antenna with sufficient processing is able to create the fixed beam pattern of a lens based solution. However, it was concluded that this was at considerable system architecture complexity increase in comparison to the 'moving-cells-in-the-sky' approach.

A brief discussion was provided to consider the effects of both multi-satellite gain and coding/processing gain for the 'cell-in-the-sky' approach, concluding that there is much further work to be carried out in this area.

The conclusion of the performance comparison demonstrated that, even without the additional benefits of coding gain, the ‘moving-cells-in-the-sky’ approach provided significant performance gain and system simplicity compared with the other approaches considered in this Section. And, further, provided the increased and improved spectrum efficiency identified as a need for the problem of improved communication system spectrum in the high altitude and low orbit environment, as described in Sections 1 and 2.

This page intentionally blank to aid printing.

Chapter 7

Discussion, Conclusion and Further Work

7.1 Discussion

The initial premise for this study was to investigate the possibility of providing a 'layered' communication capability in the high altitude low Earth orbit region to alleviate spectrum availability issues as increasing numbers spectrum users, requiring higher data rates are predicted.

It was determined that there was very little in the literature on such an approach, and as such investigation began at first principles by considering RF transmission through the atmosphere and how this might be manipulated to produce distinct and vertically separable RF regions that could provide spectrum re-use.

Though amplitude and phase/frequency modulation approaches were investigated, the outcome was not satisfactory in resolving the fundamental spectrum availability issue. The work was progressed by the addition of coded modulation that would result in spatial correlation regions, and which in essence appeared to be a translation of GPS from time based to spatial based processing. Again, however, the outcome was not satisfactory it was unable to create the 'layered communication' seen as the best way to provide spectrum efficiency and re-use.

It was found during the work that spatial modelling of complex wavefront propagation in Matlab did not scale and quickly ran into memory, processing and time limitations. Further, the results of using a wavefront propagation modelling approach did not provide sufficient understanding of the underlying mechanisms, and as a result many of the false starts in the analysis work were caused by simple oversights that were not evident in the starting conditions, but only in the simulation results.

The key step in being able to create a 'layered communication' system was arrived at by going back to first principles and considering beamforming techniques. During

this work investigation of lens antennas showed promise in creating the multiple narrow beams that were the seeming conclusion to providing 'layered communication' from the previous simulation work.

In and of itself the directional antenna approach did not fulfil a generic vertical layering of spectrum re-use, however, with the application of the other techniques a method was created that provided not just 'layered communication' but a 'moving-cells-in-the-sky' approach. In which regions of space could be referenced as though they were individual cells, in an analogous manner to mobile phone cells, but with the enormous benefit of not requiring a transmitter in each cell, in effect creating cells at a distance. A solution that would be of great interest for mobile phone cellular development but a topic for further study and not covered in this thesis.

The study of beamforming and lens antenna techniques resulted in a viable solution to the spectrum efficiency issue by demonstrating vertical spectrum re-use through the provision of RF 'cells in the sky' from a combination of signal processing techniques from satellites in orbit. Based on the literature review, and previous experience of mobile phone and satellite system design, the selection, via objective trade-off, of additions to the beamforming and lens antenna approach included incorporating SDMA (Space Division Multiple Access), DSSS (Direct Sequence Spread Spectrum), 3G mobile phone management of the radio environment through consideration of addition of elements of the RNC (Radio Network Controller) and MSC (Master Switching Centre), along with inter-linking of satellites using features of MU-MIMO-CoMP (Multi-User MIMO with Cooperative Multi-point), and using this system configuration to provide multiple overlapping RF beams that form 'moving-cells-in-the-sky'. Further work demonstrated how the return path (the uplink) could function within this system.

A step in understanding the system was to model the lens antennas and to consider if RF signals from multiple satellite transmissions could form the necessary cell structure, which it was found is achievable.
The next step in understanding the viability of the system was to conclude a performance analysis and to compare that with other techniques. The techniques

chosen include point-to-point satellite to platform links, MIMO, both SU-MIMO and MU-MIMO with CoMP, and both time domain and frequency domain beamforming.

In order to perform all the path loss calculations, it was realised early on that to keep the calculations consistent would require settling on a standard model to allow the results to be comparable. After deciding to use the ITU-R standards it was quickly realised that for the number of calculations required to create the data required for the comparison charts and trade-off studies that the standards would need to be coded for multiple parametrised execution. This led to a search for commercial tool to achieve what was required, however, none could be identified that allowed the fine parameterisation required to carry out the performance comparisons and trade-offs. And given the limitations of Matlab it was decided to hand code the ITU-R standards, in particular the space-Earth link standards referenced in ITU-R P.2041, in C. This took significant effort for two reasons. First, the standards are exceptionally specific in some areas, very generic in others, and unclear in many areas. And second there are no pro-forma data sets to confirm that an implementation is correct to the standards.

Implementing the ITU-R standards required converting the areas where there was too much detail for this thesis to a more generic approach that could be reapplied with confidence in repeatability of the result. One of the key areas in this regard was in averaging the detailed datasets for Worldwide modelling of atmospheric pressure, density and water vapour to create a more straightforward calculation for comparison. Another key area was in correctly modelling rain and fog, which is a statistical calculation that relies on Worldwide estimates of precipitation and a subjective statistical model of the ‘exceedance’ of rain or fog for a given location. To ensure comparable results the statistics were selected to ensure that there would be no requirement for the provision of location on Earth, and that rain and fog levels were representative of realistic values from the measured data in literature. Finally, the complexity of implementing unclear areas of the standards can result in many false results being generated that must then be understood, assessed, and the code iterated in order to understand what the authors of the standard intended to be the calculations. This was particularly the case for concluding an implementation of the

line-by-line algorithm for gaseous absorption, and the mathematics for the calculation of attenuation due to clouds.

The lack of pro-forma test data to confirm an implementation of the ITU-R standards is a considerable oversight by the standards working group, and although WG3 (Working Group 3) does publish a dataset for gaseous absorption, there is not enough information in the dataset to make a comparison to an implementation of the ITU-R standard. The situation for the other atmospheric modelling standards, such as those for clouds, fog, rain, ionospheric and tropospheric scintillation is equally frustrating with no datasets available. In the literature, it was found that ESA (European Space Agency) had sponsored work to derive pro-forma datasets for confirmation of implementation of the ITU-R standards, but these results appear to no longer be supported and were not accessible. The only method to provide at least some level of confidence in the implementation of the ITU-R standard was to overlay plots of the generated data with those produced by others, this is the method used to demonstrate correct implementation of the gaseous absorption standard in the thesis, though it was quickly found that many authors in the literature do not include sufficient detail of the parameters used to create their results. Differences in pressure, density, water vapour etc. all play a part, and comparison is not possible if these values are not given in the literature. In conclusion therefore, the implementation of the ITU-R standards for space-Earth communication provided in this thesis is as accurate as can be given these constraints. The main purpose of the standards in this thesis is to provide consistent results for comparison of techniques, and the implementation achieves this with realistic results being produced.

Refraction of the signals in the atmosphere is difficult to reduce to a single calculation value since it requires a ray-tracing to create realistic models of atmospheric excursion. It was decided to not implement a ray-tracing model and to maintain a linear approach to signal propagation. Adding frequency and location dependent ray-trace modelling to the C-code would be an item for further work.

To complement the C-coded ITU-R standards model a dataset of typical altitudes and frequencies used by platforms such as aircraft and UAVs/RPAS, and satellites was derived based on extensive literature survey and study of the Ofcom and ITU

frequency datasets and allocations. These datasets were required in order to reduce the number of calculations needed for performance comparison of techniques whilst retaining realism in the communication topologies.

A feature of the 'moving-cells-in-the-sky' approach is that it enables signals from multiple satellites to combine at each cell. As such there was the possibility to explore whether various processing gain approaches would provide benefit. For example, the transmit power of the satellites could be reduced so that the signal, when combined in the cell could be easily recovered, but the individual satellite transmissions were low enough that at ground level they would fall within the noise floor. The signal would be difficult to recover at ground level because it would require the ground station to be within or have access to the signals from multiple wedges that cross at the cell.

Additionally, consideration was made of whether transmission power could be further reduced by making use of coding gain in the DSSS waveform. This would make the signal power outside the cell lower and create opportunities for further spatial spectrum efficiency. The benefit of spatial spectrum efficiency could be exploited in a number of ways, including the re-use of spectrum spatially with non-cooperative electromagnetic spectrum users. And offers the ability to selectively 'enable' communication with a ground station, for example, by controlling the processed receive power in a cell that includes the ground station. These are interesting topics to explore, but are left for further work.

Finally, in order to accomplish trade-off and performance comparisons of the 'moving-cells-in-the-sky' approach against other approaches required the creation of a number of scenarios. The most complex scenario to develop was one that could realistically, based on the literature review data, represent a real constellation of satellites. To achieve this, simulations were run using STK to provide revisit times, overflight times, and to provide graphical representations of the scenario. The data from the STK simulation was then fused with the ITU-R path loss modelling results to create a channel model that could be used to compare data rates using typical

values from the literature for transmission powers, frequency, bandwidths, and modulation.

7.2 Conclusion

The key conclusions of the thesis are that (i) it is indeed feasible to create a 'layered communication' system, and in fact an improved version that creates 'moving-cells-in-the-sky' and which (ii) provides spectral efficiency, increased spectrum spatial availability and provides higher data rates for platforms operating in the high altitude low orbit environment.

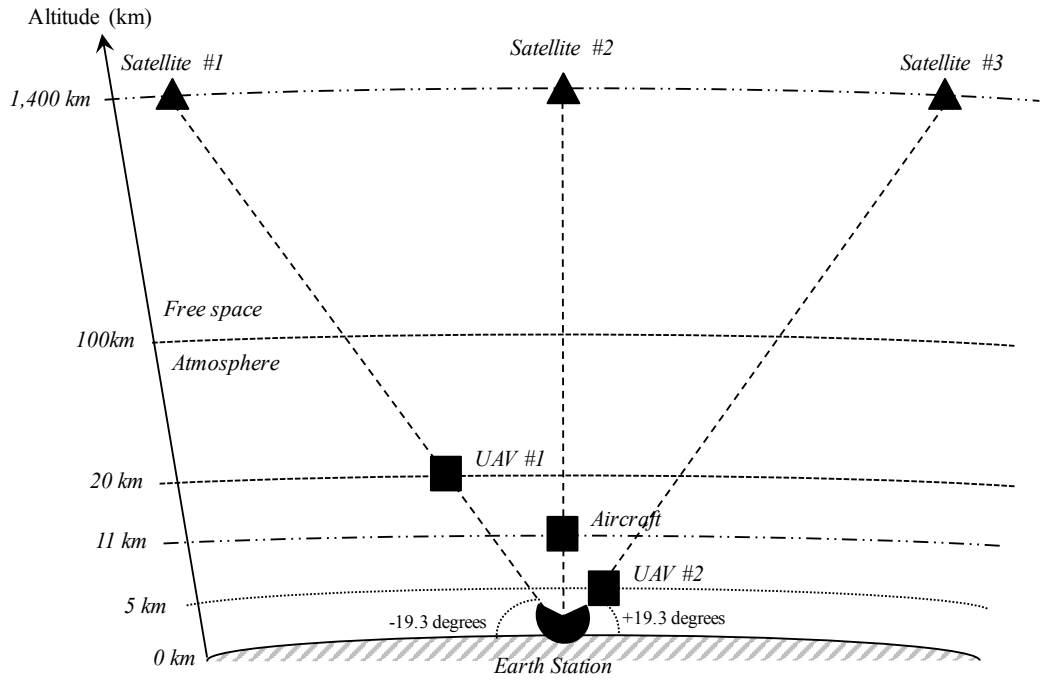

Figure 7.1 – Derived scenario for performance comparison

A performance comparison was made between a point-to-point communication approach, the 'moving-cells-in-the-sky' approach, MIMO in the form of SU-MIMO and MU-MIMO with CoMP, and both time domain and frequency domain beamforming.

The following charts show the uplink and downlink data rate performance comparison for a derived 324 satellite constellation scenario (Figure 7.1) based on a

three satellite along track configuration with a three plane frequency re-use repeat and with realistic representation of UAV/RPAS, aircraft platforms and ground station altitudes and frequencies for point-to-point and 'moving-cells-in-the-sky' approaches (Figures 7.2 and 7.3).

Data for each approach is presented in Tables 7.1 and 7, and indicate the performance level achievable by the 'moving-cells-in-the-sky' approach in relation to other approaches.

MIMO is only able to beamform effectively with closed loop feedback of the channels, as is the case for time domain beamforming, and since this is extremely difficult to achieve, compared to the simplicity of the 'moving-cells-in-the-sky' open loop approach, the two are not included in the performance comparison. However, for reference, at best, and with feedback, the performance of both time domain beamforming and MIMO (in particular MU-MIMO with CoMP) could only match that of point-to-point for the performance comparison scenario.

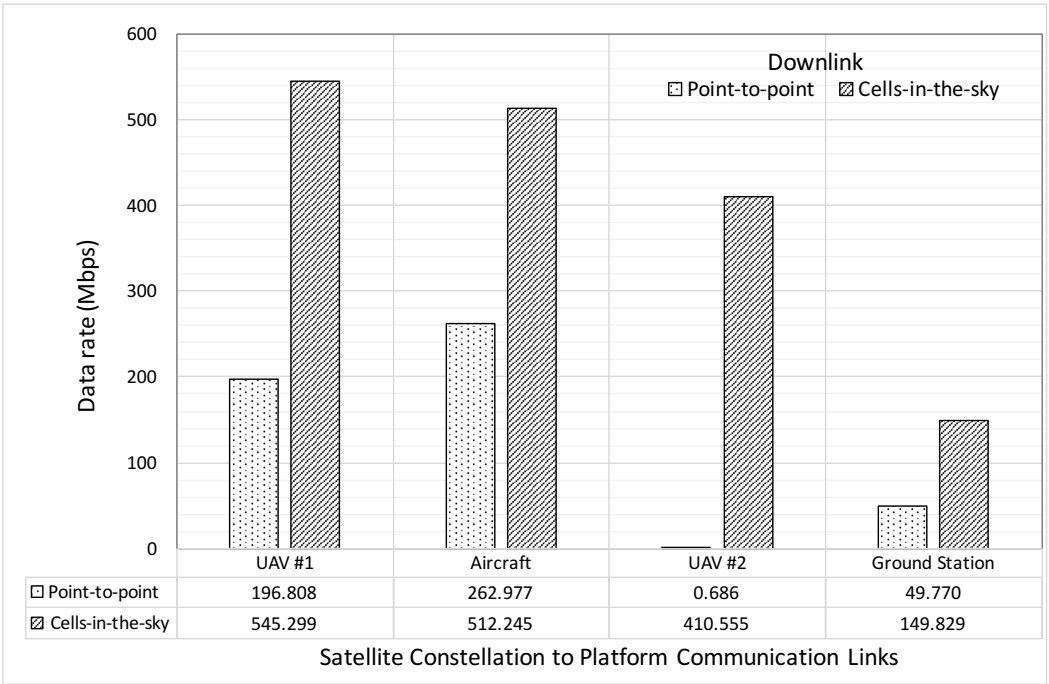

Figure 7.2 – Downlink data rate performance comparison

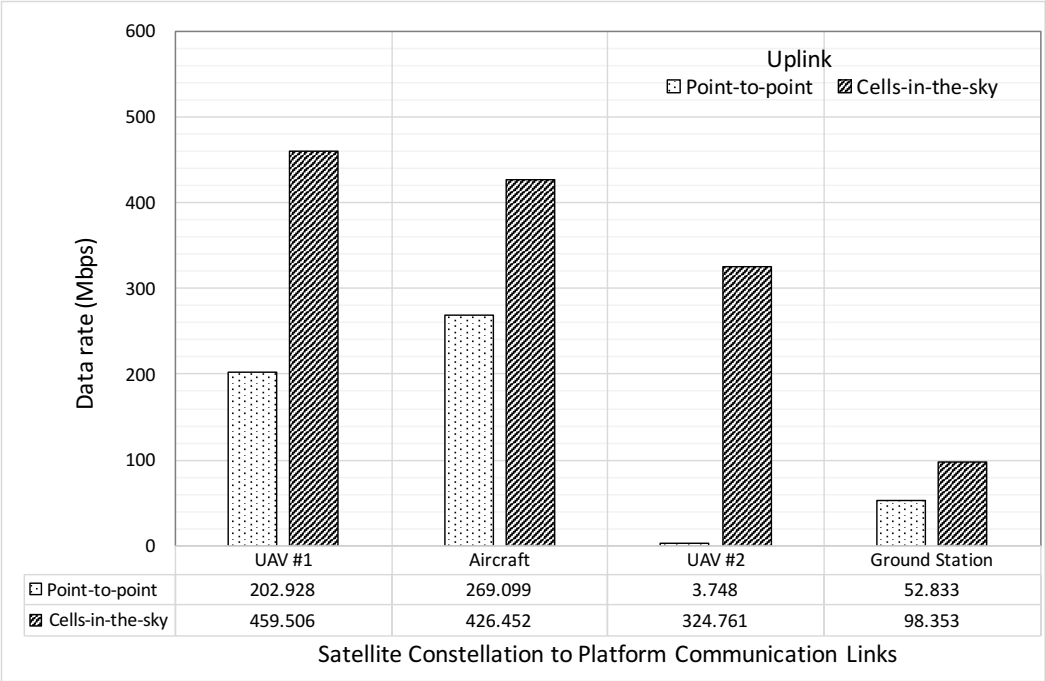

Figure 7.3 – Uplink data rate performance comparison

Approach	Donwnlink data rate to aircraft [Mbps]	Uplink data rate from aircraft [Mbps]	Constellation bi-section bandwidth [Gbps]	System Architecture Complexity	Spectrum Efficiency [bits/sec/ Hz]
Point-to-point	262.977	286.099	4.734	Low	47.336
'Moving-cells-in-the-sky'	512.245	426.452	9.220	Medium	92.204
Time domain beamforming	See text	---	---	---	---
Frequency domain beamforming	512.245	426.452	9.220	High	92.204
MIMO	See text	---	---	---	---

Table 7.1 – Performance comparison scenario results by metric

Approach	System Architecture Complexity	Spectrum Efficiency (bits/sec/ Hz)	Figure of merit
Point-to-point	Low (3)	47.336	142.008
'Moving-cells-in-the-sky'	Medium (2)	92.204	184.408
Time domain beamforming	See text	---	---
Frequency domain beamforming	High (1)	92.204	92.204
MIMO	See text	---	---

Table 7.2 – Performance comparison scenario approaches by metric

In conclusion, from the performance analysis it is clear that the 'moving-cells-in-the-sky' approach provides higher performance and better spectrum efficiency at lower system complexity than other solutions. And, as the aim of the thesis was to demonstrate improved spectrum efficiency, spatial availability improvement and data rate performance in the high altitude low orbit environment, it can be stated that the 'moving-cells-in-the-sky' approach fulfils these goals.

7.3 Further work

During the development of this thesis several areas of further work were identified that could move the work on and into different research directions.

The first of these is the ability to remotely create communication cells using beamforming or lens antennas and a supporting system architecture. This has application beyond the high altitude low orbit environment and offers the possibility of developing mobile phone cells in which the parameters may be remotely set for each frequency in each cell. Opening the potential for remote cell creation with different standards and different frequency bands in each cell.

The second area for further work is in the development of pro-forma test data for confirmation of implementation of the ITU-R standards.

A third area of further work is the addition of frequency and location dependent ray-trace modelling to the thesis models in order to more fully understand what happens to the cells as the satellites pass overhead.

A fourth area of further work is in the provision of hand-over between cells. Unlike in ground mobile phone cell systems where the base station transmitters are stationary at fixed locations, the ‘moving-cells-in-the-sky’ approach results in, what are in effect, moving base station transmitters as represented by satellite transmissions. Measuring, managing and performing hand over in this environment, particularly with platforms that are also moving, poses a particular problem that would require further work to resolve.

Finally, the benefit of spatial spectrum efficiency could be exploited for the re-use of spectrum spatially with non-cooperative electromagnetic spectrum users. Further, spatial spectrum management offers the ability to selectively ‘enable’ communication with a ground station, for example, by controlling the processed receive power in a cell that includes the ground station. These are interesting topics for further work.

Appendix A

Implementation of ITU-R P.2041

Prediction of path attenuation on links between a ground or airborne platform and Space and between a space platform and airborne or ground platform

C-code implementation of the calculations outlined in this thesis, providing an implemention of the ITU-R P.2041 standard and supporting standards

attenITUPathLoss
aircraftAltitudeData
satelliteAltitudeData
earthSpaceFrequencyListData
spaceEarthFrequencyListData
spaceSpaceFrequencyListData
temperatureData
pressureData
waterVapourDensityData
averagedGlobalColumnarContentOfReducedCloudLiquidWater
spectroscopicDataForOxygenAttenuation
spectroscopicDataForWaterVapourAttenuation
slantPathCalculation
attenGaseousFunction
attenCloudsFunction
attenRainFunction
attenTropoScintillationFunction
attenIonosphericEffectsFunction
attenRefractionFunction
freeSpacePathLossFunction
main (general function for running simulations)

```
//
//  attenITUPathLoss.h
//  ITUPathLossModel
//
//  Created on 25/01/2016.
//  Updated with slant and path calculation version on 22/04/2017.
//  Copyright © 2016 Emma Jones. All rights reserved.
//

#ifndef attenITUPathLoss_h
#define attenITUPathLoss_h

// Data
#include "aircraftAltitudeData.h"
#include "satelliteAltitudeData.h"
#include "earthSpaceFrequencyListData.h"
#include "spaceEarthFrequencyListData.h"
#include "spaceSpaceFrequencyListData.h"

// Functions
// ITU-R P.2041 - propagation for Earth, Air, Space paths
#include "attenGaseousFunction.h"            // ITU-R P.676 and ITU-
R P.835
#include "attenCloudsFunction.h"             // ITU-R P.840 and ITU-
R P.1144
#include "attenRainFunction.h"               // ITU-R P.618, ITU-R
P.837 and ITU-R P.838
#include "attenTropoScintillationFunction.h" // ITU-R P.618, ITU-R
P.839 and ITU-R P.453
#include "attenRefractionFunction.h"         // ITU-R P.453
#include "attenIonosphericEffectsFunction.h" // ITU-R P.618, ITU-R
P.531 and ITU-R P.1239
#include "freeSpacePathLossFunction.h"       // ITU-R P.525
#include "slantPathCalculation.h"            //


double attenITUPathLoss (double frequency, double platform1Altitude,
double platform2Altitude, double slantAngle1To2, double
earthAntennaDiameter, int enableFSPL, int enableClouds, int
enableRain, int enableTropospherics, int enableIonospherics, int
enableGaseous, int enableGaseousTestMode, int
useAircraftAltitudeData, int useSatelliteAltitudeData, int
useEarthSpaceFrequencyListData, int useSpaceEarthFrequencyListData,
int useSpaceSpaceFrequencyListData)
{
    // PARAMETERS
    //  frequency (GHz)
    //  platform 1 altitude (km)  0 is mean sea level
    //  platform 2 altitude (km)  0 is mean sea level
    //  slant Angle between platform 1 and 2 (degrees)
    //      angle is positive for platform 2 being at a higher
altitude than platform 1
    //      angle from the altitude tangent abscissa
    //  EarthAntennaDiameter (metres)
    //  enableFSPL
    //  enableClouds
    //  enableRain
    //  enableTropospheric effects
    //  enableIonospheric effects
```

```
    //  enableGaseous attenuation
    //  enableGaseousTestMode with fixed known values
    //  useAircraftAltitudeData (0 = off, >0 = dataset entry)
    //  useSatelliteAltitudeData (0 = off, >0 = dataset entry)
    //  useEarthSpaceFrequencyListData (0 = off, >0 = dataset entry)
    //  useSpaceEarthFrequencyListData (0 = off, >0 = dataset entry)
    // useSpaceSpaceFrequencyListData (0 = off, >0 = dataset entry)
    //  Returns:
    //    path loss attenuation including all effects (dB)
    //


    // VARIABLES
    //
    double  attenuationITU = 0.0;
    double  attenuationFSPL = 0.0;
    double  attenuationGaseous = 0.0;
    double  attenuationCloudsAndFog = 0.0;
    double  attenuationRain = 0.0;
    double  attenuationTropoScint = 0.0;
    double  attenuationIonosScint = 0.0;
    double  attenValue = 0.0;
    double  faradayRotation = 0.0;
    double  groupDelay = 0.0;
    double  fsplPathLength = 0.0;
    double  rainHeightPathLength = 0.0;
    double  gaseousPathLength = 0.0;
    int     testMode = 0;


    // CONSTANTS
    //
    const double rainHeight = 6.36;  // km      // ITU-R
P.839    (hR)
    const int TRUE = 1;


    // IMPLEMENTATION
    //

    // Free Space Path Loss
    if (enableFSPL == TRUE)
    {
        if (platform1Altitude > platform2Altitude)
        {
            fsplPathLength = slantPathLengthFunction
(platform1Altitude, platform2Altitude, slantAngle1To2);
        }
        if (platform2Altitude >= platform1Altitude)
        {
            fsplPathLength = slantPathLengthFunction
(platform2Altitude, platform1Altitude, slantAngle1To2);
        }
        if (fsplPathLength > 0.0)
        {
            attenuationFSPL = freeSpacePathLossFunction
(fsplPathLength, frequency);
        }
    }
```

```
    // output the full pathlength if required
    // printf("Frequency = %f    FSPLPathLength = %f\n\n",
frequency, fsplPathLength);


    if (enableIonospherics == TRUE)
    {
        // Is the path in the ionospheric layers
        //
        if (((platform1Altitude>60.0) && (platform1Altitude<800.0))
||
            ((platform2Altitude>60.0) && (platform2Altitude<800.0))
||
            ((platform1Altitude<=60.0) &&
(platform2Altitude>=800.0)) ||
            ((platform2Altitude<=60.0) &&
(platform1Altitude>=800.0)))
        {
            (void) attenIonosphericEffectsFunction ((double)
frequency, &attenValue, &faradayRotation, &groupDelay);
            attenuationIonosScint = attenValue;
        }
    }


    if (enableRain == TRUE)
    {
        attenuationRain = attenuationRainFunction ((int)
platform1Altitude, (int) frequency, slantAngle1To2);
    }
    if (enableClouds == TRUE)
    {
        attenuationCloudsAndFog = attenuationCloudsAndFogFunction
((int) platform1Altitude, (int) frequency, slantAngle1To2);
    }
    if (enableTroposphерics == TRUE)
    {
        attenuationTropoScint = attenTropoScintillationFunction
((int) frequency, slantAngle1To2, earthAntennaDiameter);
    }


    // How much of the path is in the atmosphere
    //
    if ((platform1Altitude < 100.0) && (platform2Altitude < 100.0)
&& (platform1Altitude < platform2Altitude))
    {
        gaseousPathLength = slantPathLengthFunction
(platform2Altitude, platform1Altitude, slantAngle1To2);
    }
    else if ((platform1Altitude < 100.0) && (platform2Altitude <
100.0) && (platform1Altitude > platform2Altitude))
    {
        gaseousPathLength = slantPathLengthFunction
(platform1Altitude, platform2Altitude, slantAngle1To2);
    }
    else if ((platform1Altitude < 100.0) && (platform2Altitude >
100.0))
```

```
    {
        gaseousPathLength = slantPathLengthFunction (100.0,
platform1Altitude, slantAngle1To2);
    }
    else if ((platform2Altitude < 100.0) && (platform1Altitude >
100.0))
    {
        gaseousPathLength = slantPathLengthFunction (100.0,
platform2Altitude, slantAngle1To2);
    }
    else
    {
        gaseousPathLength = 0.0;  // assumes no horizontal
separation of platforms
    }
    // Are the test mode values to be used
    testMode = 0;
    if (enableGaseousTestMode == TRUE)
    {
        testMode = 1;
    }
    if (enableGaseous == TRUE)
    {
        attenuationGaseous =
attenuationGaseousFunction(platform1Altitude, frequency, testMode) *
gaseousPathLength;
    }

    /*// calculation check
    if ((attenuationFSPL < 0.0) || (attenuationGaseous < 0.0) ||
(attenuationRain < 0.0) || (attenuationCloudsAndFog < 0.0) ||
(attenuationTropoScint < 0.0) || (attenuationIonosScint < 0.0))
    {
        printf ("Error: negative value: attenuation:\n");
        printf ("fspl, gaseous, rain, clouds-fog, Tropo, Iono\n");
        printf ("%le, %le, %le, %le, %le, %le\n", attenuationFSPL,
attenuationGaseous, attenuationRain, attenuationCloudsAndFog,
attenuationTropoScint, attenuationIonosScint);
        printf ("path length:\n");
        printf ("fspl, rainHeight, gaseous\n");
        printf ("%le, %le, %le\n\n", fsplPathLength,
rainHeightPathLength, gaseousPathLength);
    }*/


    attenuationITU = attenuationFSPL + attenuationGaseous + sqrt(
((attenuationRain + attenuationCloudsAndFog)*(attenuationRain +
attenuationCloudsAndFog)) + (attenuationTropoScint *
attenuationTropoScint) ) + attenuationIonosScint;  // dB

    return (attenuationITU);
}


#endif /* attenITUPathLoss_h */
```

```
//
//  aircraftAltitudeData.h
//  ITUPathLossModel
//
//  Created on 10/01/2016.
//  Copyright © 2016 Emma Jones. All rights reserved.
//

//
//  Aircraft altitude data based on analysis in PhD thesis
//


#ifndef aircraftAltitudeData_h
#define aircraftAltitudeData_h

const int aircraftListSize = 12;  // entries

// Altitude [km]
const double  aircraftAltitudeListData[aircraftListSize] = {27, 25,
20, 18, 16, 15, 13, 12, 11, 5, 3, 1};

#endif /* aircraftAltitudeData_h */
```

```
//
//  satelliteAltitudeData.h
//  ITUPathLossModel
//
//  Created on 10/01/2016.
//  Copyright © 2016 Emma Jones. All rights reserved.
//

//
//  Communications satellite altitude data based on analysis in PhD
thesis
//


#ifndef satelliteAltitudeData_h
#define satelliteAltitudeData_h

const int satelliteListSize = 6;  // entries

// Altitude [km]
const double  satelliteAltitudeListData [satelliteListSize] =
{35768, 1400, 930, 825, 750, 630};

#endif /* satelliteAltitudeData_h */
```

```
//
//  earthSpaceFrequencyListData.h
//  ITUPathLossModel
//
//  Created on 10/01/2016.
//  Copyright © 2016 Emma Jones. All rights reserved.
//

//
//  Earth-Space allocated communications frequency data based on
analysis in PhD thesis
//


#ifndef earthSpaceFrequencyListData_h
#define earthSpaceFrequencyListData_h

const int earthSpaceFrequencyListSize = 14;  // entries

// Frequency [GHz]
const double  earthSpaceFrequencyList
[earthSpaceFrequencyListSize][2] =
{
    {1.427,1.429},
    {1.616, 1.6265},
    {1.785, 1.88},
    {2.025, 2.11},
    {7.145, 7.235},
    {10.7, 11.7},
    {12.5, 12.75},
    {17.3, 18.4},
    {19.3, 19.7},
    {28.5, 30},
    {40, 40.5},
    {47.5, 47.9},
    {48.2, 48.4},
    {49.44, 50.2}
};

#endif /* earthSpaceFrequencyListData_h */
```

```
//
//  spaceEarthFrequencyListData.h
//  ITUPathLossModel
//
//  Created on 10/01/2016.
//  Copyright © 2016 Emma Jones. All rights reserved.
//

//
//  Space-Earth allocated communications frequency data based on
analysis in PhD thesis
//


#ifndef spaceEarthFrequencyListData_h
#define spaceEarthFrequencyListData_h

const int spaceEarthFrequencyListSize = 16;  // entries

// Frequency [GHz]
const double  spaceEarthFrequencyList
[spaceEarthFrequencyListSize][2] =
{
    {0.137, 0.143},
    {1.525, 1.535},
    {2.2, 2.29},
    {8.025, 8.175},
    {8.4, 8.5},
    {10.7, 11.7},
    {12.5, 12.75},
    {14.4, 14.47},
    {17.3, 18.4},
    {19.3, 19.7},
    {25.5, 27.0},
    {37.0, 40.5},
    {47.5, 47.9},
    {48.2, 48.54},
    {49.44, 50.2},
    {74.0, 84.0}
};

#endif /* spaceEarthFrequencyListData_h */
```

```
//
//  spaceSpaceFrequencyListData.h
//  ITUPathLossModel
//
//  Created on 10/01/2016.
//  Copyright © 2016 Emma Jones. All rights reserved.
//

//
//  Space-Space allocated communications frequency data based on
analysis in PhD thesis
//


#ifndef spaceSpaceFrequencyListData_h
#define spaceSpaceFrequencyListData_h

const int spaceSpaceFrequencyListSize = 3;  // entries

// Frequency [GHz]
const double  spaceSpaceFrequencyList
[spaceSpaceFrequencyListSize][2] =
{
    {8.0, 12.0},
    {23.18, 23.38},
    {33.0, 75.0}
};

#endif /* spaceSpaceFrequencyListData_h */
```

```
//
//  temperatureData.h
//  ITUPathLossModel
//
//  Created on 10/01/2016.
//  Copyright © 2016 Emma Jones. All rights reserved.
//

//
//  Based on Rec. ITU-R P.835-5 - Reference standard atmospheres
//  Data processed to provide global seasonal and latitude average
temperature with altitude
//

#ifndef temperatureData_h
#define temperatureData_h


const int temperatureListSize = 101;  // entries

//Height [km], Overall Average Temp (K)
const double temperatureListData [temperatureListSize][2] =
{
    {0,285.4707},
    {1,281.168052},
    {2,276.309028},
    {3,270.978358},
    {4,265.260772},
    {5,259.241},
    {6,253.003772},
    {7,246.633818},
    {8,240.215868},
    {9,234.259757},
    {10,228.5285667},
    {11,225.3338703},
    {12,222.1194013},
    {13,218.8830113},
    {14,216.8182187},
    {15,214.75735},
    {16,212.7004053},
    {17,210.6083333},
    {18,211.7453109},
    {19,212.8846768},
    {20,214.0264504},
    {21,215.1706515},
    {22,216.3172999},
    {23,217.4664155},
    {24,218.9312066},
    {25,220.4011209},
    {26,221.8762009},
    {27,223.3564892},
    {28,224.8420287},
    {29,226.332863},
    {30,227.8290356},
    {31,229.6847573},
    {32,231.545906},
    {33,233.4125264},
    {34,235.8441804},
```

```
{35,238.281397},
{36,240.7242219},
{37,243.1727016},
{38,245.6268828},
{39,248.0868124},
{40,250.5525381},
{41,253.0241077},
{42,255.5015694},
{43,257.9849719},
{44,260.4743643},
{45,262.9697959},
{46,265.4713168},
{47,268.0554857},
{48,268.7916667},
{49,269.1458333},
{50,269.5},
{51,269.5},
{52,269.5},
{53,268.4762},
{54,266.2272948},
{55,263.6878105},
{56,261.1347921},
{57,258.5674028},
{58,255.984754},
{59,253.385902},
{60,250.7698448},
{61,248.1355187},
{62,245.4817938},
{63,242.8074707},
{64,240.1112756},
{65,237.391856},
{66,234.6477758},
{67,231.8775101},
{68,229.0794396},
{69,226.2518451},
{70,223.3929008},
{71,220.5006682},
{72,217.5730888},
{73,214.6079769},
{74,211.6030117},
{75,208.5557287},
{76,205.4635112},
{77,202.3235806},
{78,199.1329864},
{79,195.8884958},
{80,190.1096667},
{81,189.8318333},
{82,189.554},
{83,189.2761667},
{84,188.9983333},
{85,188.7205},
{86,188.4426667},
{87,188.1648333},
{88,187.887},
{89,187.6091667},
{90,187.3313333},
{91,187.0535},
{92,186.7756667},
{93,186.4978333},
```

```
    {94,186.22},
    {95,185.9421667},
    {96,185.6643333},
    {97,185.3865},
    {98,185.1086667},
    {99,184.8308333},
    {100,184.553}
};

#endif /* temperatureData_h */
```

```
//
//  pressureData.h
//  ITUPathLossModel
//
//  Created on 10/01/2016.
//  Copyright © 2016 Emma Jones. All rights reserved.
//

//
//  Based on Rec. ITU-R P.835-5 - Reference standard atmospheres
//  Data processed to provide global seasonal and latitude average
pressure with altitude
//

#ifndef pressureData_h
#define pressureData_h


const int pressureListSize = 101;  // entries

//Height [km], Overall Average Pressure (hPa)
const double pressureListData [pressureListSize][2] =
{
    {0,1012.442183},
    {1,901.616},
    {2,798.9409167},
    {3,704.4169333},
    {4,618.04405},
    {5,539.8222667},
    {6,469.7515833},
    {7,407.832},
    {8,354.0635167},
    {9,308.4461333},
    {10,255.18825},
    {11,220.5749806},
    {12,190.6579536},
    {13,164.7998151},
    {14,142.4497339},
    {15,123.1316526},
    {16,106.4341342},
    {17,92.00158874},
    {18,79.52669023},
    {19,68.74382438},
    {20,59.42342565},
    {21,51.36708347},
    {22,44.40331292},
    {23,38.38389977},
    {24,33.18074172},
    {25,28.68311859},
    {26,24.79533307},
    {27,21.43467178},
    {28,18.52964321},
    {29,16.01845473},
    {30,13.84769648},
    {31,11.97120379},
    {32,10.34907411},
    {33,8.946817308},
    {34,7.734621303},
```

```
{35,6.686717391},
{36,5.780831678},
{37,4.997710969},
{38,4.320712993},
{39,3.735452229},
{40,3.229493792},
{41,2.792088854},
{42,2.413945963},
{43,2.087033381},
{44,1.804408248},
{45,1.560068913},
{46,1.3488273},
{47,1.166198589},
{48,1.008305858},
{49,0.871797656},
{50,0.753776765},
{51,0.651738614},
{52,0.563518049},
{53,0.48724332},
{54,0.421296312},
{55,0.364278161},
{56,0.314979538},
{57,0.272354961},
{58,0.235500588},
{59,0.203635022},
{60,0.176082719},
{61,0.15225964},
{62,0.131660856},
{63,0.113849828},
{64,0.09844914},
{65,0.085132489},
{66,0.073617761},
{67,0.063661045},
{68,0.055051457},
{69,0.047606668},
{70,0.041169035},
{71,0.035602257},
{72,0.030788485},
{73,0.026203215},
{74,0.02230159},
{75,0.01898157},
{76,0.016156363},
{77,0.013752141},
{78,0.011706104},
{79,0.009964829},
{80,0.00848287},
{81,0.007221567},
{82,0.006148026},
{83,0.005234266},
{84,0.004456477},
{85,0.003794404},
{86,0.003230811},
{87,0.002751031},
{88,0.002342587},
{89,0.00199486},
{90,0.001698812},
{91,0.001446754},
{92,0.001232141},
{93,0.001049405},
```

```
    {94,0.000893804},
    {95,0.000761304},
    {96,0.000648472},
    {97,0.000552384},
    {98,0.000470552},
    {99,0.000400859},
    {100,0.000341501}
};

#endif /* pressureData_h */
```

```
//
//  waterVapourDensityData.h
//  ITUPathLossModel
//
//  Created on 10/01/2016.
//  Copyright © 2016 Emma Jones. All rights reserved.
//

//
//  Based on Rec. ITU-R P.835-5 - Reference standard atmospheres
//  Data processed to provide global seasonal and latitude average
water vapour density with altitude
//

#ifndef waterVapourDensityData_h
#define waterVapourDensityData_h


const int waterVapourDensityListSize = 101;  // entries

// Height [km],Overall Average Water Vapour Denisty (g/m^3)
const double waterVapourDensityListData
[waterVapourDensityListSize][2] =
{
    {0,11.22611667},
    {1,7.912932421},
    {2,5.019896243},
    {3,2.969790611},
    {4,1.681682159},
    {5,0.925366512},
    {6,0.49823849},
    {7,0.262935685},
    {8,0.135701576},
    {9,0.068030622},
    {10,0.032735676},
    {11,0.014105413},
    {12,0.006178222},
    {13,0.002740007},
    {14,0.001370167},
    {15,0.000806731},
    {16,0},
    {17,0},
    {18,0},
    {19,0},
    {20,0},
    {21,0},
    {22,0},
    {23,0},
    {24,0},
    {25,0},
    {26,0},
    {27,0},
    {28,0},
    {29,0},
    {30,0},
    {31,0},
    {32,0},
    {33,0},
```

```
{34,0},
{35,0},
{36,0},
{37,0},
{38,0},
{39,0},
{40,0},
{41,0},
{42,0},
{43,0},
{44,0},
{45,0},
{46,0},
{47,0},
{48,0},
{49,0},
{50,0},
{51,0},
{52,0},
{53,0},
{54,0},
{55,0},
{56,0},
{57,0},
{58,0},
{59,0},
{60,0},
{61,0},
{62,0},
{63,0},
{64,0},
{65,0},
{66,0},
{67,0},
{68,0},
{69,0},
{70,0},
{71,0},
{72,0},
{73,0},
{74,0},
{75,0},
{76,0},
{77,0},
{78,0},
{79,0},
{80,0},
{81,0},
{82,0},
{83,0},
{84,0},
{85,0},
{86,0},
{87,0},
{88,0},
{89,0},
{90,0},
{91,0},
{92,0},
```

```
    {93,0},
    {94,0},
    {95,0},
    {96,0},
    {97,0},
    {98,0},
    {99,0},
    {100,0}
};

#endif /* waterVapourDensityData_h */
```

```
//
//  averagedGlobalColumnarContentOfReducedCloudLiquidWater.h
//  ITUPathLossModel
//
//  Created on 13/01/2016.
//  Copyright © 2016 Emma Jones. All rights reserved.
//

//
//  Global averaged values for averaged global columnar content of
reduced
//  cloud liquid water. Pre-processed data from the multiple
datasets in
//  ITU-R P.840. Because of the use of averaging, ITU-R P.1144 is
not
//  required.
//


#ifndef averagedGlobalColumnarContentOfReducedCloudLiquidWater_h
#define averagedGlobalColumnarContentOfReducedCloudLiquidWater_h

const int aveGlobColContentOfReducedCloudLiquidWaterListSize =
18;  // entries

double aveGlobColContentOfReducedCloudLiquidWaterData
[aveGlobColContentOfReducedCloudLiquidWaterListSize] [2] =
{
    {0.1,   2.188025698},
    {0.2,   2.02791611},
    {0.3,   1.921926806},
    {0.5,   1.772215178},
    {1,     1.533142779},
    {2,     1.249186163},
    {3,     1.064061685},
    {5,     0.816097759},
    {10,    0.477493778},
    {20,    0.198620424},
    {30,    0.090050815},
    {50,    0.019200008},
    {60,    0.008691059},
    {70,    0.00335253},
    {80,    0.000899379},
    {90,    8.62723E-05},
    {95,    1.42688E-05},
    {99,    1.67631E-07},
};

#endif /* averagedGlobalColumnarContentOfReducedCloudLiquidWater_h
*/
```

```
//
//  spectroscopicDataForOxygenAttenuation.h
//  ITUPathLossModel
//
//  Created on 10/01/2016.
//  Copyright © 2016 Emma Jones. All rights reserved.
//

//
//  Data table from ITU-R P.676
//


#ifndef spectroscopicDataForOxygenAttenuation_h
#define spectroscopicDataForOxygenAttenuation_h

const int spectroscopicDataForOxygenAttenuationDataSize = 44;  //
entries

//  f0 -frequency   a1  a2  a3  a4  a5  a6
const double  spectroscopicDataForOxygenAttenuationData
[spectroscopicDataForOxygenAttenuationDataSize][7] =
{
    {50.474214, 0.975, 9.651, 6.690, 0.0, 2.566, 6.850},
    {50.987745, 2.529, 8.653, 7.170, 0.0, 2.246, 6.800},
    {51.503360, 6.193, 7.709, 7.640, 0.0, 1.947, 6.729},
    {52.021429, 14.320, 6.819, 8.110, 0.0, 1.667, 6.640},
    {52.542418, 31.240, 5.983, 8.580, 0.0, 1.388, 6.526},
    {53.066934, 64.290, 5.201, 9.060, 0.0, 1.349, 6.206},
    {53.595775, 124.600, 4.474, 9.550, 0.0, 2.227, 5.085},
    {54.130025, 227.300, 3.800, 9.960, 0.0, 3.170, 3.750},
    {54.671180, 389.700, 3.182, 10.370, 0.0, 3.558, 2.654},
    {55.221384, 627.100, 2.618, 10.890, 0.0, 2.560, 2.952},
    {55.783815, 945.300, 2.109, 11.340, 0.0, -1.172, 6.135},
    {56.264774, 543.400, 0.014, 17.030, 0.0, 3.525, -0.978},
    {56.363399, 1331.800, 1.654, 11.890, 0.0, -2.378, 6.547},
    {56.968211, 1746.600, 1.255, 12.230, 0.0, -3.545, 6.451},
    {57.612486, 2120.100, 0.910, 12.620, 0.0, -5.416, 6.056},
    {58.323877, 2363.700, 0.621, 12.950, 0.0, -1.932, 0.436},
    {58.446588, 1442.100, 0.083, 14.910, 0.0, 6.768, -1.273},
    {59.164204, 2379.900, 0.387, 13.530, 0.0, -6.561, 2.309},
    {59.590983, 2090.700, 0.207, 14.080, 0.0, 6.957, -0.776},
    {60.306056, 2103.400, 0.207, 14.150, 0.0, -6.395, 0.699},
    {60.434778, 2438.000, 0.386, 13.390, 0.0, 6.342, -2.825},
    {61.150562, 2479.500, 0.621, 12.920, 0.0, 1.014, -0.584},
    {61.800158, 2275.900, 0.910, 12.630, 0.0, 5.014, -6.619},
    {62.411220, 1915.400, 1.255, 12.170, 0.0, 3.029, -6.759},
    {62.486253, 1503.000, 0.083, 15.130, 0.0, -4.499, 0.844},
    {62.997984, 1490.200, 1.654, 11.740, 0.0, 1.856, -6.675},
    {63.568526, 1078.000, 2.108, 11.340, 0.0, 0.658, -6.139},
    {64.127775, 728.700, 2.617, 10.880, 0.0, -3.036, -2.895},
    {64.678910, 461.300, 3.181, 10.380, 0.0, -3.968, -2.590},
    {65.224078, 274.000, 3.800, 9.960, 0.0, -3.528, -3.680},
    {65.764779, 153.000, 4.473, 9.550, 0.0, -2.548, -5.002},
    {66.302096, 80.400, 5.200, 9.060, 0.0, -1.660, -6.091},
    {66.836834, 39.800, 5.982, 8.580, 0.0, -1.680, -6.393},
    {67.369601, 18.560, 6.818, 8.110, 0.0, -1.956, -6.475},
    {67.900868, 8.172, 7.708, 7.640, 0.0, -2.216, -6.545},
```

```
    {68.431006, 3.397, 8.652, 7.170, 0.0, -2.492, -6.600},
    {68.960312, 1.334, 9.650, 6.690, 0.0, -2.773, -6.650},
    {118.750334, 940.300, 0.010, 16.640, 0.0, -0.439, 0.079},
    {368.498246, 67.400, 0.048, 16.400, 0.0, 0.000, 0.000},
    {424.763020, 637.700, 0.044, 16.400, 0.0, 0.000, 0.000},
    {487.249273, 237.400, 0.049, 16.000, 0.0, 0.000, 0.000},
    {715.392902, 98.100, 0.145, 16.000, 0.0, 0.000, 0.000},
    {773.839490, 572.300, 0.141, 16.200, 0.0, 0.000, 0.000},
    {834.145546, 183.100, 0.145, 14.700, 0.0, 0.000, 0.000}
    };

#endif /* spectroscopicDataForOxygenAttenuation_h */
```

```
//
//  spectroscopicDataForWaterVapourAttenuation.h
//  ITUPathLossModel
//
//  Created on 10/01/2016.
//  Copyright © 2016 Emma Jones. All rights reserved.
//

//
//  Data table from ITU-R P.676
//


#ifndef spectroscopicDataForWaterVapourAttenuation_h
#define spectroscopicDataForWaterVapourAttenuation_h

const int spectroscopicDataForWaterVapourAttenuationDataSize =
35;  // entries

//  f0 -frequency   b1  b2  b3  b4  b5  b6
const double  spectroscopicDataForWaterVapourAttenuationData
[spectroscopicDataForWaterVapourAttenuationDataSize][7] =
{
    {22.235080, 0.1130, 2.143, 28.11, 0.69, 4.800, 1.00},
    {67.803960, 0.0012, 8.735, 28.58, 0.69, 4.930, 0.82},
    {119.995940, 0.0008, 8.356, 29.48, 0.70, 4.780, 0.79},
    {183.310091, 2.4200, 0.668, 30.50, 0.64, 5.300, 0.85},
    {321.225644, 0.0483, 6.181, 23.03, 0.67, 4.690, 0.54},
    {325.152919, 1.4990, 1.540, 27.83, 0.68, 4.850, 0.74},
    {336.222601, 0.0011, 9.829, 26.93, 0.69, 4.740, 0.61},
    {380.197372, 11.5200, 1.048, 28.73, 0.54, 5.380, 0.89},
    {390.134508, 0.0046, 7.350, 21.52, 0.63, 4.810, 0.55},
    {437.346667, 0.0650, 5.050, 18.45, 0.60, 4.230, 0.48},
    {439.150812, 0.9218, 3.596, 21.00, 0.63, 4.290, 0.52},
    {443.018295, 0.1976, 5.050, 18.60, 0.60, 4.230, 0.50},
    {448.001075, 10.3200, 1.405, 26.32, 0.66, 4.840, 0.67},
    {470.888947, 0.3297, 3.599, 21.52, 0.66, 4.570, 0.65},
    {474.689127, 1.2620, 2.381, 23.55, 0.65, 4.650, 0.64},
    {488.491133, 0.2520, 2.853, 26.02, 0.69, 5.040, 0.72},
    {503.568532, 0.0390, 6.733, 16.12, 0.61, 3.980, 0.43},
    {504.482692, 0.0130, 6.733, 16.12, 0.61, 4.010, 0.45},
    {547.676440, 9.7010, 0.114, 26.00, 0.70, 4.500, 1.00},
    {552.020960, 14.7700, 0.114, 26.00, 0.70, 4.500, 1.00},
    {556.936002, 487.4000, 0.159, 32.10, 0.69, 4.110, 1.00},
    {620.700807, 5.0120, 2.200, 24.38, 0.71, 4.680, 0.68},
    {645.866155, 0.0713, 8.580, 18.00, 0.60, 4.000, 0.50},
    {658.005280, 0.3022, 7.820, 32.10, 0.69, 4.140, 1.00},
    {752.033227, 239.6000, 0.396, 30.60, 0.68, 4.090, 0.84},
    {841.053973, 0.0140, 8.180, 15.90, 0.33, 5.760, 0.45},
    {859.962313, 0.1472, 7.989, 30.60, 0.68, 4.090, 0.84},
    {899.306675, 0.0605, 7.917, 29.85, 0.68, 4.530, 0.90},
    {902.616173, 0.0426, 8.432, 28.65, 0.70, 5.100, 0.95},
    {906.207325, 0.1876, 5.111, 24.08, 0.70, 4.700, 0.53},
    {916.171582, 8.3400, 1.442, 26.70, 0.70, 4.780, 0.78},
    {923.118427, 0.0869, 10.220, 29.00, 0.70, 5.000, 0.80},
    {970.315022, 8.9720, 1.920, 25.50, 0.64, 4.940, 0.67},
    {987.926764, 132.1000, 0.258, 29.85, 0.68, 4.550, 0.90},
    {1780.000000, 22300.0000, 0.952, 176.20, 0.50, 30.500, 5.00}
```

```
};

#endif /* spectroscopicDataForWaterVapourAttenuation_h */
```

```
//
//  slantPathCalculation.h
//  ITUPathLossModel
//
//  Created on 22/10/2017.
//  Copyright © 2017 Emma Jones. All rights reserved.
//

#ifndef slantPathCalculation_h
#define slantPathCalculation_h

#include <math.h>


double slantPathLengthFunction (double h, double hA, double thetaS)
{
    // Parameters:
    //
    // h        altitude of altitude/orbit/satellite above the Earth
(km)
    // hA       altitude of the transmitting platform (km)
    // thetaS   slant angle (deg)
    //
    // Returns:
    //    slant path (km)
    //
    // Calculation based on Sine rule
    //

    const double rE = 6371; // radius of the Earth (km)

    double A, thetaA;
    double B, thetaB;
    double C, thetaC;

    double sinThetaB;

    C = rE + h;
    B = rE + hA;
    thetaC = (3.1415926536/180.0) * (thetaS + 90);  // radians
    sinThetaB = B * sin (thetaC) / C;  // asin radians
    thetaB = asin(sinThetaB);  // radians
    thetaA = 3.1415926536 - thetaB - thetaC;  // radians
    A = sin(thetaA) * (C / sin(thetaC));  // slant path (km)

    return (A);
}

#endif /* slantPathCalculation_h */
```

```
//
//  attenGaseousFunction.h
//  ITUPathLossModel
//
//  Created on 10/01/2016.
//  Copyright © 2016 Emma Jones. All rights reserved.
//

//
//  Gaseous attenuation calculation implemented based on ITU-R P.676
Annex 1 line-by-line method
//


#ifndef attenGaseousFunction_h
#define attenGaseousFunction_h

#include <math.h>

#include "temperatureData.h"                              // ITU-R
P.835
#include "pressureData.h"                                 // ITU-R
P.835
#include "waterVapourDensityData.h"                       // ITU-R
P.835

#include "spectroscopicDataForOxygenAttenuation.h"        // ITU-R
P.676
#include "spectroscopicDataForWaterVapourAttenuation.h"   // ITU-R
P.676


double attenuationGaseousFunction (double altitudeD, double
frequency, int testMode)
{
    // PARAMETERS
    // altitude            (km)
    // frequency           (GHz) (f)
    // testMode            = 1 (on) for standard values, = 0 (off)
for normal calculation
    // Returns:
    //   gaseous attenuation (dB/km)

    // VALIDITY
    //
    // 1 to 1,000GHz frequency range
    // positive values of altitude
    //

    // PROCEDURE
    //
    // Step 1:  retrieve temperature, pressure and water vapour
density values from tables of averaged reference standard atmosphere
    // Step 2:  calculate the underlying continuum attenuation
    // Step 3:  calculate the attenuation contribution from the
Oxygen lines
    // Step 4:  calcuate the attenuation contribution from the Water
Vapour lines
```

```
    // Step 5:  calculate the overall attenuation

    // Check parameter validity
    //
    if ((altitudeD < 0.0) || (frequency < 0.0) || (frequency >
1000.0))
    {
        return (0.0);
    }

    // VARIABLES
    //
    // Step 1: retrieve values from tables
    double temperature;                 // K      (T)
    double pressure;                    // hPa    (p)
    double waterVapourDensity;          // g/m^3  (d)
    double waterVapourPartialPressure;  // hPa    (e)
    int altitude = (int) altitudeD;

    // Step 2: calculate continuum
    double dw = 0.0;
    double v1, v2, v3;
    double N_dash_dash_D = 0.0;

    // Step 3: Oxygen attenuation calculation
    int index;
    double fiOxygen = 0.0;
    double a1, a2, a3, a4, a5, a6;
    double theta = 0.0;
    double siaOxygen = 0.0;
    double deltaOxygen = 0.0;
    double deltaFOxygen = 0.0;
    double FiLSFOxygen = 0.0;
    double lineSumOxygen = 0.0;
    double N_dash_dash_Oxygen = 0.0;

    // Step 4: Oxygen attenuation calculation
    double fiWaterVapour = 0.0;
    double b1, b2, b3, b4, b5, b6;
    double sibWaterVapour = 0.0;
    double deltaWaterVapour = 0.0;
    double deltaFWaterVapour = 0.0;
    double FiLSWaterVapour = 0.0;
    double lineSumWaterVapour = 0.0;
    double N_dash_dash_WaterVapour = 0.0;

    // Step 5: calculate the overall attenuation
    double attenuationGaseousResult = 0.0;      // dB/km


    // IMPLEMENTATION
    //
    // Step 1:  Retrieve the temperature (T), pressure (p), and
water vapour density (d) values from tables of averaged reference
standard atmosphere
    //
    if (testMode == 0)  // test mode off
    {
```

```
        temperature                =
temperatureListData[altitude][1];
        pressure                   = pressureListData[altitude][1];
        waterVapourDensity         =
waterVapourDensityListData[altitude][1];
    }
    else
    {
        // Standard values for tests
        temperature         = 288.0;
        pressure            = 1013.0;
        waterVapourDensity  = 7.5; // or 0.0 for 'dry'
    }

    waterVapourPartialPressure = (waterVapourDensity * temperature)
/ 216.7; // (e) Water vapour partial pressure in hPa


    // Step 2:  Calculate the underlying continuum attenuation
    //
    theta = 300.0/temperature;
    dw = 5.6e-
4*(pressure+waterVapourPartialPressure)*pow(theta,0.8);  // dw is
the width parameter for the Debye spectrum
    v1 = frequency * pressure * pow(theta,2);
    v2 = 6.14e-5/(dw*(1+pow((frequency/dw),2)));
    v3 = (1.4e-12*pressure*pow(theta,1.5))/(1+((1.9e-
5)*pow(frequency,1.5)));
    N_dash_dash_D = v1 * (v2 + v3);


    // Step 3:  Calculate Oxygen attenuation
    //
    for (index=0;
index<spectroscopicDataForOxygenAttenuationDataSize; index++)
    {
        fiOxygen =
spectroscopicDataForOxygenAttenuationData[index][0]; // line
frequency for Oxygen

        // Add the contribution from the spectral line at this index
        // Retrieve the parameters from the table
        a1 = spectroscopicDataForOxygenAttenuationData[index][1];
        a2 = spectroscopicDataForOxygenAttenuationData[index][2];
        a3 = spectroscopicDataForOxygenAttenuationData[index][3];
        a4 = spectroscopicDataForOxygenAttenuationData[index][4];
        a5 = spectroscopicDataForOxygenAttenuationData[index][5];
        a6 = spectroscopicDataForOxygenAttenuationData[index][6];

        siaOxygen = a1 *pow(10,-7) * pressure * pow(theta,3) *
exp(a2*(1-theta));  // Si is the strength of the ith line
        deltaOxygen = (a5+(a6*theta))*pow(10,-
4)*(pressure+waterVapourPartialPressure)*pow(theta,0.8);  // δ is a
correction factor due to interference effects in oxygen lines
        deltaFOxygen = (a3 * pow(10,-4)) * (pressure *
pow(theta,(0.8-a4)) + (1.1 * waterVapourPartialPressure *
theta));  // Δf is the width of the line
```

```
        deltaFOxygen = sqrt(pow(deltaFOxygen,2)+(2.25*pow(10,-
6)));    // The line width Δf is modified to account for Doppler
broadening
        FiLSFOxygen = (frequency / fiOxygen) * ( ((deltaFOxygen -
(deltaOxygen*(fiOxygen - frequency)))/(pow((fiOxygen - frequency),2)
+ pow(deltaFOxygen,2))) + ((deltaFOxygen - deltaOxygen*(fiOxygen +
frequency)) / (pow((fiOxygen + frequency),2) + pow(deltaFOxygen,2)))
);      // line shape factor
        lineSumOxygen += siaOxygen * FiLSFOxygen;
    }
    N_dash_dash_Oxygen = lineSumOxygen + N_dash_dash_D;


    // Step 4:  Calculate Water Vapour attenuation
    //
    for (index=0;
index<spectroscopicDataForWaterVapourAttenuationDataSize; index++)
    {
        fiWaterVapour =
spectroscopicDataForWaterVapourAttenuationData[index][0]; // line
frequency for Oxygen

        // Add the contribution from the spectral line at this index
        // Retrieve the parameters from the table
        b1 =
spectroscopicDataForWaterVapourAttenuationData[index][1];
        b2 =
spectroscopicDataForWaterVapourAttenuationData[index][2];
        b3 =
spectroscopicDataForWaterVapourAttenuationData[index][3];
        b4 =
spectroscopicDataForWaterVapourAttenuationData[index][4];
        b5 =
spectroscopicDataForWaterVapourAttenuationData[index][5];
        b6 =
spectroscopicDataForWaterVapourAttenuationData[index][6];

        sibWaterVapour = b1 *pow(10,-1) * waterVapourPartialPressure
* pow(theta,3.5) * exp(b2*(1-theta));  // Si is the strength of the
ith line
        deltaWaterVapour = 0.0;
        deltaFWaterVapour = (b3 * pow(10,-4)) * (pressure *
pow(theta,(b4)) + (b5 * waterVapourPartialPressure *
pow(theta,b6)));  // Δf is the width of the line
        deltaFWaterVapour = (0.535 * deltaFWaterVapour) + sqrt(
(0.217 * pow(deltaFWaterVapour,2)) + ( (2.1316*pow(10,-
12)*pow(fiWaterVapour,2))/theta));    // The line width Δf is
modified to account for Doppler broadening
        FiLSWaterVapour = (frequency / fiWaterVapour) * (
((deltaFWaterVapour - (deltaWaterVapour*(fiWaterVapour -
frequency)))/(pow((fiWaterVapour - frequency),2) +
pow(deltaFWaterVapour,2))) + ((deltaFWaterVapour -
deltaWaterVapour*(fiWaterVapour + frequency)) / (pow((fiWaterVapour
+ frequency),2) + pow(deltaFWaterVapour,2))) );      // line shape
factor
        lineSumWaterVapour += sibWaterVapour * FiLSWaterVapour;
    }
    N_dash_dash_WaterVapour = lineSumWaterVapour + N_dash_dash_D;
```

```
    // Step 5:  Sum the values
    //
    attenuationGaseousResult = (0.1820 * frequency *
N_dash_dash_Oxygen) + (0.1820 * frequency *
N_dash_dash_WaterVapour);

    return (attenuationGaseousResult);
}

#endif /* attenGaseousFunction_h */
```

```
//
//  attenCloudsFunction.h
//  ITUPathLossModel
//
//  Created on 12/01/2016.
//  Copyright © 2016 Emma Jones. All rights reserved.
//

// ITU-R P.2041:
// "It is difficult to predict cloud attenuation from an airborne
platform
// to space since different cloud types are at different altitudes
with
// different vertical extents. However, a conservative approach is
to assume
// the cloud base is at the rain height specified in Recommendation
// ITU-R P.839 and the cloud top is at 6 km. Compute the cloud
attenuation
// per Recommendation ITU-R P.840 as follows: use 100% of the total
columnar
// content of cloud liquid water for altitudes below the rain
height, 0% of
// the total columnar content of cloud liquid water for altitudes
above the
// cloud top, with a linear transition of total columnar content of
cloud
// liquid water between the cloud base and the cloud top.
//

// In this model we assume clouds from the rain Height of 6.36km
(from ITU-R P.839)
// all the way to the ground, this being a conservative case

#ifndef attenCloudsFunction_h
#define attenCloudsFunction_h

#include <math.h>

// ITU-R P.840 - attenuation due to clouds and fog
// valid from 10GHz up to 1000GHz
// using pre-processed global averages of the Lred value from tables
// provided with the standard

#include
"averagedGlobalColumnarContentOfReducedCloudLiquidWaterData.h"


double attenuationCloudsAndFogFunction (int altitude, int frequency,
double slantAngle)
{
    // PARAMETERS
    //
    //  altitude     (km)
    //  frequency    (GHz)
    //  slant angle  (degrees)
    //  returns: cloud and fog attenuation (dB)
    //
```

```
    // VALIDITY
    //
    // 10GHz to 1,000GHz frequency range
    // positive values of altitude
    //

    // VARIABLES
    //
    double theta = 0.0;
    double epsilon0 = 0.0;
    double epsilon1 = 0.0;
    double epsilon2 = 0.0;
    double epsilon_dash = 0.0;
    double epsilon_dash_dash = 0.0;  // complex dielectric
permittivity of water
    double fp = 0.0;                 // principal relaxation
frequency (GHz)
    double fs = 0.0;                 // secondary relaxation
frequency (GHz)
    double eta = 0.0;
    double Lred = 0.0;
    double Kl = 0.0;                 // specific attenuation
coefficient (dB/km)/(g/m3)
    double v1;
    double attenuationClouds = 0.0;  // dB/km
    double temperature = 273.0;      // K (0 degC)
    double probabilityOfExceedance = 0.0;   // %

    // CONSTANTS
    //
    const double rainHeight = 6.36;  // km      // ITU-R P.839

    // Check parameter validity
    //
    if ((altitude < 0) || (frequency < 10) || (frequency > 1000))
    {
        return (0.0);
    }


    // IMPLEMENTATION
    //
    if ((double)altitude<=rainHeight)    // as per ITU-R P.2041
    {
        probabilityOfExceedance = 0.1;
        Lred = aveGlobColContentOfReducedCloudLiquidWaterData[0][1];
    }
    else
    {
        probabilityOfExceedance = 99.0;
        Lred =
aveGlobColContentOfReducedCloudLiquidWaterData[aveGlobColContentOfRe
ducedCloudLiquidWaterListSize-1][1];
    }
    theta = 300.0 / temperature;
    epsilon0 = 77.66 + (103.3*(theta - 1.0));
    epsilon1 = 0.0671 * epsilon0;
    epsilon2 = 3.52;
```

```
    fp = 20.20 - (146 * (theta - 1.0)) + (316.0 * pow ((theta -
1.0), 2.0));  // GHz
    fs = 39.8 * fp; // GHz
    epsilon_dash = ( ( (epsilon0 - epsilon1) / (1.0 +
pow((frequency/fp),2.0)) ) + ( (epsilon1 - epsilon2) /
(1+pow((frequency/fs),2.0)) ) + epsilon2);
    epsilon_dash_dash = ( ( (frequency * (epsilon0-epsilon1)) / (fp
* (1.0 + pow((frequency/fp),2.0))) ) + ( (frequency * (epsilon1-
epsilon2)) / (fs * (1.0 + pow((frequency/fs),2.0))) ) );
    eta = (2.0 * epsilon_dash) / epsilon_dash_dash;
    Kl = (0.819 * frequency) / (epsilon_dash_dash) * (1.0 + pow(eta,
2));  // (dB/km)/(g/m3)

    v1 = sin(slantAngle*3.1415926536/180.0);  // with slant angle
converted from degrees to radians
    attenuationClouds = (Lred * Kl) / v1;  // dB

    return (attenuationClouds);
}

#endif /* attenCloudsFunction_h */
```

```
//
//  attenRainFunction.h
//  ITUPathLossModel
//
//  Created on 12/01/2016.
//  Copyright © 2016 Emma Jones. All rights reserved.
//

#ifndef attenRainFunction_h
#define attenRainFunction_h

#include <math.h>

// ITU-R P.2041 Prediction of path attenuation on links between an
airborne platform and Space and between an airborne platform and the
surface of the Earth
// ITU-R P.618  Propagation data and prediction methods required for
the design of Earth-space telecommunications systems
// ITU-R P.837  Characteristics of precipitation for propagation
modelling (and dataset)
// ITU-R P.838  Specific attenuation model for rain for use in
prediction methods (to extend prediction to 1,0000 GHz)
// ITU-R P.1511 Topography for Earth-space propagation modelling
// ITU-R P.1144 Guide to the application of methods

// From ITU-R P.2041:
// "Rain attenuation is predicted from Recommendation ITU-R P.618
which computes the slant-path length, Ls,
// from hs, the height of the Earth station above mean sea level.
For a path between an airborne platform
// and space, hs  is replaced by the altitude of the airborne
platform above mean sea level with the
// constraint that if hs is greater than or equal to hR, then the
rain attenuation is 0 dB."



// ITU-R P.837
//
double ITURP837 (void)
{
    // VARIABLES
    //
    double Mc;
    double Ms;
    double P0;
    double a, b, c, A, B, C;
    double Rp;

    // CONSTANTS
    //
    double const Pr6  = 33.76053194;      // Averaged from
ESARAIN_PR6_v5.TXT
    double const MT   = 708.5443737;      // Averaged from
ESARAIN_MT_v5.TXT
    double const Beta = 0.244772161;      // Averaged from
ESARAIN_BETA_v5.TXT
```

```
    double const p = 0.01;  // (percentage)

    // IMPLEMENTATION
    //
    // Step 1: extract the variables (above)

    // Step 2: obtain the variables at the latitude and longitude
required
    // In this case we use worldwide averaged values (above)

    // Step 3: convert the variables
    Mc = Beta * MT;
    Ms = (1-Beta) * MT;

    // Step 4: derive the percentage probability of rain in an
average year (P0)
    P0 = Pr6 * (1 - pow (2.7182818285, (-0.0079*(Ms/Pr6))));
    if (Pr6 == 0.0)
    {
        return (0.0);
    }

    // Step 5: derive the rainfall rate
    a = 1.09;
    b = (Mc + Ms)/ (21797 * P0);
    c = 26.02 * b;
    A = a * b;
    B = a + c * log(p/P0);
    C = log(p/P0);
    Rp = (-B + sqrt((B*B)-(4*A*C))) / (2 * A);

    return (Rp);
}



// ITU-R P.838
//
void ITURP838 (double *k, double *alpha, double frequency, double
slantAngle)
{
    //  PARAMETERS
    //   frequency             (GHz)
    //   slantAngle            (deg)
    //   returns: k,alpha = specific attenuation power law
coeficients
    //   (specific attenuation (dB/km) = k * RainRate^alpha)


    // CONSTANTS
    //

    // Horizontal Parameters  (ITU-R P.838 TABLE 1)
    const double Haj[4] = { -5.33980, -0.35351, -0.23789, -0.94158
};
    const double Hbj[4] = { -0.10008,  1.26970,  0.86036,  0.64552
};
    const double Hcj[4] = {  1.13098,  0.45400,  0.15354,  0.16817
};
```

```
    const double HMk = -0.18961;
    const double HCk =  0.71147;

    // Vertical Parameters (ITU-R P.838 TABLE 2)
    const double Vaj[4] = { -3.80595, -3.44965, -0.39902, 0.50167 };
    const double Vbj[4] = {  0.56934, -0.22911,  0.73042, 1.07319 };
    const double Vcj[4] = {  0.81061,  0.51059,  0.11899, 0.27195 };
    const double VMk = -0.16398;
    const double VCk =  0.63297;

    // Horizontal Parameters  (ITU-R P.838 TABLE 3)
    const double Hai[5] = { -0.14318,  0.29591,  0.32177, -5.37610,
16.1721  };
    const double Hbi[5] = {  1.82442,  0.77564,  0.63773, -0.96230,
-3.29980 };
    const double Hci[5] = { -
0.55187,  0.19822,  0.13164,  1.47828,  3.43990 };
    const double HMa =  0.67849;
    const double HCa = -1.95537;

    // Vertical Parameters (ITU-R P.838 TABLE 4)
    const double Vai[5] = { -0.07771,  0.56727, -0.20238, -
48.2991,  48.5833  };
    const double Vbi[5] = {  2.33840,  0.95545,  1.14520,  0.791669,
0.791459 };
    const double Vci[5] = { -0.76284,  0.54039,  0.26809,  0.116226,
0.116479 };
    const double VMa = -0.053739;
    const double VCa =  0.83433;

    const double polarisationTiltAngle = 45.0;  // degrees  -
average value
    const double pi = 3.1415926536;

    // VARIABLES
    //
    int index;
    double L10f;
    double Hk, Vk, Ha, Va;


    // IMPLEMENTATION
    //
    L10f = log10(frequency);

    Hk = 0.0;
    Vk = 0.0;
    for (index=0; index<4; index++)
    {
        Hk += (Haj[index] * exp(-(pow(((L10f-
Hbj[index])/Hcj[index]), 2.0))) + HMk * L10f + HCk);
        Vk += (Vaj[index] * exp(-(pow(((L10f-
Vbj[index])/Vcj[index]), 2.0))) + VMk * L10f + VCk);
    }
    Hk = pow(10,Hk);
    Vk = pow(10,Vk);

    Ha = 0.0;
    Va = 0.0;
```

```
    for (index=0; index<5; index++)
    {
        Ha += (Hai[index] * exp( -(pow(((L10f-
Hbi[index])/Hci[index]), 2.0))) + HMa * L10f + HCa);
        Va += (Vai[index] * exp( -(pow(((L10f-
Vbi[index])/Vci[index]), 2.0))) + VMa * L10f + VCa);
    }

    // returned values
    *k     = (Hk+Vk+(Hk-Vk)*(pow(cos(slantAngle*pi/180.0),
2.0))*cos(2.0*(polarisationTiltAngle*pi/180.0)))/2;
    *alpha = (Hk*Ha+Vk*Va+(Hk*Ha-
Vk*Va)*(pow(cos(slantAngle*pi/180.0),
2.0))*cos(2*(polarisationTiltAngle*pi/180.0)))/(2.0* *k);
}



double attenuationRainFunction (int altitude, int frequency, double
slantAngle)
{
    // PARAMETERS
    //
    // altitude        = altitude of airborne platform (km)    (hS)
    // frequency       = frequency (GHz)
    // slantAngle      = elevation angle (degrees)
    // returns: Ap     = average annual fade exceeded at given
percentage (dB)
    // limits: valid only between 7GHz to 55GHz
    //

    // VALIDITY
    //
    // 7GHz to 55GHz frequency range
    // positive values of altitude
    //

    //  PROCEDURE
    //  Calculation as described in ITU-R P.618 section 2.2.1.1
    //
    //  Step 1:  determine the rain height
    //  Step 2:  calculate the slant path length
    //  Step 3:  calculate the horizontal projection of the slant
path
    //  Step 4:  obtain the rainfall rate exceeded for 0.01% of an
average year from ITU-R P.837
    //  Step 5:  obtain the specific attenuation using the frequency
dependent coefficients in ITU-R P.838
    //  Step 6:  calculate the horizontal reduction factor
    //  Step 7:  calculate the vertical adjustment factor
    //  Step 8:  calculate the effective path length
    //  Step 9:  calculate the predicted attenuation exceeded for
0.01% of an average year
    //  Step 10: calculate the estimated attenuation


    // VARIABLES
    //
```

```
    // Step 2: calculate the slant path length
    double slantPathLength;


    // Step 3: calculate the horizontal projection of the slant path
    double horizontalProjection;

    // Step 4: obtain the rainfall rate
    double rainfallRate;

    // Step 5: obtain the specific attenuation
    double k;
    double alpha;
    double gammaR;

    // Step 6: calculate the horizontal reduction factor
    double horizontalReductionFactor;

    // Step 7: calculate the vertical adjustment factor
    double zeta;
    double verticalAdjustmentFactor;
    double chi;
    double nu001;

    // Step 8: calculate the effective path length
    double effectivePathLength;

    // Step 9: calculate the predicted attenuation
    double averageYearAttenuation;

    // Step 10:
    double beta;
    double Ap;


    // CONSTANTS
    //
    const double rainHeight = 6.36;  // km      // ITU-R
P.839    (hR)
    const double pi = 3.1415926536;
    const double radiusOfEarth = 6371.0;  // km  average radius of
the Earth
    const double latitudeOfEarthStation = 45.0;  // degrees     -
average position  (phi)
    const double timePercentages = 1.0;  //  (p)   - estimated

    // Check parameter validity
    //
    if ((altitude < 0) || (frequency < 7) || (frequency > 55))
    {
        return (0.0);
    }


    // IMPLEMENTATION
    //
    // Step 1: determine the rain height
    //
    if ((double) altitude >= rainHeight)
```

```
    {
        return (0.0);   // as noted in ITU-R P.2041 and ITU-R P.618
above the rainHeight the attenuation due to rain is of course zero
    }


    // Step 2: calculate the slant path length
    //
    // altitude is below the rainHeight with the slantPath being
that part of the path traversing the rain
    //
    if (slantAngle >= 5.0)  // degrees
    {
        slantPathLength = (rainHeight-
(double)altitude)/sin(slantAngle*pi/180.0);
    }
    else
    {
        slantPathLength = (2.0 * (rainHeight-(double)altitude)) / (
sqrt(pow(sin(slantAngle*pi/180.0), 2.0) + ((2.0 * (rainHeight-
(double)altitude)) / radiusOfEarth)) +
sin(slantAngle*pi/180.0));   // km  (LS)
    }


    // Step 3: calculate the horizontal projection of the slant path
    //
    horizontalProjection = slantPathLength *
cos(slantAngle*pi/180.0);  // km  (LG)


    // Step 4: obtain the rainfall rate exceeded for 0.01% of an
average year from ITU-R P.837
    //
    rainfallRate = ITURP837();  //


    // Step 5: obtain the specific attenuation using the frequency
dependent coefficients in ITU-R P.838
    //
    k = 0.0;
    alpha = 0.0;
    ITURP838 (&k, &alpha, (double)frequency, slantAngle);  // ITU-R
P.838
    gammaR = k * pow(rainfallRate, alpha);         // dB/km


    // Step 6: calculate the horizontal reduction factor
    //
    horizontalReductionFactor = 1.0/( 1.0 + 0.79 *
sqrt(horizontalProjection * gammaR / (double)frequency) - 0.38 * (
1.0 - exp(-2.0 * horizontalProjection) ) );   //  (r0.01)


    // Step 7: calculate the vertical adjustment factor
    //
    zeta = atan((rainHeight-(double)altitude)/(horizontalProjection
* horizontalReductionFactor));
```

```
    if (zeta>(slantAngle*pi/180.0))
    {
        verticalAdjustmentFactor = (horizontalProjection *
horizontalReductionFactor) / cos(slantAngle*pi/180.0);  // (LR)
    }
    else
    {
        verticalAdjustmentFactor = (rainHeight -
(double)altitude)/sin(slantAngle*pi/180.0);  // (LR)
    }

    if (fabs(latitudeOfEarthStation)<36.0)  // degrees
    {
        chi = 36.0-fabs(latitudeOfEarthStation); // degrees
    }
    else
    {
        chi = 0;  // degrees
    }

    nu001 =
sqrt(latitudeOfEarthStation*gammaR)/pow((double)frequency,2.0);
    nu001 = 31.0 * ( 1.0-exp( -( slantAngle/( 1.0+chi ) ) ) ) *
nu001 - 0.45;
    nu001 = 1.0 + sqrt( sin(slantAngle*pi/180.0) ) * nu001;
    nu001 = 1.0 / nu001;


    // Step 8: calculate the effective path length
    //
    effectivePathLength = verticalAdjustmentFactor * nu001;  //
km  (LE)


    // Step 9: calculate the predicted attenuation exceeded for
0.01% of an average year
    //
    averageYearAttenuation = gammaR * effectivePathLength;   //
dB  (A0.01)


    // Step 10: calculate the estimated attenuation
    //
    beta = -0.005 * (fabs(latitudeOfEarthStation)-36.0) + 1.8 -
4.25*sin(slantAngle*pi/180.0);

    if ((timePercentages>=1.0) ||
(fabs(latitudeOfEarthStation)>=36.0))
    {
        beta = 0.0;
    }

    if ((timePercentages<1.0) && (fabs(latitudeOfEarthStation)<36.0)
&& (slantAngle>=25.0))
    {
        beta = -0.005*(fabs(latitudeOfEarthStation)-36);
    }
```

```
    Ap = averageYearAttenuation * pow((timePercentages/0.01),( -
(0.655+0.033*log(timePercentages)-0.045*log(averageYearAttenuation)
- beta *(1-timePercentages)*sin(slantAngle*pi/180.0) ) ));

    return (Ap);
}


#endif /* attenRainFunction_h */
```

```
//
//  attenTropoScintillationFunction.h
//  ITUPathLossModel
//
//  Created on 13/01/2016.
//  Copyright © 2016 Emma Jones. All rights reserved.
//

// ITU-R P.618


#ifndef attenTropoScintillationFunction_h
#define attenTropoScintillationFunction_h

# include <math.h>

#include "temperatureData.h"                                // ITU-R
P.835
#include "pressureData.h"                                   // ITU-R
P.835
#include "waterVapourDensityData.h"                         // ITU-R
P.835

#include "attenRefractionFunction.h"


double attenTropoScintillationFunction (int frequency, double
slantAngle, double earthAntennaDiameter)
{
    // PARAMETERS
    //
    //  frequency               (GHz)
    //  slantAngle              (degrees)
    //  earthAntennaDiameter    (metres)
    //  Returns:
    //    tropospheric scintillation fade depth (dB)
    // limits: valid only between 7GHz to 14GHz
    //

    // VALIDITY
    //
    // 7GHz to 14GHz frequency range
    // positive values of altitude
    //

    // PROCEDURE
    //
    // from 7GHz up to at least 14GHz and slant angle >= 5 degrees
(ITU-R P.618)
    //
    // Part 1:  Prediction of the amplitude scintillation fading at
free-space elevation angles >= 5° (§ 2.4.1).
    // Step 1:  For the value of t, calculate the saturation water
vapour pressure es (hPa) (ITU-R P.453)
    // Step 2:  Compute the wet term of the radio refractivity,
Nwet, corresponding to es, t and H  (N-units) (ITU-R P.453)
    // Step 3:  Calculate the standard deviation of the reference
signal amplitude
```

```
    // Step 4:  Calculate the effective path length
    // Step 5:  Estimate the effective antenna diameter
    // Step 6:  Calculate the antenna averaging factor
    // Step 7:  Calculate the standard deviation of the signal for
the applicable period and propagation path
    // Step 8:  Calculate the time percentage factor, a( p), for the
time percentage, p, in the range between 0.01% < p <= 50%
    // Step 9:  Calculate the fade depth
    //


    // VARIABLES
    //
    double x = 0.0;
    double v1 = 0.0;
    double sigma = 0.0;
    double sigmaRef = 0.0;
    double Nwet = 0.0;                        // N-units
    double effectivePathLength = 0.0;         // metres
    double effectiveAntennaDiameter = 0.0;  // metres
    double antennaAveragingFactor = 0.0;
    double efWater = 0.0;
    double scintillationFadeDepth = 0.0;    // dB
    double timePercentageFactor = 0.0;      // %
    double saturationWaterVapourPressure = 0.0; // hPa  (es)
    double temperature = 0.0;                 // Kelvin (t)
    double dryAtmosphericPressure = 0.0;    // hPa (P)
    double waterVapourPressure = 0.0;       // hPa (e)


    // CONSTANTS
    //
    const double pi = 3.1415926536;

    const double antennaEfficiency = 0.5;    // conservative
estimate as recommended in ITU-R P.618
    const double heightOfTheTurbulentLayer = 1000.0;  // m
    const double timePercentage = 8.33;  //  (p)    "for a period of
one month or longer" (ITU-R P.618)


    // The following constants are for water and cover the
temperature range -40degC to +50degC as described in ITU-R P.453
    //
    const double a = 6.1121;
    const double b = 18.678;
    const double c = 257.14;
    const double d = 234.5;

    const int altitude = 0; // metres  - ITU-R P.2041 if below the
rainHeight, tropospheric scintillation is calculated as being at the
ground

    // Check parameter validity
    //
    if ((altitude < 0) || (frequency < 7) || (frequency > 14))
    {
        return (0.0);
    }
```

```
    // IMPLEMENTATION
    //
    // Step 1: For the value of t calculate the saturation water
vapour pressure from ITU-R P.453
    //
    temperature = temperatureListData[altitude][1];  // (t)
    dryAtmosphericPressure = pressureListData[altitude][1]; // (P)

    efWater = 1e-4 * (7.2 + (dryAtmosphericPressure * (0.00320 +
(5.9e-7 * pow(temperature, 2.0)))));  // water
    saturationWaterVapourPressure = efWater * a * exp((((b-
(temperature/d))*temperature))/(temperature+c));  // (es) saturation

    // Step 2: Compute the wet term of the radio refractivity, Nwet,
corresponding to es, t and H as given in ITU-R P.453
    //
    waterVapourPressure = (waterVapourDensityListData[altitude][1] *
temperature) / 216.7;  // conversion from water vapour density to
pressure
    Nwet = (72.0 *(waterVapourPressure/temperature)) + (3.75e5 *
(waterVapourPressure/pow(temperature, 2.0)));  // N-units

    // Step 3: calculate the standard deviation of the reference
signal amplitude
    //
    sigmaRef = 3.6e-3 + (1e-4 * Nwet);  // dB

    // Step 4: calculate the effective path length
    //
    effectivePathLength = (2.0 * heightOfTheTurbulentLayer) /
(sqrt((sin(slantAngle*3.1415926536/180.0)*(sin
(slantAngle*3.1415926536/180.0))) + (2.35e-4)) +
sin(slantAngle*3.1415926536/180.0));

    // Step 5: calculate the effective antenna diameter
    //
    effectiveAntennaDiameter = sqrt(antennaEfficiency) *
earthAntennaDiameter;  // metres

    // Step 6: calculate the antenna averaging factor
    //
    x = 1.22 * pow(effectiveAntennaDiameter, 2.0) *
((double)frequency / effectivePathLength);

    double aa = (3.86 * pow((pow(x, 2.0) + 1), (11/12)));
    double ee = 1/x;
    double dd = ((11/6) * atan(ee));
    double bb = 3.86*(sin (dd));
    double cc = (7.08 * pow(x, (5/6)));
    v1 = (aa+bb)-cc;
    if (v1 < 0.0)
    {
        return (0.0);  // "If the argument of the square root is
negative, the predicted scintillation fade depth for any time
percentage is zero and the following steps are not required." (ITU-R
P.618)
    }
```

```
    antennaAveragingFactor = sqrt(v1);

    // Step 7:
    //
    sigma = sigmaRef * pow((double)frequency, (7/12)) *
(antennaAveragingFactor/ (pow (sin(slantAngle*pi/180.0), 1.2)));

    // Step 8:
    //
    timePercentageFactor = (-0.061 * (pow(log10(timePercentage),
3.0))) + (0.072 * pow(log10(timePercentage), 2.0)) - (1.71 *
log10(timePercentage)) + 3.0;

    // Step 9:
    scintillationFadeDepth = timePercentageFactor * sigma;  // dB


    return (scintillationFadeDepth);
}

#endif /* attenTropoScintillationFunction_h */
```

```
//
//  attenIonosphericEffectsFunction.h
//  ITUPathLossModel
//
//  Created on 15/01/2016.
//  Copyright © 2016 Emma Jones. All rights reserved.
//

#ifndef attenIonosphericEffectsFunction_h
#define attenIonosphericEffectsFunction_h

// ITU-R P.531
//
// ATMOSPHERIC LAYERS
// D Layer
//  60 - 90 km
//  Mainly 10MHz and below
//
// E layer
//  90 - 160 km
//  Kennely-Heaviside layer
//  Mainly 10MHz and below
//
// Es sporadic E layer
//  can cause reflection up to 50MHz
//
// F layer
//  Appleton-Barnett layer
//  150 - 800km
//
// F1 layer
//  150 - 220km (only during daylight)
//  Merges into the F2 layer at night
//
// F2 layer
//  220 - 800km
//

#include <math.h>


void attenIonosphericEffectsFunction (double frequency, double
*ionosphericAttenuation, double *faradayRotation, double
*groupDelay)
{
    // PARAMETERS
    //  frequency (GHz)
    //  Returns:
    //    ionosphericAttenuation (dB)
    //    faradayRotation (degrees)
    //    groupDelay (seconds)
    // limits: applies to paths traversing 60km to 800km altitude
    //

    // VALIDITY
    //
    // 30MHz to 12GHz frequency range (values approach 0.0 beyond
12GHz)
```

```
    // positive values of altitude
    //

    // VARIABLES
    //
    double peakToPeakFluctuation = 0.0;  // dB  (Pfluc)
    double sv1 = 0.0;


    // CONSTANTS
    //
    //  "For modelling purposes, the TEC value is usually quoted for
a zenith path
    //  having a cross-section of 1 m^2.
    //  The TEC of this vertical column can vary between 1e16 and
1e18 el/m2 with
    //  the peak occurring during the sunlit portion of the day."
    //
    const double pi  = 3.1415926536;
    const double Nt  = 1e18;  // electrons/m^2  (TEC)
    const double Bav = (25000e-9 + 65000e-9)/2.0;  // Wb/m^2
(Teslas)


    // IMPLEMENTATION
    //
    // Faraday rotation
    //
    *faradayRotation = (2.36e-14 * ((Bav * Nt) / pow(frequency,
2.0))) * (180.0/pi);  // degrees


    // Group delay
    //
    *groupDelay = 1.345 * Nt / pow((frequency*1e9), 2.0) * 1e-7;  //
seconds


    // Absorption
    //
    //  "When direct information is not available, ionospheric
absorption loss can
    //  be estimated from available models according to the (sec i )
/ f^2 relationship
    //  for frequencies above 30 MHz, where i is the zenith angle of
the propagation
    //  path in the ionosphere."
    //  "... for a one-way traverse of the ionosphere at vertical
incidence, the absorption
    //  at 30 MHz under normal conditions is typically 0.2 to 0.5
dB.
    //  During a solar flare, the absorption will increase but will
be less than 5 dB."
    //
    *ionosphericAttenuation = 0.5 * (0.030/pow(frequency, 2.0));  //
dB  (at 30MHz, decreasing as 1/f)


    // Scintillation
```

```
    //
    //  Assumes an average scintillation level of S4 = 0.5 at 4GHz

    if (frequency <= 4.0)  // GHz
    {
        peakToPeakFluctuation = 20;  // dB - equivalent to S4 = 0.5
at 4GHz
    }
    else if ((frequency > 4.0) && (frequency <=12.0))  // GHz
    {
        peakToPeakFluctuation = 20;  // dB - equivalent to S4 = 0.5
at 4GHz
        // scaled from the 4GHz value to zero at 12GHz using 1/f
        sv1 = peakToPeakFluctuation / (12.0 - 4.0);
        peakToPeakFluctuation = peakToPeakFluctuation-
(sv1*(frequency-4.0));
    }
    else
    {
        peakToPeakFluctuation = 0.0;
    }

    *ionosphericAttenuation += peakToPeakFluctuation;
}

#endif /* attenIonosphericEffectsFunction.h */
```

```
//
//  attenRefractionFunction.h
//  ITUPathLossModel
//
//  Created on 21/01/2016.
//  Copyright © 2016 Emma Jones. All rights reserved.
//

// ITU-R P.453
//
// "For Earth-satellite paths, the refractive index at any height is
obtained using
// equations (1), (2) and (10) ..., together with the appropriate
values for the
// parameters given in Recommendation ITU-R P.835, Annex 1. The
refractive indices
// thus obtained may then be used for numerical modelling of ray
paths through
// the atmosphere."
//

#ifndef attenRefractionFunction_h
#define attenRefractionFunction_h

#include <math.h>

#include "temperatureData.h"                                // ITU-R
P.835
#include "pressureData.h"                                   // ITU-R
P.835
#include "waterVapourDensityData.h"                         // ITU-R
P.835


double attenuationRefractionFunction (int altitude)
{
    // PARAMETERS
    //
    //  altitude    (km)
    //  Returns:
    //      radioRefractivity   (N-units)

    // VARIABLES
    //
    double radioRefractivity = 0.0;         // (N)  N-units
    double temperature = 0.0;               // (T)  K
    double waterVapourPressure = 0.0;       // (e)  hPa
    double dryAtmosphericPressure = 0.0;    // (P)  hPa


    // IMPLEMENTATION
    //
    temperature = temperatureListData[altitude][1];
    dryAtmosphericPressure = pressureListData[altitude][1];
    waterVapourPressure = (waterVapourDensityListData[altitude][1] *
temperature) / 216.7;  // conversion from water vapour density to
pressure
```

```
    radioRefractivity = (77.6 *
(dryAtmosphericPressure/temperature)) + (72.0 *
(waterVapourPressure/temperature)) + (3.75e5 *
(waterVapourPressure/(pow(temperature, 2.0))));

    return (radioRefractivity);
}

#endif /* attenRefractionFunction_h */
```

```
//
//  freeSpacePathLossFunction.h
//  ITUPathLossModel
//
//  Created on 24/01/2016.
//  Copyright © 2016 Emma Jones. All rights reserved.
//

#ifndef freeSpacePathLossFunction_h
#define freeSpacePathLossFunction_h

// From ITU-R P.525
//


#include <math.h>

double freeSpacePathLossFunction (double pathLength, double
frequency)
{
    // PARAMETERS
    //
    //  pathlength (km)
    //  frequency (GHz) - converted to MHz for calculation
    //  Returns:
    //    free space path loss (dB)

    if (frequency == 0.0)
    {
        return (0.0);  // to prevent returning NaN
    }
    else
    {
        return ((20*log10(pathLength)) +
(20*log10(frequency*1000.0)) + 32.45);
    }
}

#endif /* freeSpacePathLossFunction_h */
```

```c
//
//  main.c
//  ITUPathLossModel
//
//  Created on 10/01/2016.
//  Updated to generic calculation 2017.
//  Copyright © 2016 Emma Jones. All rights reserved.
//


#include <stdio.h>
#include <math.h>

#include "temperatureData.h"                // ITU-R P.835
#include "pressureData.h"                   // ITU-R P.835
#include "waterVapourDensityData.h"         // ITU-R P.835

#include "aircraftAltitudeData.h"           // from PhD thesis
#include "satelliteAltitudeData.h"          // from PhD thesis
#include "earthSpaceFrequencyListData.h"    // from PhD thesis
#include "spaceEarthFrequencyListData.h"    // from PhD thesis
#include "spaceSpaceFrequencyListData.h"    // from PhD thesis

#include "slantPathCalculation.h"           // from PhD thesis

#include "attenITUPathLoss.h"               // from PhD thesis

//Functions written in PhD thesis from ITU-R standards
#include "attenGaseousFunction.h"           // ITU-R P.676 and ITU-
R P.835
#include "attenCloudsFunction.h"            // ITU-R P.840 and ITU-
R P.1144
#include "attenRainFunction.h"              // ITU-R P.618, ITU-R
P.837 and ITU-R P.838
#include "attenTropoScintillationFunction.h" // ITU-R P.618, ITU-R
P.839 and ITU-R P.453
#include "attenIonosphericEffectsFunction.h" // ITU-R P.618, ITU-R
P.531 and ITU-R P.1239
#include "attenRefractionFunction.h"        // ITU-R P.453
#include "freeSpacePathLossFunction.h"      // ITU-R P.525



// Total path loss attenuation ITU-R P.2041
int main(int argc, const char * argv[])
{
    // Constants - change to modify output
    const int TRUE = 1;
    const int FALSE = 0;

    const int enableFSPL = TRUE;
    const int enableClouds = TRUE;
    const int enableRain = TRUE;
    const int enableTropospherics = TRUE;
    const int enableIonospherics = TRUE;
    const int enableGaseous = TRUE;
    const int enableGaseousTestMode = FALSE;
```

```
    const int useAircraftAltitudeData = TRUE;
    const int useSatelliteAltitudeData = TRUE;
    const int useEarthSpaceFrequencyListData = FALSE;
    const int useSpaceEarthFrequencyListData = TRUE;
    const int useSpaceSpaceFrequencyListData = FALSE;

    const char* fileName = "20180128 - all effects - results.csv";

    const double startFrequency         = 1.0;     // GHz
    const double endFrequency           = 1000.0;  // GHz
    const double frequencyStep          = 10.0;    // GHz

    const double startPlatform1Altitude = 1.0;     // km
    const double endPlatform1Altitude   = 400.0;   // km
    const double platform1AltitudeStep  = 1.0;     // km

    const double startPlatform2Altitude = 0.0;     // km
    const double endPlatform2Altitude   = 400.0;   // km
    const double platform2AltitudeStep  = 1.0;     // km

    const double startSlantAngle        = 5.0;     // degrees
    const double endSlantAngle          = 90.0;    // degrees
    const double slantAngleStep         = 5.0;     // degrees

    const int startAircraftAltData      = 0;
    const int endAircraftAltData        = aircraftListSize-1;

    const int startSatelliteAltData     = 0;
    const int endSatelliteAltData       = satelliteListSize-1;

    const int startEarthSpaceFreqData   = 0;
    const int endEarthSpaceFreqData     =
earthSpaceFrequencyListSize-1;

    const int startSpaceEarthFreqData   = 0;
    const int endSpaceEarthFreqData     =
spaceEarthFrequencyListSize-1;

    const int startSpaceSpaceFreqData   = 0;
    const int endSpaceSpaceFreqData     =
spaceSpaceFrequencyListSize+1;

    const double earthAntennaDiameter   = 0.6; // m


    // Initialise VARIABLES
    //
    FILE *fileHandle;
    double atten        = 0.0;   // dB
    double frequency    = 0.0;   // GHz

    double platform1Alt = 0.0;   // km
    double platform2Alt = 400.0; // km
    double slantAngle   = 90.0;  // deg
    double frequencyValue = 0.0; // GHz

    int aircraftAltLoop  = 0;
    int satelliteAltLoop = 0;
    int earthSpaceFreqLoop = 0;
```

```
    int spaceEarthFreqLoop = 0;
    int spaceSpaceFreqLoop = 0;
    int frequencyLoop = 0;



    // IMPLEMENTATION
    //
    fileHandle = fopen(fileName, "w");
    fprintf (fileHandle, "attenuation, frequency, platform1Alt,
platform2Alt, slantAngle, earthAntennaDiameter, enableFSPL,
enableClouds, enableRain, enableTropospherics, enableIonopherics,
enableGaseous, enableGaseousTestMode, useAircraftAltitudeData,
useSatelliteAltitudeData, useEarthSpaceFrequencyListData,
useSpaceEarthFrequencyListData,
useSpaceSpaceFrequencyListData\n");  // File Headers (first line)

    for (aircraftAltLoop=startAircraftAltData;
aircraftAltLoop<=endAircraftAltData; aircraftAltLoop++)
    {
        for (satelliteAltLoop=startSatelliteAltData;
satelliteAltLoop<=endSatelliteAltData; satelliteAltLoop++)
        {
            for (earthSpaceFreqLoop=startEarthSpaceFreqData;
earthSpaceFreqLoop<=endEarthSpaceFreqData; earthSpaceFreqLoop++)
            {
                for (spaceEarthFreqLoop=startSpaceEarthFreqData;
spaceEarthFreqLoop<=endSpaceEarthFreqData; spaceEarthFreqLoop++)
                {
                    for (spaceSpaceFreqLoop=startSpaceSpaceFreqData;
spaceSpaceFreqLoop<=endSpaceSpaceFreqData; spaceSpaceFreqLoop++)
                    {
                        for (frequencyLoop=startFrequency;
frequencyLoop<=endFrequency; frequencyLoop+=frequencyStep)
                        {
                            for
(platform1Alt=startPlatform1Altitude;
platform1Alt<=endPlatform1Altitude;
platform1Alt+=platform1AltitudeStep)
                            {
                                for
(platform2Alt=startPlatform2Altitude;
platform2Alt<=endPlatform2Altitude;
platform2Alt+=platform2AltitudeStep)
                                {
                                    for (slantAngle=startSlantAngle;
slantAngle<=endSlantAngle; slantAngle+=slantAngleStep)
                                    {
                                        // Enable dataset usage
                                        if (useAircraftAltitudeData
== TRUE)
                                        {
                                            platform1Alt = (double)
aircraftAltitudeListData[aircraftAltLoop];
                                        }
                                        if (useSatelliteAltitudeData
== TRUE)
                                        {
```

```
                                                    platform2Alt = (double)
satelliteAltitudeListData[satelliteAltLoop];
                                                }
                                                frequency = (double)
frequencyValue;
                                                if
(useEarthSpaceFrequencyListData == TRUE)
                                                {
                                                    frequency =
(earthSpaceFrequencyList[earthSpaceFreqLoop][0]+earthSpaceFrequencyL
ist[earthSpaceFreqLoop][1])/2.0;  // use the average frequency
                                                }
                                                if
(useSpaceEarthFrequencyListData == TRUE)
                                                {
                                                    frequency =
(spaceEarthFrequencyList[spaceEarthFreqLoop][0]+spaceEarthFrequencyL
ist[spaceEarthFreqLoop][1])/2.0;  // use the average frequency
                                                }
                                                if
(useSpaceSpaceFrequencyListData == TRUE)
                                                {
                                                    frequency =
(spaceSpaceFrequencyList[spaceSpaceFreqLoop][0]+spaceSpaceFrequencyL
ist[spaceSpaceFreqLoop][1])/2.0;  // use the average frequency
                                                }
                                                // To prevent the
calculation from breaking geometrically, replace 90deg
                                                if ((slantAngle > 89.999999)
&& (slantAngle < 90.000001))
                                                {
                                                    slantAngle = 89.999999;
                                                }
                                                atten = attenITUPathLoss
(frequency, platform1Alt, platform2Alt, slantAngle,
earthAntennaDiameter, enableFSPL, enableClouds, enableRain,
enableTropospherics, enableIonospherics, enableGaseous,
enableGaseousTestMode, useAircraftAltitudeData,
useSatelliteAltitudeData, useEarthSpaceFrequencyListData,
useSpaceEarthFrequencyListData, useSpaceSpaceFrequencyListData);
                                                fprintf (fileHandle, "%le,
%le, %le, %le, %le, %le, %d, %d, %d, %d, %d, %d, %d, %d, %d, %d, %d,
%d\n", atten, frequency, platform1Alt, platform2Alt, slantAngle,
earthAntennaDiameter, enableFSPL, enableClouds, enableRain,
enableTropospherics, enableIonospherics, enableGaseous,
enableGaseousTestMode, useAircraftAltitudeData,
useSatelliteAltitudeData, useEarthSpaceFrequencyListData,
useSpaceEarthFrequencyListData, useSpaceSpaceFrequencyListData);
                                                // printf ("frequency =
%f,  attenuation = %f\n\n", frequency, atten);
                                            }
                                        }
                                    }
                                }
                            }
                        }
                    }
                }
            }
        }
    }
```

```
    fclose (fileHandle);
    return (0);
}
```

Appendix B

Matlab codes for Simulation

Calculation of the RF environment created by multiple satellite transmissions, for correlated signal propagation and combination as per the mathematical model described in Section 5

Matlab-code implementation of the RF calculations outlined in this thesis.

Correlated signal transmission in layered communication model

Illustration of the potential of layered communication including the concept of spatial correlation

Correlated signal transmission in layered communication model

```
// Illustration of the potential of layered communication in the
HALO environment
//  With option for additional AWGN

srcx1       = 50;       // position in kilometres
srcy1       = (500-30); // position in kilometres
srcFreq1    = 2.4; // frequency in GHz
txPwr1      =  20; // transmit power (W)
txGain1     =  17; // transmit antenna gain (dBm)
rxGaindBm1  =   3; // receive antenna gain (dBm)
rxThrshdBm1 = -67; // receive threshold (dBm)
noiseLevel1 =   0; // dBm

srcx2       = 250;       // position in kilometres
srcy2       = (500-20); // position in kilometres
srcFreq2    = 2.4; // frequency in GHz
txPwr2      =  20; // transmit power (W)
txGain2     =  17; // transmit antenna gain (dBm)
rxGaindBm2  =   3; // receive antenna gain (dBm)
rxThrshdBm2 = -67; // receive threshold (dBm)
noiseLevel2 =   0; // dBm

srcx3       = 500-50;       // position in kilometres
srcy3       = (500-30); // position in kilometres
srcFreq3    = 2.4; // frequency in GHz
txPwr3      =  20; // transmit power (W)
txGain3     =  17; // transmit antenna gain (dBm)
rxGaindBm3  =   3; // receive antenna gain (dBm)
rxThrshdBm3 = -67; // receive threshold (dBm)
noiseLevel3 =   0; // dBm

txValdBm1 = (10 * log(txPwr1*1000)) + txGain1; // dBm
txValdBm2 = (10 * log(txPwr2*1000)) + txGain2; // dBm
txValdBm3 = (10 * log(txPwr3*1000)) + txGain3; // dBm

nx = 500; ny = 500;    // define the number of elements along x and
y
x = linspace(-1, 1, nx); // define the range of x
y = linspace(-1, 1, ny); // define the range of y
[X, Y] = ndgrid(x, y);   // create a 2-D array of x and y
coordinates
haloSpace = zeros(nx, ny); //zeroise the array
xpl = [1:nx];  // Vector of values for line graphs

// Step through the haloSpace and add the signal strength at each
point
for ypos=1:1:500
   for xpos=1:1:500
      // Source 1
      distx = abs (srcx1 - xpos);  // km
      disty = abs (srcy1 - ypos);  // km
      pathLength = sqrt((distx^2)+(disty^2));  // km
      // FSPL in GHz and km
      if (pathLength == 0) then
          pathloss = 999.99;  // dB
      else
```

```
          pathLoss = (20*log(pathLength)) + (20*log(srcFreq1)) +
92.45;  // dB
      end
      pathLossVal = (10^(pathLoss/10))*1000;
      pathLossdBm = 10*log(pathLossVal);
      // Channel model
      rxSigStrength1 = txValdBm1 - pathLoss + rxGaindBm1;

      // Source 2
      distx = abs (srcx2 - xpos);  // km
      disty = abs (srcy2 - ypos);  // km
      pathLength = sqrt((distx^2)+(disty^2));  // km
      // FSPL in GHz and km
      if (pathLength == 0) then
          pathloss = 999.99;  // dB
      else
          pathLoss = (20*log(pathLength)) + (20*log(srcFreq2)) +
92.45;  // dB
      end
      pathLossVal = (10^(pathLoss/10))*1000;
      pathLossdBm = 10*log(pathLossVal);
      // Channel model
      rxSigStrength2 = txValdBm2 - pathLoss + rxGaindBm2;

      // Source 3
      distx = abs (srcx3 - xpos);  // km
      disty = abs (srcy3 - ypos);  // km
      pathLength = sqrt((distx^2)+(disty^2));  // km
      // FSPL in GHz and km
      if (pathLength == 0) then
          pathloss = 999.99;  // dB
      else
          pathLoss = (20*log(pathLength)) + (20*log(srcFreq3)) +
92.45;  // dB
      end
      pathLossVal = (10^(pathLoss/10))*1000;
      pathLossdBm = 10*log(pathLossVal);
      // Channel model
      rxSigStrength3 = txValdBm3 - pathLoss + rxGaindBm3;

      // rxMargin = rxSigStrength - rxThrsh;
      haloSpace(xpos, ypos) = (rxSigStrength1-rxThrshdBm1) +
(rand()*noiseLevel1) + (rxSigStrength2-rxThrshdBm2) +
(rand()*noiseLevel2) + (rxSigStrength3-rxThrshdBm3) +
(rand()*noiseLevel3);

   end
end

// Chart 1: 3D plot of the HALO space
//a=scf(1);
//plot3d (x, y, haloSpace);

// Chart 2: Contour  plot of the HALO space
b=scf(2);
contour (x, y, haloSpace, [200, 190, 180, 170, 160, 150, 140, 130,
120, 110, 100, 90, 80, 70, 60, 50, 40, 30, 20, 10, 0, -10, -20, -30,
-40, -50, -60, -70, -80, -90, -100, -110, -120, -130, -140, -150, -
160, -170, -180, -190, -200, -210, -220, -230, -240, -250, -260, -
270, -280, -290, -300, -310, -320, -330, -340, -350, -360, -370, -
380, -390, -400]);
```

```
// Chart 3: plot the signal strength for an aircraft flying at a
fixed altitude
//c=scf(3);
//plAlt=18; //km
//for xy=1:1:500
//    xpl(xy)=-145;
//end
//for xx=175:1:325
//    xpl(xx-174)=haloSpace(xx, plAlt);
//end
//plot(xpl);

// Chart 4: plot the signal strength for an aircraft flying a zoomy
//d=scf(4);
//plXPos=150; //km
//for xy=1:1:500
//    xpl(xy)=-145;
//end
//for xy=16:1:110
//    xpl(xy-15)=haloSpace(plXPos, xy);
//end
//plot(xpl);
```

Illustration of the potential of layered communication including the concept of spatial correlation

```
// Illustration of the potential of layered communication in the
HALO environment
// Model including concept of spatial correlation

srcx1       = 250; // position in kilometres
srcy1       = 499; // position in kilometres
srcFreq1    = 2.4; // frequency in GHz
txPwr1      = 100; // transmit power (W)
txGain1     =  17; // transmit antenna gain (dBm)
rxGaindBm1  =   3; // receive antenna gain (dBm)
rxThrshdBm1 = -67; // receive threshold (dBm)
noiseLevel1 =   0; // dBm

srcx2       = 499; // position in kilometres
srcy2       = 250; // position in kilometres
srcFreq2    = 2.4; // frequency in GHz
txPwr2      = 100; // transmit power (W)
txGain2     =  17; // transmit antenna gain (dBm)
rxGaindBm2  =   3; // receive antenna gain (dBm)
rxThrshdBm2 = -67; // receive threshold (dBm)
noiseLevel2 =   0; // dBm

chipDistance1 = 50; // km
chipDistance2 = 50; // km

distRatio = 1;

txValdBm1 = (10 * log(txPwr1*1000)) + txGain1; // dBm
txValdBm2 = (10 * log(txPwr2*1000)) + txGain2; // dBm

nx = 500; ny = 500;       // define the number of elements along x
and y
x = linspace(0, 500, nx); // define the range of x
y = linspace(0, 500, ny); // define the range of y
[X, Y] = ndgrid(x, y);    // create a 2-D array of x and y
coordinates
haloSpace = zeros(nx, ny); //zeroise the array
xpl = [1:nx];  // Vector of values for line graphs

// Animate the sequence of wavefront propagation
for animTime=1:10:500
    valid = 0;

// Step through the haloSpace and add the signal strength at each
point
for ypos=1:5:500
   for xpos=1:5:500

      dist1 = sqrt ((abs (srcx1-xpos)^2)+(abs (srcy1-ypos)^2));
      dist2 = sqrt ((abs (srcx2-xpos)^2)+(abs (srcy2-ypos)^2));

      haloSpace(xpos, ypos) = 0.0; // start with a blank sheet

      distMin1AtAnimTime = animTime-chipDistance1;  //km
      if  (distMin1AtAnimTime <0) then
          distMin1AtAnimTime = 0;        // prevent negative
distances
```

```
      end
      distMax1AtAnimTime = animTime;     //km

      distMin2AtAnimTime = animTime-chipDistance2;  //km
      if  (distMin2AtAnimTime <0) then
          distMin2AtAnimTime = 0;        // prevent negative
distances
      end
      distMax2AtAnimTime = animTime;     //km

      // Source 1
      distx = abs (srcx1 - xpos);  // km
      disty = abs (srcy1 - ypos);  // km
      pathLength = sqrt((distx^2)+(disty^2));  // km
      // FSPL in GHz and km
      if (pathLength == 0) then
          pathloss = 999.99;  // dB
      else
          pathLoss = (20*log(pathLength*distRatio)) +
(20*log(srcFreq1)) + 92.45;  // dB
      end
      pathLossVal = (10^(pathLoss/10))*1000;
      pathLossdBm = 10*log(pathLossVal);
      // Channel model
      rxSigStrength1 = txValdBm1 - pathLoss + rxGaindBm1;

      // Source 2
      distx = abs (srcx2 - xpos);  // km
      disty = abs (srcy2 - ypos);  // km
      pathLength = sqrt((distx^2)+(disty^2));  // km
      // FSPL in GHz and km
      if (pathLength == 0) then
          pathloss = 999.99;  // dB
      else
          pathLoss = (20*log(pathLength*distRatio)) +
(20*log(srcFreq2)) + 92.45;  // dB
      end
      pathLossVal = (10^(pathLoss/10))*1000;
      pathLossdBm = 10*log(pathLossVal);
      // Channel model
      rxSigStrength2 = txValdBm2 - pathLoss + rxGaindBm2;

      if ((dist1>distMin1AtAnimTime) & (dist1<distMax1AtAnimTime) &
(dist2>distMin2AtAnimTime) & (dist2<distMax2AtAnimTime)) then
        //haloSpace(xpos, ypos) = 1.0;
        haloSpace(xpos, ypos) = (rxSigStrength1-rxThrshdBm1) +
(rand()*noiseLevel1) + (rxSigStrength2-rxThrshdBm2) +
(rand()*noiseLevel2);
        valid = 1;
        if (haloSpace(xpos, ypos)<-90) then
            haloSpace(xpos, ypos)= 0.0;
            valid = 0;
        end
      end
   end
end

//aa=scf(1);
//contour (x, y, haloSpace, [0.0, 1.0]);
// Chart 1: 3D plot of the HALO space
if (valid == 1) then
```

```
  a=scf(1);
  //contour (x, y, haloSpace, [0.0, 1.0]);
  //plot3d (x, y, haloSpace);
  contour (x, y, haloSpace, [200, 190, 180, 170, 160, 150, 140, 130,
120, 110, 100, 90, 80, 70, 60, 50, 40, 30, 20, 10, 0, -10, -20, -30,
-40, -50, -60, -70, -80, -90, -100, -110, -120, -130, -140, -150, -
160, -170, -180, -190, -200, -210, -220, -230, -240, -250, -260, -
270, -280, -290, -300, -310, -320, -330, -340, -350, -360, -370, -
380, -390, -400]);
end


// Chart 2: Contour  plot of the HALO space
b=scf(2);
contour (x, y, haloSpace, [200, 190, 180, 170, 160, 150, 140, 130,
120, 110, 100, 90, 80, 70, 60, 50//, 40, 30, 20, 10, 0, -10, -20, -
30, -40, -50, -60, -70, -80, -90, -100, -110, -120, -130, -140, -
150//, -160, -170, -180, -190, -200, -210, -220, -230, -240, -250, -
260, -270, -280, -290, -300, -310, -3//20, -330, -340, -350, -360, -
370, -380, -390, -400]);

// Chart 3: plot the signal strength for an aircraft flying at a
fixed altitude
c=scf(3);
plAlt=18; //km
for xy=1:1:500
    xpl(xy)=-145;
end
for xx=175:1:325
    xpl(xx-174)=haloSpace(xx, plAlt);
end
plot(xpl);

// Chart 4: plot the signal strength for an aircraft flying a zoomy
d=scf(4);
plXPos=150; //km
for xy=1:1:500
    xpl(xy)=-145;
end
for xy=16:1:110
    xpl(xy-15)=haloSpace(plXPos, xy);
end
plot(xpl);

end
```

This page intentionally blank to aid printing.